



PhD-FSTM-2025-076  
The Faculty of Science, Technology and Medicine

## DISSERTATION

Defence held on 29/08/2025 in Luxembourg

to obtain the degree of

DOCTEUR DE L'UNIVERSITÉ DU LUXEMBOURG

EN *PHYSIQUE*

by

Nikolay POPOV

Born on 19 June 1994 in Tvardita, Moldova

## IMPACT OF NONIONIC STABILIZERS AND IONIC SOLUTES ON LIQUID CRYSTAL SHELL STABILITY AND DEFECT CONFIGURATION

### Dissertation defence committee

Dr. Jan P. F. Lagerwall, dissertation supervisor  
*Professor, Université du Luxembourg*

Dr Anupam Sengupta, Chairman  
*Associate Professor, Université du Luxembourg*

Dr. Kirsten Harth  
*Professor, Technische Hochschule Brandenburg*

Dr. Linda Hirst  
*Professor, University of California Merced*

Dr. Nicholas Abbott  
*Professor, Cornell University*





University of Luxembourg

Doctoral Thesis

Impact of nonionic stabilizers and ionic solutes on  
liquid crystal shell stability and defect configuration

*Author:*

Nikolay Popov

*Supervisor:*

Prof. Dr. Jan P. F. Lagerwall

*A thesis submitted in partial fulfillment of the requirements*

*for the degree of*

*Doctor of Philosophy in Physics*

*Department of Physics & Materials Science*

*Faculty of Science, Technology and Medicine*

*University of Luxembourg*

**August 2025**





## **Doctoral Dissertation**

Department of Physics & Materials

Science

University of Luxembourg

### **Supervisor:**

Dr. Jan P. F. Lagerwall

Department of Physics & Materials Science, University of Luxembourg

### **Jury / Promotionskommission:**

Dr. Anupam Sengupta (Chair)

Dr. Jan P. F. Lagerwall (Supervisor)

Dr. Kirsten Harth

Dr. Linda Hirst

Dr. Nicholas Abbott

**Date of defense:** 29.08.2025



*“Science knows no country because knowledge belongs to humanity and is the torch which illuminates the world. Science is the highest personification of the nation because that nation will remain the first which carries the furthest the works of thought and intelligence.”*

*Louis Pasteur (1822–1895)*



# Acknowledgments

First and foremost, I would like to express my sincere gratitude to my supervisor, Professor Jan Lagerwall, whose guidance has been instrumental throughout my PhD. His deep expertise, broad perspective, and extensive professional network have helped shape the interdisciplinary direction of this research and opened many doors for collaboration. I am especially grateful for the independence he gave me to pursue my own ideas and for his patience and encouragement during both successful and challenging periods; beyond academic support, his mentorship has greatly influenced my growth as a scientist and as a person.

I would also like to thank the members of my thesis jury, Professor Anupam Sengupta (chair), Professor Kirsten Harth, Professor Nicholas Abbott, and Professor Linda Hirst, for their time, careful reading of my dissertation, and constructive feedback that helped improve this work. I am especially grateful to Professor Abbott and Professor Hirst for their encouragement and thoughtful guidance over the course of my doctoral studies.

I warmly thank my colleagues in the ESMP group for their collaboration, insightful discussions, and daily support. I am also grateful to the broader Physics & Materials Science department for fostering a stimulating and supportive research environment. I am sincerely thankful to the University of Luxembourg for its excellent facilities and strong institutional support.

A special word of thanks goes to my undergraduate supervisor, Professor Nadezhda Vasilyevna Usol'tseva, whose early mentorship laid the foundation for my academic

path. She was the first to show me how engaging, rigorous, and rewarding scientific work can be, and her enthusiasm for careful experimentation and clear thinking has remained a lasting example for me.

I am deeply grateful to my loving parents, Valentina and Nicolai, whose unwavering belief in me and quiet perseverance have been a constant source of support and inspiration. I also thank my siblings for their constant support. I am especially grateful to my brother Peter, who first sparked my curiosity in liquid crystal materials, with whom I have shared many memorable trips and conversations, and who has remained a patient listener and thoughtful adviser throughout this journey, and to my sister Maia, whose encouragement, confidence in me, and the time we have been able to spend together despite the distance have been a source of strength and joy.

## Copyright and permissions

Several figures and schematic illustrations in this thesis have been redrawn or adapted from previously published material. Where possible, I have used open-access articles published under Creative Commons Attribution (CC BY 4.0) licenses, including those from MDPI and other publishers; these sources are indicated in the relevant figure captions and references. All such material is used in accordance with the terms of the respective licenses, with full acknowledgment of the original authors and publishers.

Some additional figures have been reproduced, and where appropriate slightly adapted, from articles published by the American Physical Society, Elsevier, the American Chemical Society, and The Royal Society of Chemistry under reuse licenses obtained by the author. The corresponding sources and acknowledgments are given in the figure captions and bibliography, and all such material is reused in accordance with the respective license terms, with gratitude to the original authors and publishers.

# Abstract

Liquid crystals combine fluidity with long-range molecular order and respond sensitively to interfaces, curvature, and chemical or biological species. Spherical liquid-crystal shells, where a thin nematic layer is confined between two aqueous phases, provide a platform for studying topological defects and for reconfigurable photonics and sensing. This thesis explores how nonionic polymer stabilizers and ionic solutes affect the stability, director-field configuration, and light-guiding behavior of nematic liquid-crystal shells.

The intrinsic birefringence of nematic shells enables polarization-controlled total internal reflection. Under suitable incident polarization, light is guided within the shell and emerges as bright spots for tangential anchoring and as rotating arcs for radial anchoring. These reflection signatures depend on refractive-index contrast and shell geometry and provide a simple, reflection-only route for distinguishing anchoring conditions using low-cost microscopy, without requiring transmission imaging.

We track the motion of topological defects in tangentially aligned shells as the director field anneals under buoyancy-induced wall-thickness gradients. Both unit-strength  $+1$  and half-strength  $+\frac{1}{2}$  surface defects migrate toward the thinner hemisphere during this relaxation. By varying the concentration and degree of hydrolysis of poly(vinyl alcohol), we show that moderately hydrolyzed polymer permits gravity-driven annealing, whereas highly hydrolyzed polymer suppresses this relaxation and leaves shells partitioned into defect-rich microdomains, consistent with stronger interfacial anchoring and a more rigid adsorbed layer.

A kinetic description of shell stability as a function of polymer concentration accounts for both shell collapse and fusion events. We develop a coupled kinetic scheme that describes frequent shell rupture (“popping”) and the much rarer fusion events that can precede it, focusing on the dominant rupture pathway while incorporating representative fusion rates. This analysis shows how encounter frequencies depend on interfacial polymer coverage and how stabilizer content governs shell lifetimes.

Electrolyte composition and bacterial lipopolysaccharide can further restructure director fields and optical textures in polymer-stabilized shells. Adding a saline buffer to the aqueous phases, thereby increasing the ionic strength, is associated with a shift in defect populations from configurations dominated by positive half-strength defects toward textures with a higher fraction of  $+1$  defects. This evolution is interpreted using our proposed interfacial capacitor picture: a curvature-induced asymmetry between inner and outer electrical double layers generates internal fields that may promote additional defect coalescence in thin regions. Preliminary observations indicate that amphiphilic lipopolysaccharide molecules can nucleate lipid-rich domains across the shells, including cases where domains appear to emerge from defect cores; these domains can then grow and migrate along shell-thickness gradients, lowering elastic and interfacial free energy.

Taken together, the results show that nonionic polymers and ionic solutes reshape director fields in nematic liquid-crystal shells and thereby tune light guiding, defect dynamics, shell lifetimes, and biochemical response. Collectively, these optical, mechanical, and interfacial controls support the use of nematic shells as soft, reconfigurable photonic and biosensing materials.

**Keywords:** nematic liquid-crystal shells; topological defects; director-field annealing; shell stability; total internal reflection; poly(vinyl alcohol); coaxial microfluidics; electrolytes; lipopolysaccharide; biosensing.

# Acronyms

## *Liquid-crystal materials and theory*

<b>LC</b>	Liquid crystal
<b>5CB</b>	4-cyano-4'-pentylbiphenyl
<b>E7</b>	Eutectic nematic LC mixture (5CB, 7CB, 8OCB, 5CT)
<b>LdG</b>	Landau-de Gennes theory

## *Surfactants and interfacial additives*

<b>SDS</b>	Sodium dodecyl sulfate
<b>PVA</b>	Poly(vinyl alcohol)
<b>Tween 20</b>	Nonionic surfactant (Polysorbate 20)
<b>CMC</b>	Critical micelle concentration
<b>HLB</b>	Hydrophilic-lipophilic balance

## *Optical and microscopic techniques*

<b>POM</b>	Polarizing optical microscopy
<b>OPD</b>	Optical path difference

## *Bioassay and endotoxin detection*

<b>LPS</b>	Lipopolysaccharide
<b>LAL</b>	Limulus amebocyte lysate endotoxin assay
<b>RT</b>	Room temperature ( $\approx 25^\circ\text{C}$ )

## *Electrolytes and interfacial electrostatics*

<b>PBS</b>	Phosphate-buffered saline
<b>EDL</b>	Electrical double layer (Stern + diffuse layers)



# Publications and conference contributions

The list below comprises peer-reviewed articles and conference contributions from this PhD project (2021–2025); all conference talks and posters were presented by the author.

## Peer-reviewed articles

1. Popov, N.; Lagerwall, J.P.F. *Birefringence-modulated total internal reflection in liquid-crystal shells*. *Front. Soft Matter* **2022**, 2, 991375.
2. Najiya, N.\*; Popov, N.\*; Jampani, V.S.R.; Lagerwall, J.P.F. *Continuous flow microfluidic production of arbitrarily long tubular liquid crystal elastomer peristaltic pump actuators*. *Small* **2023**, 18, 2204693.

## Conference contributions

- **Oral — ILCC 2024**, Rio de Janeiro (BR), Jul 2024: *Kinetics of annealing of LC shells vs. wall thickness*. Popov, N.; Lagerwall, J.P.F.
- **Oral — GLCC 2023**, Stuttgart (DE), Mar 2023: *Arbitrarily long tube-shaped LCE actuators*. Popov, N.; Najiya, N.; Jampani, V.S.R.; Lagerwall, J.P.F.
- **Poster — GRC 2023**, Manchester, NH (US), Jun 2023: *Synergistic effects of surfactants and amino acids on LC alignment*. Popov, N.; Lagerwall, J.P.F.
- **Poster — MRT/DPhyMS PhD Day 2022**, Luxembourg (LU), Apr 2022: *Microfluidic production and stabilization of LC shells*. Popov, N.; Jampani, V.S.R.; Lagerwall, J.P.F.

---

\* Shared first authorship.



# Contents

<b>Acknowledgments</b>	<b>iii</b>
Copyright and permissions . . . . .	iv
<b>Abstract</b>	<b>v</b>
<b>Acronyms</b>	<b>vii</b>
<b>Publications and conference contributions</b>	<b>ix</b>
<b>1 Introduction and overview</b>	<b>1</b>
1.1 Motivation and main results . . . . .	1
1.2 Structure of the thesis . . . . .	4
<b>2 Fundamentals of nematic liquid crystals</b>	<b>5</b>
2.1 Liquid crystals: basics . . . . .	5
2.2 Liquid crystal classification . . . . .	6
2.3 Overview of liquid–crystalline phases . . . . .	8
2.4 Oseen–Frank elastic free energy density . . . . .	10
2.5 Anchoring energy . . . . .	12
2.6 LC optical anisotropy: birefringence . . . . .	14
2.7 Polarizing optical microscopy . . . . .	19
2.8 Topological defects . . . . .	21
2.9 Nematic LCs in electric fields . . . . .	23

2.9.1	LC droplets: bipolar vs. radial . . . . .	24
2.9.2	Electric-field response of droplets . . . . .	25
2.9.3	LC shells in electric fields . . . . .	27
<b>3</b>	<b>Liquid crystal–water interfaces</b>	<b>31</b>
3.1	Liquid-crystal shells . . . . .	31
3.1.1	Anchoring at LC–water interfaces: canonical textures . . . . .	33
3.2	PVA as a stabilizer for LC shells . . . . .	34
3.2.1	Mechanism and magnitude . . . . .	34
3.2.2	Adsorption kinetics . . . . .	35
3.3	Electrolytes at nematic LC–water interfaces . . . . .	39
3.3.1	Electrolytes and LC films . . . . .	40
3.3.2	Electrolytes and LC droplets . . . . .	41
3.3.3	Electrolytes and LC shells . . . . .	42
3.3.4	Summary: fields and electrolytes at LC–water interfaces . . . . .	44
3.4	Water-dissolved amphiphiles: relevance to biosensors . . . . .	45
3.4.1	Generic structure of amphiphilic molecules . . . . .	45
3.4.2	Packing parameter in aqueous self-assembly . . . . .	49
3.4.3	Lipopolysaccharides: biological relevance and overview . . . . .	51
3.4.4	Molecular architecture of LPS . . . . .	52
3.4.5	Critical aggregation of LPS (operational “CMC”) . . . . .	55
3.5	Bio- and chemosensors . . . . .	58
3.5.1	Historical background . . . . .	58
3.5.2	Wearable applications and market context . . . . .	60
3.5.3	Market landscape and validation . . . . .	60
3.5.4	Liquid crystal–based sensors . . . . .	61
3.5.5	Summary of LC-based sensing mechanisms . . . . .	67

<b>4</b>	<b>Reflection-mode POM in nematic LC shells</b>	<b>69</b>
4.1	Tangential alignment: transmission vs. reflection . . . . .	72
4.1.1	Appearance in transmission mode . . . . .	72
4.1.2	Appearance in reflection mode . . . . .	73
4.2	Radial alignment: transmission vs. reflection . . . . .	75
4.2.1	Appearance in transmission mode . . . . .	75
4.2.2	Appearance in reflection mode . . . . .	76
4.3	Total internal reflection and light guiding in nematic shells . . . . .	77
4.3.1	Origin of TIR-mediated light guiding . . . . .	77
4.3.2	Implications for shell characterization and applications . . . . .	78
4.4	Summary and outlook . . . . .	80
<b>5</b>	<b>Annealing kinetics of director fields in nematic shells</b>	<b>83</b>
5.1	Shell preparation and annealing metrics . . . . .	85
5.1.1	Shell production and imaging . . . . .	85
5.1.2	Thickness batches and definition of the annealing time . . . . .	86
5.2	Annealing in shells with moderately hydrolyzed PVA . . . . .	87
5.2.1	Defect dynamics in shells . . . . .	87
5.2.2	Annealing time versus wall thickness . . . . .	92
5.3	Discussion: annealing kinetics and scaling . . . . .	93
5.3.1	Exponential-with-offset relaxation of defect separations . . . . .	93
5.3.2	Scaling argument for the characteristic annealing time . . . . .	95
5.3.3	Unified relations between different defect–pair separations . . . . .	97
5.3.4	Summary and outlook for moderately hydrolyzed PVA . . . . .	98
5.4	Director fields in shells with highly hydrolyzed PVA . . . . .	100
5.4.1	Effect of PVA concentration . . . . .	101
5.4.2	Robustness of shells across nematic–isotropic cycles . . . . .	104
5.4.3	Hydrolysis-dependent adsorption and PVA crystallization . . . . .	106
5.4.4	Mechanistic hypotheses . . . . .	107

5.4.5	Liquid-crystal shells as optical reporters . . . . .	108
5.5	Implications for LC shell biosensing . . . . .	108
5.5.1	Hypothesis: shell vulnerability in the isotropic state . . . . .	109
5.5.2	Summary and outlook for highly hydrolyzed PVA . . . . .	109
5.6	Overall conclusions for PVA-stabilized LC shells . . . . .	110
<b>6</b>	<b>Lifetimes of nematic shells</b>	<b>111</b>
6.1	Initial analysis of nematic-shell lifetimes . . . . .	112
6.2	Shell stability at minimum PVA concentrations . . . . .	114
6.2.1	Collapse of shells at ultra-low PVA concentrations . . . . .	115
6.2.2	Shell–droplet fusion at ultra-low PVA concentrations . . . . .	117
6.2.3	Shell–shell fusion at ultra-low PVA concentrations . . . . .	118
6.2.4	Theoretical kinetic model for shell popping and fusion . . . . .	119
6.2.5	Kinetic pathways . . . . .	121
6.2.6	Expected curves for reasonable rate values . . . . .	121
6.2.7	Analyzing the popping rates of 5CB shells . . . . .	123
6.3	Summary and outlook . . . . .	126
<b>7</b>	<b>Electrolyte and endotoxin effects in nematic shells</b>	<b>129</b>
7.1	Electrolyte effects on nematic shells . . . . .	131
7.1.1	Ionic-strength effects on shell director fields . . . . .	131
7.1.2	Curvature-modulated interfacial “capacitor” model . . . . .	134
7.1.3	Effect of PBS ions on PVA anchoring . . . . .	140
7.2	Impact of LPS on LC ordering in shells . . . . .	140
7.2.1	Shells without PVA: defect-seeded lipid islands . . . . .	141
7.2.2	Slow LPS island nucleation in PVA-stabilized shells . . . . .	143
7.3	Summary and outlook . . . . .	147
<b>8</b>	<b>Overall conclusions and outlook</b>	<b>151</b>

<b>Appendices</b>	<b>155</b>
<b>A Microfluidic device fabrication and shell production</b>	<b>157</b>
A.1 Capillary preparation and device assembly . . . . .	157
A.1.1 Cutting capillaries . . . . .	157
A.1.2 Surface treatment of capillaries . . . . .	159
A.2 Shell production . . . . .	160
<b>B Counting shells and droplets</b>	<b>163</b>
<b>C Coupled kinetic model for 5CB shells</b>	<b>169</b>
<b>References</b>	<b>172</b>



# Chapter 1

## Introduction and overview

### 1.1 Motivation and main results

This thesis describes how nonionic polymer stabilizers and ionic solutes influence the director fields, stability, and optical response of nematic liquid-crystal (LC) shells. Double-emulsion 5CB shells provide a curved, tunable geometry in which anchoring, shell thickness, gravity, and electrostatics all compete to organize topological defects. Compared with classical flat LC cells and droplets, shells offer additional handles — curvature, shell asymmetry, and two coupled LC–water interfaces — that can be used to program defect locations and optical signatures, but they also introduce new challenges for stabilization and control.

Chapters 2 and 3 provide the theoretical and experimental background for this work. Chapter 2 reviews key concepts in LC physics and optics, including elasticity, interfacial anchoring, topological defects, birefringence, polarizing optical microscopy, and the electric-field response of nematic droplets and shells. These concepts are used throughout the thesis to interpret how the director field responds to stabilizers, ionic solutes, and curvature. Chapter 3 focuses on LC–water interfaces and components relevant to biosensing: it details the formation and stabilization of LC shells as water–5CB–water double emulsions, discusses the roles of PVA stabilizers

and electrolytes at LC–water interfaces, and introduces representative biological amphiphiles such as lipopolysaccharides. It also outlines the landscape of LC-based bio- and chemosensors and provides the conceptual background needed to understand the questions addressed in the subsequent chapters.

Chapters 4–7 contain the core research contributions. Chapter 4 shows that shell birefringence can be harnessed for polarization-controlled total internal reflection, enabling guided optical modes in achiral nematic shells. The resulting bright spots and rotating arcs in reflection provide a simple, robust signature of tangential versus radial anchoring that complements, and in some contexts can replace, conventional transmission-mode polarizing microscopy. Chapter 5 then quantifies the “annealing” of director fields containing topological defects. For shells stabilized with moderately hydrolyzed PVA (87–89 %), gravity-induced wall-thickness gradients drive  $+1$  and  $+\frac{1}{2}$  defects toward the thinner upper hemisphere, and the time-dependent defect separations follow exponential-with-offset kinetics, defining a characteristic annealing time that depends on shell thickness. In contrast, shells stabilized with highly hydrolyzed PVA ( $\geq 98\%$ ) also exhibit tangential anchoring but essentially no annealing of the director field: numerous defects, mostly  $\pm\frac{1}{2}$ , remain nearly immobile and form defect-rich microdomains across the surface, pointing to strong interfacial pinning, plausibly associated with shear-induced PVA crystallization at the LC surface.

In Chapter 6, we turn to shell stability. Within the low-concentration PVA regime, we show that shell lifetimes range from tens of minutes at the lowest stabilizer levels to many hours and up to several weeks as the PVA content is increased. Experiments reveal that shell decay is not purely exponential in time (especially at very low stabilizer concentrations) and that rare fusion events occur between shells and between shells and droplets when stabilizer coverage is very low. To rationalize these behaviors, we introduce a coupled kinetic model that includes shell rupture, shell–droplet fusion, shell–shell fusion, and subsequent rupture of mixed shells. This

model captures both the dominant rupture (“popping”) pathway and the rare fusion pathways. It provides a fitted rate constant for the main rupture process and uses representative order-of-magnitude values for the much rarer fusion events; together, these parameters encode how interfacial polymer coverage sets the frequency of shell–shell and shell–droplet encounters.

Chapter 7 explores biochemical responsiveness by comparing shells formed in aqueous PVA solution with shells formed in saline buffer (PBS), with and without PVA, and by introducing bacterial endotoxin (LPS). In PBS, we find that ionic strength shifts defect patterns in tangentially anchored shells: populations dominated by four  $+\frac{1}{2}$  defects give way to mixed states with more  $+1$  defects and occasional  $+\frac{3}{2}$ -like configurations. We propose a curvature-selective interfacial-capacitor hypothesis to rationalize these trends, in which even a small imbalance between inner and outer electrical double layers produces a thickness-modulated internal field that can promote defect coalescence in the thinnest regions of asymmetric nematic shells. In shells exposed to LPS, preliminary observations suggest that lipid-rich microdomains can nucleate at or near defect cores and then migrate along shell-thickness gradients, echoing defect-seeded lipid islands reported for other amphiphiles but with time scales and coverage thresholds that appear specific to LPS and PVA-stabilized interfaces.

Finally, Chapter 8 connects these topics and highlights how the four strands — reflection-based light guiding, defect annealing under gravity and PVA, shell stability under dilute stabilizer conditions, and electrolyte/LPS-induced textural changes — fit together into a unified picture of how nonionic stabilizers and ionic solutes shape the behavior of nematic LC shells. Technical details and numerical methods are presented in the appendices.

## 1.2 Structure of the thesis

The remainder of this thesis is organized as follows.

- **Chapter 2** reviews the fundamentals of nematic liquid crystals and polarizing microscopy used throughout the thesis.
- **Chapter 3** introduces LC–water interfaces, shell production, and materials relevant to biosensing, including PVA, electrolytes, and LPS.
- **Chapter 4** presents reflection-mode POM studies of nematic shells based on birefringence-modulated total internal reflection.
- **Chapter 5** analyzes the annealing kinetics of director fields in tangentially aligned shells stabilized by PVA.
- **Chapter 6** investigates the lifetimes of shells stabilized by low PVA concentrations and introduces a coupled kinetic model for shell collapse and fusion.
- **Chapter 7** explores how electrolytes and LPS reshape director-field textures in nematic shells.
- **Chapter 8** summarizes the overall conclusions of the thesis and outlines perspectives for nematic LC shells in reconfigurable optics and biosensing.
- **Appendices** compile additional experimental procedures, device-fabrication details, image-analysis routines, and numerical implementations that support the main chapters.

## Chapter 2

# Fundamentals of nematic liquid crystals and polarizing microscopy

This chapter presents key principles and topics relevant to this thesis, with a focus on nematic liquid crystals. It reviews essential concepts, definitions, and phenomena used in the following chapters.

### 2.1 Liquid crystals: basics

Liquid crystals (LCs) were first observed in 1888 by the Austrian botanist Friedrich Reinitzer, who discovered the double melting points of cholesteryl benzoate [1]. The substance first became a milky fluid at  $145.5^{\circ}\text{C}$  and then cleared again at  $178.5^{\circ}\text{C}$  [2]. Reinitzer sought help from the German physicist Otto Lehmann, who used a polarizing microscope to confirm that the fluid exhibited optical anisotropy similar to that of a crystalline solid. Lehmann reported this new phenomenon in 1889 in his paper “Über fließende Krystalle” (“On flowing crystals”) [3].

Liquid crystals constitute a state of matter that exists between the crystalline solid phase and the ordinary (isotropic) liquid phase. They flow like liquids, yet maintain long-range orientational order reminiscent of crystals. This intermediate behavior defines the **mesomorphic state** (or **mesophase**), which typically occurs

between the solid (Cr) and isotropic (Iso) states over specific temperature ranges. Molecules or particles capable of producing such behavior are called **mesogens** [4].

## 2.2 Liquid crystal classification

LCs are classified into two broad types: thermotropic and lyotropic [5]. Thermotropic LCs change phase in response to temperature alone, while lyotropic LCs form mesophases primarily in response to mesogen concentration in a solvent exceeding a critical threshold (Fig. 2.1), with their stability and phase type only secondarily affected by temperature [6]. Thermotropic LCs are typically water-insoluble, enabling

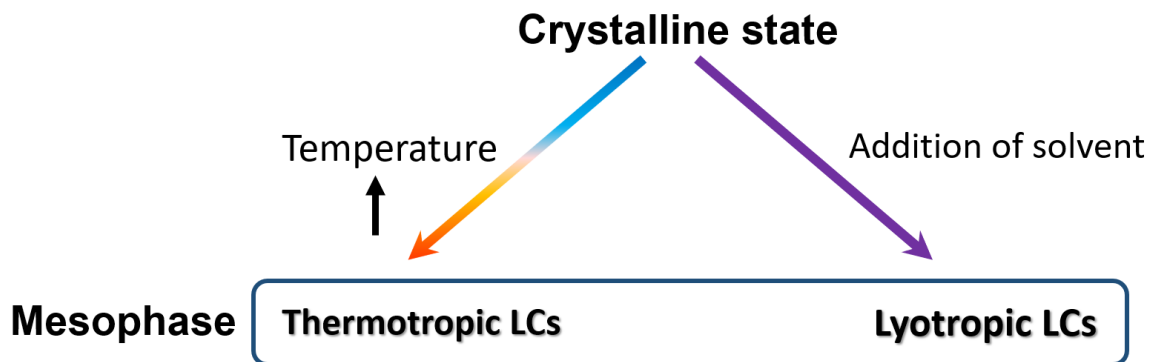


Figure 2.1: Simple representation of phase transitions from the crystalline state to the thermotropic and lyotropic mesophases.

a stable aqueous/LC interface that can be functionalized for molecular recognition. Both classes comprise anisotropic molecules — rod-like (calamitic) or disc-shaped (discotic) — that self-assemble into phases exhibiting long-range orientational and/or positional order. Their optical anisotropy gives rise to birefringence<sup>1</sup>, a key property utilized in LC-based optical devices. This microscopic-to-macroscopic link was already noted in the early theory by Max Born [9].

In this thesis, the focus is on **calamitic LCs**, a key class of mesogens characterized by their elongated, rod-like molecular shape. The molecular length ( $l$ ) is the extension

<sup>1</sup> Birefringence (double refraction) is the splitting of a light beam into an ordinary (o) and an extraordinary (e) wave with indices  $n_o$  and  $n_e(\theta)$ , respectively; here  $\theta$  is the angle between the wave normal  $\mathbf{k}$  and the optic axis (measured in the plane containing both); see Sec.2.6 [7, 8].

along the axis of highest rotational symmetry (the long molecular axis), while the molecular width ( $w$ ) is the dimension perpendicular to this axis. Calamitic mesogens typically consist of a rigid (hetero)aromatic core with one or two flexible terminal chains; a polar terminal group (e.g., -CN) is often present, and lateral substituents may also be found. The rigid elongated core contributes to shape anisotropy, whereas flexible terminal chains impart flexibility (Fig. 2.2). Such rod-like mesogens typically have a length-to-width ratio of about 5 or more.

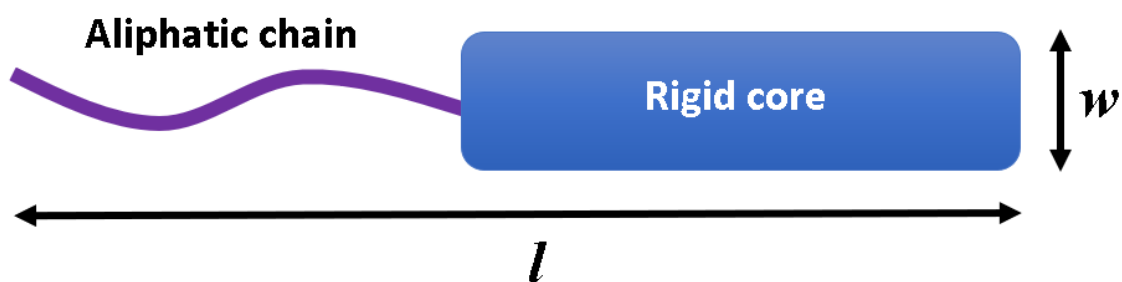


Figure 2.2: Simplified schematic of a calamitic mesogen with a rigid core (typically aromatic) and a flexible aliphatic chain. Some calamitic mesogens, however, carry two terminal chains attached on opposite sides of the core.

This thesis primarily uses 4-cyano-4'-pentylbiphenyl (5CB), a widely used nematic liquid crystal. Its cyanobiphenyl-based asymmetric structure gives 5CB a large dielectric anisotropy and a strong electric dipole moment, in contrast to more symmetric rod-like nematics. The extended linear aromatic structure (biphenyl + cyano termination) influences 5CB's electro-optical properties, including significant birefringence ranging from 0.15 to 0.21 in the THz frequency range [10], making 5CB effective for applications involving modulation and polarization control of electromagnetic radiation.

In the nematic phase, 5CB molecules often adopt an antiparallel arrangement, aligning their cyanobiphenyl cores in opposite directions to minimize the net dipole and to enhance aromatic  $\pi$ - $\pi$  stacking [11, 12]; see Fig. 2.3. This tendency to dimerize and its high supercooling ability, where it remains in the nematic phase below its melting point of 23 °C, reflect its unique molecular structure and distinguish

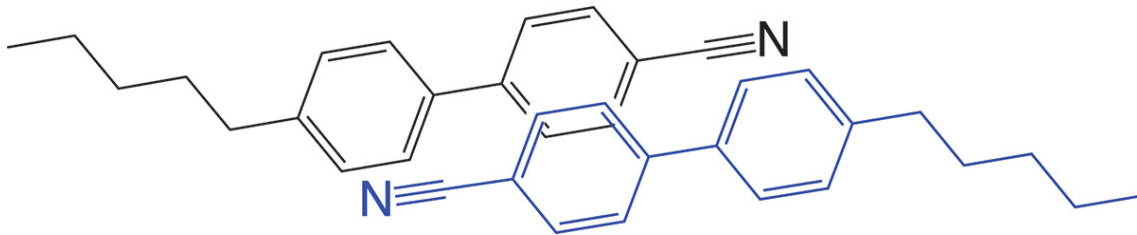


Figure 2.3: Illustration of the spontaneous antiparallel dimerization of 5CB molecules, which maximizes aromatic overlap. The resulting dimer follows the classic Vorländer mesogen architecture, with a rigid central core flanked by flexible terminal chains [13], licensed under CC BY 4.0.

it from symmetric rod-like LCs [13]. The latter typically have more predictable phase transitions and do not exhibit the same level of supercooling. The molecular length is typically a few nanometers for common calamitic mesogens. The mesophases exhibit both orientational order of molecules, similar to that in crystalline solids, and fluidity, characteristic of isotropic liquids.

## 2.3 Overview of liquid–crystalline phases

In the nematic phase<sup>2</sup>, elongated molecules align on average along a common direction, the director  $\mathbf{n}$ , and the material flows as a liquid [5]. Figure 2.4 schematizes the liquid–crystalline phases of a calamitic thermotropic LC [4, 14].

The measure of collective orientational alignment in an LC ensemble is the order parameter, denoted by  $S$ . It is mathematically defined as

$$S = \frac{1}{2} \langle 3 \cos^2 \delta - 1 \rangle. \quad (2.1)$$

Here  $\delta$  is the angle between a molecule’s long axis and the local director, and  $\langle \cdot \rangle$  denotes a temporal or spatial average over all molecules. The order parameter provides a macroscopic measure of molecular directional alignment. In theory, the value of  $S$  ranges from  $-0.5$  to  $1$ , where negative values correspond to oblate (antinematic)

<sup>2</sup> Nematic phase: a fluid mesophase with long-range orientational (three-dimensional) order but no long-range translational order [6, 14].

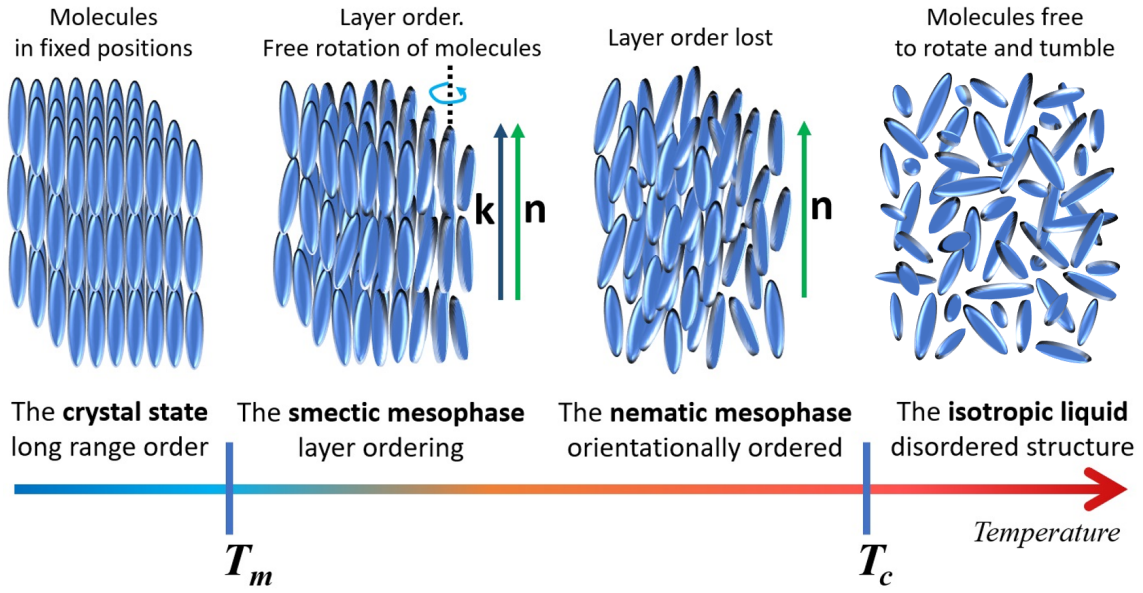


Figure 2.4: The schematic depicts the collective arrangement of molecules in various phases of a calamitic thermotropic LC, ranging from the crystal state and the melting point ( $T_m$ ) to the clearing point ( $T_c$ ), followed by isotropic liquid. The director  $\mathbf{n}$  is the average molecular orientation, while  $\mathbf{k}$  denotes the layer normal in smectic mesophases (shown for completeness — many LCs do not form smectic phases).

alignment — that is, when long molecular axes are on average perpendicular to the director. A completely disordered state, like that of an isotropic liquid, has an order parameter of 0, while a perfectly positively ordered crystalline solid has  $S = 1$ . For nematic LCs,  $S$  typically lies between 0.4 and 0.6 and decreases as temperature increases.

For temperatures below the clearing transition  $T_c$ , the relationship between the order parameter  $S$  and the ambient temperature  $T$  is often modeled as

$$S(T) = \left(1 - \frac{T}{T^*}\right)^\beta, \quad (2.2)$$

where  $T^*$  is a mean-field fit parameter close to  $T_c$ , and  $\beta$  is a material- and temperature-dependent constant that is typically near 0.5 in mean-field approximations. The degree of orientational order influences a variety of physical properties in LCs, including their refractive indices, dielectric behavior, magnetic properties, elasticity, and viscosities.

This thesis focuses on thermotropic liquid crystals, which transition from the melting point ( $T_m$ ) to the clearing point ( $T_c$ ) upon heating (Fig. 2.4). The clearing point describes the shift from a turbid to a clear liquid, as first noted by Reinitzer.

## 2.4 Oseen–Frank elastic free energy density

Within the nematic mesophase, spontaneous symmetry breaking gives rise to a unit director field  $\mathbf{n}(\mathbf{r}) \equiv -\mathbf{n}(\mathbf{r})$  that can adopt any orientation and vary with position. The free energy increases with spatial distortions of  $\mathbf{n}$ . This bulk contribution is the Oseen–Frank elastic free energy [15], which excludes surface effects. The total free energy is written as:

$$F = F_0 + F_{\text{Frank}} + F_s, \quad F_{\text{Frank}} = \int_V f(\mathbf{r}) dV, \quad F_s = \int_{\partial V} f_s(\mathbf{r}) dA, \quad (2.3)$$

where  $F_0$  collects all other contributions to the total free energy,  $f$  is the bulk Oseen–Frank energy density [ $\text{J}/\text{m}^3$ ], and  $f_s$  is the surface anchoring energy density [ $\text{J}/\text{m}^2$ ]. Here  $V$  denotes the LC volume (bulk) and  $\partial V$  its boundary (interfaces);  $dV$  and  $dA$  are the volume and area elements, respectively.

In a nematic bulk, three primary distortions of the director  $\mathbf{n}$  are distinguished — splay, twist, and bend (Fig. 2.5). The corresponding Oseen–Frank density is [15, 17]:

$$f(\mathbf{r}) = \frac{1}{2} [K_1(\nabla \cdot \mathbf{n})^2 + K_2(\mathbf{n} \cdot (\nabla \times \mathbf{n}))^2 + K_3(\mathbf{n} \times (\nabla \times \mathbf{n}))^2], \quad (2.4)$$

where  $K_1$ ,  $K_2$ , and  $K_3$  are the Frank elastic constants for splay, twist, and bend, respectively. For 5CB, typical values are  $K_1 = 0.6 \times 10^{-11} \text{ N}$ ,  $K_2 = 0.3 \times 10^{-11} \text{ N}$ , and  $K_3 = 1.0 \times 10^{-11} \text{ N}$  [18], so usually  $K_3 > K_1 > K_2$ . Because these constants are comparable in magnitude, a one-constant approximation  $K_1 = K_2 = K_3 \equiv K$  is

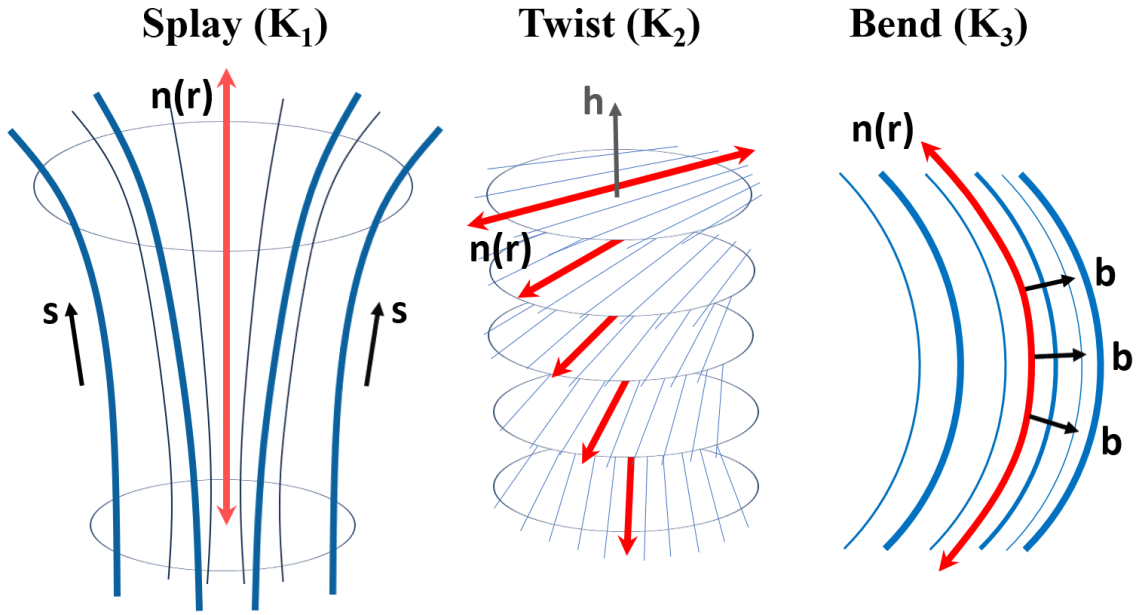


Figure 2.5: Schematics of the three elastic deformations of a nematic LC: splay, twist, and bend of the director field  $\mathbf{n}(\mathbf{r})$ . Double-headed red arrows indicate the apolar nature of the director. Redrawn from [16].

often used, yielding [4]:

$$f(\mathbf{r}) \approx \frac{1}{2} K \left[ (\nabla \cdot \mathbf{n})^2 + |\nabla \times \mathbf{n}|^2 \right]. \quad (2.5)$$

**Intuition.** Distorting the orientational order generates a restoring torque; near equilibrium this torque is linear in the deformation, and the Frank moduli  $K_1, K_2, K_3$  play the role of angular “spring constants” (units of N). In the one-constant approximation the density reduces to the continuum analog of Hooke’s law,  $f \simeq \frac{1}{2} K (\nabla \mathbf{n})^2$ .

*Remark (saddle-splay).* The term:

$$f_{24} = -K_{24} \nabla \cdot [(\mathbf{n} \cdot \nabla) \mathbf{n} - (\nabla \cdot \mathbf{n}) \mathbf{n}]$$

is a total divergence; upon integration it reduces to a surface contribution and is grouped with  $F_s$  unless explicitly needed.

## 2.5 Anchoring energy

**Surface anchoring energy** is the interfacial free energy (reversible work per unit area) that penalizes deviations from a preferred orientation (easy axis) of the LC director  $\mathbf{n}$  at a boundary. These boundary conditions couple to bulk deformations through the Frank elastic energy (Sec. 2.4). The characteristic distance over which surface alignment controls the interior is the *extrapolation length*  $\ell = K/W$ , where  $K$  is the relevant Frank elastic constant and  $W$  the corresponding anchoring strength ( $\text{J/m}^2$ ). For typical thermotropic nematics with  $K \sim 10^{-11}$  N and  $W \sim 10^{-6}$ – $10^{-4}$   $\text{J/m}^2$ , one finds  $\ell \sim 0.1$ – $10$   $\mu\text{m}$ . Thin (tens-of-micrometer) layers are usually well oriented, whereas optically thick cells (hundreds of micrometers to millimeters) can develop light scattering due to thermally excited director fluctuations [4, 19]. Beyond the director-level Frank–Oseen description used here, a tensorial Landau–de Gennes (LdG) Q-tensor framework can treat degenerate planar anchoring and surface-induced biaxiality [20]; we mention it for completeness.

Two anchoring contributions are distinguished (Fig. 2.6):

- **Polar (zenithal) anchoring** with coefficient  $W_\Theta$  ( $\text{J/m}^2$ ), penalizing deviations of the tilt angle  $\Theta$  from the surface normal relative to its preferred value  $\Theta_0$ .
- **Azimuthal anchoring** with coefficient  $W_\phi$  ( $\text{J/m}^2$ ), penalizing in-plane rotations by the angle  $\phi$  away from the preferred in-plane direction  $\phi_0$  (the penalty vanishes as  $\Theta \rightarrow 0$ ).

A convenient phenomenological description is the (anisotropic) Rapini–Papoular form for the surface anchoring energy density  $f_s$  [21]:

$$f_s(\Theta, \phi) = \frac{1}{2} [W_\Theta \sin^2(\Theta - \Theta_0) + W_\phi \sin^2\Theta \sin^2(\phi - \phi_0)], \quad (2.6)$$

which has units of  $\text{J/m}^2$ . The corresponding surface contribution is  $F_s$  from Eq. (2.3). In Eq. (2.6), the polar term reaches its maximum  $W_\Theta/2$  for  $|\Theta - \Theta_0| = 90^\circ$  (e.g.,

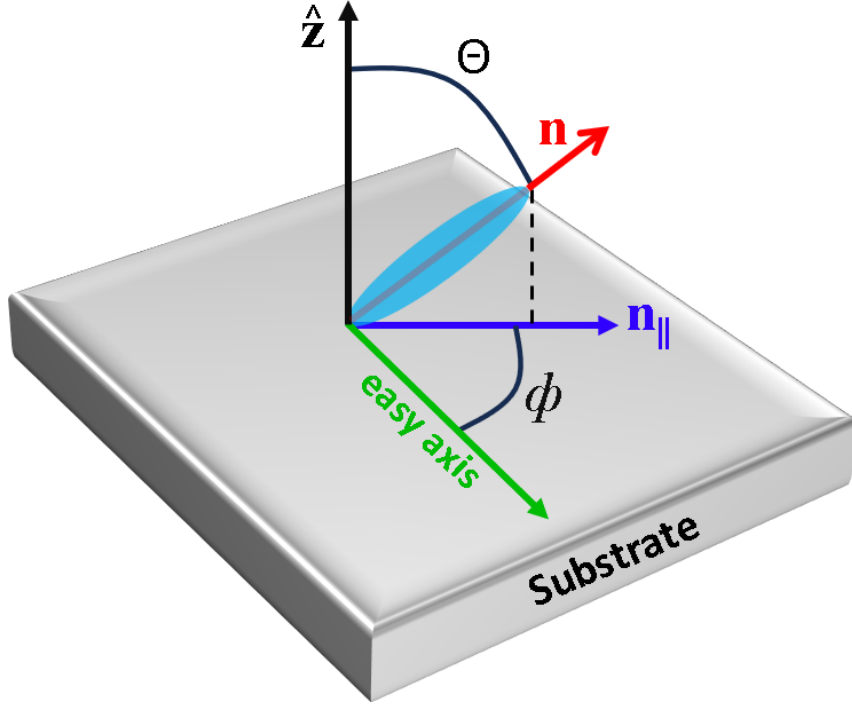


Figure 2.6: Schematic of the LC director  $\mathbf{n}$  at a surface. The polar (zenithal) angle  $\Theta$  is measured from the surface normal  $\hat{\mathbf{z}}$ ; the azimuthal angle  $\phi$  is measured in the substrate plane from the easy axis to the in-plane projection  $\mathbf{n}_{\parallel}$  of  $\mathbf{n}$ . Planar easy axis corresponds to  $\Theta_0 = 90^\circ$  (homeotropic  $\Theta_0 = 0^\circ$ ).

$\Theta = 0^\circ$  for a planar easy axis  $\Theta_0 = 90^\circ$ , or  $\Theta = 90^\circ$  for a homeotropic axis  $\Theta_0 = 0^\circ$ ). The azimuthal term reaches  $W_\phi/2$  for  $|\phi - \phi_0| = 90^\circ$  when the director lies in-plane ( $\Theta = 90^\circ$ ). Near the easy axis, the small-angle curvatures are  $W_\Theta$  in  $\Theta$  and  $W_\phi \sin^2 \Theta_0$  in  $\phi$  (equal to  $W_\phi$  for planar anchoring,  $\Theta_0 = 90^\circ$ ). In the strongly planar limit ( $\Theta_0 = 90^\circ$  and  $W_\Theta \gg W_\phi$ ),  $\Theta \simeq 90^\circ$  and Eq. (2.6) reduces to  $f_s \simeq \frac{W_\phi}{2} \sin^2(\phi - \phi_0) + \text{const}$ , i.e., only the in-plane misalignment is relevant.

For small deviations at a flat interface, the anchoring extrapolation lengths are:

$$\ell_\Theta = \frac{K_{\text{eff}}}{W_\Theta} \text{ (tilt)} \quad \ell_\phi = \frac{K_{\text{eff}}}{W_\phi} \text{ (in-plane rotation; if finite)}, \quad (2.7)$$

where  $K_{\text{eff}}$  is the mode-appropriate elastic constant (e.g.,  $K_{33}$  bend,  $K_{11}$  splay; one-constant:  $K_{\text{eff}} \approx K$ ). At clean LC–water interfaces (our base case), in-plane orientation is typically degenerate ( $W_\phi \approx 0$ ), so only  $W_\Theta$  sets the preferred tilt [22,23].

## 2.6 LC optical anisotropy: birefringence

Building on the previous discussion of nematic order, we now describe how this orientational order produces optical anisotropy and birefringence, with direction-dependent refractive indices and characteristic intensity patterns under crossed polarizers.

**Refractive index.** The refractive index  $n$  of a medium is the dimensionless ratio of the speed of light in vacuum to the phase velocity in that medium,  $n = c/v$ .

**Optical anisotropy and optic axis.** Optical anisotropy means that light interacts with a medium differently depending on its polarization and on the propagation direction relative to the material's internal structural order. In nematic LCs, the anisotropic molecular shape and long-range orientational order produce uniaxial optical behavior. A uniaxial medium has a single optic axis. For propagation along the optic axis (i.e., when the wave normal  $\mathbf{k}$  is parallel to it,  $\theta = 0$ ), the material still supports two distinct polarization eigenmodes, but for light whose electric field oscillates perpendicular to the director only the transverse eigenmode is excited. In this case the beam samples a single refractive index,  $n_e(0) = n_o = n_\perp$ , so the effective optical anisotropy for that propagation direction vanishes and no double refraction is observed (see Eqs. (2.9)–(2.10)). In regular nematics without optical activity, the director  $\mathbf{n}$  defines the optic axis [4].

**Optical indicatrix.** The optical indicatrix (index ellipsoid) is a geometric representation of how the refractive index varies with the direction of the wave normal  $\mathbf{k}$  [24]. For a uniaxial LC, it is an ellipsoid with principal indices  $n_\parallel$  (along the director/optic axis) and  $n_\perp$  (perpendicular); see Fig. 2.8b. Most thermotropic nematics are optically positive, with  $n_\parallel > n_\perp$  [14].

**Double refraction (birefringence).** Birefringence splits an incident beam into the ordinary (o) and extraordinary (e) eigenwaves [7, 8]. The o-wave experiences

a direction-independent index  $n_o$  (equal to  $n_{\perp}$ ), whereas the e-wave has an angle-dependent effective index  $n_e(\theta)$  set by the angle  $\theta$  between the wave normal  $\mathbf{k}$  and the optic axis (defined in their common plane; see Eqs. (2.9)–(2.10)). At an interface with an isotropic medium (e.g., air or glass), the o-wave refraction obeys **Snell's law** [7]:

$$n_1 \sin \theta_1 = n_2 \sin \theta_2, \quad (2.8)$$

where  $n_1$  and  $n_2$  are the refractive indices of the incident and transmitted media, and  $\theta_1$  and  $\theta_2$  are the angles of incidence and refraction measured from the surface normal; see Fig. 2.7. By contrast, the e-wave has an ellipsoidal index (normal) surface rather than a spherical one. As a result, the effective refractive index depends

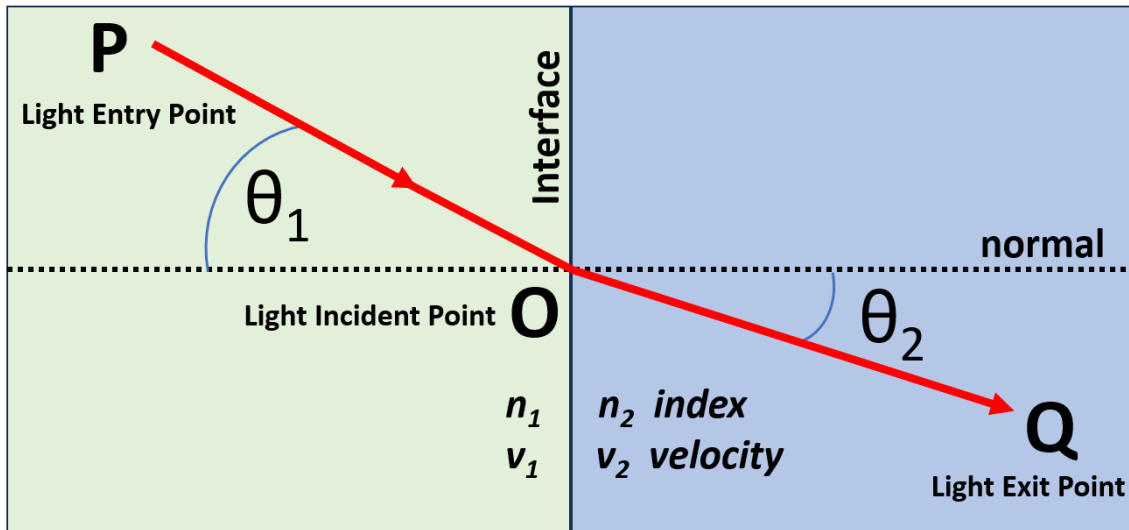


Figure 2.7: Snell's law at an isotropic interface with  $n_1 < n_2$  (Eq. 2.8).

on propagation direction and polarization, refraction becomes anisotropic, and the Poynting vector (energy flow per unit area) is generally not collinear with  $\mathbf{k}$ , which gives rise to beam walk-off [7], as illustrated by the o/e splitting in Fig. 2.8c [24].

**Molecular origin of optical anisotropy.** A representative mesogen (Fig. 2.8a) exhibits larger electronic polarizability along its long molecular axis than transverse to it. In the nematic phase, long-range orientational order amplifies this nanoscopic anisotropy of molecular polarizability to the optical scale, giving two principal refrac-

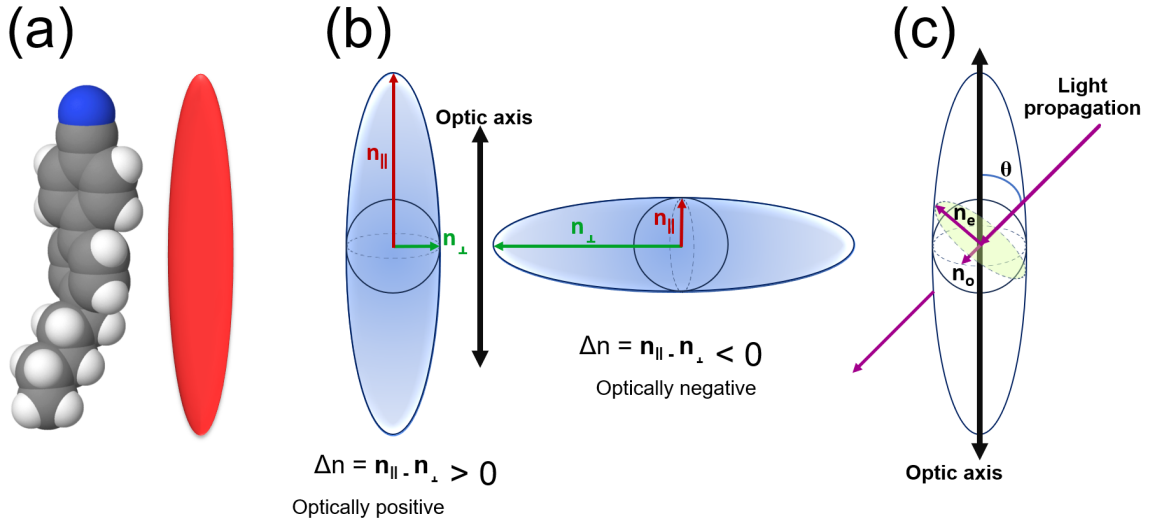


Figure 2.8: Optical anisotropy in a nematic LC. (a) Rotationally averaged ellipsoidal shape of a 5CB mesogen. (b) Uniaxial indicatrix: optically positive (left) and negative (right). (c) For incidence at angle  $\theta$  to the optic axis, the beam splits into ordinary ( $n_o$ ) and extraordinary ( $n_e(\theta)$ ) waves (Eqs. 2.9–2.10). Sketch (b) redrawn from [14].

tive indices:  $n_{\parallel}$  (parallel to the director/optic axis) and  $n_{\perp}$  (perpendicular). Their directional dependence is conveniently described by the uniaxial optical indicatrix (index ellipsoid) shown in Fig. 2.8b [24].

**Indices of the o- and e-wave.** For a uniaxial LC, the ordinary index equals the transverse principal index,  $n_o = n_{\perp}$  (2.9), while the extraordinary index depends on the angle  $\theta$  between the wave normal  $\mathbf{k}$  (phase-propagation direction) and the optic axis (measured in the plane containing both directions):

$$n_e(\theta) = \frac{n_{\parallel} n_{\perp}}{\sqrt{n_{\parallel}^2 \cos^2 \theta + n_{\perp}^2 \sin^2 \theta}}. \quad (2.10)$$

The angular birefringence is  $\Delta n(\theta) = n_e(\theta) - n_o$ ; see also Fig. 2.8c. As consistency checks,  $n_e(0) = n_{\perp} = n_o$  (no birefringence along the optic axis) and  $n_e(90^\circ) = n_{\parallel}$  [7, 24].

**Phase retardation and optical path difference (OPD).** When two eigenwaves

traverse a thickness  $d$  (at normal incidence), their phase difference is [7]:

$$\Delta\phi = \frac{2\pi}{\lambda} \Delta n d, \quad (2.11)$$

and  $\text{OPD} = \Delta n d$  (2.12). Here  $\Delta n = n_e(\theta) - n_o$  is the birefringence for the given geometry,  $d$  is the sample thickness along the propagation direction, and  $\lambda$  is the vacuum wavelength.

**Crossed polarizers (transmission and reflection).** Between crossed linear polarizer and analyzer, the transmitted intensity for a uniform uniaxial plate at normal incidence is:

$$\frac{I}{I_0} = \sin^2(2\alpha) \sin^2\left(\frac{\pi \Delta n d}{\lambda}\right), \quad (2.13)$$

where  $I_0$  and  $I$  are the incident and transmitted intensities,  $\alpha$  is the angle between the sample's optic axis (director) and the polarizer,  $\Delta n$  is the birefringence for the given geometry,  $d$  is the optical path length through the sample (thickness along the propagation direction), and  $\lambda$  is the vacuum wavelength (cf. Eq. (1) and Eq. (6) in [25]). Under these assumptions (ideal crossed linear polarizers, normal incidence, negligible absorption, uniform optic axis in the sample plane), the intensity is maximal at  $\alpha = 45^\circ$  and minimal at  $0^\circ$  or  $90^\circ$ . In a reflective double-pass configuration (the sample on an isotropic mirror or reflective backing at normal incidence), the beam traverses the birefringent layer twice, so the phase retardation doubles,  $\Delta\phi_{\text{refl}} = 2\Delta\phi = 4\pi\Delta n d/\lambda$ , giving:

$$\frac{I_{\text{refl}}}{I_0} = \sin^2(2\alpha) \sin^2\left(\frac{2\pi \Delta n d}{\lambda}\right). \quad (2.14)$$

This “double-pass doubles retardance” equivalence is the same principle by which a quarter-wave plate behaves like a half-wave plate upon reflection [8, 26].

The effect of birefringence under crossed polarizers is illustrated in Fig. 2.9. The transmitted light depends on the alignment of the optic axis relative to the polarizers:

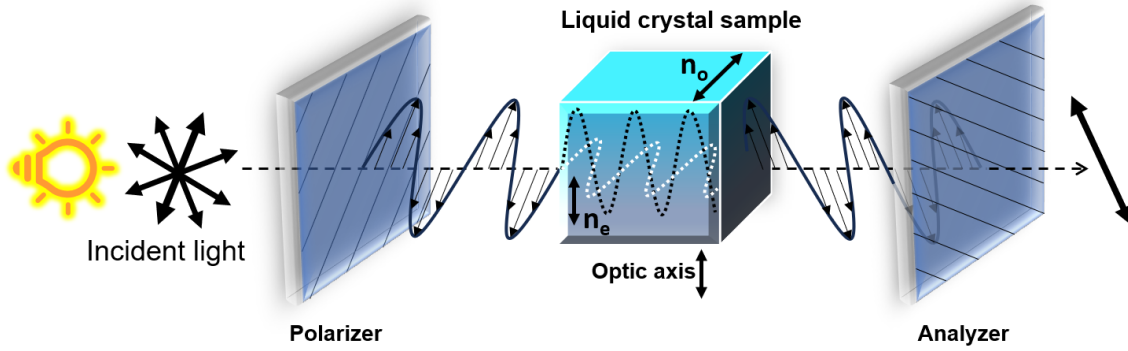


Figure 2.9: Illustration of the phase shift introduced by a birefringent nematic LC sample between crossed polarizers. Light linearly polarized at  $45^\circ$  to the director (optic axis) splits into ordinary (white dashed) and extraordinary (black dashed) waves. When the sample has  $OPD = \lambda/2$  (acting as a half-wave plate), a polarizer at  $+45^\circ$  and an analyzer at  $-45^\circ$  are ideally matched to the plate: the LC sample rotates the polarization into alignment with the analyzer, giving maximal transmission.

maxima occur when the optic axis lies in the sample plane (perpendicular to the propagation direction) and is at  $45^\circ$  to the polarizer/analyzer; minima occur at  $0^\circ$  or  $90^\circ$ , consistent with Eq. (2.13).

**Michel–Lévy chart and  $\lambda$ -plate (compensation).** When white light passes through a birefringent sample, the wavelength dependence of Eq. (2.11) produces interference colors. The Michel–Lévy chart, introduced by the French geologist Auguste Michel–Lévy, relates the observed color to OPD (Eq. 2.12) (Fig. 2.10) [27]. To determine the in-plane optic-axis direction and the sign of birefringence, one commonly inserts a  $\lambda$ -plate (first-order red compensator) with retardation  $\Delta_\lambda \approx 530$  nm, oriented at  $45^\circ$  to the polarizer/analyzer. The  $\lambda$ -plate has a marked slow axis (direction of higher index for the relevant polarization). Depending on its orientation relative to the sample’s slow axis, the net OPD is either increased (additive) or decreased (subtractive):

$$OPD_{\text{tot}} = |OPD_{\text{sample}} \pm \Delta_\lambda|, \quad \Delta_\lambda \approx 530 \text{ nm}, \quad (2.15)$$

with “+” when the sample’s slow axis is parallel to the plate’s slow axis (additive compensation), and “−” when they are perpendicular (subtractive compensation).

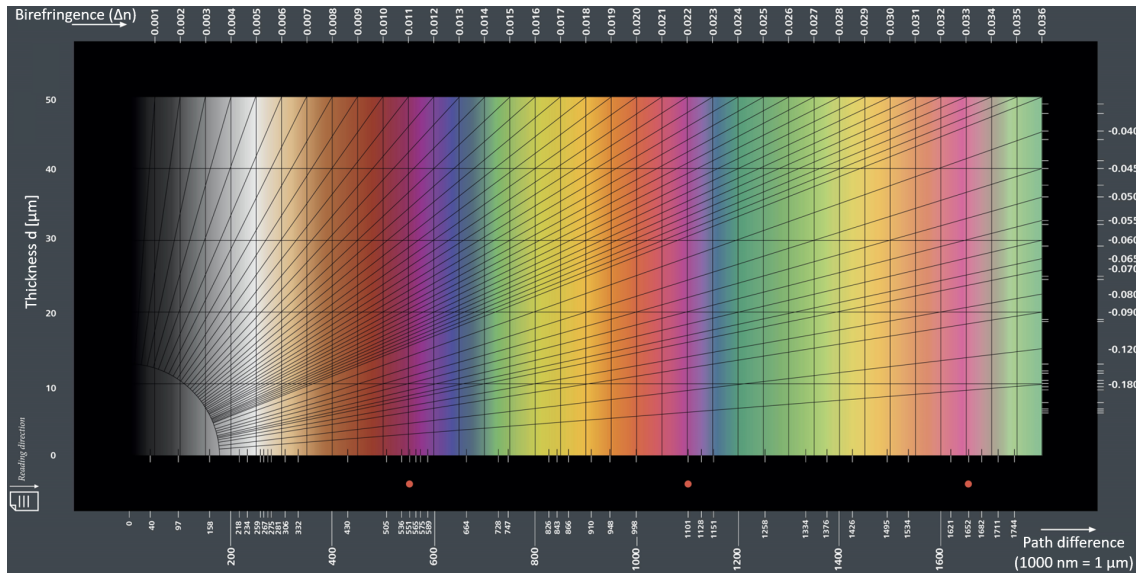


Figure 2.10: Michel-Lévy birefringence chart (adapted from ZEISS Microscopy, CC BY-SA 2.0). Bottom axis: OPD; left: thickness; top/right: birefringence.

On the Michel-Lévy chart this shifts the color band by roughly one first-order interval, to the right for additive and to the left for subtractive. For example, a nearly black (very low OPD) region becomes magenta upon additive compensation. These procedures assume normal incidence, negligible absorption, and reasonably uniform thickness.

## 2.7 Polarizing optical microscopy

In polarizing optical microscopy (POM), the sample (specimen) is observed between a **polarizer (P)** and an **analyzer (A)**. Plane-polarized light passes through the birefringent sample and acquires a phase retardation  $\Delta\phi$ ; between crossed P and A this produces intensity contrast (cf. Eq. (2.13)).

A transmission POM typically comprises a bright-field **illumination source** (e.g., LED), a **condenser** (focuses light onto the sample) with **field** and **aperture diaphragms**, a rotatable **polarizer (P)** below or inside the condenser, the **specimen stage** (sample holder; often rotatable), **objectives** ( $4\times$ ,  $10\times$ ,  $20\times$ ,  $50\times$ ; magnify the image), an **analyzer (A)** — the second polarizer located in the observation tube

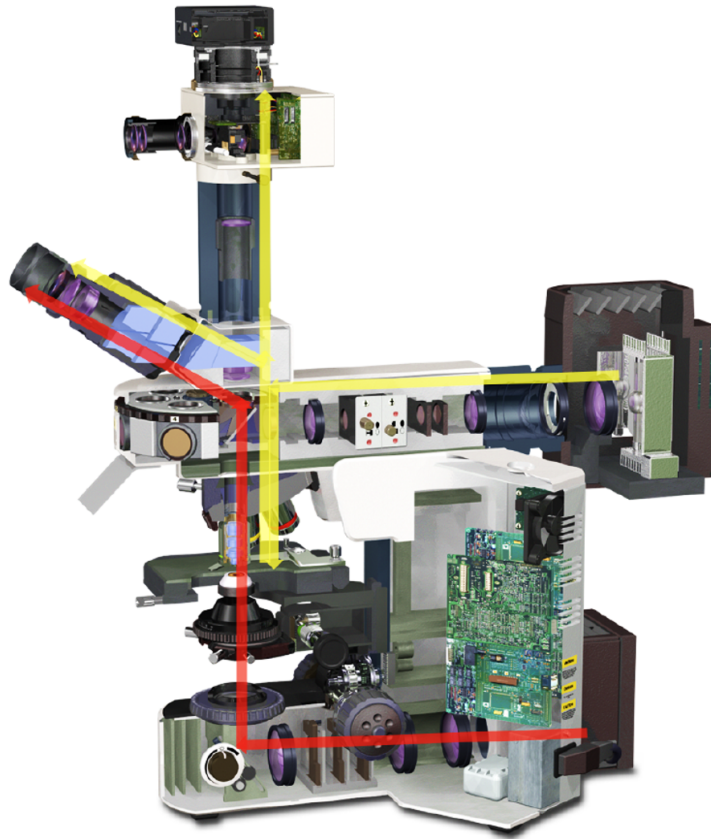


Figure 2.11: Schematic of optical paths in the Olympus stand: transmission (red) and reflection (yellow). Adapted from the Olympus user manual.

after the objective — and an **eyepiece or camera** (image formation and capture). Optional accessories include a **compensator slot** (e.g., a  $\lambda$ -plate or a quarter-wave plate) and a **Bertrand lens** for conoscopic (back-focal-plane) observation. Crossed polarizers correspond to  $P \perp A$  ( $90^\circ$ ).

The microscopes used in this work support both transmission and reflection (epi-illumination) POM. We used two upright stands (Olympus BX51; Nikon ECLIPSE LV100N POL) and one inverted stand (Nikon ECLIPSE TS100). The optical paths are analogous; the main difference is the geometry of illumination and stage (upright vs. inverted), which we select according to the sample.

In Fig. 2.11 the transmission path (red) is: **illumination source**  $\rightarrow$  **field-/aperture diaphragms**  $\rightarrow$  **polarizer (P)**  $\rightarrow$  **condenser**  $\rightarrow$  **sample on stage**  $\rightarrow$  **objective**  $\rightarrow$  **analyzer (A)**  $\rightarrow$  **eyepiece/camera**. In reflection POM (yellow),

a dedicated **epi-illuminator** and **beam splitter** send polarized light through the **objective** onto the sample; the reflected light returns through the same objective, passes the **analyzer**, and is imaged by the **eyepiece/camera**.

## 2.8 Topological defects

Topological defects in LCs are singularities of the director field, where the orientational order parameter breaks down and the director orientation becomes undefined. Because the nematic director is apolar ( $\mathbf{n} \equiv -\mathbf{n}$ ), the allowed strengths are half-integers,  $s = m/2$  with  $m \in \mathbb{Z}$ . In nematics, defects distort the orientational order; in layered phases (e.g., smectics) they can also distort the positional order [4, 18]. Topological point defects in quasi-two-dimensional nematic and smectic systems, including freely suspended films, sandwich cells, and LC shells, are reviewed in detail in Ref. [28].

A practical way to assess the defect strength is polarized-light microscopy. Placing a sample with defects between crossed polarizers produces dark brushes around the cores (Fig. 2.12a), indicating regions where the director is parallel or perpendicular to the polarizers (see Sec. 2.7). The defect strength is  $|s| = N/4$ , where  $N$  is the

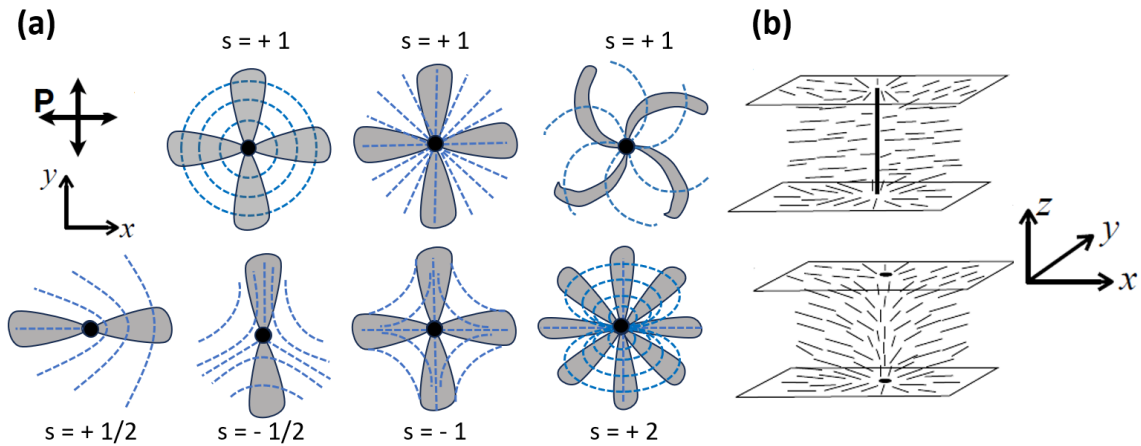


Figure 2.12: Topological defects. (a) Schematic brush patterns between crossed polarizers for defects with various strengths  $s$  (author's drawing based on the standard brush-counting method [14]). (b) A  $+1$  disclination line between two parallel plates transforms into two surface point defects (boojums) of charge  $+1$  when the director escapes into the third dimension [29, 30].

number of dark brushes [14]. The sign is determined by rotating the sample while keeping the polarizers crossed: if the brushes rotate in the same sense as the sample, the defect is positive; if in the opposite sense, it is negative.

Topological defects interact analogously to electric charges (opposite signs attract, like signs repel) [18]. For a straight disclination line, the line energy (per unit length) in the one-constant Oseen–Frank approximation (cf. Sec.2.4, Eq. 2.5) [4] is

$$F_{\text{line}} = F_c + \int_{r_c}^R f 2\pi r \, dr, \quad (2.16)$$

where  $f$  is the bulk elastic free-energy density [ $\text{J}/\text{m}^3$ ],  $r_c$  is the defect core radius (inner cutoff), and  $R$  is a macroscopic cutoff (of order of the sample size).

In the one-constant approximation  $K_1 = K_2 = K_3 \equiv K$ , a planar nematic with director  $\mathbf{n} = (\cos \varphi, \sin \varphi, 0)$  has [4, 18]

$$f = \frac{K}{2} |\nabla \varphi|^2. \quad (2.17)$$

3

For a defect of strength  $s$ , the director angle winds as

$$\varphi(\mathbf{r}) = s \chi,$$

where  $\chi$  is the polar angle describing a rotational path about the defect (so that  $\chi = 2\pi$  for a complete turn around the defect). Hence  $|\nabla \varphi| = |s|/r$ , and therefore

$$f = \frac{K s^2}{2 r^2}. \quad (2.18)$$

Integrating over the cross-section yields the standard Oseen–Frank result [4, 18]:

$$F_{\text{line}} = F_c + \pi K s^2 \ln \left( \frac{R}{r_c} \right), \quad (2.19)$$

---

<sup>3</sup> The  $\frac{1}{2}$  prefactor follows the standard Hookean convention (cf.  $\frac{1}{2} k x^2$ ); see [31].

where  $F_c$  is the core contribution and the cutoffs  $r_c$  and  $R$  are as defined above. Because  $F \propto s^2$ , an  $s = \pm 1$  line has higher energy than two  $s = \pm \frac{1}{2}$  lines of the same total topological charge (ignoring core terms and boundary effects). Indeed,

$$\frac{F(1)}{2F(\frac{1}{2})} = \frac{\pi K \ln(R/r_c)}{2\pi K (\frac{1}{2})^2 \ln(R/r_c)} = \frac{1}{1/2} = 2.$$

A radial configuration corresponding to an  $s = +1$  line connecting two plates is therefore unstable in three dimensions. The director can lower the elastic energy by tilting out of the plane so that the singular line disappears; the line then terminates at the bounding surfaces as two  $+1$  surface point defects (boojums). This is the classical escape into the third dimension mechanism [29, 30]. Although the simple treatment above considers an idealized straight disclination line with a single winding number, real three-dimensional nematic disclination lines are more complex. In general, they can exhibit mixed wedge–twist character, with local core structures varying continuously along their length [32].

## 2.9 Nematic LCs in electric fields

Nematic LCs reorient in electric fields because of their dielectric anisotropy  $\Delta\varepsilon \equiv \varepsilon_{\parallel} - \varepsilon_{\perp}$  (difference between the director-parallel and director-perpendicular components of the dielectric permittivity tensor). For materials with  $\Delta\varepsilon > 0$  (e.g., 5CB), the director tends to align with the electric field ( $\mathbf{n} \parallel \mathbf{E}$ ) to lower the electrostatic free energy (for  $\Delta\varepsilon < 0$ , it prefers  $\mathbf{n} \perp \mathbf{E}$ ).<sup>4</sup>

Before turning to curved geometries, a brief note on flat films: in planar or hybrid-aligned nematic cells with  $\Delta\varepsilon > 0$ , applying a field normal to the plates triggers the well-known Frederiks transition<sup>5</sup> once the field exceeds a material- and

---

<sup>4</sup> Classic treatments of nematic electrostatics and the Frederiks transition in thin films can be found in [4, 19].

<sup>5</sup> **Frederiks transition:** threshold reorientation of a uniformly aligned nematic under an external field. For a planar cell with normal electric field  $\mathbf{E}$  and  $\Delta\varepsilon > 0$ ,  $E_c = \frac{\pi}{d} \sqrt{K_{11}/(\varepsilon_0 \Delta\varepsilon)}$  (use  $K_{22}/K_{33}$  for twist/bend). *Notation:*  $\varepsilon_0$  — vacuum permittivity;  $d$  — cell thickness (plate

thickness-dependent threshold  $E_c$ ; above threshold, the director tilts toward the field and the normal-incidence optical retardance decreases [4,19]. In strictly homeotropic cells with  $\Delta\varepsilon > 0$  no such instability occurs (the director is already along  $\mathbf{E}$ ), whereas for  $\Delta\varepsilon < 0$  a bend-type transition can appear [4]. This simple balance between surface anchoring and bulk field coupling provides a useful framework for discussing droplets and shells.

### 2.9.1 LC droplets: bipolar vs. radial

In spherical droplets, interfacial anchoring fixes the defect topology by constraining the nematic director field  $\mathbf{n}$ . Two canonical textures are observed:

- **Bipolar droplet (planar anchoring).** Tangential anchoring yields two antipodal surface point defects (boojums) at the poles, with director streamlines running smoothly between them; see Fig. 2.13a. This configuration and boojum dynamics were established in early work by Volovik and Lavrentovich [35]. Experimentally, common thermotropic nematics like 5CB in deionized water (near neutral pH, without added surfactants) adopt planar anchoring at the LC–water interface and thus form bipolar droplets [36–38].
- **Radial (hedgehog) droplet (homeotropic anchoring).** The director is everywhere normal to the interface, producing a spherically symmetric field organized around a single bulk  $+1$  point defect at the center (a  $+1$  hedgehog); see Fig. 2.13b. In LdG/Frank models for a homeotropic sphere, a competing equilibrium can be an equatorial disclination loop (“Saturn ring”); however, this ring is a well-known competing configuration for a sphere with homeotropic anchoring (especially in the ‘particle-in-nematic’ problem); for droplets with strong homeotropy, the central  $+1$  defect is typically stable [39,40].<sup>6</sup>

---

spacing). First seen in a magnetic field (Frederiks & Repiewa, 1927 [33]); the electric-field case followed (Frederiks & Zolina, 1933 [34]).

<sup>6</sup> The equatorial Saturn ring (quadrupolar) state is favored for  $a/\ell \lesssim 1$  ( $a$  : sphere radius,  $\ell = K/W$ ), or with moderate/weak homeotropic anchoring or elastic anisotropy penalizing

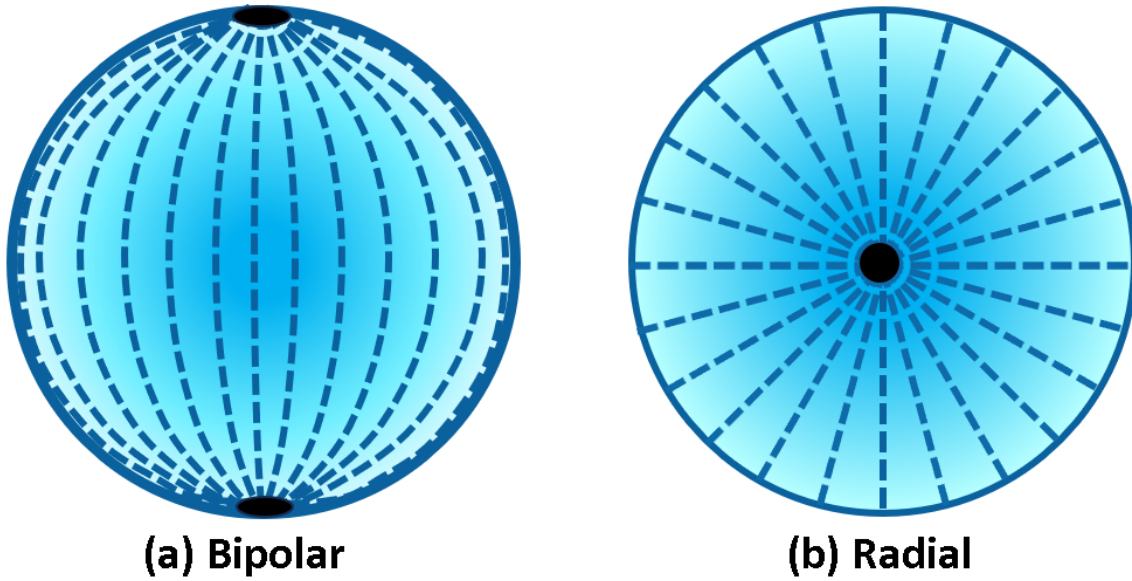


Figure 2.13: (a) Bipolar: tangential director; two antipodal boojums (surface point defects). (b) Radial (hedgehog): normal director; central inner +1 defect.

### 2.9.2 Electric-field response of droplets

An external electric field  $\mathbf{E}$  (rms amplitude  $E$ ) competes with bulk elasticity and surface anchoring; convenient measures are the electric coherence length  $\xi_E$ <sup>7</sup> [4, 19] and, for a droplet of radius  $a$ , the dimensionless control parameter  $\Lambda$  [41]:

$$\xi_E = \sqrt{\frac{K_{\text{eff}}}{\varepsilon_0 |\Delta\varepsilon| E^2}}, \quad \Lambda \equiv \left( \frac{a}{\xi_E} \right)^2 = \frac{\varepsilon_0 |\Delta\varepsilon| E^2 a^2}{K_{\text{eff}}}. \quad (2.20)$$

For  $\Lambda \ll 1$  the field is weak and produces only local tilts of  $\mathbf{n}(\mathbf{r})$ ;  $\Lambda \sim 1$  corresponds to droplet-scale reorientation or distortion; and  $\Lambda \gg 1$  indicates a field-dominated regime with possible topology changes.<sup>8</sup>

**Bipolar droplets.** The lowest-cost response is a continuous rotation of the droplet/optical axis toward the orientation favored by the sign of  $\Delta\varepsilon$  defined in

---

dipolar distortions; larger  $a/\ell$  and strong homeotropic anchoring favor the dipolar (point-hedgehog).

<sup>7</sup> **Electric coherence length  $\xi_E$ :** field-elastic balance length scale (one-constant Oseen-Frank); the LdG form is equivalent with  $L$  in place of  $K_{\text{eff}}$ .

<sup>8</sup> **Typical  $E$  vs.  $a$  for 5CB (RT).** Setting  $\Lambda = 1$  in Eq. (2.20) with  $K_{\text{eff}} \approx 7 \text{ pN}$  and  $\Delta\varepsilon \approx 13$  (representative values for 5CB at room temperature [42, 43]) gives, for  $a = (1, 5, 10) \mu\text{m}$ ,  $E \approx (0.25, 0.05, 0.025) \text{ V } \mu\text{m}^{-1}$  [(0.25, 0.05, 0.025) kV mm<sup>-1</sup>]. Thresholds shift with anchoring  $W$  and elastic anisotropy  $K_1/K_3$ .

Sec. 2.9, while the two-boojum topology is preserved [44]. In free suspensions the entire droplet can rotate as a rigid body, whereas in immobilized systems (e.g., PDLCs) the internal director tilts and the two boojums slide along the interface to follow the new axis [45, 46]. In ideal, unpinned samples the response is often thresholdless (continuous tilt with boojum glide); however, Frederiks-like thresholds can appear under strong anchoring or constrained poles [41]. The axial tilt grows roughly with  $\Lambda$  and saturates as alignment is reached; upon field removal the two-boojum state is recovered [46].

**Radial droplets.** Above a material- and size-dependent threshold, the central +1 hedgehog becomes unstable and the equilibrium switches to a configuration with the equatorial Saturn ring encircling the droplet [39, 40]. Continuum theory predicts a first-order transition with hysteresis [47, 48]: upon increasing  $E$ , a ring nucleates (typically off-equator) and migrates toward the equator; upon decreasing  $E$ , it persists to a lower field before collapsing back to the hedgehog. Experiments in uniform magnetic fields<sup>9</sup> observe the analogous hedgehog→Saturn-ring transition with hysteresis [50]. A useful scaling estimate for the onset is

$$E^* \sim \frac{1}{a} \sqrt{\frac{K_{\text{eff}}}{\varepsilon_0 |\Delta\varepsilon|}} \Phi\left(\frac{Wa}{K_{\text{eff}}}, \frac{K_1}{K_3}\right), \quad (2.21)$$

where  $\Phi(\cdot)$  is an order-one factor capturing anchoring and elastic anisotropy; here  $E^*$  is the nucleation threshold field for Saturn-ring formation [41].

**Experimental signatures (POM).** *Extinction directions:* stage angles of minimum transmittance; *two-lobe pattern:* two opposite bright caps, most evident when the local optic axis near the caps is at  $\sim 45^\circ$  to the polarizer–analyzer, with the rest of the droplet nearly dark.

**Practical note.** To probe dielectric reorientation cleanly, experiments typically use kHz–tens-of-kHz AC to suppress electrode polarization and ionic screening; very

---

<sup>9</sup> Here “magnetic field” refers to the magnetic flux density  $\mathbf{B}$  (vector, SI unit: tesla). The magnetic field strength is  $\mathbf{H}$  ( $\text{A m}^{-1}$ ); in vacuum  $\mathbf{B} = \mu_0 \mathbf{H}$  (linear isotropic media:  $\mathbf{B} = \mu_0 \mu_r \mathbf{H}$ ) [49].

low frequencies introduce Maxwell–Wagner charging<sup>10</sup>, whereas sufficiently high frequencies recover the quasi-electrostatic response [44].

### 2.9.3 LC shells in electric fields

Here we consider *liquid-crystal (LC) shells*, i.e. thin films (typically  $h \sim 3\text{--}20\ \mu\text{m}$ ) of LC confined in a spherical geometry between two immiscible isotropic phases, typically water, with the LC as the oil phase. A detailed discussion of shell geometry, symmetry (symmetric vs. asymmetric shells), and anchoring at LC–water interfaces is given in Sec. 3.1; here we focus on how external fields reconfigure their director and defect patterns.

External electric fields offer a direct handle to reconfigure the director and defect patterns of nematic shells, enabling valence control (the number of surface defects that act as binding sites).<sup>11</sup> For a uniform field and a nematic with positive dielectric anisotropy ( $\Delta\varepsilon > 0$ ), theory and large-scale simulations predict a field-driven transition from the common *tetravalent* state (four  $+\frac{1}{2}$  disclinations) to a *bipolar* state with two  $+1$  boojums aligned with the field—i.e., pairwise coalescence of  $+\frac{1}{2}$  defects into two  $+1$  boojums with total charge conserved [53]. A schematic of this pathway is shown in Fig. 2.14a–c; increasing the dimensionless field strength  $\eta$  (as defined in [53]) drives the  $4 \rightarrow 2$  transition.

Beyond homogeneous fields, simulations with spatially structured fields (e.g., quadrupolar) show that defect positions follow the imposed field symmetry, enabling controlled repositioning and field-tunable valence [53]. In realistic shells, thickness inhomogeneity biases defect motion and can pin defects at symmetry-selected locations (e.g., equatorial vs. polar); this thickness-guided organization and the associated “curvature/inversion walls” that connect defect pairs are well documented

---

<sup>10</sup> Maxwell–Wagner charging (interfacial polarization) arises in heterogeneous dielectrics with finite conductivity contrast: mobile charges accumulate at interfaces (e.g., LC–water or at electrodes), partially screening the applied field; for  $\omega \ll \tau_{\text{MW}}^{-1}$  interfacial charges track the field and distort the internal field distribution [4, 44, 51, 52].

<sup>11</sup> Here “valence” means the count of surface defects available for directional interactions; the total topological charge on a sphere remains  $+2$ .

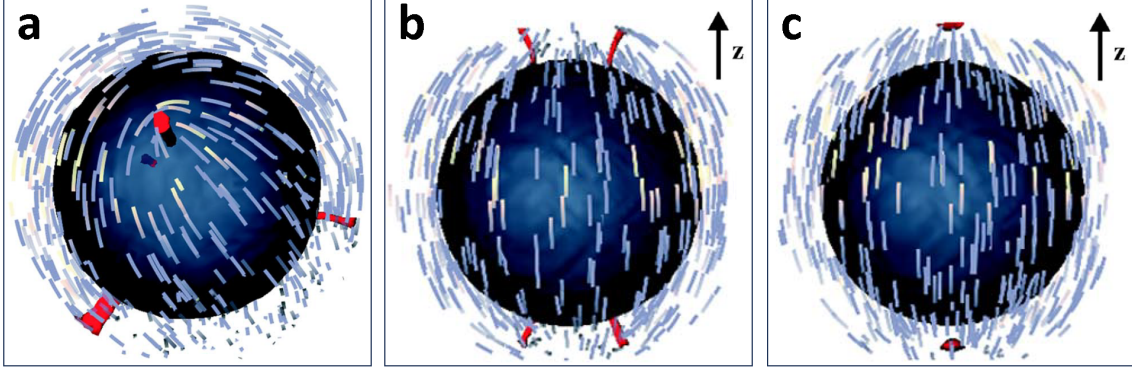


Figure 2.14: Uniform electric-field response of a nematic shell ( $\mathbf{E} \parallel \mathbf{z}$ ,  $\Delta\epsilon > 0$ ). (a)  $E = 0$ : tetravalent state with four  $+\frac{1}{2}$  disclinations. (b,c) viewed  $\perp \mathbf{z}$ : (b) weak field ( $\eta = 0.03$ ) — defects drift toward the poles; (c) stronger field ( $\eta = 0.06$ ) — coalescence into a bipolar state with two  $+1$  boojums at opposite poles. Streamlines depict the director; red marks indicate defect cores; the dark sphere is the inner interface. Reprinted with permission from G. Skačej and C. Zannoni, Phys. Rev. Lett. **100**, 197802 (2008). © 2008 American Physical Society.

[54]. On aspherical (e.g., dumbbell-like) shells, molecular dynamics (MD) simulations show that the response depends sensitively on field direction: direction-dependent relocation and a crossover from early-time drift to late-time relaxation as defects reorient relative to the long axis [55]. For  $\Delta\epsilon < 0$ , LdG simulations of a boojum at a planar boundary predict field-induced “fingertip” elongation, significant only when the electric coherence length  $\xi_E$  approaches the biaxial core scale  $\xi_b$ <sup>12</sup> (LdG:  $\xi_b \simeq \sqrt{L/A_{\text{eff}}}$  [4, 18]), i.e.,  $E \approx 10^8 \text{ V m}^{-1}$  for 5CB [56].<sup>13</sup>

**Experimental status.** Direct electric-field switching on nematic shells is still limited, but the key prediction is confirmed using magnetic fields (which couple to nematic order in the same quadratic way as electric fields): under a strong uniform magnetic field, tetravalent shells evolve to a bipolar state via pairwise migration and merging of  $+\frac{1}{2}$  defects at opposite poles; the defect trajectories are guided by inversion/curvature walls, following the field projection on the shells [57].<sup>14</sup>

<sup>12</sup>  $\xi_b$ : intrinsic, field-independent defect-core length where nematic order becomes biaxial.

<sup>13</sup> Planar case (Kurioz *et al.*). For 5CB ( $K \sim 6\text{--}10 \text{ pN}$ ,  $|\Delta\epsilon| \sim 10$ ),  $\xi_E \approx 1 \text{ } \mu\text{m}$  at  $E \sim 10^6 \text{ V m}^{-1}$ , while  $\xi_E \approx \xi_b \approx 20 \text{ nm}$  only at  $E \sim 10^8 \text{ V m}^{-1}$  [4, 56].

<sup>14</sup> In the continuum free energy, field couplings enter as quadratic terms in the director projection:  $f_E \propto -\Delta\epsilon(\mathbf{E} \cdot \mathbf{n})^2$  for electric fields and  $f_B \propto -\Delta\chi(\mathbf{B} \cdot \mathbf{n})^2$  for magnetic fields. Hence, aside from replacing  $\Delta\epsilon$  by  $\Delta\chi$ , the director-level response is analogous; see the explicit field term and length-scale definitions in [56], and magnetic-field shell experiments in [57].

**Implications for nematic shells.** Field-driven reconfiguration enables (i) on/off valence switching for patchy colloids [53], (ii) controlled placement of defects, and thus of defect-bound inclusions, by steering defect locations with uniform or patterned fields [56], and (iii) reversible tuning of optical responses via controlled changes in director topology and defect arrangement. In summary, when  $\Lambda \gtrsim 1$  (cf. Eq. (2.20)), electric fields reorient the director, reshape and relocate defects, and switch valence in nematic shells, as demonstrated by theory and simulations [53,55,56] and corroborated by magnetic-field experiments on shells [57].

Taken together, the concepts introduced in this chapter provide the continuum and optical framework used throughout this thesis, from director elasticity and anchoring to birefringent contrast and field-driven reconfiguration. In Chapter 3 we turn to the actual materials and interfaces that realize these ideas in experiments. We introduce LC–water interfaces and nematic shells as water–oil–water double emulsions, describe how microfluidics, PVA, and ionic surfactants set shell geometry, anchoring, and stability, and show how electrolytes generate interfacial electric fields that compete with elastic and imposed fields. We then extend the discussion to water-dissolved amphiphiles, with a particular focus on bacterial LPS, and link their packing, aggregation, and regulatory context to biosensing. These interfacial and materials concepts set the stage for the experimental chapters that follow, where they are applied to reconfigurable nematic shells in optical characterization and LC-based biosensing.



## Chapter 3

# Liquid crystal–water interfaces

### 3.1 Liquid-crystal shells

Having discussed the field-driven reconfiguration of nematic shells in Sec. 2.9.3, we now turn to their geometry, symmetry, and LC–water interfacial physics.

**Geometry.** Figure 3.1 contrasts symmetric and asymmetric shells. A shell is characterized by its outer radius, inner radius, and mean wall thickness, defined as the difference between these radii. We call a shell symmetric when the inner and outer

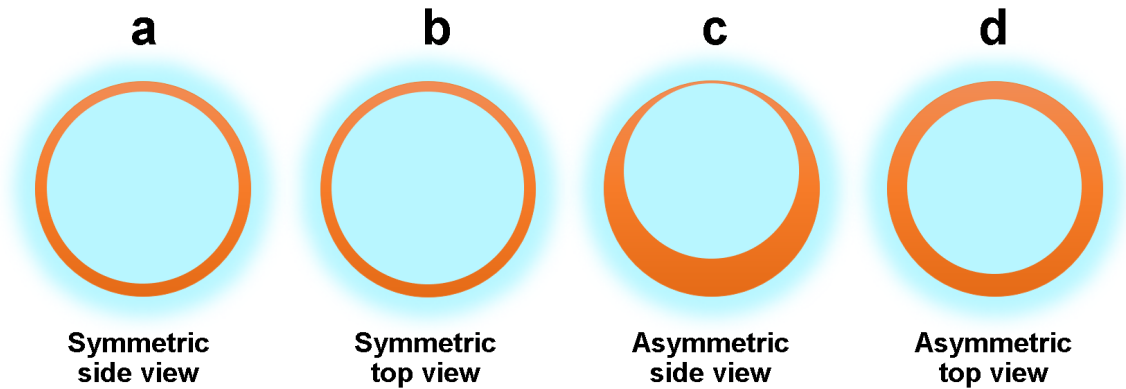


Figure 3.1: Symmetric vs. asymmetric LC shells. (a) Symmetric, side view: concentric interfaces  $\Rightarrow$  uniform wall thickness. (b) Symmetric, top view. (c) Asymmetric, side view: off-center inner aqueous droplet  $\Rightarrow$  wall-thickness gradient (thin upper pole, thick lower pole). (d) Asymmetric, top view: circular in projection; the thickness variation lies along the viewing axis and is therefore not visible. The symmetric shell is drawn with a thinner wall because nearly symmetric shells are typically thin-walled; however, exact symmetry is controlled primarily by density matching.

LC–water interfaces share the same center, with a uniform wall thickness (Fig. 3.1a,b). Displacing the inner aqueous droplet off-center makes the shell asymmetric, producing a wall-thickness gradient (thin upper pole, thick lower pole) (Fig. 3.1c,d). The pole position thicknesses are set by buoyancy, i.e., by the relative densities of the LC and surrounding aqueous phases.

**Origin of shell asymmetry.** Asymmetry mainly reflects density mismatch: if the LC (middle) phase is lighter or heavier than the aqueous phases, the inner droplet floats or sinks under gravity and the shell off-centers. Unequal interfacial tensions  $\gamma$ , surfactant coverage, or gentle handling flows can also bias the droplet position but typically play a secondary role. Symmetric shells are easier to maintain when thin-walled and when density mismatch and handling flows are minimized.

These shells are water–oil–water (w/o/w) double emulsions. Because the LC–water interfacial tension is relatively high (for 5CB in water,  $\sim 30 \text{ mN m}^{-1}$ ), stabilizers are needed [58]. Examples include poly(vinyl alcohol) (PVA) and sodium dodecyl sulfate (SDS), which lower  $\gamma$  and, crucially, set anchoring at LC–water interfaces. Their chemical structures are shown in Fig. 3.2a (PVA, degree of hydrolysis  $x$ ) and Fig. 3.2b (SDS).

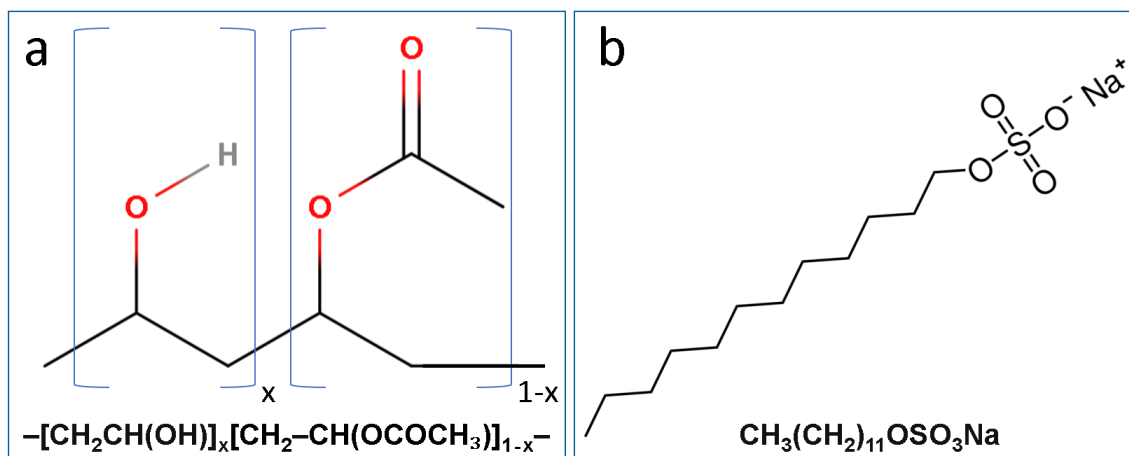


Figure 3.2: Chemical structures of partially hydrolyzed PVA (87–89% hydrolyzed), depicted as a random copolymer of  $-\text{[CH}_2\text{CH(OH)]}_x$  and  $-\text{[CH}_2\text{CH(OCOCH}_3\text{)]}_{1-x}$  units, where  $x = 0.87\text{--}0.89$  and  $1 - x = 0.11\text{--}0.13$  (a), and SDS (b).

### 3.1.1 Anchoring at LC–water interfaces: canonical textures

Anchoring at LC–water interfaces sets the boundary conditions for the director field  $\mathbf{n}$  and, through Oseen–Frank elasticity, controls the bulk response. Angle conventions are defined in Fig. 2.6; for further details on the Rapini–Papoular surface energy (Eq. (2.6)) and bulk elasticity, see Secs. 2.5 and 2.4. Here we briefly review three common LC–water anchoring modes (planar, tangential/degenerate planar, and homeotropic) and the canonical textures they impose on closed spherical boundaries.

**Planar (homogeneous) anchoring.** The director lies parallel to the surface ( $\Theta_0 = 90^\circ$ ) and a single preferred in-plane azimuth  $\phi_0$  is selected (nondegenerate, finite  $W_\phi$ ) [19].

**Tangential anchoring (degenerate planar).** The director is locally tangent to the interface ( $\Theta_0 = 90^\circ$ ), but no unique in-plane easy axis is selected (azimuthal degeneracy, effectively  $W_\phi \approx 0$ ). This situation is common at fluid LC–water interfaces stabilized by adsorbed polymers such as PVA and on curved surfaces [19, 22]. *Note.* With finite  $W_\Theta$  and interfacial curvature  $1/R$ , small tilt deviations  $\Delta\Theta \sim K/(W_\Theta R)$  can arise in the one-constant Frank approximation (see Eq. (2.5)); their penetration is set by the extrapolation length  $\ell_\Theta = K_{\text{eff}}/W_\Theta$  (Eq. (2.7)) [4].

**Homeotropic (normal) anchoring.** The director is perpendicular to the surface ( $\Theta_0 = 0^\circ$ ); the azimuth is irrelevant due to axial symmetry about the normal. Physically, dense monolayers of low–surface-energy chains oriented approximately normal to the interface — e.g., vertical-alignment polyimides or alkylsilanes on solids, and ionic surfactants such as SDS (C12, anionic) or CTAB (C16, cationic) at LC–water interfaces — expose lipophilic alkyl tails toward hydrocarbon nematics (e.g., 5CB) while polar headgroups face water. This lowers the interfacial free energy and yields a positive  $W_\Theta$ , favoring  $\Theta = 0^\circ$  [19, 22].

**Geometry. Radial (“hedgehog”) configuration (droplets/shells).** This is a bulk texture induced by homeotropic anchoring on closed spherical boundaries

rather than a distinct anchoring type. In spherical droplets, the total topological charge  $+1$  is realized as a central  $+1$  point defect or as surface boojums, depending on the size and anchoring strength. In spherical shells with homeotropic anchoring on both boundaries, the uniform radial field satisfies the boundary conditions across the thickness and can be defect-free at equilibrium [4, 18].

## 3.2 PVA as a stabilizer for LC shells

PVA is a water-soluble coil-like polymer that adsorbs at LC–water interfaces, very mildly reduces  $\gamma$ , and stabilizes shells against collapse and coalescence (Fig. 3.3a,b). In  $n$ -CBs, water already promotes tangential (degenerate planar) anchoring; PVA preserves and strengthens this alignment while providing steric stabilization [23, 59].

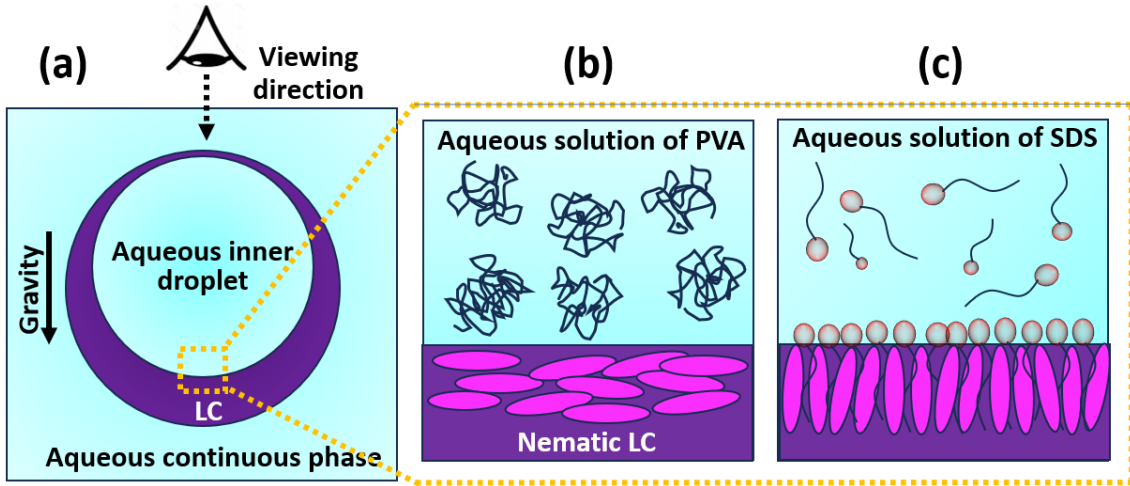


Figure 3.3: (a) Cross-section of an LC shell between two aqueous phases; density mismatch off-centers the inner droplet and creates a thickness gradient. (b,c) Enlarged schematics of the blue region in (a): tangential anchoring (b) stabilized by a polymeric adsorbate (PVA) and homeotropic (c) stabilized by a surfactant (SDS).

### 3.2.1 Mechanism and magnitude

Partially hydrolyzed PVA is a random copolymer of vinyl alcohol (87–89 %) and vinyl acetate (11–13 %). Relatively hydrophobic acetate pendants bias toward LC, while hydroxyl-rich segments remain hydrated; this mild amphiphilicity promotes

adsorption and a hydrated steric layer. Hence 5CB–water interfaces exhibit robust tangential anchoring, and even 10 wt.% PVA lowers  $\gamma_{5\text{CB–water}}$  only slightly, from  $\sim 31$  to  $\sim 28.4$  mN/m [58, 60]. By contrast, low-molecular-weight ionic surfactants such as SDS reach near-saturated interfacial coverage at sub-CMC [61]<sup>1</sup> bulk concentrations and switch the anchoring to homeotropic (see schematic in Fig. 3.3c) [62]. They markedly reduce  $\gamma$  (to  $\sim 10$  mN/m at 6 mM) [58] — i.e., below the  $\sim 8.2$  mM CMC [61].

### 3.2.2 Adsorption kinetics

For PVA of the same degree of hydrolysis (87–89 %), lower- $M_w$  chains reach and adsorb at the interface faster, producing a rapid initial drop in  $\gamma$  [63, 64]. Higher- $M_w$  chains adsorb more slowly, but form a more effective steric barrier and a more viscoelastic interfacial layer at equilibrium [63, 65]. This trend reflects (i) the larger diffusion coefficient of shorter coils ( $D \uparrow$  as hydrodynamic size  $\downarrow$ ), (ii) a higher number of chains available at fixed wt.% ( $\propto 1/M_w$ ), which accelerates early interfacial coverage, and (iii) shorter chain reconfiguration/flattening times for low- $M_w$ ; conversely, longer coils (larger  $R_g$ , radius of gyration<sup>2</sup>) form longer loops/tails and may interlock/entangle at the interface, yielding higher interfacial moduli and thicker steric layers at equilibrium [64, 65]. **Basis of comparison:** at equal mass fraction (wt.%), the chain number concentration scales as  $1/M_w$ , so lower- $M_w$  grades saturate newly created 5CB interfaces faster and suppress early coalescence; at equal chain molarity, the larger coils of high- $M_w$  polymers yield higher interfacial moduli and a thicker steric barrier at equilibrium. **Classic**

<sup>1</sup> **Critical micelle concentration (CMC):** bulk concentration at which surfactant monomers begin forming micelles. Below CMC monomers dominate; above it, extra surfactant goes into micelles and  $\gamma(c) \Rightarrow$  plateaus. CMC depends on  $T$ , ionic strength, and counterion identity.

<sup>2</sup>  **$R_g$  (radius of gyration)** quantifies the size of a polymer coil as the root-mean-square distance of segments from the chain’s center of mass:  $R_g^2 \equiv \frac{1}{N} \sum_{i=1}^N \langle (\mathbf{r}_i - \mathbf{r}_{\text{cm}})^2 \rangle$ . Here,  $N$  is the number of Kuhn (statistical) segments,  $b$  is the Kuhn length (the length of an equivalent freely jointed segment; for a wormlike chain  $b \approx 2l_p$  with  $l_p$  the persistence length),  $\mathbf{r}_i$  are segment positions, and  $\mathbf{r}_{\text{cm}}$  is the chain center of mass. For an ideal (Gaussian) chain,  $R_g = \sqrt{Nb^2/6}$ ; in a good solvent, excluded-volume interactions swell the coil so that  $R_g \propto N^\nu$ , where  $\nu$  is the Flory (swelling) exponent ( $\nu \approx 0.588$  in 3D). See, e.g., Rubinstein & Colby [66]; for the classical treatment, see Flory [67].

**measurements on PVA|paraffin–water interfaces** also show two kinetic regimes: at very low  $c$ , early-time  $\gamma(t)$  follows<sup>3</sup> a diffusion-controlled  $t^{1/2}$ , whereas at higher  $c$  the approach to steady state is reconfiguration-controlled with hour-scale exponential relaxations; moreover, the dependence of steady-state  $\gamma$  on  $M_w$  is modest and not strictly monotonic, with supplier-to-supplier differences attributed to microstructure (randomness/blockiness of acetate groups, branching, 1,2-diol content) that modulates loop–loop interactions [65]. In other words, the influence of molecular weight is not large and not unequivocal; this points to a segmental control of interfacial properties: primarily the numbers of adsorbing acetate-bearing (hydrophobic) chain segments that anchor on the oil side and non-adsorbing vinyl-alcohol-rich, hydrated segments that form loops/tails govern  $\gamma$  and interfacial elasticity (with the anchor density set by the degree of hydrolysis and acetate blockiness), rather than the mere count of macromolecules [65, 69]. **In practice**, nematic LC–shell experiments typically dose PVA by mass and add it to both inner and outer aqueous phases at concentrations of  $\sim 1$  wt.% (with occasional lower values when additional amphiphiles are present), which robustly imposes planar anchoring and suppresses droplet coalescence; e.g., the seminal nematic-shell study used 1 wt.% on both sides [59]. To tune away from purely planar anchoring, an ionic surfactant is often added to the outer phase — e.g., SDS at  $\sim 1$  wt.% [23] or CTAB in the low-millimolar range (0.5–8 mM) with PVA in the inner phase [70] — yielding hybrid or homeotropic anchoring depending on concentration and temperature. At these PVA concentrations, standard microfluidic production of nematic LC shells rapidly generates new LC–water interfacial area — both at the inner water|LC and outer LC|water surfaces. Nevertheless, the in-channel residence time during droplet breakup and shell assembly is sufficient for

<sup>3</sup> **Diffusion-controlled adsorption** (Ward–Tordai). For a planar interface in contact with a semi-infinite bulk, the early-time surface excess obeys  $\Gamma(t) \approx 2c_0\sqrt{Dt/\pi}$ , where  $\Gamma(t)$  is the surface excess [ $\text{mol m}^{-2}$ ],  $c_0$  the far-field solute concentration [ $\text{mol m}^{-3}$ ],  $D$  the diffusion coefficient [ $\text{m}^2\text{s}^{-1}$ ], and  $t$  time [s]. At low coverages  $\Delta\gamma \propto \Gamma$ , hence  $\gamma(t) \approx \gamma_0 - A c_0\sqrt{Dt}$ , where  $\gamma(t)$  is the interfacial tension [ $\text{N m}^{-1}$ ],  $\gamma_0$  its clean-interface value, and  $A$  a system-dependent proportionality constant [ $\text{N m mol}^{-1}$ ]. Deviations from the  $\sqrt{t}$  law arise once back-diffusion, site saturation/kinetic barriers, or slow polymer-chain reconfiguration become significant. See [65, 68].

PVA to reach near-complete coverage by the end of shell formation [23]. Low- $M_w$  PVA (at a given wt.%) provides faster early-time coverage and better resistance to coalescence; after LC-shell formation, a short resting period (minutes in the collection reservoir) allows even slower-adsorbing high- $M_w$  chains to complete adsorption and reconfiguration. Accordingly, long-term stabilization can be achieved either by increasing the concentration of low- $M_w$  PVA (increasing the number of interfacial segments) or by using a mixture of low- and high- $M_w$  PVA, thereby combining rapid early-time adsorption with stronger steric protection and higher interfacial moduli at equilibrium [63].

For clarity, we group the canonical inner–outer boundary-condition pairs into three anchoring configurations. As shown in Fig. 3.4, these are fully tangential (a,d), hybrid (b,e), and fully homeotropic (c,f).

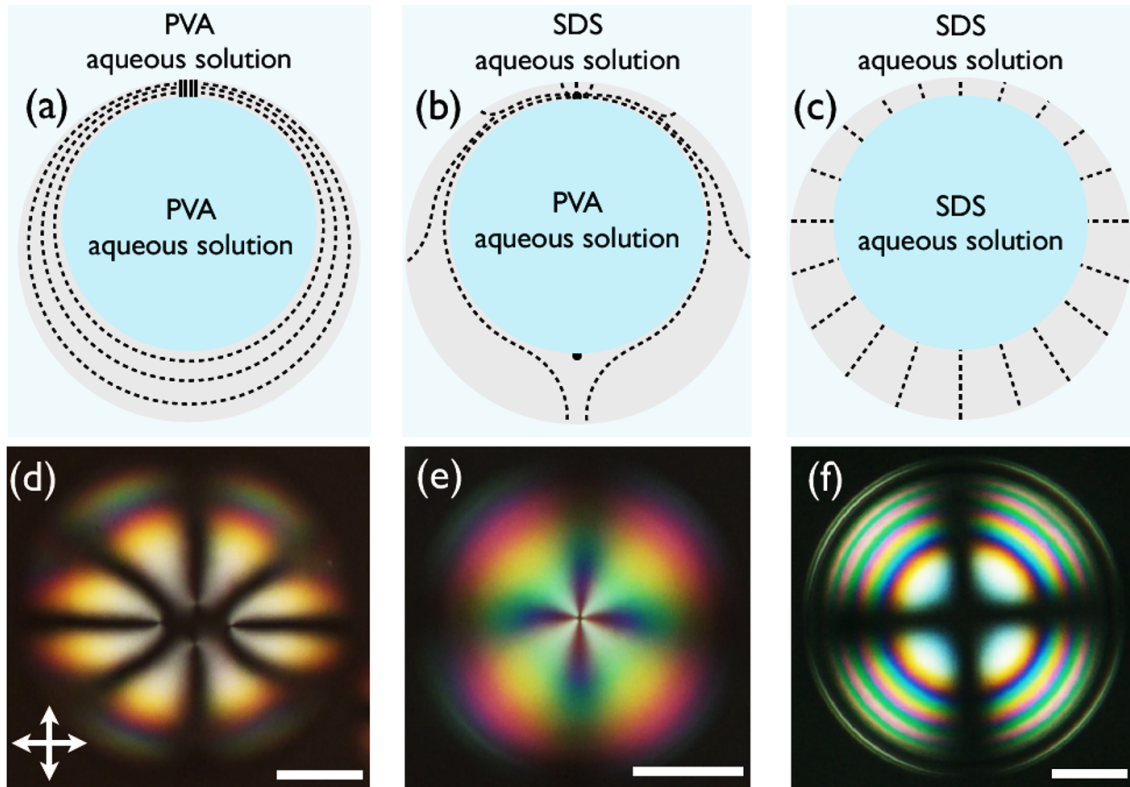


Figure 3.4: (a–c) Cross-section schematics of nematic shells under (a) tangential, (b) hybrid, and (c) radial/homeotropic anchoring. Dashed lines indicate the director fields. (d–f) POM images for each case (focal plane in the upper shell half). Scale bars: 50  $\mu\text{m}$ . Reproduced from Ref. [71].

**Fully tangential (PVA–PVA).** Each spherical interface carries a total topological charge  $+2$  (Poincaré–Hopf), realized as, e.g., four  $+\frac{1}{2}$  defects, two  $+\frac{1}{2}$  plus one  $+1$ , or two  $+1$  per interface. In practice, defects drift toward the thinnest region of the shell because there the total length of the disclination segments spanning the shell (connecting boojums on the inner and outer interfaces) is minimized, thereby lowering the line energy [54].

**Hybrid (PVA–SDS or SDS–PVA).** The director bends from tangential to normal across the shell, yielding a bipolar texture with two antipodal  $+1$  boojums on the tangential interface. The normal interface is defect-free in equilibrium, and half-integer disclinations do not persist due to the imposed mixed anchoring [72].

**Fully homeotropic (SDS–SDS).** A defect-free radial director field produces a Maltese-cross with concentric interference rings under crossed polarizers. This conoscopic-like pattern reflects the radial symmetry and the increased effective birefringent retardation across the shell [23].

### 3.3 Electrolytes at nematic LC–water interfaces

Ionic solutes in the aqueous phase can indirectly act like an interfacial electric field via an electrical double layer<sup>4</sup> (EDL) (Fig. 3.5). At a charged interface, counter-ions from the electrolyte<sup>5</sup> accumulate; the inner, specifically adsorbed Stern layer<sup>6</sup> sits adjacent to the surface, while a diffuse layer of counter-ions (and depleted co-ions) screens the remaining charge into the bulk solution [74, 75]. The potential drops steeply across these layers. The zeta potential<sup>7</sup>  $\zeta$  at the shear plane<sup>8</sup> therefore generally differs from the true surface potential<sup>9</sup> at the immediate interface [74].

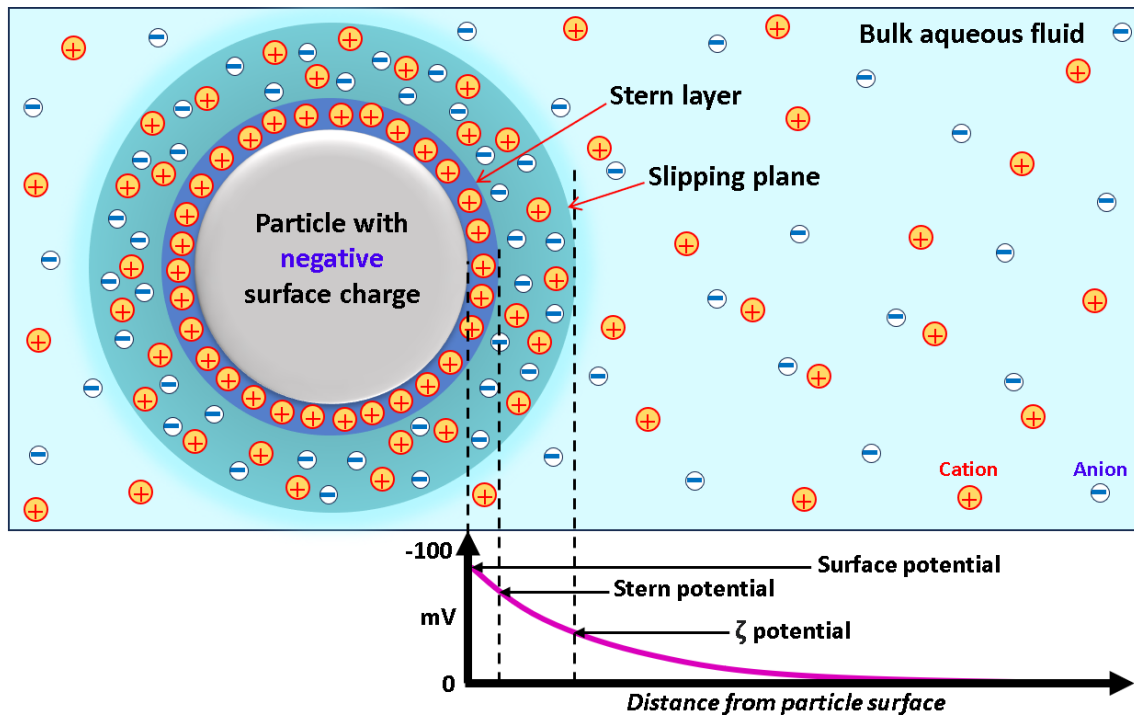


Figure 3.5: Schematic of the EDL around a colloidal particle (not to scale).

<sup>4</sup> Interfacial charge-screening structure: compact Stern layer + diffuse layer [73].

<sup>5</sup> Solute whose (partial/complete) dissociation yields mobile ions and conductivity.

<sup>6</sup> Compact, specifically adsorbed layer of counter-ions directly at the surface; quasi-immobile [73].

<sup>7</sup> Electrokinetic potential difference between the bulk liquid and the shear (slipping) plane [73].

<sup>8</sup> EDL hydrodynamic boundary between the near-immobile interface and the flowing bulk [73].

<sup>9</sup> Electrostatic potential right at the immediate interface set by interfacial charge and dipoles [73].

### 3.3.1 Electrolytes and LC films

In nematic LCs in contact with water, this generic EDL physics has a concrete manifestation: at high pH, hydrophobic LC–water interfaces tend to adsorb  $\text{OH}^-$ , rendering the interface negatively charged. The associated interfacial potential—screened on the aqueous side by the Stern plus diffuse layers and, on the LC side, by a dilute space-charge region (an “internal” EDL)—creates an effective surface-normal field in 5CB ( $\Delta\epsilon > 0$ ) that can reorient the easy axis [76]. Carlton *et al.* used  $\sim 20\ \mu\text{m}$ -thick 5CB films with near-flat LC–water interfaces and observed a continuous planar→homeotropic anchoring transition as pH increased (more negative interfacial potential) and as ionic strength  $I$  rose, strengthening the interfacial double-layer field [76]. At fixed pH = 12.8, the director tilt (from the surface normal) decreased from  $\sim 56^\circ$  at low  $I$  to  $0^\circ$  by 0.7–1 M NaCl; tilt was extracted from optical retardance (Berek) [76]. Even as the aqueous-side  $\zeta$  potential approaches  $\sim 0$  near 1 M NaCl, the thin-film transition persists, consistent with a persistent interfacial field (e.g., interfacial charge/internal EDL on the LC side) and/or salt-induced water-flux torques at LC–water interfaces [77]. A control geometry with a preset in-plane easy axis also transitioned, indicating easy-axis rotation rather than weakened anchoring strength [76].

Beyond ionic strength, ion identity matters. In similar 5CB films presenting a near-flat LC–water interface, Carlton *et al.* observed Hofmeister-type<sup>10</sup> behavior: chaotropic<sup>11</sup>, weakly hydrated anions ( $\text{I}^-$ ,  $\text{ClO}_4^-$ ,  $\text{SCN}^-$ ) at molar concentrations trigger rapid ( $\lesssim 20\ \text{s}$ ) planar→homeotropic realignment, whereas more strongly hydrated/kosmotropic<sup>12</sup> anions ( $\text{F}^-$ ,  $\text{SO}_4^{2-}$ , acetate; also  $\text{Cl}^-$ ,  $\text{Br}^-$ ,  $\text{NO}_3^-$ ,  $\text{ClO}_3^-$  under the same conditions) cause little change [79]. Mechanistically, the trend reflects anion

<sup>10</sup> *Hofmeister effects* are specific-ion (beyond ionic-strength) influences from differences in ion hydration and polarizability/dispersion, ranking ions from kosmotropes to chaotropes [78].

<sup>11</sup> *Chaotropic anions*: large/polarizable, weakly hydrated (low charge density); often show enhanced interfacial affinity [78].

<sup>12</sup> *Kosmotropic anions*: small, strongly hydrated (high charge density); typically avoid hydrophobic interfaces [78].

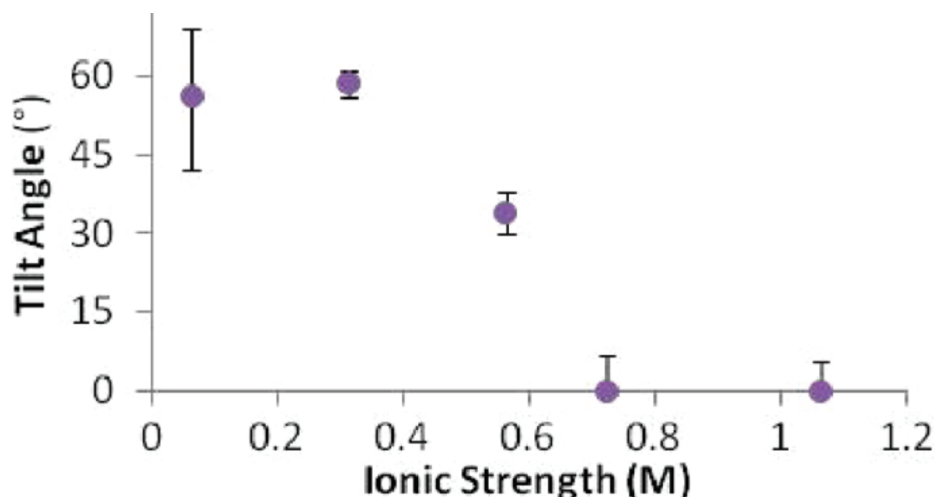


Figure 3.6: Tilt angle of 5CB relative to the surface normal after 1 hour in NaCl solution (pH 12.8) for flat films with planar LC–water interfaces. Reproduced with permission from Carlton *et al.* [76]. © 2012 American Chemical Society.

adsorption at the interface (Stern-layer enrichment) and specific interactions with the cyanobiphenyl nitrile that reshape the interfacial charge; the response persists in nitrile-containing E7 but largely vanishes in weak-dipole TL205, and films with a preset in-plane easy axis still transition—implying a rotation of the easy axis at the LC–water boundary rather than a mere reduction of anchoring strength [79]. Supporting measurements are consistent: Langmuir-monolayer isotherms show tighter packing and reduced molecular tilt with chaotropes, and X-ray reflectivity reveals  $\text{I}^-$  enrichment near cyanobiphenyl headgroups ( $\text{Br}^-$  much weaker), correlating with homeotropic order [79, 80]. Together with pH and ionic-strength control, these specific-ion effects provide practical handles to tune anchoring, while LC orientation serves as a sensitive optical probe of interfacial charge and EDL strength [76].

### 3.3.2 Electrolytes and LC droplets

In nematic LC droplets dispersed in aqueous electrolytes, the same EDL mechanism governs the anchoring and defect topology. Miller and Abbott studied  $d \sim 4\text{--}6\ \mu\text{m}$  5CB droplets in PBS and showed that the fraction of droplets undergoing the bipolar→radial transition in response to trace amphiphile (endotoxin) is strongly

modulated by ionic conditions that set the interfacial double-layer field: at fixed pH = 7.2, reducing ionic strength from 90 mM to 9 mM (constant PBS composition ratios) decreased the radial fraction from  $80 \pm 2\%$  to  $2 \pm 2\%$ ; at fixed  $I = 90$  mM, lowering pH from 7–8 to 5–6 reduced the radial fraction from  $\sim 95\%$  to  $52 \pm 1\%$ – $85 \pm 3\%$ .<sup>13</sup> Interpreted within an anchoring/elasticity model, these data indicate that increasing pH or  $I$  strengthens the interfacial double-layer field that promotes homeotropic anchoring of 5CB (with  $\Delta\epsilon > 0$ ), effectively rotating the easy axis at the LC–water boundary and biasing the droplets toward radial configurations [81].

Complementary experiments on LC droplets in electrolyte solutions directly varied  $I$  and pH (using NaCl and NaOH) and mapped structure across mixtures of nematics with opposite dielectric anisotropy. Dubtsov *et al.* showed that raising salinity from 0.1 to 1 M NaCl (with pH  $\approx 11.2$ ) shrinks the Debye length<sup>14</sup> and amplifies the interfacial field so that 5CB-rich droplets (  $\Delta\epsilon > 0$  ) favor homeotropic (radial) order over a broad composition window (e.g., radial droplets appear for 5CB mass fraction  $c \approx 0.20$ – $0.75$  at 1 M), whereas droplets of a weakly polar azoxybenzene mixture (  $\Delta\epsilon < 0$  ) favor tangential alignment; the sign of  $\Delta\epsilon$  sets whether the EDL field drives normal or parallel orientation to the LC–water interface [82]. A simple electrostatic model (internal EDL on the LC side) captures these trends and rationalizes electrolyte control of droplet anchoring and the associated bipolar  $\leftrightarrow$  radial defect transformations [82].

### 3.3.3 Electrolytes and LC shells

Nematic shells present two LC–water interfaces, so electrolytes act on both boundaries. Ions influence shells by (i) setting anchoring through specific adsorption

---

<sup>13</sup> For 5CB-in-water emulsions,  $\zeta$  becomes more negative with increasing pH and approaches  $\approx 0$  in 1 M NaCl due to screening at the hydrodynamic shear plane; anchoring and droplet ordering nonetheless indicate substantial interfacial charging and an internal EDL on the LC side at high  $I$  [76]; see also droplet ordering vs.  $I$  & pH [81] and an internal EDL on the LC side [82].

<sup>14</sup> The Debye length,  $\lambda_D$ , is the characteristic screening length in an electrolyte: the electrostatic potential decays as  $\phi(r) \propto e^{-r/\lambda_D}$ . It decreases with ionic strength  $I = \frac{1}{2} \sum_i z_i^2 c_i$ ; for water at 25°C (1:1 salts)  $\lambda_D[\text{nm}] \approx 0.304/\sqrt{I(\text{M})}$ , i.e.,  $\sim 0.96$  nm at 0.1 M and  $\sim 0.30$  nm at 1 M [74].

and double-layer fields at each interface and (ii) altering shell thermodynamics via water partitioning/osmotic effects that change the wall thickness  $h$  and thereby the elastic/anchoring balance. Direct, shell-specific maps of defect valence versus simple salts alone (at otherwise surfactant-free, fixed interfaces) remain scarce; most studies adjust boundary conditions using ionic or polymeric stabilizers (e.g., SDS, PVA) and then vary aqueous composition.

As established (Sec. 3.1.1, Fig. 3.3), SDS imposes homeotropic anchoring and PVA enforces tangential anchoring. Since SDS is an electrolyte surfactant ( $\text{Na}^+\text{DS}^-$ ):  $\text{Na}^+$  counter-ions reside in the interfacial Stern layer and screen the sulfate headgroups, reducing lateral repulsion and allowing tighter, more upright SDS packing with alkyl tails into the LC, which strengthens radial alignment [74]. Increasing ionic strength (e.g., NaCl) further screens  $\text{DS}^-$  and lowers the CMC of SDS, increasing surface excess at the LC–water boundary and reinforcing the homeotropic bias (standard surfactant behavior); replacing SDS with neutral PVA minimizes this electrolyte-mediated effect on anchoring [23, 74].

Two electrolyte-linked routes are therefore most relevant for shells. First, interfacial charging and specific adsorption (including ionic surfactants) rotate the easy axis and modulate the Rapini–Papoular anchoring strengths  $W_\Theta$  (polar) and  $W_\phi$  (azimuthal) at each LC–water boundary; ion-specific trends known from flat films/droplets can carry over to shells when interfaces are comparable [76, 79]. Second, adding salts lowers water activity and generates transient water fluxes at LC–water boundaries that can reorient the director via flow-induced torques in planar geometries without requiring ion penetration into the LC [77]. In nematic shells, osmotic flows modify the wall thickness  $h$  and influence defect reorganizations; combined with the known tendency of defects to migrate toward thinner regions, this provides a natural route for flux–thickness coupling to guide defect motion [54, 83].

*Scope and outlook.* For nematic shells, comprehensive salt-only maps of valence/defect trajectories at fixed, surfactant-free interfaces are still lacking. Existing

shell studies show that electrolyte-defined boundary chemistry (ionic surfactant vs. polymer) sets anchoring asymmetry and can split phase transitions [23]; by analogy with films and droplets, pH, ionic strength, and specific ions should offer practical routes to tune anchoring and defect positioning, warranting a systematic survey focused on shells [76, 77, 79]. In addition, theoretical studies of electrical double layers on curved surfaces indicate that convex and concave interfaces of the same material can exhibit measurably different capacitances and ion distributions even at the same applied potential [84–87]. This curvature-dependent double-layer response motivates the curvature-modulated interfacial capacitor hypothesis for nematic shells developed in Sec. 7.1.2.

### 3.3.4 Summary: fields and electrolytes at LC–water interfaces

**Scales.** External fields compete with surface anchoring. The electric coherence length is  $\xi_E = \sqrt{L/(\varepsilon_0|\Delta\varepsilon|E^2)}$  (with  $L$  the single-constant LdG elastic coefficient; equivalently, in the one-constant Oseen–Frank form,  $\xi_E \simeq \sqrt{K/(\varepsilon_0|\Delta\varepsilon|)} E^{-1}$ ), and the size–field parameter is  $\Lambda = (\ell/\xi_E)^2$ , with  $\ell = a$  (droplet radius or inner shell radius) or  $\ell = h$  (local wall thickness in shells). These scales set the baseline response to imposed fields; electrolyte-defined interfacial fields act analogously, with their effective strength controlled by pH, ionic strength, and ion identity.

- **Droplets (uniform  $\mathbf{E}$ ):** Bipolar: director tilt is often continuous with boojums gliding; Frederiks-like thresholds can appear under strong anchoring or constrained poles. Radial: for  $E \gtrsim E^* \sim a^{-1} \sqrt{K/(\varepsilon_0|\Delta\varepsilon|)}$  a Saturn ring is favored; the switch is first-order and can be hysteretic [47, 48, 50].
- **Shells (fields,  $\Delta\varepsilon > 0$ ):** Simulations (uniform  $\mathbf{E}$ ) predict pairwise defect coalescence  $4 \times (+\frac{1}{2}) \rightarrow 2 \times (+1)$  (valence  $4 \rightarrow 2$ ) as the dimensionless field parameter  $\eta$  increases; simulations (non-uniform/multipolar  $\mathbf{E}$ ) show symmetry-imprinted defect positioning via the local  $E^2$  landscape [53]. Experiments

(uniform  $\mathbf{B}$ ) observe the same  $4 \rightarrow 2$  pathway, while thickness inhomogeneity guides defect motion toward thinner regions and can pin defects in local free-energy minima; curvature/inversion walls connect defect pairs and delineate the migration paths [54, 57]<sup>15</sup>.

- **Electrolytes at LC–water interfaces (mechanism):** The EDL acts as an interfacial field. Higher pH (enhanced interfacial  $\text{OH}^-$ , hence a more negative interfacial potential) and/or higher ionic strength (shorter  $\lambda_D$ ) generally promote homeotropic bias for 5CB ( $\Delta\epsilon > 0$ ); specific anions ( $\text{I}^-$ ,  $\text{ClO}_4^-$ ,  $\text{SCN}^-$ ) can rotate the easy axis via adsorption (Hofmeister trends). At high  $I$ , persistent reorientation may arise from interfacial charging and/or salt-induced transient water-flux torques; the balance is system-dependent [76, 77, 79].
- **Shells with electrolytes (two interfaces):** Stabilizers set inner vs outer anchoring (SDS  $\rightarrow$  homeotropic; PVA  $\rightarrow$  tangential), and hybrid shells can show split N–I transitions [23]. Beyond stabilizers, pH, ionic strength, and specific ions tune anchoring at each interface and, together with thickness gradients, bias defect trajectories; comprehensive salt-only, surfactant-free state maps for shells are still lacking.

## 3.4 Water-dissolved amphiphiles: relevance to biosensors

### 3.4.1 Generic structure of amphiphilic molecules

**Amphiphiles** (amphipathic molecules) contain both polar and nonpolar moieties, combining hydrophilicity (water affinity) with lipophilicity (affinity for hydrocarbons). The term derives from the Greek *amphis* (“both”) and *philia* (“love”). Common classes

---

<sup>15</sup> Curvature/inversion walls are thin bands connecting defect pairs that trace low-energy pathways for defect migration in shells.

include surfactants, lipids, phospholipids, and lipoproteins [88].

### Structure and properties

Amphiphiles comprise at least one lipophilic (typically hydrocarbon) segment and one hydrophilic headgroup. The hydrophilic portion may be charged (e.g., cationic ammonium,  $\text{RNH}_3^+$ ; anionic carboxylate,  $\text{RCO}_2^-$ ; phosphate,  $\text{ROPO}_3^{2-}$ ; sulfate,  $\text{ROSO}_3^-$ ; sulfonate,  $\text{RSO}_3^-$ ) or neutral (e.g., poly(ethylene oxide), alcohols). Surfactants are commonly classified by headgroup charge as anionic, cationic, nonionic, and zwitterionic. Representative molecules of each class are shown in Fig. 3.7: an anionic surfactant, sodium dodecyl sulfate (SDS, a); a cationic surfactant, cetyltrimethylammonium bromide (CTAB, b); a nonionic surfactant, decyl-tetraoxyethylene glycol monoether ( $\text{C}_{10}\text{E}_4$ , c); and a zwitterionic lipid, phosphatidylethanolamine (PE, d).

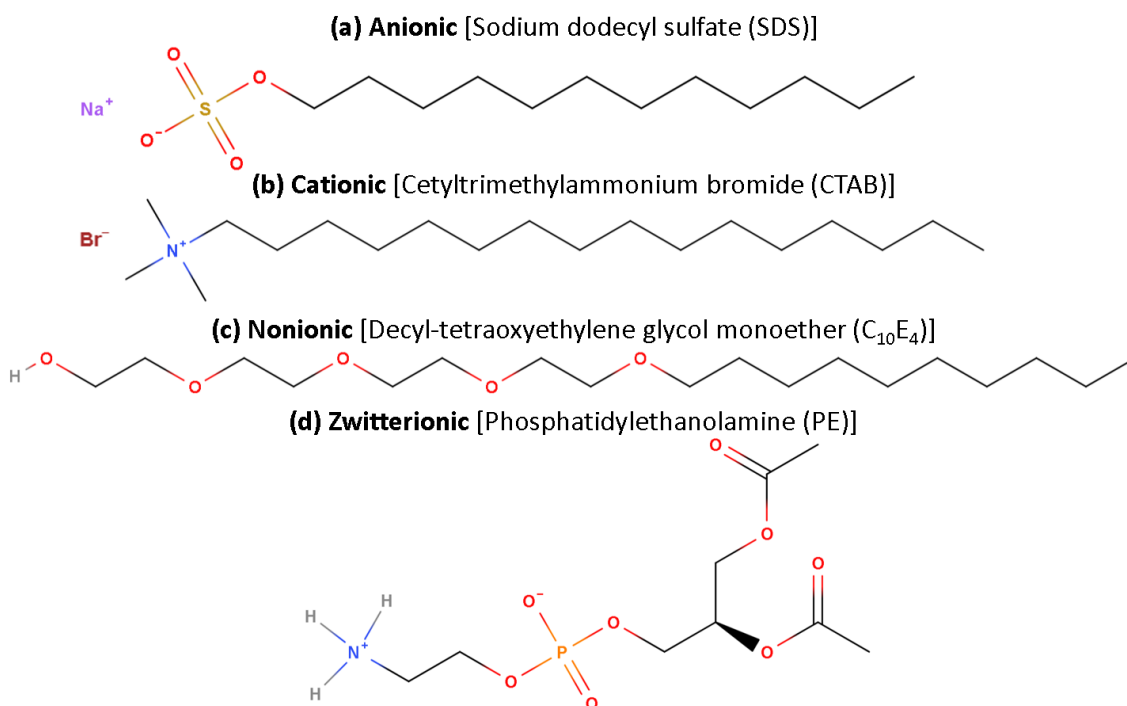


Figure 3.7: Examples of common amphiphiles: (a) anionic SDS, (b) cationic CTAB, (c) nonionic  $\text{C}_{10}\text{E}_4$ , and (d) zwitterionic PE.

Zwitterionic headgroups (e.g., betaines, sulfobetaines, phosphocholines) carry both positive and negative charges and are overall neutral across a broad pH range; some

carboxybetaine-type zwitterions are pH-responsive [89]. Amphiphiles dissolve to varying extents in water and organic solvents and partition accordingly in biphasic mixtures (e.g., water/oil). Practical detergency arises because amphiphiles concentrate at interfaces and assemble into aggregates that bind hydrophobes from surfaces and dispersions [88].

### Self-assembly in water

In aqueous media, amphiphiles adsorb to air–water or solid–liquid interfaces. For surfactants whose molecular shape allows micellization, there is a critical micelle concentration (CMC); above the CMC they spontaneously self-assemble into micelles with hydrophilic exteriors and hydrophobic cores. The primary driving force is the hydrophobic effect (release of constrained water) together with favorable tail packing, offset by headgroup repulsion and chain-packing penalties [75, 90]. For ionic surfactants, the CMC typically decreases with added electrolyte (screening headgroup charge), and increasing tail length generally lowers the CMC [88].

Beyond micelles, amphiphiles can also form bilayers and liposomes. Regular double-chain phospholipids generally have a packing parameter too large for micelles and instead assemble into bilayers and vesicles, so a micellar CMC is not defined for them [75]. Aggregate shape correlates with the molecular packing parameter (Sec. 3.4.2, Eq. (3.1)), which we later connect explicitly to LPS curvature preferences in Sec. 3.4.4 [75, 91].

### Interfaces and surface tension

Water’s polarity underlies strong hydrogen bonding and a relatively high surface tension. Amphiphiles lower surface tension by adsorbing at interfaces with headgroups in water and tails oriented away from it; adsorption is linked to  $\gamma$  through the Gibbs adsorption equation [92]. At sufficiently high bulk concentration, interfacial coverage saturates and micellization (aggregation) begins [93].

### Key physicochemical parameters

Key physicochemical parameters for surfactant self-assembly include **CMC**: concentration threshold for micellization, sensitive to tail length, headgroup charge/size, temperature, and ionic strength [88,93]; **Krafft point**: for many ionic surfactants, the temperature above which solubility rises sharply and micelles can form (solubility  $\approx$  CMC) [94]; **hydrophilic–lipophilic balance (HLB)**: empirical Griffin scale for emulsifier selection, with higher HLB favoring O/W and lower HLB favoring W/O [95]; and the **packing parameter**: semi-empirical predictor of aggregate geometry (see Sec. 3.4.2) [91].

### Relevance of amphiphiles to nematic LC biosensors

Amphiphiles are central to nematic LC (NLC) biosensors because their self-assembly at LC–water or LC–solid interfaces sets—and can dynamically retune—the director anchoring “felt” by the LC (Sec. 2.5). Headgroup charge or dipole, tail packing, and lateral order determine the preferred orientation and the anchoring strength  $W$  in the Rapini–Papoular description, Eq. (2.6) [4,19]. At clean LC–water interfaces the director is usually constrained to lie tangentially to the interface (planar boundary condition), with weak azimuthal anchoring ( $W_\phi \approx 0$ ; Sec. 2.5). Adsorption of amphiphiles can then promote a non-tangential director by changing the preferred polar angle at the interface and tuning the anchoring strength  $W$  [22,23], while the in-plane degeneracy typically remains. Biochemical events that change interfacial coverage  $\Gamma$  or charge (binding, displacement, enzymatic cleavage, conformational change) shift  $W(\Gamma)$  and/or the preferred polar angle  $\Theta_0$ , which then competes with the bulk Frank elasticity (Sec. 2.4, Eq. (2.4)) across a sample of thickness  $d$  [96]. A practical criterion for reorientation is  $d/\ell \sim 1$  with  $\ell = K/W$  (equivalently  $Wd/K \sim 1$ ; Sec. 2.5, Eq. (2.7)) [43]. Because distortions propagate over micrometer scales for typical  $K$  and  $W$ , small molecular changes are elastically amplified into macroscopic optical readouts under crossed polarizers, enabling label-free sensing [4,19,96]. Hybrid-

aligned 5CB films, for example, have been used to identify the critical surfactant concentration for the hybrid-to-homeotropic transition as a function of pH, providing an LC-based readout of pH-dependent sensitivity to ionic surfactants such as SDS [97].

### 3.4.2 Packing parameter in aqueous self-assembly

The shape and size of aggregates depend on molecular architecture (tail volume and length, headgroup area) and solution conditions (concentration, temperature, pH, ionic strength). As a first estimate, the packing parameter (often denoted  $P$  and also written here as the critical packing factor  $C_{\text{pp}}$ ) provides a compact predictor of preferred interfacial curvature [91], expressed by

$$C_{\text{pp}} = \frac{V}{a_0 \ell_c}. \quad (3.1)$$

where  $V$  is the effective hydrophobic tail volume (hydrocarbon chain volume),  $a_0$  is the effective headgroup area, and  $\ell_c$  is the maximum chain length.

As summarized in Fig. 3.8, increasing  $C_{\text{pp}}$  changes the effective molecular shape from a cone ( $C_{\text{pp}} < \frac{1}{3}$ ) to a truncated cone ( $\frac{1}{3} < C_{\text{pp}} < \frac{1}{2}$ ), then to a truncated cone approaching a cylinder ( $\frac{1}{2} < C_{\text{pp}} < 1$ ). The corresponding preferred morphologies are spherical micelles, cylindrical micelles, and bilayer vesicles, respectively. For a nearly cylindrical shape ( $C_{\text{pp}} \approx 1$ ), lamellar phases are favored, whereas an inverted truncated cone ( $C_{\text{pp}} > 1$ ) favors reverse micelles (also called inverse or inverted micelles) and water-in-oil microemulsions [75].

#### Vesicles and reverse aggregates

Phospholipids (one hydrophilic head and typically two hydrophobic tails) readily form bilayers and liposomes (vesicles, i.e., closed shells of lipid bilayer encapsulating an aqueous interior and dispersed in an aqueous phase) in water; in the packing-parameter picture this corresponds to  $C_{\text{pp}} \approx 1$ , i.e., a near-cylindrical molecular

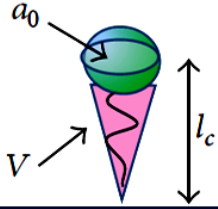

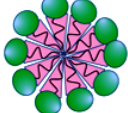


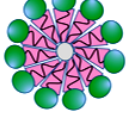
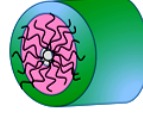

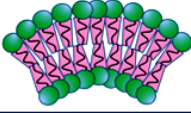
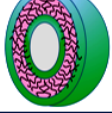

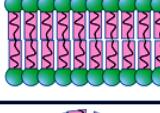


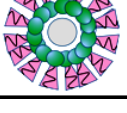
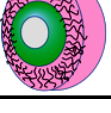
Critical packing parameter $C_{pp} = V/(a_0 \cdot l_c)$		Aggregate morphology	
			
	Cone $C_{pp} < 1/3$		Spherical micelles 
	Truncated cone $1/3 < C_{pp} < 1/2$		Cylindrical micelles 
	Truncated cone $1/2 < C_{pp} < 1$		Bilayer vesicles 
	Cylinder $C_{pp} \approx 1$		Lamellar phases 
	Truncated cone (inverted) $C_{pp} > 1$		Inv. micelles or microemulsions 

Figure 3.8: Amphiphile shapes and aggregate morphologies vs.  $C_{pp} = V/(a_0 l_c)$ . Green = hydrophilic headgroups; pink = hydrophobic chains. *Adapted from Lombardo et al., Adv. Condens. Matter Phys. (2015), Fig. 5 (CC BY) [98].*

shape [99, 100]. In thermodynamically stable oil-continuous microemulsions, the interface adopts negative curvature ( $C_{pp} > 1$ ) and forms reverse micellar aggregates. For example, in an AOT<sup>16</sup>-based microemulsion, surfactant molecules form a monolayer at the oil–water interface with tails in oil and headgroups toward water; typical droplet radii are on the order of 5–50 nm [101, 102]. More complex amphiphile topologies and mixtures broaden the accessible morphologies and phase behavior.

<sup>16</sup> AOT = sodium di-2-ethylhexylsulfosuccinate, an anionic surfactant widely used to form reverse micelles and stabilize microemulsions.

### 3.4.3 Lipopolysaccharides: structure, biological relevance, and self-organization

**Lipopolysaccharide (LPS).** LPS is an amphiphilic glycolipid and the major lipid component of the outer leaflet of the asymmetric outer membrane of Gram-negative bacteria, whose inner leaflet consists mainly of phospholipids. For its three-part architecture (lipid A, core oligosaccharide, O-antigen), see Sec. 3.4.4 and Fig. 3.10 [103].

**Exotoxins.** Exotoxins are secreted proteins produced by Gram-negative and Gram-positive bacteria; they are not structural membrane components like LPS and often act as enzymes that modify or cleave host targets [104]. Figure 3.9 contrasts protein exotoxin secretion (a) with LPS release (b).

**Endotoxin.** In practice, “endotoxin” is often used as a near-synonym for LPS. More precisely, the endotoxic activity of LPS resides in lipid A: when detected by the host

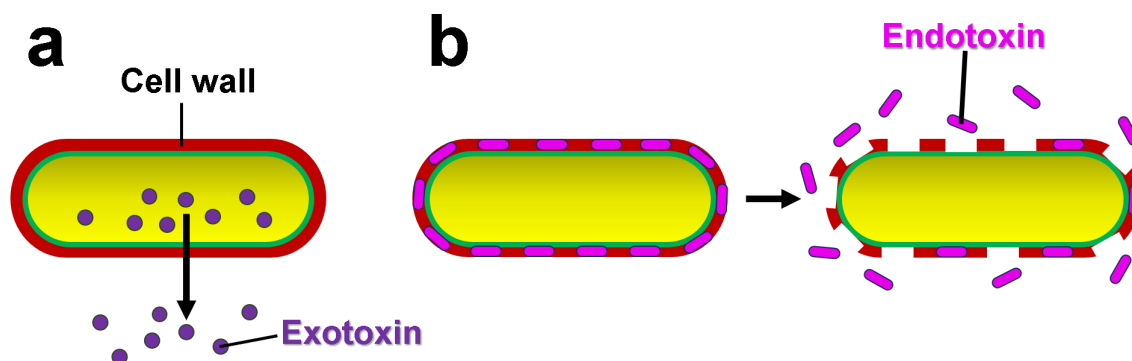


Figure 3.9: Exotoxin secretion (a) versus endotoxin (LPS) release (b) in Gram-negative bacteria. In (a) protein exotoxins synthesized in the cytosol are secreted across the cell envelope; in (b) LPS—a structural component of the outer membrane—is shed upon membrane disruption/lysis. Adapted from [104].

immune system, it triggers cytokine release and, at high exposures, can escalate to sepsis [105]. LPS is released upon cell lysis and, during growth, is shed in outer membrane vesicles (OMVs) [106, 107]. Accordingly, “endotoxin testing” typically means detecting LPS—specifically its lipid A—in a sample [108].

**Serotype and strain terminology.** A serotype names bacteria by surface antigens.

The LPS O-antigen and the flagellar H antigen define the “O#:H#” format (e.g., O157:H7) in *E. coli*; in *Salmonella*, the White–Kauffmann–Le Minor scheme also uses O and H antigens [109]. A wild-type strain is the naturally occurring, non-mutant reference within a species. Mutations in LPS-biosynthesis genes can remove the O-antigen or truncate the core, producing rough (R) strains that are useful for dissecting how LPS regions affect membrane stability and host recognition [110]. See Sec. 3.4.4 for how the O-antigen maps onto the molecular architecture.

### Self-assembly and aggregation in water

Because LPS is amphiphilic and highly charged, it self-assembles in aqueous buffers into supramolecular aggregates, predominantly bilayer-derived lamellae and vesicles rather than classical spherical micelles. These structures are often stabilized by divalent cations such as  $\text{Mg}^{2+}$  or  $\text{Ca}^{2+}$ . LPS has very low critical aggregation concentrations, and aggregate size and shape can strongly influence its biological activity and detection (see Sec. 3.4.5) [111].

### 3.4.4 Molecular architecture of LPS

Bacterial LPS molecules typically have molecular masses on the order of 10–20 kDa for smooth (S) LPS, i.e., molecules bearing an O-antigen polysaccharide [103,112]. By contrast, rough (R) LPS lacking the O-antigen (often referred to as lipooligosaccharide, LOS, especially in mucosal pathogens) are smaller and comprise lipid A with a truncated core [113]. Smooth LPS consists of three covalently linked regions (Fig. 3.10): **lipid A** — the hydrophobic membrane anchor and principal endotoxic moiety [103,112]; **core oligosaccharide** — a hydrophilic segment linking lipid A to the O-antigen [103,113]; and **O-antigen** — a repeating oligosaccharide chain whose composition varies by serotype [103,109].

The lipid A moiety consists of a  $\beta$ -glucosamine-(1 $\rightarrow$ 6)-glucosamine-1-phosphate backbone bearing fatty acid esters whose chain length varies by species but is uniform



Figure 3.10: Structure of bacterial lipopolysaccharide (LPS): lipid A, core oligosaccharide, and O-antigen polysaccharide chain. Reproduced from OpenStax, *Microbiology*, Fig. 15.13 (CC BY 4.0).

within each species. The inner core typically contains one to four 3-deoxy-D-mannooctulosonic acid (Kdo) residues. In wild-type enteric bacteria, Kdo is essential for viability; growth without Kdo has only been achieved in engineered or suppressor strains [114].

L-glycero- $\alpha$ -D-manno-heptopyranose also features in the inner core, and phosphorylation of these sugars imparts negative charge and membrane stability [115, 116]. The outer core adds sugars such as glucose, galactose, and N-acetylglucosamine and shows greater structural diversity than the inner core. The O-antigen, consisting of repeating units of typically 3–6 sugars, defines serogroups in bacteria like *E. coli*, *Salmonella enterica*, and *Vibrio cholerae* [117].

As schematized in Fig. 3.11, LPS can assemble into vesicles (a), lamellar stacks/bilayers (b), micelles (c), and dispersed monomeric units (d), depending on ionic conditions and surfactants. LPS is intrinsically heterogeneous and self-associates already below the operational CMC into oligomers and bilayer-derived aggregates; above this threshold, aggregate size and order increase [111]. In terms of the packing parameter (Sec. 3.4.2), multitailed lipid A confers a large hydrocarbon volume  $V$ , while divalent-cation bridging reduces the effective headgroup area  $a_0$ ; both effects raise  $C_{pp} = V/(a_0\ell_c)$  and bias LPS toward bilayer/lamellar morphologies (Fig. 3.11a,b) rather than spherical micelles (Fig. 3.11c) [118, 119]. Under monovalent conditions ( $\text{Ca}^{2+}/\text{Mg}^{2+}$ -free PBS), LPS reorganizes supported bilayers into lipid tubules and micron-scale perforations, whereas adding  $\text{Ca}^{2+}/\text{Mg}^{2+}$  biases morphology toward multilamellar stacks and sheet-like lamellae (Fig. 3.11a,b) [119, 120].

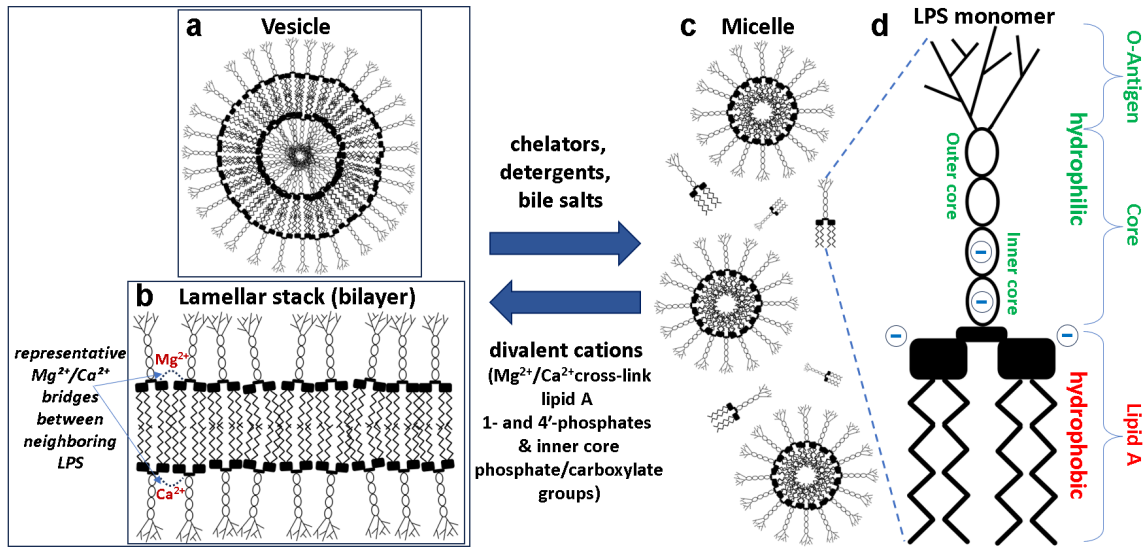


Figure 3.11: LPS self-assembly modes and how ions/surfactants shift them: vesicle (a), lamellar stack/bilayer (b), micelle (c), schematic monomer (d). Monomer sketch (d) adapted from a Wikimedia icon by “kupirijo” (CC BY-SA 3.0); other elements by the author.

Conversely, chelators (EDTA, citrate) and surfactants/bile salts (SDS, Tween 20, sodium cholate/deoxycholate) disrupt these bridges and disperse LPS into smaller mixed micelles or monomeric units (Fig. 3.11c,d) [121].

### Functions and applications

Within Gram-negative bacteria, LPS in the outer membrane forms a permeability barrier that limits entry of bile salts and many hydrophobic antibiotics [115]. As heat-stable endotoxins, LPS are key mediators of septic shock in humans and potent inducers of the immune response [112,122]. Galanos and co-workers found essentially identical endotoxic effects for synthetic and natural *E. coli* lipid A [122]. LPS preparations have served as model tools to study LPS structure, metabolism, immunology, physiology, and toxicity [123] and to stimulate cytokine production such as interleukins [124]. Because of the central role of LPS in septicemia, significant effort targets antibodies against LPS and inhibitors of its biosynthesis [125,126].

### 3.4.5 Critical aggregation of LPS (operational “CMC”)

Unless otherwise noted, “CMC” here denotes the operational critical aggregation concentration (CAC) in aqueous buffers without added divalent cations. Divalent cations (e.g.,  $\text{Mg}^{2+}$ ,  $\text{Ca}^{2+}$ ) can bridge phosphate groups in lipid A and promote aggregation at lower apparent concentrations [127]. Because LPS is chemically heterogeneous across serogroups and sample preparations, such CMCs are strongly condition-dependent (pH, ionic strength, surfactants, proteins).

#### Representative CMC measurements

Early light-scattering work by Santos *et al.* (Biophys. J. 2003) on *E. coli* O26:B6 identified an apparent CMC of  $14\ \mu\text{g mL}^{-1}$  and revealed premicellar oligomers below this threshold [111]. More recently, Noronha *et al.* quantified micelles formed by *E. coli* O113 LPS and determined a CMC of  $0.020\ \text{mg mL}^{-1}$  using a pyrene polarity probe. At  $0.043\ \text{mg mL}^{-1}$  they achieved drug loadings of 20–28% and encapsulation efficiencies of 74–83% for chloroquine, curcumin, vemurafenib, and doxorubicin, with micelle size increasing with LPS concentration and depending on the encapsulated drug [128]. For amphiphiles like LPS, which favor bilayer-derived aggregates, such reported “CMCs” are best viewed as CACs marking the onset of higher-order aggregation rather than classic spherical micellization [119].

#### CMC/CAC determination by pyrene $I_{373}/I_{393}$

The CAC was determined from pyrene fluorescence using the standard  $I_1/I_3$  method originally developed for CMC measurements. The ratio of the first and third vibronic maxima,  $I_{373}/I_{393}$  (often written  $I_1/I_3$ ), reports local polarity and changes when pyrene partitions into hydrophobic aggregate domains. Figure 3.12 plots  $I_{373}/I_{393}$  versus LPS concentration; the CAC is taken as the intersection of two linear fits (pre- and post-aggregation regimes), consistent with standard pyrene-based analyses [129].

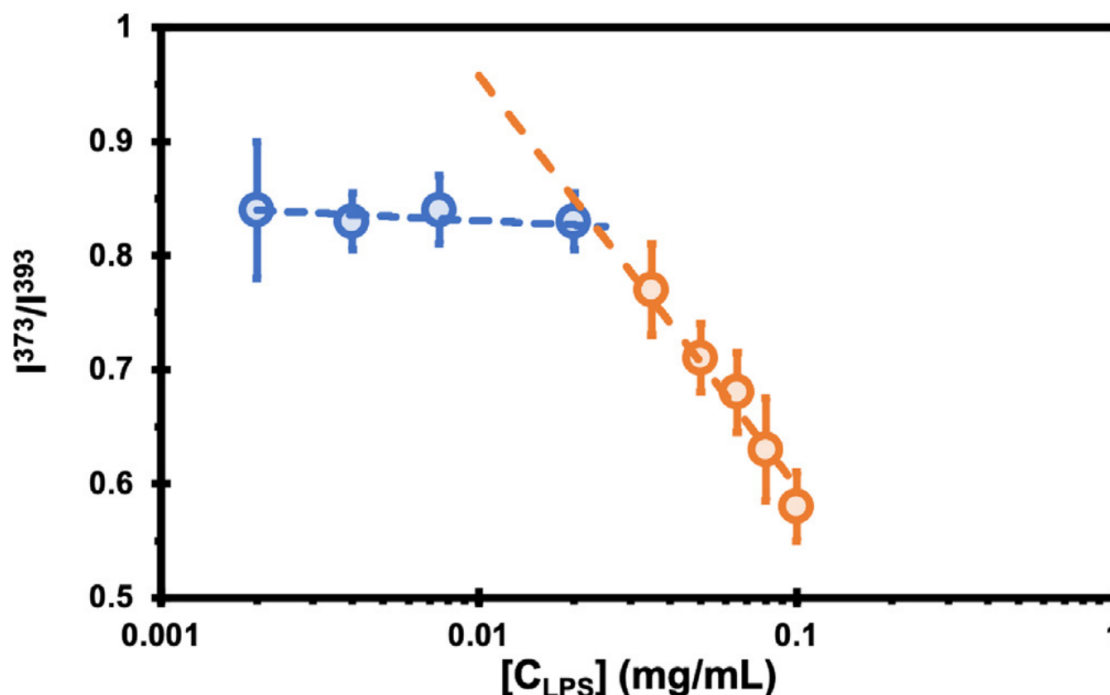


Figure 3.12: Fluorescence intensity ratio  $I_{373}/I_{393}$  versus LPS concentration at 25 °C, used to determine the operational CMC/CAC of LPS in water. Reproduced from Noronha *et al.* [128], *J. Mol. Liq.* **372**, 121154 (2023), with permission from Elsevier. © 2023 Elsevier B.V.

### Implications for formulation

Above the CAC, LPS forms higher-order aggregates stable on experimental timescales—most often bilayer-derived vesicles/lamellae; micelles have also been reported for certain preparations and in the presence of hydrophobic payloads (e.g., curcumin) [128]. Aggregate dimensions and loading capacity depend on serogroup and solution conditions. These features motivate exploration of LPS-based assemblies as nanocarriers in research settings; any *in vivo* use is constrained by endotoxin safety limits.

### Regulatory limits and unit conventions

Parenteral endotoxin limits use the pharmacopoeial limit =  $K_{\text{MDD}}/M$  relation in the *Bacterial Endotoxins Tests* (BET) chapters, where  $K_{\text{MDD}}$  is the maximum allowed endotoxin dose per kg body weight and  $M$  is the maximum labeled dose per kg (for infusions, the maximum dose delivered in one hour) [130, 131]. Endotoxin Units

(EU) quantify assay response in the bacterial endotoxins test (BET), which uses either LAL (Limulus ameocyte lysate, horseshoe crab clotting cascade) or rFC (recombinant Factor C, crab-free fluorometric assay). They are not a unit of mass; EU  $\leftrightarrow$  ng conversions are lot-specific [132].

### **LAL and rFC assays**

- BET methods include gel-clot, turbidimetric, and chromogenic LAL [130]. These use the horseshoe-crab coagulation cascade and can be inhibited or enhanced by matrix components (e.g., surfactants, chelators, proteins) [133].
- rFC provides a crab-free, fluorometric alternative recognized in Ph. Eur. (General Chapter 2.6.32; effective 2021-01-01) [134].
- Sandwich ELISA-like formats (e.g., ENDOLisa) capture LPS using a high-affinity phage-derived ligand, perform wash steps to reduce interference, and detect with Factor C/rFC; these systems can mitigate low endotoxin recovery in challenging matrices [135].

### **Biological- and chemical-based LPS sensors**

- Biosensors often employ affinity elements that capture LPS from complex samples, including endogenous carriers such as LPS-binding protein, engineered peptides, or aptamers; transduction can be optical or electrochemical [136].
- Generic LPS sensors, whose receptors target conserved lipid A or core regions, typically lack serogroup resolution without serotype-specific elements [137].

### **LC droplet assays for endotoxin**

- Picogram-per-mL endotoxin triggers bipolar $\rightarrow$ radial ordering transitions in micrometer LC droplets at surface coverages below  $10^{-5}$  Langmuir [138].

- The fraction of radial droplets decreases with increasing droplet size at fixed endotoxin, and the response is modulated by ionic strength and pH; modeling identifies the saddle–splay constant  $K_{24}$  as a central control parameter and estimates a droplet free-energy change of  $\sim 10^{-17}$  J [81].
- Coupling LC droplets to flow cytometry and convolutional neural networks enables high-throughput classification of bacterial sources and quantification over a dynamic range spanning many orders of magnitude [139].

## Conclusion

Linking LPS molecular structure to supramolecular assembly and immune recognition is essential for sensing and safety. Because aggregation is highly sensitive to ions, surfactants, and sample preparation, any reported CMC must specify buffer and assay conditions. LC-droplet platforms have been explored as potential complements to BET (LAL/rFC) and immunoassays by providing rapid, label-free readouts over wide dynamic ranges; with proper calibration and controls, they can aid source attribution and quantification [134, 139].

## 3.5 Bio- and chemosensors

Numerous biosensors and chemosensors [140, 141] detect a wide range of biological and chemical analytes, with applications spanning waste management, healthcare, agriculture, forensics, bioscience, and water monitoring.

### 3.5.1 Historical background

From 1896 onwards, following J. S. Haldane’s work on “afterdamp”, caged canaries were used as sentinels in coal mines: their rapid response to CO and hypoxia provided an early audible and visual warning of hazardous atmospheres [142]. By the late 20th century, this role had been assumed by electronic CO meters. Early electrochemical

sensing began in 1906 when Cremer linked acid concentration ( $\text{H}^+$  activity) to the potential across a glass membrane, laying the groundwork for the pH concept introduced by Sørensen in 1909 [143]. Hughes developed the first practical glass pH electrode in 1922 [144].

In parallel, Nelson and Griffin’s 1916 work on immobilized invertase on  $\text{Al}(\text{OH})_3$  gel and activated charcoal provided an early proof of principle for enzyme-based sensing [145,146]. A decisive step toward modern biosensors came in 1956, when Leland C. Clark Jr. introduced the polarographic dissolved- $\text{O}_2$  electrode (“Clark electrode”) for measuring oxygen in aqueous media. In 1962, he and co-workers demonstrated one of the first true biosensors<sup>17</sup>: an amperometric enzyme electrode for glucose detection, followed by a potentiometric urea biosensor in 1969 [148,149]. In 1975, Yellow Springs Instruments (YSI) commercialized an enzymatic glucose sensor for blood glucose analysis, combining glucose oxidase with selective membranes to achieve robust clinical measurements [150]. Since then, biosensing has advanced rapidly, aided by portable blood-analysis systems, point-of-care diagnostics, and, more recently, a large and growing commercial market for biosensor-based devices [151,152].

A generic biosensor architecture is illustrated in Fig. 3.13: sample matrix  $\rightarrow$  sensing element  $\rightarrow$  electronics  $\rightarrow$  readout. For canonical block diagrams see [147,153]. In LC systems, analyte binding perturbs the interface and director, producing an optical response that is captured by the detector, digitally processed, and displayed.

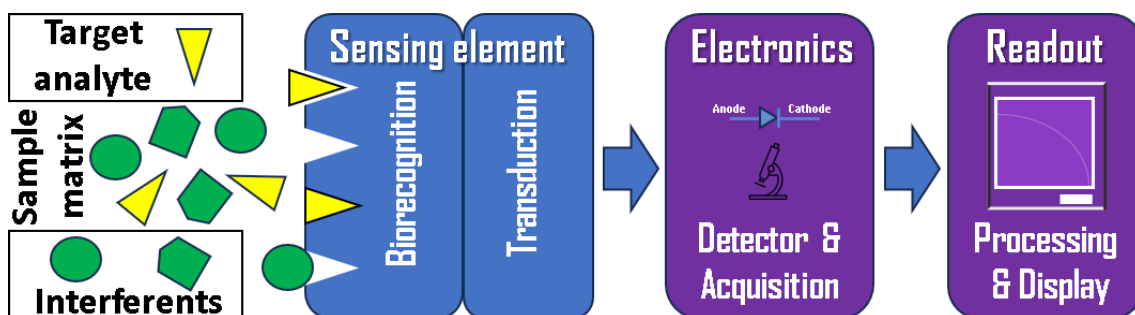


Figure 3.13: Simplified schematic diagram of a biosensor.

<sup>17</sup> **Biosensor:** an analytical device that couples biorecognition with a physicochemical transducer to yield a signal related to the analyte [147]. The Clark dissolved- $\text{O}_2$  electrode lacks biorecognition (chemical sensor); the enzyme glucose electrode (1962) is the canonical biosensor.

### 3.5.2 Wearable applications and market context

Wearable biosensors and sensorized garments are being developed for continuous monitoring of physiological indicators such as heart rate, breathing, skin temperature, and sweat composition [154,155]. Most systems are still at the prototype or early-clinical-evaluation stage, but they illustrate how textiles can host integrated sensor arrays that provide real-time data outside traditional clinical settings [154].

Glucose monitoring is a central application because of its importance for diabetes management. Beyond finger-prick tests and minimally invasive continuous glucose monitors, textile-based glucose biosensors aim to extract glucose information from sweat or interstitial fluid. Khosravi and co-workers reported a screen-printed, textile electrochemical sensor that uses glucose oxidase to transduce sweat-glucose concentrations into a current directly on fabric [156]. Such platforms are intended to complement established wearable devices rather than replace them and highlight the broader trend toward noninvasive, fabric-integrated sensing [155,156].

### 3.5.3 Market landscape and validation

Over the past decade, the biosensor literature and market have expanded rapidly [157]. The global biosensor market, valued at roughly USD 30 billion in the early 2020s, is projected to grow at a high single-digit compound annual growth rate, driven mainly by medical adoption (particularly for diabetes monitoring), demand for point-of-care tests, and portable analytical instruments [152]. The COVID-19 pandemic further boosted this demand by creating large-scale need for rapid diagnostics, with biosensor-based point-of-care tests central to rapid screening. At the same time, recent high-profile fraud cases in blood diagnostics highlight that successful translation requires rigorous clinical validation, transparent performance metrics, and robust quality control, lessons that are directly relevant to any future deployment of LC-based biosensors.

### 3.5.4 Liquid crystal–based sensors

Because of their long-range orientational order and interfacial sensitivity, LCs transduce nanoscale binding or adsorption events into optically readable textures. LC-based sensor platforms offer label-free and potentially low-cost readouts, but challenges remain to achieve molecular specificity and high sensitivity for small analytes [158,159]. Anchoring and texture conventions follow Sec.3.1.1 and Fig. 3.4. LC platforms include planar films, droplets, and shells, each suited to different assay formats [158,159], and in this thesis we focus primarily on nematic shells, referring to nematic droplets only when they play a supporting role.

In thermotropic LC sensors, adsorption or specific interfacial binding perturbs the bulk–surface energy balance (anchoring notation as in Sec.3.1.1), reorienting the director and thereby changing the optical response [160]; this competition between interfacial anchoring and elasticity is the basic signal-transduction mechanism in LC-based sensors. Abbott and co-workers applied this principle in nematic films and droplets to demonstrate robust optical biosensing [158]. For planar-film formats, P. Popov *et al.* showed that analyzing LC alignment between circular polarizers enables accurate optical detection of amphiphiles at LC–water interfaces by suppressing azimuthal texture degeneracy and isolating director tilt changes [161].

Beyond planar films, curved LC geometries such as droplets and shells amplify interfacial events and yield defect-mediated textures. For definitions of symmetric vs. asymmetric shells and w/o/w production, see Sec.3.1 and Fig. 3.1. Monodisperse droplets and double-emulsion shells are readily generated by microfluidics and can be used as-is or after biochemical functionalization [23,162–166]. More broadly, such devices fall within the emerging field of liquid crystal microfluidics, where flow, elasticity, and surface anchoring jointly shape director fields and defect structures [167].

### Unfunctionalized droplets report bacterial envelopes

As illustrated in Fig. 3.14, unfunctionalized nematic 5CB droplets in water report bacterial envelope chemistry: exposure to Gram-negative *E. coli* (and enveloped viruses) transfers outer-membrane lipids to the LC–water interface, promoting homeotropic anchoring and driving a bipolar  $\rightarrow$  radial transition with the characteristic “Maltese cross” under POM [168]. Gram-positive bacteria, lacking an outer lipid membrane, typically leave droplets bipolar (tangential) under the same conditions (Fig. 3.14, bottom-right) [168]. This mirrors the interfacial-sensing principle established for planar films [160].

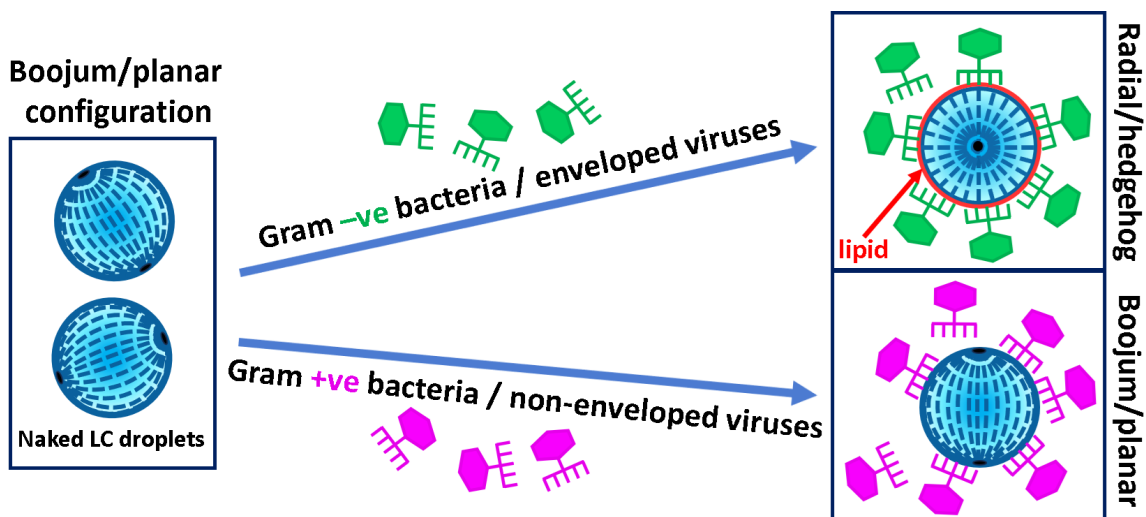


Figure 3.14: Interaction of naked LC droplets (aqueous phase without added stabilizers) with bacterial or viral surfaces. Gram-negative bacteria and enveloped viruses (green) induce a transition to a radial/hedgehog configuration, whereas Gram-positive bacteria and non-enveloped viruses (magenta) leave the droplets in the boojum/planar texture (no transition). Bacteria and viruses are shown schematically as cartoons. Adapted and redrawn for clarity from [168].

### WGMs reveal surfactant adsorption

Humar and Muševič used whispering-gallery-mode (WGM) lasing<sup>18</sup> of Nile-red-doped 5CB microdroplets to sense adsorption of SDS at the LC–water interface [36]. As the SDS concentration increases, anchoring evolves from tangential (bipolar) to

<sup>18</sup> WGM: optical resonances where light circulates around the droplet equator by total internal reflection; small changes in refractive index or radius shift the lasing modes.

homeotropic (radial): an inner ring defect appears near 0.2 mM, a central point defect near 0.8 mM, and fully homeotropic alignment around 2.0 mM (Fig. 3.15); WGM spectral changes are detectable already at sub-millimolar concentrations [36]. In the radial configuration, sharp WGM resonances are visible in the fluorescence spectra and lasing occurs above a relatively low pump threshold, whereas in the bipolar configuration WGM resonances are absent below threshold and lasing requires higher pump intensities with less stable output [36]. This corresponds to the same SDS-induced tangential  $\rightarrow$  homeotropic anchoring transition described earlier for nematic shells in Sec. 3.2. Mechanistically, interfacial SDS increases the radial symmetry of the effective refractive-index profile, which shifts WGM resonance families and lowers the lasing threshold. Optically trapped droplets in a microfluidic channel further enabled in-flow readout of the WGM response [36].

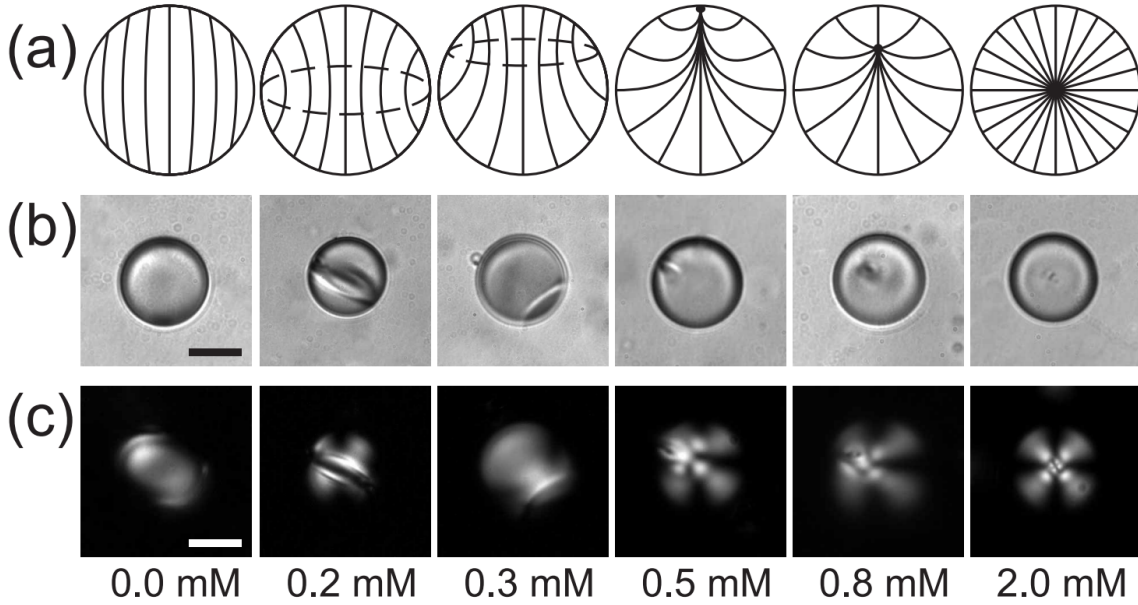


Figure 3.15: 5CB droplet director field configuration vs. SDS concentration. (a) Schematics: planar at low SDS, radial at 2.0 mM. (b) Bright-field: inner ring at 0.2 mM; central point defect by 0.8 mM (scale bars 10  $\mu$ m). (c) Corresponding POM images. Reproduced from Humar *et al.* [36] (CC BY 4.0).

### Sessile droplets report bacterial viability

Wei and co-workers showed that sessile 5CB droplets can distinguish between live and dead Gram-negative *E. coli*: lipids from intact outer membranes transfer to the LC–water interface of nearby droplets, driving homeotropic anchoring and a radial texture, whereas dead cells with disrupted membranes leave droplets tangential with characteristic fan-shaped POM patterns [169]. In their work, chitosan-reinforced graphene oxide (CS–GO) served as the antibacterial agent; as CS–GO progressively compromised the *E. coli* membranes, the LC-droplet response switched from radial (live) to planar (CS–GO-killed), providing a simple, label-free optical readout of antibacterial activity [169]. The sensing contrast thus reflects both the composition and integrity of the lipid envelope, so sessile LC droplets report envelope structure and bacterial viability.

Functionalized nematic droplets provide another route to biosensing: Gleeson and co-workers demonstrated on-chip detection of antimicrobial peptides using phospholipid-coated LC droplets trapped in PDMS microfluidic devices [170]. Peptide binding to the lipid monolayer disrupts the lipid coating and thus the homeotropic anchoring, driving a radial–bipolar reorientation and yielding a clear optical transition under POM [170,171]. These systems complement endotoxin-triggered transitions in LC droplets by extending LC-based sensing to specific peptide targets.

### Defect-targeting by LPS/lipid A enables ultralow detection

LC droplets can be exceptionally sensitive to endotoxin: in micrometer-sized 5CB droplets, *E. coli* LPS, via its lipid A moiety, was shown to trigger bipolar-to-radial ordering transitions at picogram-per-milliliter concentrations by defect-localized adsorption at surface coverages below  $10^{-5}$  Langmuir (far from monolayer saturation) [138]. Mechanistically, multitailed lipid A amphiphiles accumulate at defect-proximal regions (boojums), where imposing local homeotropic anchoring yields a disproportionate reduction of elastic free energy; because the energy gain

scales with defect strength rather than global surface coverage, only trace lipid A is needed to switch the texture [138]. Synthetic six-tailed lipid A mimics reproduce the same transitions at ultralow concentrations, indicating that multivalent hydrophobic architecture, rather than detailed saccharide chemistry, is the key driver [172].

### **Shells: stabilizers, alignment, and curvature**

Boundary conditions in 5CB shells are set by adsorbed polymers and surfactants, as detailed in Sec.3.2 and Sec.3.2.1 (schematics in Fig. 3.3; canonical textures in Fig. 3.4). Briefly, SDS promotes homeotropic anchoring, while PVA preserves tangential anchoring; when inner and outer phases differ, hybrid shells may arise and the nematic–isotropic transition can split into two steps [23]. Below CMC, the surfactant headgroup and chain length tune anchoring thresholds: longer chains promote radial alignment at lower  $C_N$ <sup>19</sup>, with curvature-dependent differences between inner and outer interfaces [173].

### **Microfluidic LC–gel microspheres for local pH sensing**

As shown in Fig. 3.16a,b, Xie *et al.* formed LC–gel core–shell microspheres by microfluidics, using the nematic mixture E7 doped with 4-pentylbiphenyl-4-carboxylic acid (PBA) as the LC core and an alginate gel shell encapsulating bacteria [174]. The protonation state of the PBA carboxyl groups modulates the interfacial charge density at the LC–gel boundary and thereby the LC anchoring: under acidic conditions, protonated PBA favors an axially symmetric, homeotropic configuration, whereas deprotonation at higher pH restores tangential anchoring and a bipolar texture, which can be read out under POM [174]. The reported pH resolution reaches  $\sim 0.1$  in situ, enabling localized, real-time, three-dimensional monitoring of bacterial microenvironmental pH in proof-of-concept experiments [174].

---

<sup>19</sup>  $C_N \equiv c/c_{\text{CMC}}$ : dimensionless surfactant concentration normalized to its CMC.

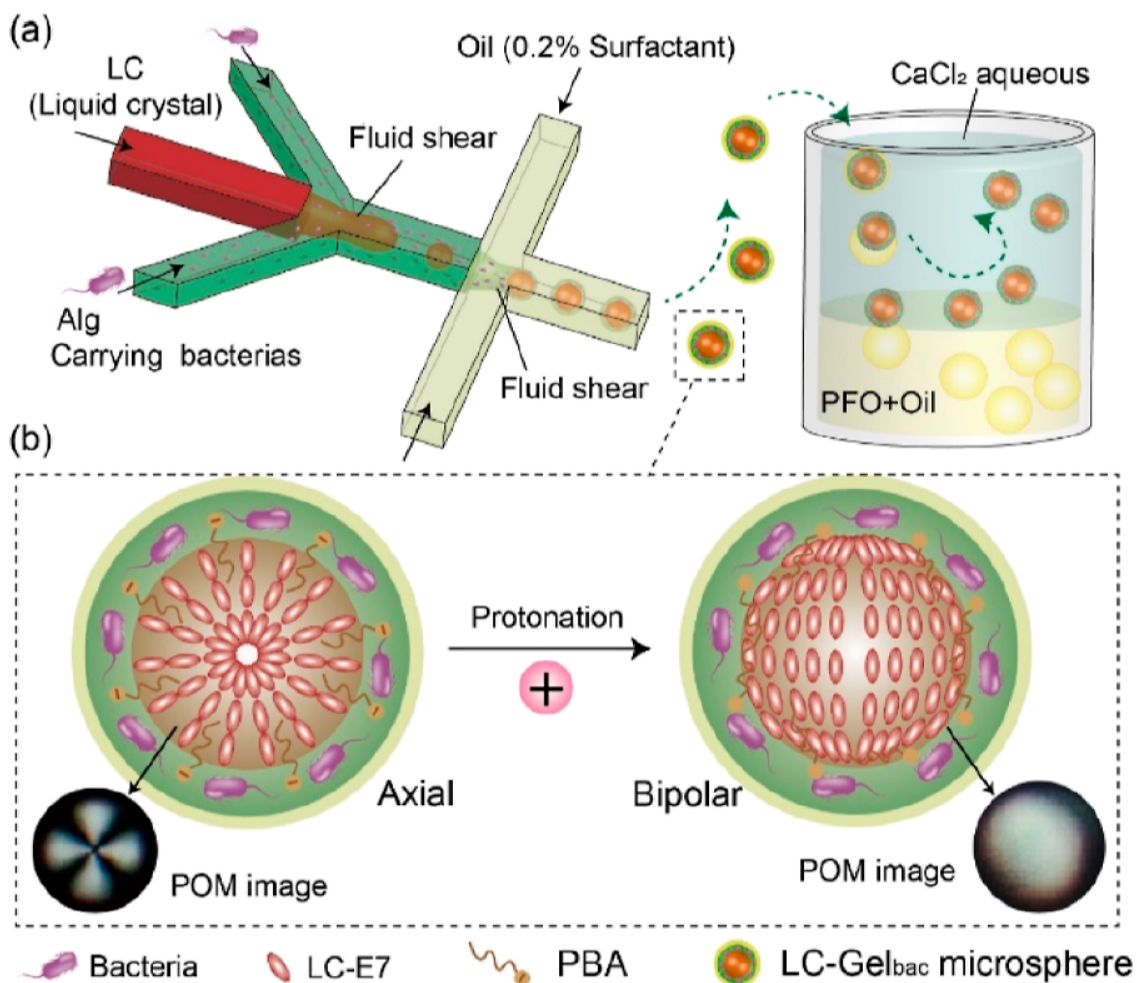


Figure 3.16: Preparation of LC-Gel<sub>bac</sub> core-shell microspheres by flow-focusing microfluidics and protonation-induced texture changes observed by POM. Reproduced from Ref. [174] with permission from the American Chemical Society.

### Lipid islands and elastic coupling on shells

At sufficient coverage, lipid monolayers on LC shells phase-separate into spindle-shaped lipid islands (condensed domains) that impose local homeotropic anchoring and generate elastic distortions in the LC bulk [175]. The condensed/expanded coexistence creates line tension at island rims and a non-uniform anchoring field; islands migrate along thickness gradients toward the thin pole in asymmetric shells (cf. Fig. 3.1c), where interfacial, elastic, and curvature energies are best balanced. Lipids subsequently transfer through the LC to the opposite interface, where secondary islands form; elastic interactions then drive island alignment and “sandwich” stacking

(island–LC–island), yielding a dynamic, label-free readout of lipid accumulation and trans-shell transport [175].

### 3.5.5 Summary of LC-based sensing mechanisms

Nematic LC systems, from planar films to droplets and shells, convert interfacial events into robust optical signatures via the mechanism reviewed in Sec.3.1.1: interfacial adsorption or binding perturbs anchoring, and topological constraints amplify the signal into textures that are easily read by POM. Unfunctionalized droplets differentiate Gram-negative from Gram-positive envelopes by lipid transfer; WGMs provide spectral fingerprints of surfactant adsorption; sessile droplets distinguish live from dead bacteria via membrane-integrity-dependent lipid donation; functionalized droplets transduce specific binding events at designed lipid monolayers (for example, antimicrobial peptides at phospholipid-coated interfaces) [170, 171]; and defect-targeted self-assembly of lipid A/LPS within the cores of topological defects in LC droplets yields picogram-per-milliliter detection limits [138, 172]. In shells, stabilizers, chain length, curvature, and thickness gradients tune alignment, while LC–gel microspheres extend sensing to microenvironments with  $\sim 0.1$ -unit pH resolution [23, 173–175].

Collectively, these features make nematic LC films, droplets, and shells promising, versatile, label-free transducers for biochemical sensing across formats and length scales in research settings. More extensive discussion of thermotropic liquid crystal-assisted chemical and biological sensors is given in an earlier review [176] and in a recent overview of LC biosensors [177].

In the following, we focus on nematic shells as a model platform where these interfacial and topological sensing principles can be probed in detail. As a first step, Chapter 4 examines how reflection-mode POM can distinguish tangential from radial director fields in shells from their birefringence-modulated reflection signatures, providing a complementary, reflection-only route to reading out nematic shell alignment.



## Chapter 4

# Reflection-mode POM for tangential vs. radial director-field identification in nematic LC shells

*This chapter is based on and partially reproduces material from: N. Popov and J. P. F. Lagerwall, Birefringence-modulated total internal reflection in liquid crystal shells, Frontiers in Soft Matter **2**, 991375 (2022) [178]. The article is published under the Creative Commons CC BY 4.0 license, and text and figures are reproduced or adapted here in accordance with that license.*

Conventional laboratory polarizing microscopes, equipped with both transmission and reflection modes, are widely used to probe director fields and textures in a variety of LC samples. In nematic phases, there is no intrinsic Bragg reflection<sup>1</sup>, unlike in cholesteric phases. Cholesteric LC shells, by contrast, have been extensively studied as spherical Bragg reflectors: their multicolored internal and external reflection patterns and the role of wall-thickness asymmetry have been analyzed in detail [179, 180]. In this thesis, cholesteric phases therefore appear only as a reference point; all

---

<sup>1</sup> In cholesteric (chiral nematic) LCs, Bragg reflection denotes the selective reflection of circularly polarized light with the same handedness as the cholesteric helix, with central wavelength  $\lambda_0 \approx \bar{n}p$ , where  $p$  is the pitch and  $\bar{n}$  the average refractive index.

experimental work focuses on achiral nematic shells. In nematic shells, transmission-mode POM readily reveals the director-field configurations and the locations of surface defects in tangentially aligned shells. Although transmission-mode POM has dominated optical studies of nematics, the reflection response of nematic LC shells has received comparatively little attention to date [178]. As we show in this chapter, reflection-mode POM reveals additional optical phenomena arising from the interplay of boundary conditions, topology, and birefringence in LC shells.

High-quality research microscopes remain bulky, delicate, and expensive. By contrast, frugal microscopes aimed at point-of-care biosensing, such as clip-on mobile-phone microscopes that read colorimetric or fluorescence assays, are typically designed to work in reflection rather than transmission. Illumination and detection share a common optical axis, so there is no straightforward way to back-illuminate the sample. Most low-cost microscopes are thus constrained to reflection, whereas nematic shells have so far been characterized primarily in transmission. The central observation in this chapter is that rotating the polarizer in reflection mode can cause bright spots or arcs to appear, disappear, or rotate around nematic shells. This polarization-sensitive response, without relying on any transmission image, is sufficient to distinguish tangentially from radially aligned shells. A natural target application for this effect is a smartphone-based clip-on microscope that is portable and low-cost, similar in spirit to previously reported smartphone-based polarized microscopes and LC sensing devices [181, 182]. In this work, we characterized this reflection response using a conventional research polarizing microscope operated in reflection mode, while keeping in mind the constraints of low-cost, low-resolution optics so that our conclusions can, in principle, be transferred to reflection-only platforms.

Nematic LC shells are promising biosensors because surface binding events distort their director fields, producing distinctive textures under crossed polarizers [23, 183]. Here we focus on double-emulsion shells made from the nematic mixture E7 (Synthon

Chemicals) as the middle phase between two aqueous phases. Materials and shell-production protocols are summarized in the Materials and methods section and in Ref. [178]. These experiments show that birefringence-modulated total internal reflection (TIR) produces striking bright spots and arcs in reflection. Building on this, we establish a simple reflection-mode protocol for distinguishing LC-shell alignment that is compatible with low-cost, portable hardware.

Sections 4.1 and 4.2 present experimental findings for shells with different surface anchoring: tangential and radial, respectively, comparing their familiar transmission appearances to the newly explored reflection textures. Section 4.3 then discusses the origin of these reflection patterns. We attribute them to TIR-mediated light-guiding paths that are sensitive to the local optic-axis orientation. This framework explains why bright arcs or spots appear at specific locations on the shell, and why they vanish or rotate when the illumination polarization is rotated.

## Sample preparation and shell production

### Liquid-crystal shells and stabilizing solutions

The LC shells studied in this chapter were prepared using the E7 nematic mixture as the LC middle phase. Two types of aqueous stabilizing solutions were used to control the surface anchoring. For tangential anchoring, both inner and outer aqueous phases contained 1 wt.% PVA (Sigma-Aldrich,  $M_w = 13\text{--}23\text{ kg mol}^{-1}$ , 87–89% hydrolyzed). For homeotropic (normal) anchoring, both inner and outer phases contained 0.025 wt.% Tween-20 (polyethylene glycol sorbitan monolaurate, Sigma-Aldrich). Unless stated otherwise, PVA in this thesis refers to this 13–23 kg mol<sup>−1</sup>, 87–89% hydrolyzed grade. Stock solutions of PVA and Tween-20 were prepared by dissolving the compounds in distilled water at elevated temperature until optically clear and then filtering through 1.2  $\mu\text{m}$  syringe filters.

## Shell production and handling

LC shells were produced in a glass-capillary microfluidic device operating in the dripping regime, following Ref. [163]. The inner aqueous phase was injected into E7 and subsequently sheared by the outer aqueous phase to form water–E7–water double emulsions with matched inner and outer compositions (Sec. 4). Shell diameters and wall thicknesses were controlled via the applied pressures. Double emulsions were collected in sealed glass capillaries. For optical characterization, capillaries were mounted in a Linkam hot stage on a Nikon polarizing microscope and observed in the nematic range of E7; further details are given in Appendix A.2 and Ref. [178].

## 4.1 Tangential alignment: transmission vs. reflection

### 4.1.1 Appearance in transmission mode

As discussed in Sec. 3.2.2 and illustrated in Fig. 3.4, tangentially anchored nematic shells carry a total topological charge  $+2$  on each spherical interface, realized by various combinations of  $+1$  and  $+\frac{1}{2}$  defects. In strongly asymmetric shells, where the top is very thin and the bottom comparatively thick, defects drift toward the thinnest region because this minimizes the total length of the disclination segments connecting the inner and outer interfaces and thereby reduces the total elastic energy associated with the defect lines [54]. When these defects are sufficiently close to each other, they behave optically as an effective  $+2$  defect at the top of the shell.

Under transmission POM, such shells characteristically display an eight-brush pattern radiating outward from this defect region, as shown in Fig. 4.1. When the shell symmetry axis is aligned with the polarizer or analyzer, we typically observe eight distinct brushes, corresponding to alternating regions of high and low transmitted intensity. Shells whose orientations deviate from the polarizer–analyzer axes tend to exhibit more complex or blurred textures, especially in the thicker regions of the

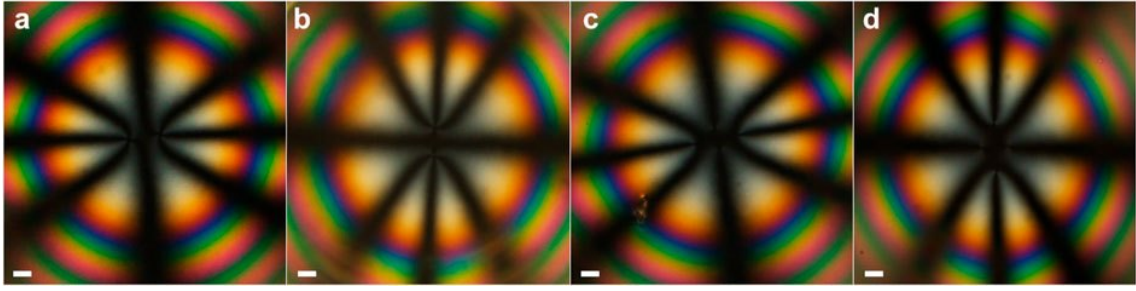


Figure 4.1: Transmission POM micrographs of tangentially aligned E7 shells, zooming in on the thinnest region where the defects are collected. The 8-brush pattern indicates the presence of a defect region near the thinnest area. We find shells with two  $+1$  defects (a and b) and four  $+\frac{1}{2}$  defects (c and d). Scale bar (thick white line) is  $10\ \mu\text{m}$ .

shell. This blurring is attributed to lensing and beam-splitting effects caused by the extended optical path and high birefringence in the thick parts of the shell.

An additional metric for characterization becomes available when some shells rupture. The resulting LC droplets in the sample have a volume equal to the LC core of the original shell. By measuring the shell radius  $r_s$  and the droplet radius  $r_d$  from micrographs, one can determine the inner droplet radius  $r_i$  and hence a mean shell thickness  $\bar{d} \approx r_s - r_i$ . For the shells analyzed in Ref. [178], this procedure yields  $\bar{d} \approx 15.6\ \mu\text{m}$ , implying that the bottom (thickest) part of the shell reaches thicknesses of order  $30\ \mu\text{m}$ . Such thicknesses lead to multi-order optical retardation and strong lensing and scattering effects in transmission, which can obscure the defect texture in crowded or polydisperse samples.

### 4.1.2 Appearance in reflection mode

In reflection mode, tangentially aligned shells, instead of the familiar transmission brush pattern, typically reveal two bright spots or arcs near the shell perimeter along the “equator” perpendicular to the defect axis, with the shape depending on the shell orientation and numerical aperture. Rotating the polarization of the illuminating light causes these bright spots to extinguish when the incident polarization aligns with the local director at the perimeter. The underlying mechanism is TIR at the LC–water interfaces, modulated by the local optic-axis orientation (discussed in Sec. 4.3),

which selectively enables or suppresses guided light paths. These antipodal bright spots (Fig. 4.2c,d) correspond spatially to the dark arcs observed in transmission mode (Fig. 4.2a). In other words, they mark regions where guided light does not

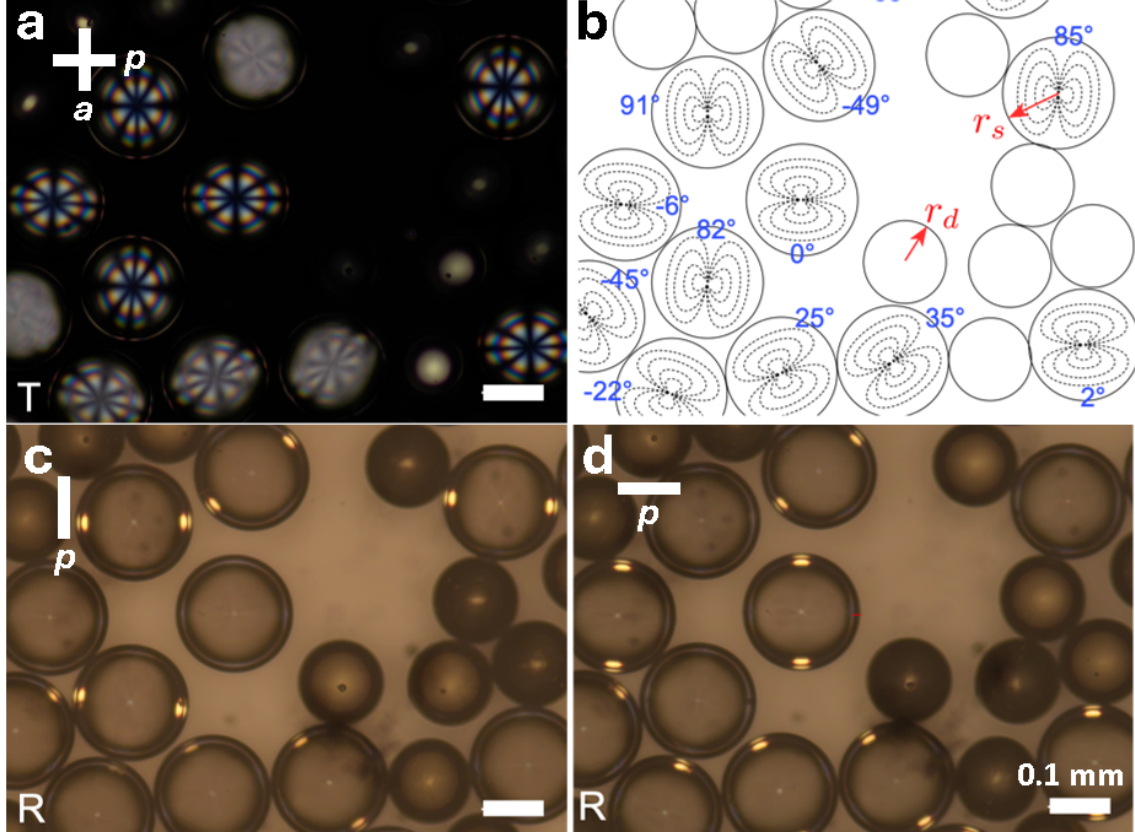


Figure 4.2: Transmission and reflection micrographs of thin-topped, tangentially aligned E7 shells (radius  $r_s$ ) and droplets (radius  $r_d$ ), the latter originating from ruptured shells, all recorded at 39°C. (a) Transmission-mode (T) POM between crossed polarizers, showing the characteristic eight-brush defect patterns at the thin upper hemispheres; the polarizer ( $p$ ) and analyzer ( $a$ ) directions are indicated with white lines. (b) Drawing of shell and droplet contours with sketched director fields; the configurations are inferred from the appearance in (c) and (d). Blue numbers give the angle between the polarizer axis and the shell symmetry axis used for quantitative orientation analysis, while red arrows define  $r_s$  and  $r_d$ . (c,d) Corresponding reflection-mode (R) micrographs without analyzer for two orientations of a single polarizer  $p$ . Two bright antipodal spots or short arcs along the shell perimeter rotate with the polarizer, providing a signature of tangential alignment. Scale bar is 0.1 mm.

reach the detector in transmission. For practical purposes, these high-contrast bright spots in reflection provide a reliable handle: if bright antipodal spots appear and disappear as the polarizer is rotated, the shell is tangentially aligned. Figure 4.2b sketches the corresponding director-field configurations and shell/droplet contours

from (a).

## 4.2 Radial alignment: transmission vs. reflection

### 4.2.1 Appearance in transmission mode

As summarized in Sec. 3.2.2, shells with fully homeotropic (SDS/SDS) anchoring exhibit a defect-free radial director field. In transmission POM, such radially aligned shells produce conoscopy-like patterns: each shell shows a characteristic Maltese cross with concentric interference rings (Fig. 4.3). These patterns arise from the interference of polarized light traversing the curved radial director field, where

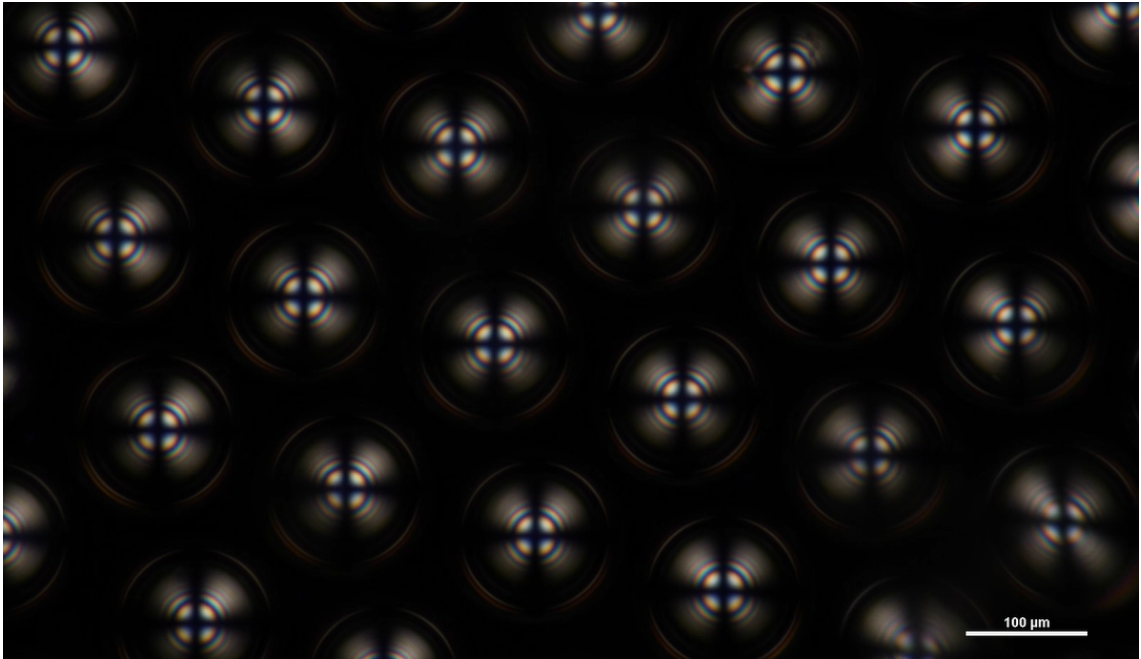


Figure 4.3: Transmission POM micrograph of radially aligned nematic shells, showing the characteristic Maltese cross and concentric interference rings.

variations in optical path length across the shell lead to constructive and destructive interference. As a result, even under standard orthoscopic illumination, the texture closely resembles the conoscopy pattern of a homeotropically aligned flat nematic cell.

### 4.2.2 Appearance in reflection mode

In reflection mode with crossed polarizers, radially aligned shells exhibit an intensely bright ring around the perimeter, typically interrupted by darker zones along the polarizer–analyzer axes. Removing the analyzer (i.e., using a single polarizer) transforms the image: rather than a continuous ring, we see two bright arcs separated by two dark spots (Fig. 4.4a). As the polarizer is rotated, the bright arcs rotate in sync, with the dark spots following accordingly. Figure 4.4b shows the corresponding reflection-mode texture between crossed polarizers, with four bright arcs and dark regions aligned with the polarizer and analyzer directions. Scale bar (thin white line) is  $100\ \mu\text{m}$ .

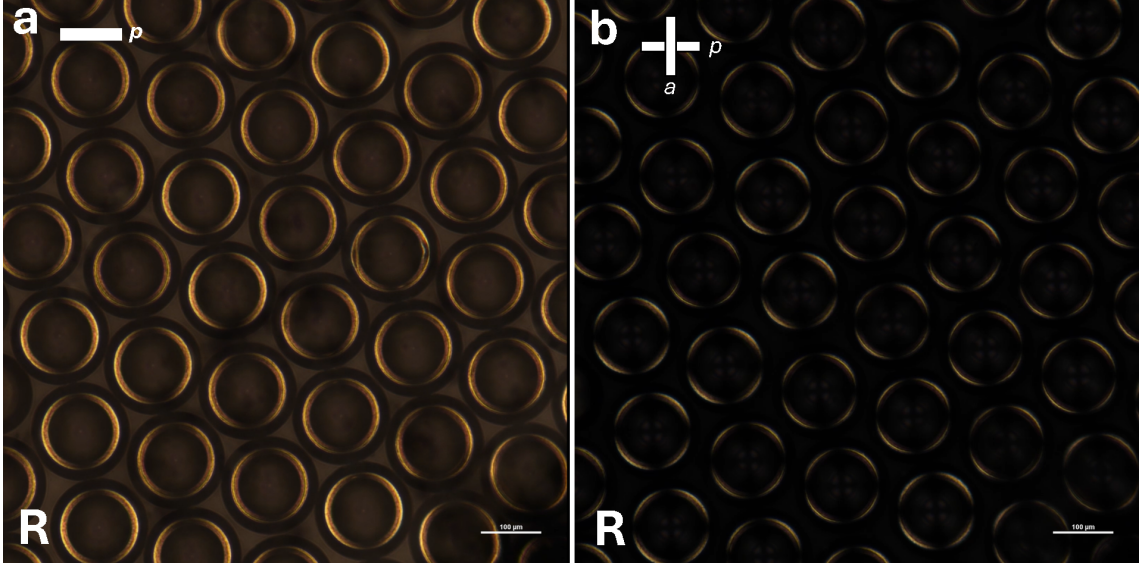


Figure 4.4: Reflection-mode POM micrographs of radially aligned nematic E7 shells. (a) Polarizer only (no analyzer), showing two bright arcs separated by dark spots. (b) Crossed polarizer and analyzer, showing four bright arcs and dark regions along the polarizer and analyzer directions. Scale bar (thin white line) is  $100\ \mu\text{m}$ .

This rotating pattern of bright arcs is due to birefringence-modulated TIR at the LC–water interfaces (see Sec. 4.3). Because the director field is radial, different perimeter segments satisfy the TIR condition for different polarizer orientations: where the local director is favorably oriented with respect to the incident polarization, guided light returns to the objective and produces a bright arc, whereas segments where the TIR condition is not met appear dark. From the point of view of a low-cost

reflection-only microscope, the operational rule is therefore simple: if rotating a single polarizer causes two bright arcs on the shell perimeter to rotate continuously around the shell, separated by two dark spots that track the polarizer, the shell is radially aligned.

## 4.3 Total internal reflection and light guiding in nematic shells

### 4.3.1 Origin of TIR-mediated light guiding

Building on our birefringence framework introduced in Sec. 2.6, we now show how TIR at the LC–water interfaces generates the bright arcs and spots observed in reflection-mode images of nematic shells. The way these TIR-guided features respond to polarizer rotation provides an unambiguous signature of tangential vs. radial alignment, information that would normally require a high-quality transmission image.

For TIR to take place, the refractive index  $n_{\text{LC}}$  of the LC shell must exceed that of the surrounding isotropic aqueous medium ( $n_{\text{iso}}$ ), and the light must strike the interface at a sufficiently oblique angle relative to the normal. Using Snell’s law at this interface (Eq. 2.8) with  $n_1 = n_{\text{LC}}$  and  $n_2 = n_{\text{iso}}$ , we have  $n_{\text{LC}} \sin \theta_{\text{LC}} = n_{\text{iso}} \sin \theta_{\text{iso}}$ . Total internal reflection occurs when the angle of refraction would formally reach  $\theta_{\text{iso}} = 90^\circ$ , i.e., when the refracted ray would propagate along the interface, which implies  $\theta_{\text{LC}} \geq \arcsin(n_{\text{iso}}/n_{\text{LC}})$ .

For a positive-birefringence nematic such as E7 at  $39^\circ\text{C}$ , with principal indices  $n_\perp \approx 1.525$  and  $n_\parallel \approx 1.71$  (Sec. 2.6), the resulting critical angles are

- for light experiencing  $n_\parallel$  (extraordinary index):  $\theta_{\text{crit}} \approx 52.7^\circ$ , which readily allows multiple TIR events and hence light guiding;
- for light experiencing  $n_\perp$  (ordinary index):  $\theta_{\text{crit}} \approx 63.1^\circ$ , making repeated TIR

much less likely, so the beam typically escapes after one or two reflections.

Thus, only the polarization that accesses the extraordinary refractive index  $n_{\parallel}$  results in effective light guiding through TIR. This explains why tangential shells exhibit bright antipodal spots only in perimeter regions where the local director orientation is favorable, and why radially aligned shells display bright arcs that follow the rotation of the incident polarization.

### 4.3.2 Implications for shell characterization and applications

From a characterization perspective, TIR-mediated light guiding observed in reflection mode provides a powerful complement to conventional transmission POM. Even thick-walled shells or shells in less favorable orientations can be effectively analyzed via their characteristic reflection patterns, which encode information about the shell's azimuthal orientation, anchoring conditions, and local director variations even when the internal texture is blurred in transmission.

To clarify the underlying mechanism, Fig. 4.5 sketches exemplary ray paths for two orthogonal polarizations. In panel (a) the incident light is polarized perpendicular to the local director, so the ray samples the ordinary refractive index  $n_{\perp} = 1.525$ . The corresponding critical angle is relatively large ( $\theta_c \approx 63.1^\circ$ ), and after the first reflection the internal incidence angle (about  $59.3^\circ$ ) already falls below  $\theta_c$ . The TIR condition is thus broken and the ray leaks into the surrounding continuous phase instead of completing a guiding loop. In panel (b) the shell is rotated by  $90^\circ$  about the vertical axis so that the director points out of the image plane. The same input polarization is now parallel to the director, and the ray experiences the extraordinary refractive index  $n_{\parallel} = n_e = 1.71$ , for which the critical angle is smaller ( $\theta_c \approx 52.7^\circ$ ). Along the illustrated path the incidence angles (between roughly  $55.6^\circ$  and  $62.5^\circ$ ) remain above this reduced  $\theta_c$ ; TIR persists over many reflections, the ray is guided around the shell, performs an optical U-turn, and emerges on the opposite side, producing the bright reflection spots and arcs. Note that the incidence angles in

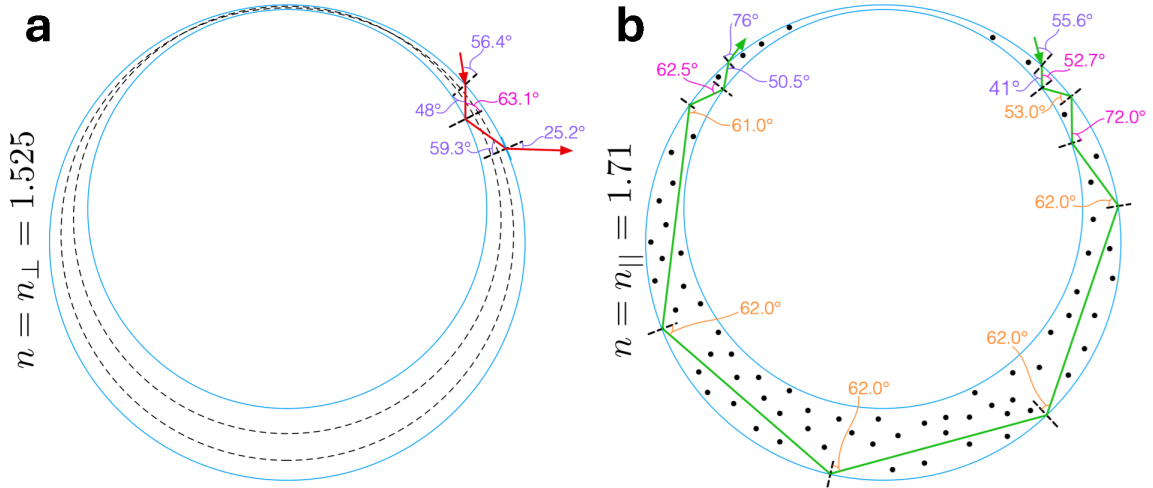


Figure 4.5: Schematic illustration of potential TIR-mediated light-guiding paths in a nematic shell. (a) When the incident light is polarized perpendicular to the local director, the ray experiences the ordinary refractive index  $n_{\perp} = 1.525$ . The corresponding critical angle is relatively large ( $\theta_c \approx 63^\circ$ ), so after the next reflection the incidence angle falls below  $\theta_c$ ; the TIR condition is lost and the ray leaks into the surrounding continuous phase instead of forming a closed guiding loop. (b) When the shell is rotated such that the light polarization is parallel to the director, the ray experiences the larger extraordinary refractive index  $n_{\parallel} = n_e = 1.71$ , which reduces the critical angle ( $\theta_c \approx 53^\circ$ ). The subsequent incidence angles, although smaller than in (a), remain above this reduced  $\theta_c$ ; as a result the ray undergoes multiple TIR events, is guided around the shell, makes a U-turn, and re-emerges on the opposite side, giving rise to the bright spots or arcs observed in reflection. Black dots mark regions where the director is perpendicular to the image plane.

panel (b) are smaller than those in panel (a), yet they still exceed the smaller critical angle associated with  $n_{\parallel}$ .

On the application side, the presence of guided light paths within the shell can have several consequences. In photopolymerizable nematic shells, guided paths may cause non-uniform polymerization, creating regions of enhanced cross-linking where the illumination is intensified by TIR, whereas areas without guiding remain less polymerized. Such light-guided polymerization could be deliberately used to imprint spatial patterns of cross-link density without complex external optical setups. Similarly, emerging light-triggered liquid-crystal elastomer (LCE) shell actuators may benefit from modulating their actuation via selective polarization, using the TIR effect to shape the internal light distribution. In cholesteric shells, where

Bragg reflection is typically the desired mechanism, it is important to be aware of TIR-mediated light guiding because it may compete with or broaden the intended optical response, for example by modifying emission bandwidths or the viewing-angle dependence of the reflected color.

## 4.4 Summary and outlook

In this chapter, we showed that reflection-mode POM reveals robust, polarization-dependent optical signatures in nematic LC shells that are closely linked to their director fields. These signatures arise from birefringence-modulated TIR at the LC–water interfaces and can be detected even with simple, low-cost optical hardware.

Our main conclusions are:

1. **Tangential vs. radial alignment can be identified from reflection alone.**

Tangentially aligned shells exhibit two bright antipodal spots on the shell perimeter, whose intensity varies strongly with polarizer orientation and which are strongly attenuated when the polarizer reaches an unfavorable orientation with respect to the local director. Radially aligned shells, in contrast, show two bright arcs that rotate continuously with the polarizer, separated by two dark spots that track the polarization direction. This qualitative difference provides a simple decision rule for director-field identification in reflection-mode images.

2. **The relevant features are in principle compatible with low-cost, low-resolution optics.**

The bright spots and arcs are large-scale, high-contrast features that do not require a high numerical aperture or high magnification to be resolved. This makes them particularly well suited for clip-on smartphone microscopes and other frugal reflection-mode devices that cannot easily operate in transmission.

3. **The underlying mechanism is birefringence-modulated TIR.**

When the incident polarization has a substantial component along the local director,

light samples the extraordinary index  $n_{\parallel}$  of E7, leading to a smaller critical angle and enabling repeated TIR events. This produces guided light paths around the shell that return light to the objective in specific perimeter regions. For polarizations that couple predominantly to the ordinary index  $n_{\perp}$ , the TIR condition is not fulfilled or is quickly lost, and the guided paths disappear. The dependence of TIR on the local director orientation explains both the spatial localization of bright spots/arcs and their strong polarization sensitivity.

Beyond these conceptual conclusions, the observed phenomena suggest several directions for future work and opportunities for harnessing the effect:

- **Portable LC-shell biosensors in reflection mode.** The decision rules established in this chapter can enable practical alignment identification and quality control of nematic shells using only a smartphone and a rotatable polarizer. In a practical biosensing scenario, this would allow one to (i) verify surface anchoring (tangential vs. radial) at the point of use and (ii) track binding-induced distortions of the director field via changes in the reflection pattern, without requiring a transmission-mode research microscope.
- **Optically guided photopolymerization and actuator design.** Because TIR-mediated light guiding enhances the local light intensity along specific paths, it could be used to pattern cross-link density in photopolymerizable shells simply by adjusting the illumination polarization. This provides a route to imprinting internal structures or anisotropic stiffness into liquid-crystal elastomer shells. The same principle could be used to tailor the actuation modes of LCE shells by aligning TIR-guided paths with desired deformation directions.
- **Managing undesired guiding in cholesteric and lasing shells.** In cholesteric shells designed for Bragg reflection or microlasing, TIR-mediated guiding may compete with the desired optical response, for example, by broad-

ening emission bands or altering polarization selectivity. Systematic reflection-mode characterization, of the kind developed here for nematics, could help disentangle and control these contributions in more complex helical systems.

- **Towards quantitative and automated analysis.** Although the present work relies on qualitative and human-readable patterns (bright spots vs. rotating arcs), the same reflection images could be analyzed quantitatively. Future studies could, for instance, relate the intensity and angular width of the bright regions to shell thickness, refractive-index contrast, or the presence of defects. In a practical smartphone-based implementation, these patterns could be classified automatically using image-analysis or machine-learning approaches, turning a simple polarizer rotation into a robust, one-click readout of shell alignment.

Overall, reflection-mode POM with birefringence-modulated TIR turns nematic LC shells into systems whose director fields can be characterized in both reflection and transmission. This widens the range of optical platforms available for LC-shell biosensors and actuators, from conventional research microscopes to future portable, low-cost devices.

Beyond these optical signatures, a practical LC-shell biosensing platform must also control when the director field reaches a stable reference state. If shells are polymerized too early, transient defect textures may be frozen in, undermining reproducibility and the interpretation of POM-based readouts. The next chapter therefore shifts from static images to annealing kinetics, quantifying how shell thickness and PVA stabilization set the relaxation time scale and define the post-production window in which a robust baseline texture is established.

## Chapter 5

# Annealing kinetics of director fields in tangentially aligned nematic shells

Nematic liquid-crystal shells are promising candidates for label-free biosensing, because small changes in interfacial chemistry can trigger large, optically visible reconfigurations of their director fields. To use LC shells as sensing elements in practical devices, we must be able to produce them in large numbers with high yield and then stabilize their internal structure, for example, by photopolymerization or by forming polymer networks in the LC phase. This raises a central question: *can we polymerize shells directly after production to lock in their internal structure, or must we first allow their director fields to anneal to a well-defined equilibrium state?* This chapter shows that the latter is necessary in practice: polymerizing immediately after production would freeze a director field that is still relaxing toward equilibrium, leading to poorly defined and irreproducible textures for sensing. The director field must first anneal to its elastically favored configuration before polymerization can reliably lock in a reproducible baseline state. The geometry and interfacial physics of these shells, as well as the role of PVA as a stabilizer, were introduced in Secs. 3.1 and 3.2; here we quantify the dependence of the annealing time on shell thickness and defect configuration in 5CB shells stabilized with moderately hydrolyzed PVA.

We usually refer to a tangentially aligned shell as “looking like” the eight-brush pattern in Fig. 5.2e–g, i.e., a canonical tangential texture as discussed in Sec. 3.2 and illustrated in Fig. 3.4a. However, that static view hides the rich transient dynamics that take place between formation and the final state. The same shell first passes through a sequence of intermediate textures (Fig. 5.2a–e), in which defects are still migrating and the disclination network is progressively confined into the thinnest polar region. By analyzing these changes quantitatively, we can gain insight into both the fundamental defect physics on curved nematic interfaces and the practical conditions required to reach a stable, reproducible sensing baseline.

LC shells with displaced inner aqueous cores are generally not of uniform thickness. A small density mismatch between the nematic middle phase and the surrounding aqueous phases shifts the inner droplet by a distance  $\delta$  away from the shell center, thereby thinning one hemisphere and thickening the opposite hemisphere, as discussed in Sec. 3.1 and illustrated schematically in Fig. 3.1. Figure 5.1 shows the same geometry in more detail, explicitly indicating the center offset  $\delta$ , the equatorial

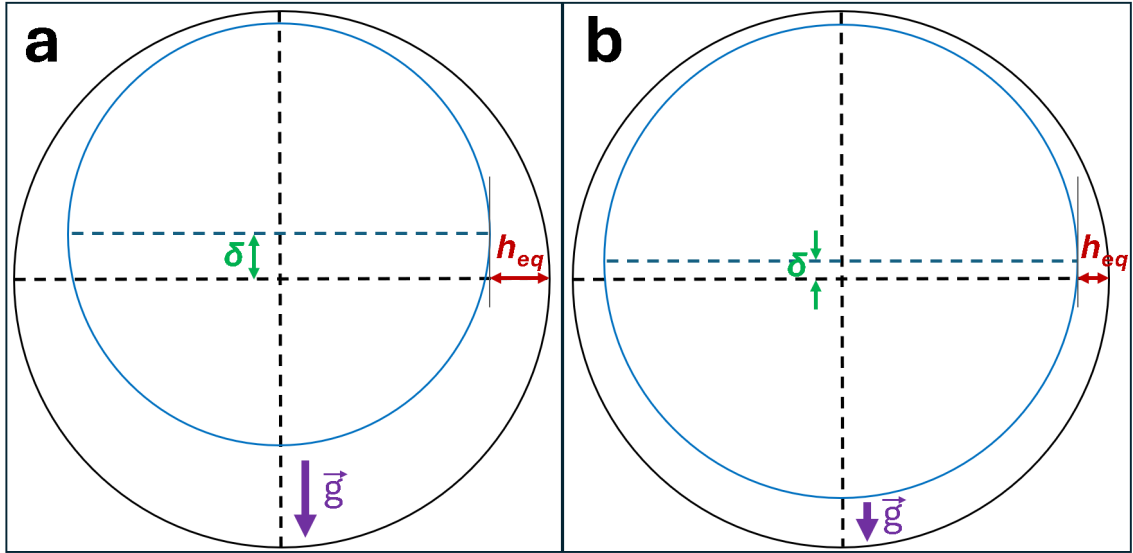


Figure 5.1: Schematic side-view cross-sections of 5CB shells in aqueous PVA, complementing the geometry in Fig. 3.1. (a) Smaller inner aqueous core: larger buoyancy-induced offset  $\delta$ , steeper top–bottom wall-thickness gradient, and a more strongly asymmetric shell. (b) Larger inner core: smaller  $\delta$ , shallower gradient, and more uniform thickness. The equatorial thickness  $h_{eq}$  serves as a proxy for the mean wall thickness; the downward arrow indicates gravitational acceleration  $\vec{g}$ . Not to scale.

thickness  $h_{\text{eq}}$ , and the direction of gravity.

For a given outer diameter, this buoyancy-induced thickness asymmetry produces a wall-thickness gradient in which thicker shells typically show a larger relative thickness contrast between the thin and thick poles. The resulting increase in elastic energy gain from shortening disclination lines in the thin cap strengthens the elastic driving force that pulls defects toward the thin pole, so we expect annealing to proceed faster in thicker shells than in thinner shells. Throughout this chapter we therefore use the equatorial wall thickness  $h_{\text{eq}}$  as a proxy for the average shell thickness and quantify how defect migration toward the thin pole, and the characteristic time required for a shell to reach its elastically favored ground state of tangential alignment, depend on  $h_{\text{eq}}$ .

## 5.1 Shell preparation and annealing metrics

### 5.1.1 Shell production and imaging

Double emulsions of aqueous PVA/5CB/aqueous PVA were produced at room temperature using a homemade glass microfluidic device operating in the dripping regime. The middle phase was 5CB; the inner and outer phases were aqueous PVA solutions with compositions specified in each experiment. Unless otherwise noted, PVA was 87–89 % hydrolyzed with a nominal molar mass of  $13\text{--}23\text{ kg mol}^{-1}$  (Sec. 3.2).

During production, shells were collected and transferred into glass capillaries with a rectangular inner cross-section of  $0.20 \times 2.00\text{ mm}^2$ . The capillaries were sealed at both ends to prevent evaporation and placed on the stage of a POM equipped with a rotating stage, typically after  $\sim 1$  min of shell production.

### 5.1.2 Thickness batches and definition of the annealing time

For each shell we determined the outer diameter  $D_{\text{outer}}$  and the equatorial wall thickness  $h_{\text{eq}}$  from bright-field transmission images acquired in the standard top-view configuration (optical axis perpendicular to the coverslip) and analyzed in ImageJ. The quantity  $h_{\text{eq}}$  was used as an operational measure of the average shell thickness. Seven shell batches were studied with mean equatorial thicknesses  $h_{\text{eq}}$  of 3.35, 5.35, 7.51, 9.86, 14.03, 17.30, and 22.28  $\mu\text{m}$ , containing 16, 39, 14, 13, 10, 15, and 12 shells, respectively (Table 5.1). In total,  $N = 119$  shells were analyzed. Across all batches, the outer diameter was nearly constant, lying in the narrow range 0.14–0.15 mm (142–147  $\mu\text{m}$ ), with an overall mean of  $\approx 145$   $\mu\text{m}$ . Here and in Table 5.1, uncertainties in  $h_{\text{eq}}$  and  $D_{\text{outer}}$  denote the standard error of the mean (SEM) over the shells in each batch, reflecting ImageJ measurement error and modest shell-to-shell size variations.

Unless otherwise noted, the thickness-batch analysis below refers to shells stabilized in 0.5 wt. % PVA (87–89 % hydrolyzed). Shells stabilized by nearly fully hydrolyzed PVA (98 %) were produced using the same microfluidic and capillary-handling protocol, with outer diameters of order 0.15 mm. In those experiments, only the PVA concentration was varied, ranging from 0.009 to 5 wt.% as specified in Sec. 5.4.

Table 5.1: Shell batches analyzed for the dependence of the relaxation time  $\tau$  on the equatorial wall thickness  $h_{\text{eq}}$ . Listed are mean  $\pm$  SEM (over the shells in each batch) for  $h_{\text{eq}}$ , outer diameter  $D_{\text{outer}}$ , and their ratio, together with the number of shells analyzed per batch in the imaged capillary region. Values of  $h_{\text{eq}}$  are rounded to one decimal place and  $D_{\text{outer}}$  to the nearest micrometer.

$h_{\text{eq}}$ ( $\mu\text{m}$ )	$D_{\text{outer}}$ ( $\mu\text{m}$ )	$h_{\text{eq}}/D_{\text{outer}}$	Number of shells
$3.4 \pm 0.1$	$145 \pm 0.1$	$0.0231 \pm 0.0004$	16
$5.3 \pm 0.1$	$142 \pm 0.2$	$0.0376 \pm 0.0008$	39
$7.5 \pm 0.1$	$147 \pm 0.2$	$0.0514 \pm 0.0005$	14
$9.9 \pm 0.1$	$143 \pm 0.2$	$0.0691 \pm 0.0005$	13
$14.0 \pm 0.2$	$142 \pm 0.3$	$0.0987 \pm 0.0013$	10
$17.2 \pm 0.1$	$146 \pm 0.3$	$0.1176 \pm 0.0008$	15
$22.3 \pm 0.2$	$144 \pm 0.6$	$0.1549 \pm 0.0014$	12

To characterize annealing, we recorded time series of POM images with crossed polarizers and a fixed sample orientation and tracked the separations between selected pairs of defects. The experimental *annealing time*  $t_{\text{eq}}$  was defined from these trajectories as the time at which the fitted defect separation reached its plateau, as described in Sec. 5.2.1. Operationally,  $t_{\text{eq}}$  was taken as the time at which the fitted distance  $s_{ij}(t)$  changes by  $|\Delta s_{ij}| = 0.5 \mu\text{m}$  over the subsequent 1000 min, corresponding to a change smaller than both the optical resolution and the measurement uncertainty. Because  $s_{ij}(t)$  is fitted by an exponential-with-offset form  $s_{ij}(t) = C + Ae^{-t/\tau}$ , the operational annealing time  $t_{\text{eq}}$  is a monotonic function of the relaxation time  $\tau$ ; within a given geometry they therefore carry equivalent information about how quickly the shell approaches its equilibrium configuration.

## 5.2 Annealing in shells with moderately hydrolyzed PVA

### 5.2.1 Defect dynamics in shells

We first consider shells stabilized in 0.5 wt. % PVA (13–23 kg mol<sup>−1</sup>, 87–89 % hydrolyzed) with equatorial thickness  $h_{\text{eq}} \approx 5.4 \mu\text{m}$ .

Figure 5.2 shows representative POM images of such shells during annealing. Within 25–35 min, the initially nearly symmetric texture (Fig. 5.2a) relaxes into an eight-brush “flower-like” pattern (Fig. 5.2e–g), consistent with defects localizing into a low-energy tangential configuration within the thin upper hemisphere (cf. fully tangential shells in Sec. 3.1).

The time-dependent separations were extracted as follows. For each shell, we measured the straight-line (chord) distance  $c$  between two selected defects in the microscope image and converted it to the corresponding surface (arc) separation  $s$  along the great circle passing through them. Writing  $R = D_{\text{outer}}/2$ , the central angle

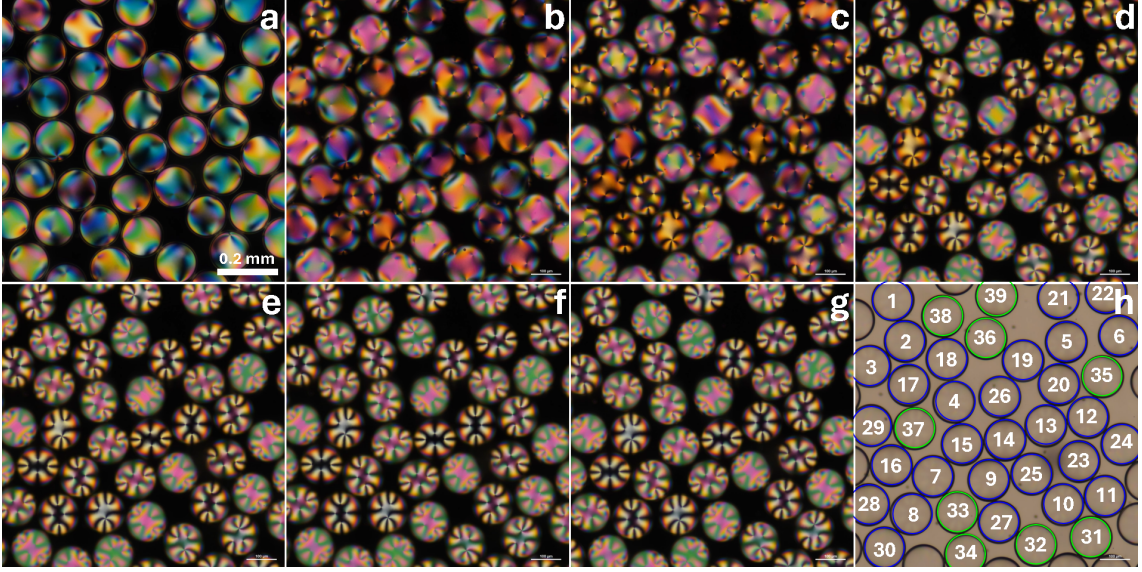


Figure 5.2: **Annealing of shells.** POM images (a–g) and bright-field image (h) of 5CB shells in 0.5 wt. % PVA ( $13\text{--}23 \text{ kg mol}^{-1}$ , 87–89% hydrolyzed) at approximately 1 (a), 9 (b), 15 (c), 25 (d), 35 (e), 50 (f), and 70 min (g, h) after production. In (h), blue-labeled shells (1–30) contain two  $+\frac{1}{2}$ – $+\frac{1}{2}$  defect pairs, whereas green-labeled shells (31–39) contain one  $+1$  and two  $+\frac{1}{2}$  defects; these two populations were used for tracking defect separations over time. Scale bar in (a), same for all panels: 0.2 mm.

between defects is

$$\theta = 2 \arcsin\left(\frac{c}{2R}\right), \quad (5.1)$$

so that the arc distance along the great circle is

$$s = R\theta = 2R \arcsin\left(\frac{c}{2R}\right) = D_{\text{outer}} \arcsin\left(\frac{c}{D_{\text{outer}}}\right). \quad (5.2)$$

For the shells in Fig. 5.2,  $D_{\text{outer}} \approx 142 \mu\text{m}$ , so

$$s = 142 \mu\text{m} \arcsin\left(\frac{c}{142 \mu\text{m}}\right). \quad (5.3)$$

We denote the time-dependent arc separation between defects  $i$  and  $j$  by  $s_{ij}(t)$ ; in practice,  $s_{ij}(t)$  is given by the arc length  $s$  computed above at each time point. For brevity, we write  $s(t)$  when a single defect pair is under consideration, or when an effective pair is defined (for example, the separation between a  $+1$  defect and the center of mass of a  $+\frac{1}{2}$  defect pair). In the shells considered here, the defects of

interest remain on the visible hemisphere and close to a great circle in the imaging plane, so this great-circle approximation introduces an uncertainty smaller than the tracking error and well below the optical resolution.

Because the defects are closely spaced and partially overlapping in the first frames after shell formation, their positions cannot be reliably determined at very short times. To recover the early-time behavior, we therefore fitted the experimentally accessible part of each trajectory  $s_{ij}(t)$  with an exponential-with-offset function and extrapolated the fit back to  $t = 0$ . The maximum possible initial separation between two defects on the shell surface is the half-circumference, that is,

$$s_{\max}(0) = \frac{\pi D_{\text{outer}}}{2} \approx \frac{\pi \times 142 \text{ } \mu\text{m}}{2} \approx 223 \text{ } \mu\text{m}, \quad (5.4)$$

which provides an upper bound for physically realistic extrapolations. In practice, the extrapolated initial values stayed well below this limit, typically around 200  $\mu\text{m}$ , confirming the consistency of the fit.

As an illustration, Figure 5.3 shows the relaxation of the pairwise separations for a population of 30 shells that each host two pairs of  $+\frac{1}{2}$  defects (blue-labeled shells 1–30 in Fig. 5.2h). Following the analysis of tangential shells in Ref. [184] and Appendix A of Ref. [185], we distinguish a bend pair, in which the director field between the two  $+\frac{1}{2}$  defects is dominated by bend, and a splay pair, where splay dominates. In the POM projection the bend pair appears more compact and settles closer to the thinnest point of the shell, whereas the splay pair spans a larger arc at late times. For brevity, we refer to these as the “closer” (bend) and “distant” (splay) pairs, respectively, matching the blue and red curves in Fig. 5.3. The slight late-time oval distortion of the tangential texture (inset in Fig. 5.3) is an optical illusion arising from different effective birefringence in bend- and splay-dominated regions on the curved shell, as discussed in Appendix A of Ref. [185].

An analogous analysis was carried out for shells with a different director topology.

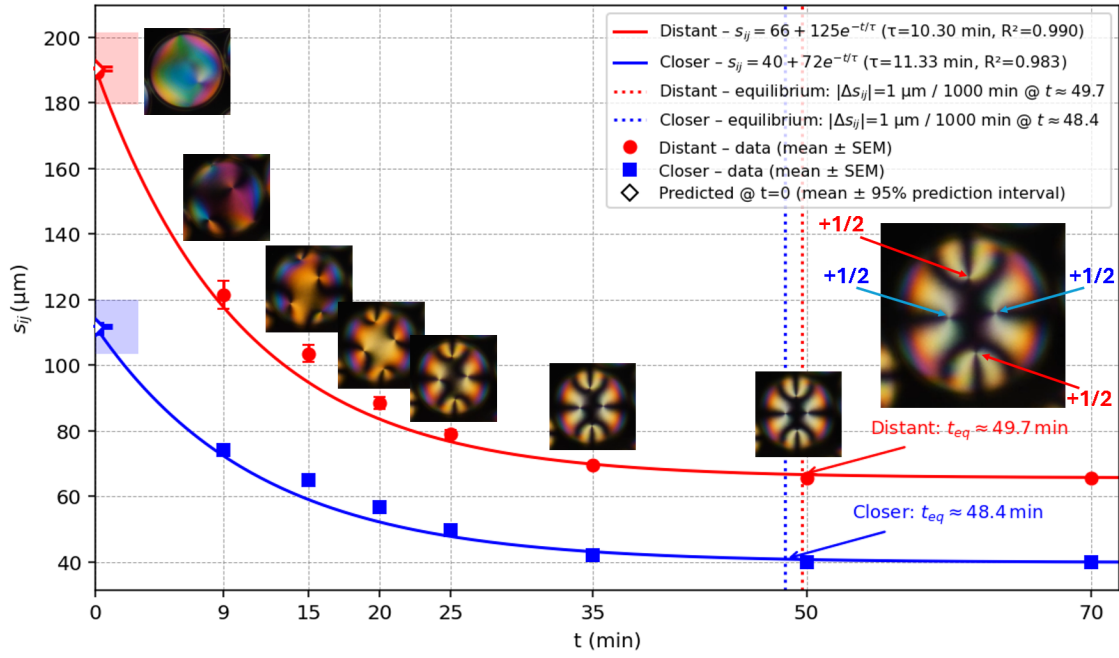


Figure 5.3: **Relaxation of the pairwise separation  $s_{ij}$  between  $+\frac{1}{2}$  defects in 5CB shells.** Blue symbols (“closer”): separation of the bend-dominated  $+\frac{1}{2}-+\frac{1}{2}$  pair; red symbols (“distant”): separation of the splay-dominated  $+\frac{1}{2}-+\frac{1}{2}$  pair. Points are means  $\pm$  SD across 30 shells; insets show POM frames from a representative shell. Solid curves are exponential-with-offset fits  $s_{ij}(t) = C + Ae^{-t/\tau}$ . Vertical dotted lines mark the annealing time  $t_{eq}$  for each pair (defined in Sec. 5.2.1); here  $t_{eq} \approx 48$  and 50 min for the bend and splay pairs, respectively.

Figure 5.4 shows the corresponding relaxation curves for a population of 9 shells that host one  $+1$  defect and one pair of  $+\frac{1}{2}$  defects (green-labeled shells 31–39 in Fig. 5.2h). These shells were produced in the same batch and imaged in the same capillary as the four- $+\frac{1}{2}$  shells in Fig. 5.3, so the two data sets differ only by their defect configuration.

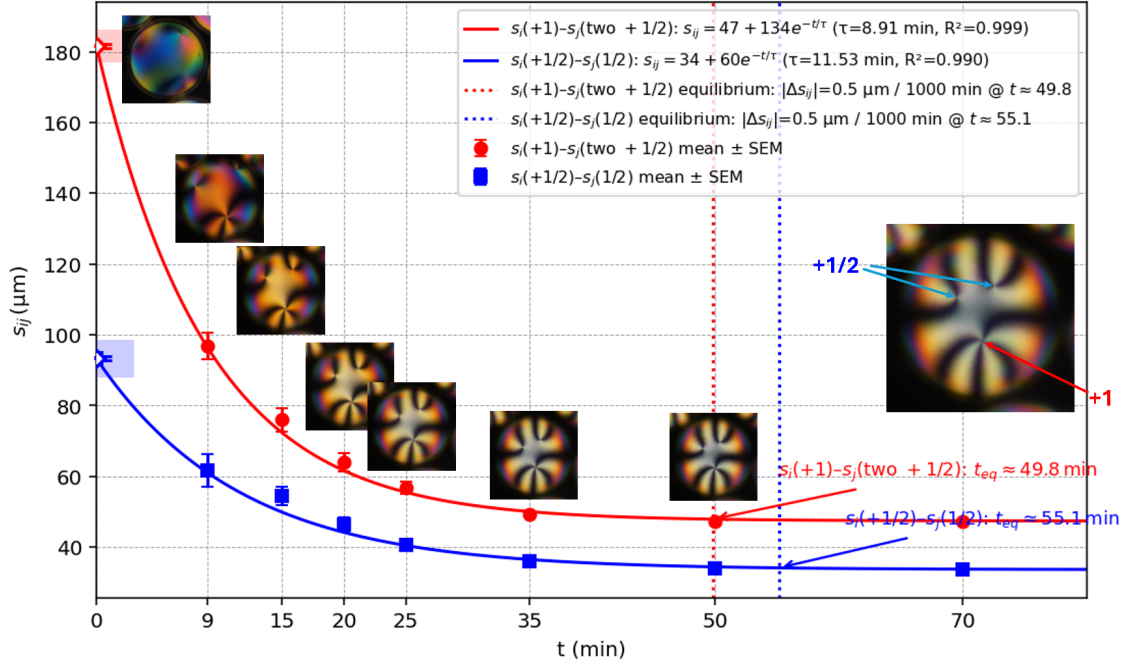


Figure 5.4: **Relaxation of pairwise separations  $s_{ij}$  between a  $+\frac{1}{2}$  defect pair and a  $+1$  defect in 5CB shells.** Blue symbols: separation between the two  $+\frac{1}{2}$  defects; red symbols: separation between the  $+1$  defect and the center of mass of the  $+\frac{1}{2}$  pair. Points are means  $\pm$  SD over 9 shells; insets show POM frames from a representative shell. Solid curves are exponential-with-offset fits  $s_{ij}(t) = C + Ae^{-t/\tau}$ . Vertical dotted lines mark the annealing time  $t_{\text{eq}}$ , defined in Sec. 5.2.1:  $t_{\text{eq}} \approx 50$  min for the  $(+1, +\frac{1}{2}$ -pair) separation and  $t_{\text{eq}} \approx 55$  min for the  $+\frac{1}{2}-+\frac{1}{2}$  separation.

In all these cases, the mean separation  $s_{ij}(t)$  decays monotonically from its initial value to a finite plateau  $C$ . The late-time plateau reflects a balance between the elastic line-tension reduction achieved by confining defects within the thin polar cap and the repulsive elastic interactions between like-signed defects on a curved surface. The exponential-with-offset form

$$s_{ij}(t) = C + Ae^{-t/\tau} \quad (5.5)$$

captures this behavior well, with a single relaxation time  $\tau$  for each defect pair type. The relaxation times  $\tau$  extracted from the fits vary systematically with the mean shell thickness, indicating that shell geometry is the primary control parameter at fixed inner and outer PVA concentration.

### 5.2.2 Annealing time versus wall thickness

To quantify how the overall annealing time depends on shell thickness, we use the characteristic relaxation time  $\tau$  extracted from the exponential-with-offset fits of defect separations. As discussed above, for a given shell geometry the operational annealing time  $t_{\text{eq}}$  is a monotonic function of  $\tau$ , so  $\tau(h_{\text{eq}})$  can be used as a proxy for the thickness dependence of  $t_{\text{eq}}$ . We compiled  $\tau$  values for shells with different equatorial thicknesses  $h_{\text{eq}}$ , all stabilized in 0.5 wt. % PVA (87–89 % hydrolyzed). As a first step, we pooled data from all defect topologies at a given  $h_{\text{eq}}$  to obtain an overall dependence of  $\tau$  on shell thickness. This averaging is not exact because different defect topologies exhibit slightly different relaxation times, but it provides a first useful overall trend. The relaxation times are summarized in Fig. 5.5, which plots  $\tau$  as a function of the normalized equatorial thickness  $h_{\text{eq}}/D_{\text{outer}}$ .

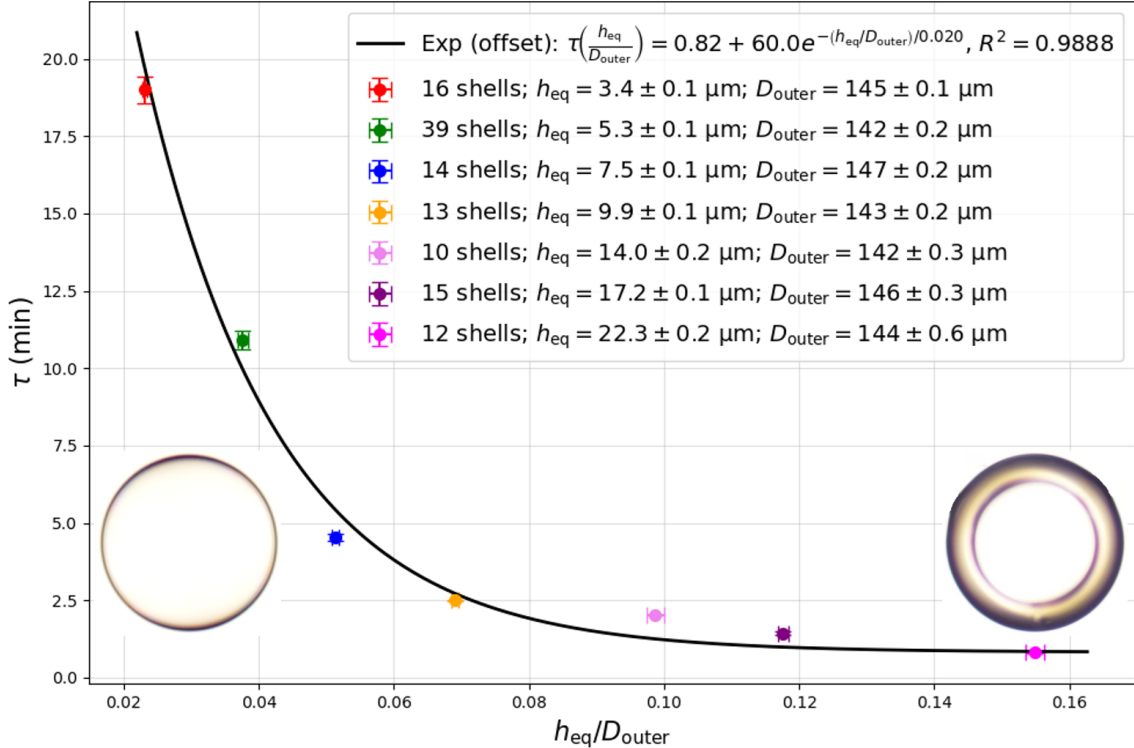


Figure 5.5: Relaxation time  $\tau$  vs. normalized wall thickness  $h_{\text{eq}}/D_{\text{outer}}$  for 5CB shells stabilized in 0.5 wt. % PVA (all defect topologies). Points: means over 10–39 shells, error bars:  $\pm 1$  SEM. Solid curve: exponential-with-offset fit  $\tau(h_{\text{eq}}/D_{\text{outer}}) = \tau_0 + A \exp[-(h_{\text{eq}}/D_{\text{outer}})/\tau_h]$  with  $\tau_0 \approx 0.82$  min.

Within the explored range, thicker shells ( $h_{\text{eq}}/D_{\text{outer}}$  larger) anneal faster than thinner ones, i.e., the relaxation time  $\tau$  decreases with increasing  $h_{\text{eq}}$ . Although one might expect thicker shells to anneal more slowly because of the larger LC volume, in our geometry the dominant effect is the strengthening of the wall-thickness gradient, which increases the elastic driving force and outweighs the modest increase in viscous dissipation. An exponential-with-offset dependence describes the data well and is consistent with the picture that buoyancy-enhanced thickness asymmetry provides a stronger elastic driving force for defect migration in thicker shells, while the relevant viscous drag is set by the local nematic flow and interfacial friction. In geometric terms, larger  $h_{\text{eq}}$  generally coincides with a steeper relative wall-thickness gradient between the thin and thick poles, which increases the elastic driving force for defects to coalesce into the thin upper cap and thereby accelerates their approach.

## 5.3 Discussion: annealing kinetics and scaling

### 5.3.1 Exponential-with-offset relaxation of defect separations

At the length and time scales of these experiments, defect motion in nematic shells is effectively overdamped: inertia is negligible and the dynamics can be viewed as gradient descent in the free-energy landscape under viscous drag [4, 31]. For notational simplicity, we denote the defect separation generically by  $d(t)$ ; in the experimental plots the same quantity is labelled  $s_{ij}(t)$ . The underlying elastic energy that penalizes distortions of the director field is described by the Oseen–Frank free energy introduced in Sec. 2.4. Near the final configuration, the distance between a chosen pair of defects,  $d$ , experiences an approximately harmonic restoring force toward a nonzero equilibrium separation  $d_{\infty}$  set by geometry, shell thickness, and interactions with the other defects.

Writing the overdamped equation of motion as

$$\dot{d} = -\mu \frac{\partial F(d)}{\partial d}, \quad (5.6)$$

with mobility  $\mu$  and an elastic free energy  $F(d)$  (part of the total free energy in Eq. (2.3)), and expanding

$$F(d) \approx F_0 + \frac{k_{\text{eff}}}{2} (d - d_\infty)^2, \quad (5.7)$$

gives the linear relaxation

$$\dot{d} \approx -\mu k_{\text{eff}} (d - d_\infty), \quad (5.8)$$

whose solution is the exponential-with-offset form

$$d(t) = d_\infty + [d(0) - d_\infty] e^{-t/\tau}, \quad \tau = \frac{1}{\mu k_{\text{eff}}}. \quad (5.9)$$

Identifying  $C = d_\infty$ ,  $A = d(0) - d_\infty$ , and  $b = -1/\tau$ , we recover the fitting function  $d(t) = C + Ae^{bt}$  used in Figures 5.3 and 5.4. The finite offset  $C$  is thus a direct measure of the equilibrium defect spacing, while  $\tau$  encodes the effective ratio of viscous drag to elastic stiffness.

Different offsets for different defect pairs or topologies arise naturally from this picture and from the elastic anisotropy of nematic 5CB, in which the bend elastic constant  $K_{33}$  exceeds the splay constant  $K_{11}$  [4, 184]:

- Two  $+\frac{1}{2}$  defects forming the bend pair are surrounded predominantly by bend distortions, which carry a higher elastic energy density because  $K_{33} > K_{11}$ . It is therefore energetically favorable to place this high-energy region as close as possible to the thinnest point of the shell, where the disclination line length is minimized, leading to a smaller equilibrium separation  $d_\infty$  for the bend pair.
- Two  $+\frac{1}{2}$  defects forming the splay pair are surrounded mainly by splay distortions, which carry a lower elastic energy density because  $K_{11} < K_{33}$ . It is therefore energetically favorable to place this low-energy region as far as possible from the thinnest point of the shell, where the disclination line length is maximized, leading to a larger equilibrium separation  $d_\infty$  for the splay pair.

tions, which have lower elastic energy density. For these defects, increasing their separation can more efficiently reduce in-plane distortions, and the cost of slightly longer disclination lines is comparatively modest. As a result, the splay pair settles at a larger equilibrium separation  $d_\infty$ , consistent with the distribution of splay- and bend-dominated regions in tangential shells reported in Ref. [184] and visualized in Appendix A of Ref. [185].

- A  $+1$  defect interacting with a  $+\frac{1}{2}$  pair has a different elastic multipole structure than a single  $+\frac{1}{2}$  defect; the resulting balance between confinement in the thin cap and repulsive interactions yields yet another  $d_\infty$ , as seen in Fig. 5.4.

Shell-to-shell variations in  $h_{\text{eq}}$ , buoyancy offset  $\delta$ , and anchoring strength at the LC–water interfaces (Sec. 2.5, Sec. 3.2) produce modest changes in both  $k_{\text{eff}}$  and  $\mu$ , which account for the spread in fitted  $\tau$  values across nominally similar shells.

### 5.3.2 Scaling argument for the characteristic annealing time

A simple scaling argument illustrates how the competition between elastic driving and viscous drag sets a characteristic time scale for annealing in nematic shells. Consider a disclination line of length  $L$  connecting surface defects within the shell. To leading order, its elastic free energy is proportional to length,

$$F_{\text{el}} \simeq KL, \quad (5.10)$$

where  $K$  is a representative Frank constant (in our shells dominated by the splay and bend moduli,  $K_{11}$  and  $K_{33}$ ; Sec. 2.4) [15, 18]. This linear dependence reflects a constant line tension per unit length of disclination [4].

Shortening the line by  $dL$  reduces the energy by

$$dF_{\text{el}} = K dL, \quad (5.11)$$

so that the axial elastic driving force is

$$f_{\text{drive}} = -\frac{\partial F_{\text{el}}}{\partial L} = -K. \quad (5.12)$$

Retraction of the line at speed  $\dot{L} = dL/dt$  requires dissipation in the nematic. In bulk nematics, motion of a line defect is usually modeled by assigning a drag per unit length  $\zeta_\ell$  of order an effective (rotational) viscosity [4], so that the total drag coefficient scales as

$$\zeta \sim \zeta_\ell L \sim \eta_{\text{eff}} L, \quad (5.13)$$

where  $\eta_{\text{eff}}$  is an effective viscosity that combines rotational dissipation and the hydrodynamic backflow induced by director reorientation. In a spherical shell with a wall-thickness gradient the detailed flow field is more complex, because the LC is confined between two interfaces and the local thickness varies along the line. For the present scaling argument, we absorb this complexity into  $\eta_{\text{eff}}$ , understood as a thickness- and geometry-averaged quantity at the scale of the moving disclination.

The viscous drag force is then

$$f_{\text{drag}} = \zeta \dot{L} \simeq (\eta_{\text{eff}} L) \dot{L}. \quad (5.14)$$

Balancing driving and drag,

$$f_{\text{drive}} + f_{\text{drag}} = 0, \quad (5.15)$$

gives the equation of motion

$$\eta_{\text{eff}} L \dot{L} = -K \quad \implies \quad \dot{L} = -\frac{K}{\eta_{\text{eff}}} \frac{1}{L}. \quad (5.16)$$

Integrating from an initial length  $L_0$  down to a final length  $L_\infty$  yields a characteristic relaxation time

$$\tau_c \sim \frac{\eta_{\text{eff}}}{2K} (L_0^2 - L_\infty^2). \quad (5.17)$$

In a simplified picture where  $L_0$  scales with the shell size and wall thickness, this expression highlights that annealing is governed by the ratio  $\eta_{\text{eff}}/K$  and by the square of a geometric length scale. The scaling time  $\tau_c$  is therefore expected to be of the same order as the relaxation time  $\tau$  extracted from the exponential fits for  $d(t)$ .

In our 5CB shells, the buoyant rise of the inner aqueous droplet breaks the up–down symmetry and thins the LC layer at the top of the shell, while the denser 5CB drains downward under gravity, inducing a shear flow in the confined LC layer (Fig. 5.1). Defect pairs migrate into the thin cap of the upper hemisphere, where the line length is minimized and the local driving is strongest. Because bend distortions are penalized more strongly than splay distortions ( $K_{33} > K_{11}$ ), bend-dominated defects may experience a larger effective driving force along the thickness gradient and thus approach the thinnest point faster than splay-dominated defects. In this dynamic picture the bend pair arrives first and occupies the energetically most favorable region, while the later-arriving splay pair is pushed to a somewhat larger separation. Our data are consistent with both this kinetic interpretation and the static energy-density argument above, and the actual evolution in the shells likely reflects a combination of the two mechanisms.

In practice, both  $K$  and  $\eta_{\text{eff}}$  depend on local confinement, temperature, and PVA coverage, while  $L_0$  and  $L_\infty$  depend on the wall-thickness gradient and on the arrangement of defects in the thin cap. The exponential-with-offset behavior observed for  $d(t)$  thus reflects the local harmonic response near the energy minimum, whereas the strong thickness dependence of the relaxation time  $\tau$  (and hence of  $t_{\text{eq}}$ ; Fig. 5.5) encodes how the effective driving and drag vary with  $h_{\text{eq}}$ .

### 5.3.3 Unified relations between different defect–pair separations

Because all defect pairs in a given shell relax under the same underlying flow and elastic fields, their separations can be related by eliminating time from their respective

exponential-with-offset fits. Let  $d_B(t)$  and  $d_S(t)$  denote the separations of two  $+\frac{1}{2}$  defects in the bend- and splay-dominated pairs in the director field of the same shell (for example, the two  $+\frac{1}{2}-+\frac{1}{2}$  pairs in Fig. 5.3), each described by

$$d_B(t) = C_B + A_B e^{b_B t}, \quad d_S(t) = C_S + A_S e^{b_S t}, \quad (5.18)$$

with  $b_B < 0$  and  $b_S < 0$ . Eliminating  $t$  gives a direct mapping

$$d_B(d_S) = C_B + A_B \left( \frac{d_S - C_S}{A_S} \right)^\nu, \quad \nu = \frac{b_B}{b_S}. \quad (5.19)$$

Writing  $\mathcal{K} = A_B A_S^{-\nu}$ , this can be expressed compactly as

$$\hat{d}_B(d_S) = C_B + \mathcal{K} (d_S - C_S)^\nu, \quad (5.20)$$

valid for  $d_S \geq C_S$ , with  $\hat{d}_B \rightarrow C_B$  as  $d_S \rightarrow C_S^+$ . An analogous relation holds between the separation of a  $+1$  defect from a  $+\frac{1}{2}$  pair and the internal separation within the pair (Fig. 5.4). These mappings provide a convenient way to predict approximately one distance from another, which could be useful for automated analysis when, among four  $+\frac{1}{2}$  defects in a tangential shell, automated image processing reliably detects only one defect pair.

### 5.3.4 Summary and outlook for moderately hydrolyzed PVA

In this chapter, we have quantified the annealing kinetics of tangentially aligned 5CB shells stabilized by moderately hydrolyzed PVA and established an exponential-with-offset description of defect motion:

- Buoyancy-induced displacement of the inner aqueous core creates a thickness gradient that thins one hemisphere and thickens the opposite hemisphere [59]. This asymmetry tends to drive all surface defects toward the thin polar cap, where the total disclination length is reduced.

- Time-resolved POM imaging of shells stabilized in 0.5 wt. % PVA (87–89 % hydrolyzed) shows that defect separations  $d(t)$  relax monotonically from their initial values to finite plateaus  $C$ , corresponding to well-defined equilibrium configurations. For both four- $+\frac{1}{2}$  and mixed  $(+1, +\frac{1}{2})$  defect topologies, the trajectories are well described by exponential-with-offset fits  $d(t) = C + Ae^{-t/\tau}$ .
- The relaxation time  $\tau$  and the equilibrium separations  $C$  depend on the defect topology and on shell-to-shell variations in  $h_{\text{eq}}$ , thickness asymmetry, and anchoring, but are reproducible within each population. The different offsets for bend- and splay-dominated pairs, and for  $(+1, +\frac{1}{2})$  combinations, can be rationalized by the interplay between elastic anisotropy ( $K_{33} > K_{11}$ ), line-tension reduction, curvature, and defect–defect repulsion [54, 184].
- The characteristic relaxation time  $\tau$ , and thus the operational annealing time  $t_{\text{eq}}$  defined as the time at which  $d(t)$  reaches its plateau within a small tolerance, decreases with increasing equatorial thickness  $h_{\text{eq}}$ . An exponential-with-offset dependence

$$\tau(h_{\text{eq}}/D_{\text{outer}}) = \tau_0 + A \exp[-\alpha(h_{\text{eq}}/D_{\text{outer}})]$$

captures this trend and suggests that, although thicker shells contain more LC material, in our geometry the stronger buoyancy-induced thickness asymmetry and steeper relative wall-thickness gradients in thicker shells may enhance the elastic driving force and lead to faster relaxation toward the ground state.

- A simple scaling analysis based on the competition between elastic line tension and viscous drag rationalizes the existence of a characteristic annealing time and highlights the role of the ratio  $\eta_{\text{eff}}/K$  and of the relevant geometric length scales, even though the full thickness dependence reflects additional variations in local elasticity, viscosity, and interfacial conditions [4, 18].

From an application perspective, these results provide practical guidelines for

using LC shells as sensing elements. First, they help define the time window after shell production during which the director field is still evolving and polymerization would freeze a non-equilibrium state. Second, they show that shells of different thicknesses relax on systematically different time scales, which can be chosen to match the desired processing or sensing protocol. In the following sections, we extend this analysis to shells stabilized by highly hydrolyzed PVA and explore how changes in stabilizer chemistry further modify the annealing pathways and time scales.

## 5.4 Director fields in shells with highly hydrolyzed PVA

To extend the analysis beyond moderately hydrolyzed PVA, we next studied 5CB shells stabilized in aqueous solutions of highly hydrolyzed PVA ( $\geq 98\%$ ). Figure 5.6 shows representative textures for shells stabilized in 0.5 wt. % PVA ( $13\text{--}23\text{ kg mol}^{-1}$ ,

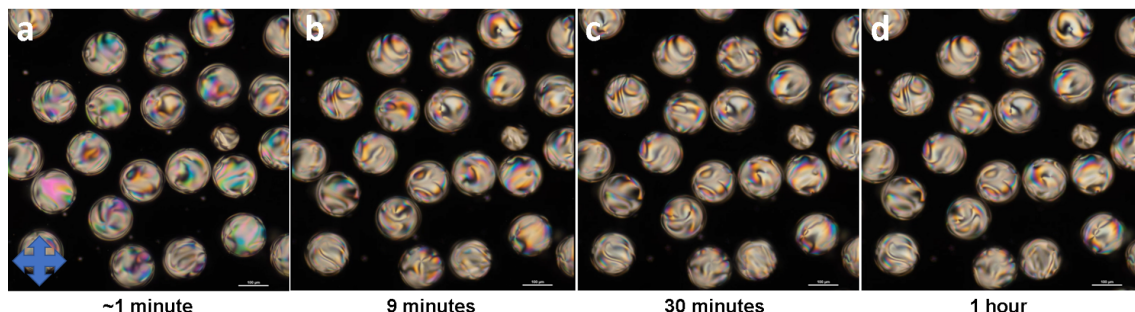


Figure 5.6: POM images of 5CB shells stabilized in 0.5 wt. % PVA ( $13\text{--}23\text{ kg mol}^{-1}$ , 98 % hydrolyzed) during the first hour after production. The director field shows an arrested non-equilibrium tangential texture with multiple defects that remain essentially frozen in place. Thin white scale bar in the lower right corner:  $100\text{ }\mu\text{m}$ .

98 % hydrolyzed). In sharp contrast to the well-defined equilibrium tangential configurations obtained with  $\sim 88\%$  hydrolyzed PVA (Fig. 5.2), shells in 98 % hydrolyzed PVA exhibit largely arrested tangential textures: the director field appears pinned, with an excess of defects scattered around each shell and only limited relaxation over time.

These observations suggest that highly hydrolyzed PVA forms a rigid interfacial layer that pins the director field. In the following, we first examine how PVA concentration modifies this arrested state, then compare the robustness of shells across nematic–isotropic cycles, and finally discuss mechanistic scenarios and implications for biosensing.

### 5.4.1 Effect of PVA concentration

We first asked how the concentration of 98 % hydrolyzed PVA affects the director field. Figure 5.7 compares freshly produced 5CB shells stabilized with different PVA concentrations. At all concentrations the textures are far from the simple four-defect

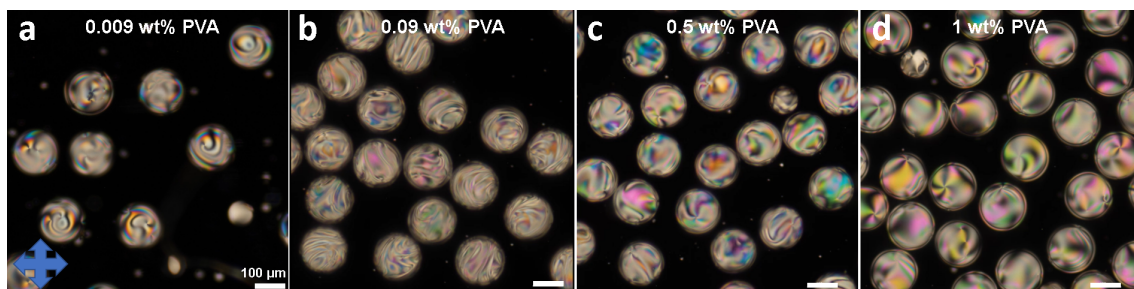


Figure 5.7: POM images of freshly produced 5CB shells stabilized with different concentrations of PVA ( $13\text{--}23\text{ kg mol}^{-1}$ , 98 % hydrolyzed). From left to right: 0.009, 0.09, 0.5, and 1 wt.%. White scale bar in the lower right corner:  $100\text{ }\mu\text{m}$ .

or eight-brush patterns obtained with  $\sim 88\%$  hydrolyzed PVA; instead, each shell shows many defects and a strongly distorted tangential field.

At concentrations (0.009, 0.09 wt.%), defects are distributed relatively evenly over the shell surface. At higher concentrations (0.5, 1, 5 wt.%), multiple defects still tend to localize near the thinner upper hemisphere, similar to shells in  $\sim 88\%$  hydrolyzed PVA, but the textures appear more densely patterned.

Before analyzing the time evolution, we verified that the 5CB phase in these shells remains liquid. Side-view POM images of the same shells in a rectangular capillary, recorded after a  $90^\circ$  rotation of the sample about the capillary axis (Fig. 5.8), show that the shells in this orientation settle downward under gravity and retain the same

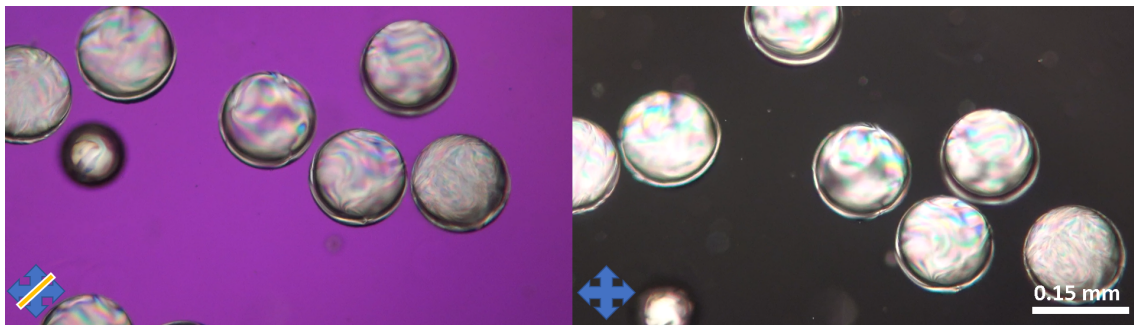


Figure 5.8: Side-view POM images of 5CB shells stabilized with 0.09 wt.% PVA ( $13\text{--}23\text{ kg mol}^{-1}$ , 98% hydrolyzed) in a capillary. In both cases the shells settle downward under gravity and retain a persistent wall-thickness asymmetry, confirming that the 5CB phase remains liquid. The left panel was recorded with a first-order  $\lambda$  plate inserted. White scale bar: 0.15 mm; same magnification in both panels.

wall-thickness asymmetry. As in shells stabilized with  $\sim 88\%$  hydrolyzed PVA, this confirms that the middle phase behaves as a gravity-settled liquid shell with an off-centered inner core rather than as a solidified capsule.

Figures 5.9–5.11 illustrate the time evolution for three representative concentrations. At 0.09 wt.% (Fig. 5.9), the initial texture is already similar to that observed after tens of hours; no substantial rearrangements occur after the first 30–60 min. At 1 wt.% (Fig. 5.10), shells are also largely arrested, with only minor local changes over 90 h. At 5 wt.% (Fig. 5.11), the tangential texture remains non-equilibrated but shows slightly more internal motion, consistent with a modest increase in director mobility at the highest PVA loading.

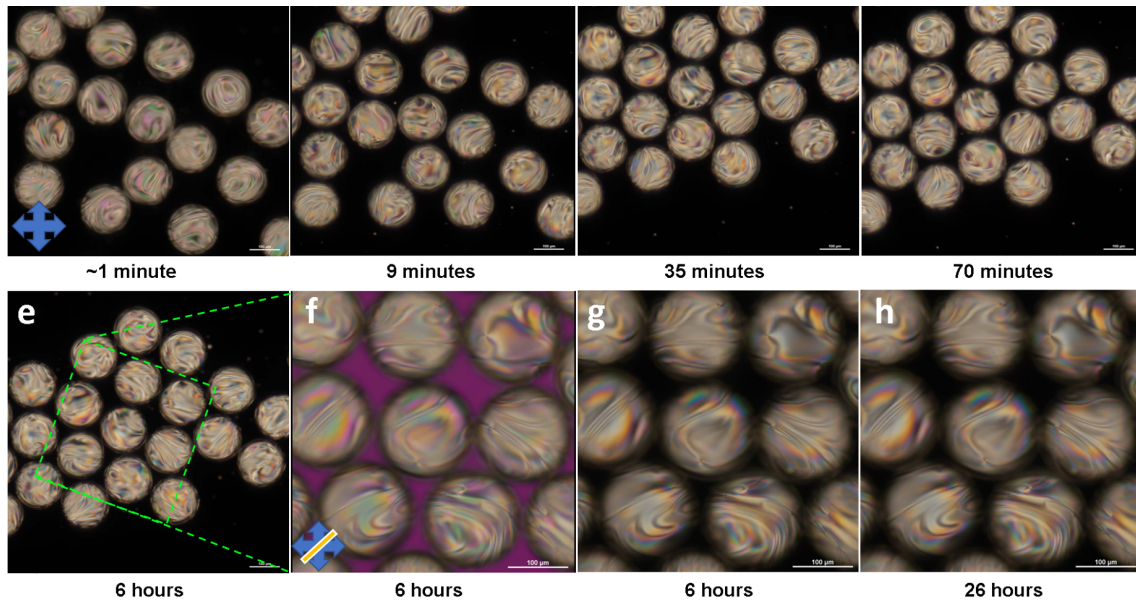


Figure 5.9: 5CB shells stabilized in 0.09 wt.% PVA ( $13\text{--}23\text{ kg mol}^{-1}$ , 98 % hydrolyzed), followed over 26 h after production. No appreciable changes in the director field are observed beyond the first  $\sim 30\text{--}60\text{ min}$ ; the initial texture is already close to the long-time state. Thin white scale bar in all panels:  $100\text{ }\mu\text{m}$ .

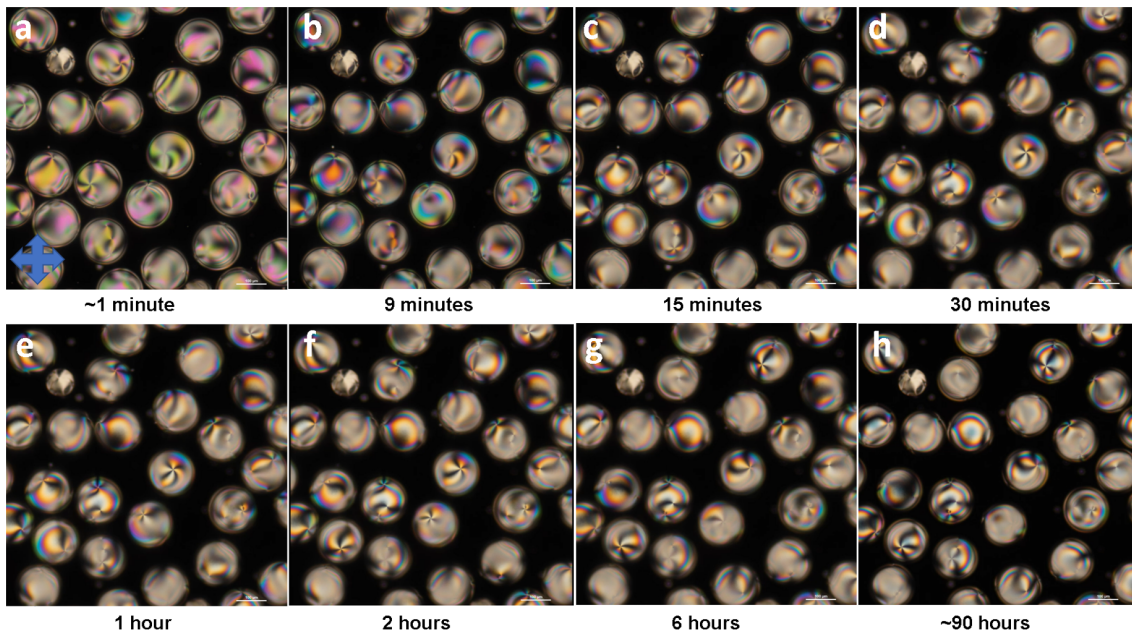


Figure 5.10: 5CB shells stabilized in 1 wt.% PVA ( $13\text{--}23\text{ kg mol}^{-1}$ , 98 % hydrolyzed), followed over 90 h after production. Beyond the first  $\sim 30\text{--}60\text{ min}$ , only very minor changes in the director field are observed, indicating a strongly arrested tangential texture. Thin white scale bar in all panels:  $100\text{ }\mu\text{m}$ .

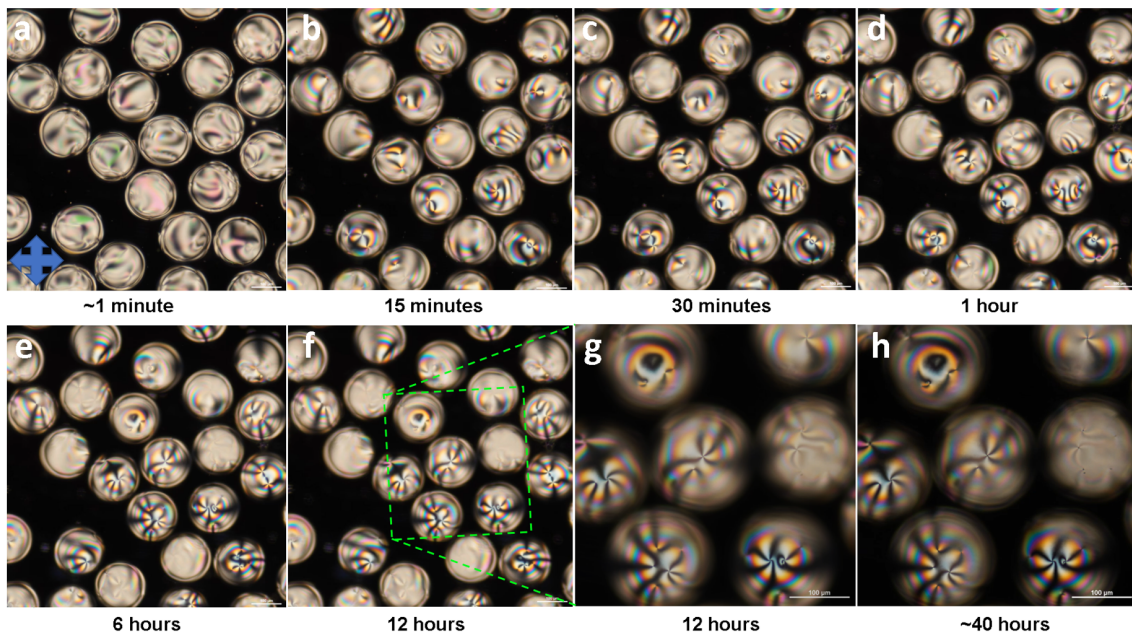


Figure 5.11: 5CB shells stabilized in 5 wt.% PVA ( $13\text{--}23\text{ kg mol}^{-1}$ , 98 % hydrolyzed) during the first 40 h after production. The tangential texture remains non-equilibrated but shows slightly more internal rearrangement than at lower PVA concentrations. Thin white scale bar in all panels:  $100\text{ }\mu\text{m}$

Overall, shells stabilized with lower concentrations (0.009–0.09 wt.%) of 98 % hydrolyzed PVA exhibit defects that are distributed more uniformly over the surface, whereas at higher concentrations (0.5–5 wt.%) many defects still preferentially accumulate in the thin upper hemisphere, as they do in  $\sim 88\%$  hydrolyzed PVA. In all cases, however, the total number of visible defects remains higher and their motion slower than in shells with partially hydrolyzed PVA, confirming that highly hydrolyzed PVA substantially suppresses annealing.

#### 5.4.2 Robustness of shells across nematic–isotropic cycles

For sensing applications, shells must often tolerate temperature changes without losing their structure. We therefore compared the stability of shells stabilized by aqueous solutions of  $\sim 88\%$  and 98 % hydrolyzed PVA under repeated nematic–isotropic cycling of 5CB. Samples were heated from RT to  $35\text{ }^{\circ}\text{C}$ , taken into the isotropic phase, and then cooled back to the nematic state; this cycle was repeated multiple

times. Figure 5.12 contrasts shells stabilized with 0.09 wt.% ( $0.05 \mu\text{mol/mL}$ ) PVA of 87–89% and 98% hydrolysis.

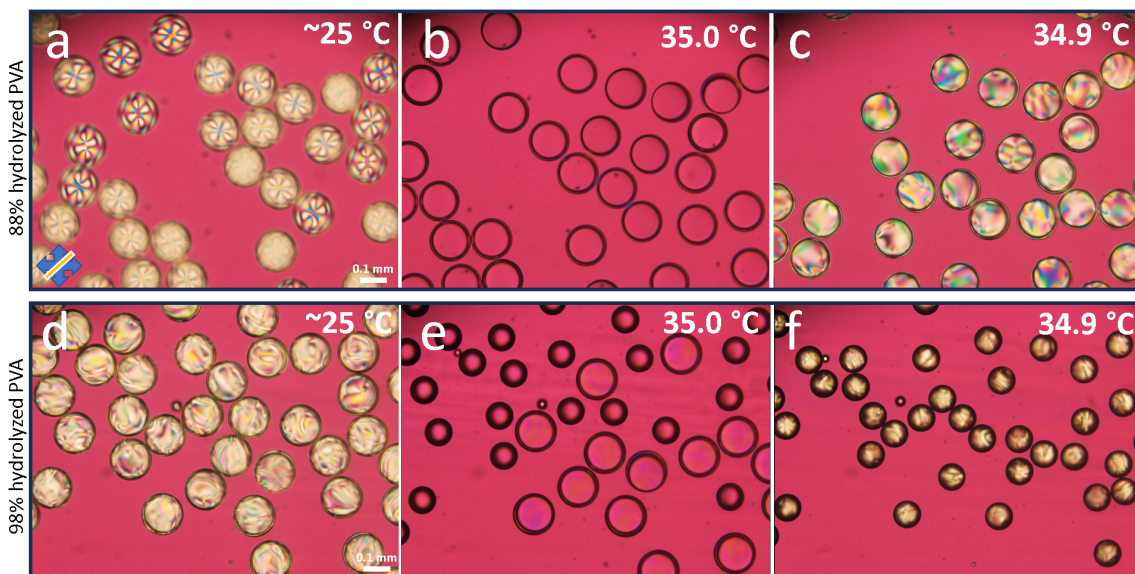


Figure 5.12: Thermal robustness of 5CB shells stabilized in PVA of different hydrolysis degrees. (a–c) 0.09 wt.% ( $0.05 \mu\text{mol mL}^{-1}$ ) PVA ( $13\text{--}23 \text{ kg mol}^{-1}$ , 87–89% hydrolyzed). (d–f) 0.09 wt.% ( $0.05 \mu\text{mol mL}^{-1}$ ) PVA ( $13\text{--}23 \text{ kg mol}^{-1}$ , 98% hydrolyzed). (b,e) After three nematic–isotropic–nematic cycles. (c,f) After  $\sim 12$  cycles. Partially hydrolyzed PVA preserves intact shells, whereas most shells in 98% hydrolyzed PVA collapse upon repeated cycling. Some shells in (c) moved out of the observation area during the experiment. White scale bar in (a,d): 0.1 mm; same magnification in all panels.

After only a few cycles, all shells in 98% hydrolyzed PVA collapse or transform into irregular droplets when 5CB enters the isotropic phase, whereas shells stabilized with  $\sim 88\%$  hydrolyzed PVA at the same molar concentration remain mechanically robust and survive repeated cycling. Notably, upon cooling back to the nematic phase, the shells that do remain intact in 98% hydrolyzed PVA recover essentially the same arrested tangential textures as before heating, indicating that the interfacial PVA structure is preserved while the shell as a whole is more fragile.

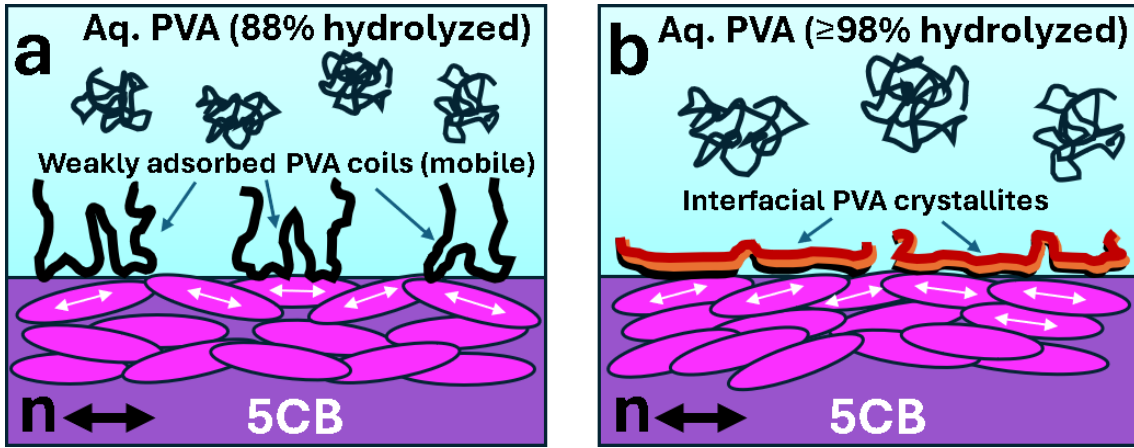


Figure 5.13: **Hypothesized limiting scenarios for PVA at the 5CB–water interface.** (a) Aqueous PVA ( $\sim 88\%$  hydrolyzed) adsorbs mainly as disordered coils (train–loop–tail), forming a mobile layer that supports degenerate planar anchoring with weak azimuthal constraints; short double-headed ticks depict random in-plane orientations of the nematic director  $\mathbf{n}$ . (b) Aqueous PVA ( $\geq 98\%$  hydrolyzed) forms a more cohesive H-bonded interfacial layer; interfacial PVA crystallites are hypothesized to strengthen planar anchoring and locally pin the azimuthal orientation of  $\mathbf{n}$ , yielding domain-like in-plane order. Schematics not to scale.

#### 5.4.3 Hydrolysis-dependent adsorption and PVA crystallization

The strong contrast between partially and nearly fully hydrolyzed PVA suggests that the degree of hydrolysis controls how PVA adsorbs and organizes at the 5CB–water interface. Figure 5.13 sketches two limiting scenarios.

- **Partially hydrolyzed PVA ( $\sim 88\%$ ).** PVA retains enough acetate groups to form small hydrophobic patches along an otherwise hydrated coil. At the water/5CB boundary, acetate-rich segments adsorb as surface-bound *trains*, whereas hydroxyl-rich segments protrude into the aqueous phase as flexible *loops* and free *tails*, giving the classic train–loop–tail structure of an adsorbed polymer layer [186]. The resulting amorphous interfacial layer imposes tangential (degenerate planar) anchoring with weak azimuthal constraints. Under these conditions, 5CB shells readily anneal into equilibrium tangential textures with a net topological charge  $+2$  collected at the thinnest pole.

- **Nearly fully hydrolyzed PVA ( $\geq 98\%$ ).** Here, PVA lacks sufficient acetate interruptions; the chains are almost entirely composed of hydroxyl-bearing segments, which can form dense inter- and intra-chain hydrogen-bond networks, consistent with the higher crystallinity and reduced free volume of highly hydrolyzed PVA films [187]. Under interfacial shear, extended backbone segments may align as surface trains and hydrogen-bond laterally, nucleating interfacial PVA crystallites [188, 189]. These crystalline patches are hypothesized to form a more cohesive, solid-like layer that strengthens planar anchoring and locally pins the azimuthal orientation of  $\mathbf{n}$ , yielding a mosaic of in-plane domains and an excess of defects scattered around the shells.

#### 5.4.4 Mechanistic hypotheses

Building on these scenarios, we summarize our working hypotheses for highly hydrolyzed PVA as follows.

##### **Hypothesis I: shear-driven interfacial crystallization and LC anchoring**

1. *Chain alignment.* During microfluidic shell production, strong shear and curvature at the water/5CB interface stretch PVA chains, increasing the number and length of surface trains.
2. *Crystallization.* For  $\geq 98\%$  hydrolyzed PVA, these trains hydrogen-bond laterally and nucleate nanocrystalline domains at the interface, whereas  $\sim 88\%$  hydrolyzed PVA remains predominantly amorphous under the same conditions [188].
3. *Director pinning.* The crystalline patches impose strong planar anchoring and locally fix the azimuth of neighboring 5CB molecules through hydrogen bonding and polar interactions, freezing the LC into a non-equilibrium, defect-rich tangential texture that cannot easily anneal.

**Hypothesis II: templating by nematic order**

- Nematic 5CB presents long-range orientational order at the interface; its aligned aromatic cores may template the orientation of adsorbed PVA chains and promote more ordered, crystalline trains in the highly hydrolyzed case.
- In an isotropic oil (for example, hexadecane), the same shear history might not produce such ordered interfacial PVA structures, or at least they would not be directly visible by POM because the bulk oil is optically isotropic.

**5.4.5 Liquid-crystal shells as optical reporters**

Because 5CB is birefringent, an immobilized LC director provides a sensitive optical readout of interfacial ordering. In our shells, the arrested, domain-like tangential textures thus act as an “optical map” of where rigid PVA domains or other interfacial structures have formed. This illustrates how LC shells can serve as optical reporters of subtle interfacial polymer ordering events in real time.

**5.5 Implications for LC shell biosensing**

The observations above have several implications for using PVA-stabilized LC shells as biosensing platforms.

- Highly hydrolyzed PVA ( $\geq 98\%$ ) can adsorb in a solid-like, partially crystalline state at the water/LC interface under shear, strongly pinning the director field and arresting tangential textures.
- The resulting non-equilibrium, defect-rich textures provide clear, easily observable optical signatures of interfacial polymer crystallization and ordering.
- By extension, LC shells could be engineered as reporters for other binding or ordering events that stiffen or crystallize interfacial polymer or biomolecular

layers, with the LC texture serving as a sensitive optical signal.

### 5.5.1 Hypothesis: shell vulnerability in the isotropic state

Upon heating 5CB from nematic to isotropic, the mechanical compatibility between the adsorbed PVA layer and the bulk phase determines shell stability.

- **Highly hydrolyzed PVA ( $\geq 98\%$ ).** Crystallized interfacial nanodomains rigidly pin the director in the nematic state. When 5CB becomes isotropic, these stiff patches may become mechanically mismatched with the surrounding isotropic, orientation-free bulk, generating local stress concentrations at the interfaces. Repeated nematic–isotropic transitions can then promote interfacial fracture, thinning, or rupture, ultimately causing shell collapse.
- **Partially hydrolyzed PVA ( $\sim 88\%$ ).** A soft, amorphous train–loop–tail layer coats the LC interface. Even in the isotropic state, this layer deforms smoothly with the bulk and redistributes stress without sharp gradients, preserving shell integrity at equivalent PVA concentrations.

### 5.5.2 Summary and outlook for highly hydrolyzed PVA

In summary, shells stabilized by nearly fully hydrolyzed PVA behave very differently from those stabilized by partially hydrolyzed PVA.

- Nearly fully hydrolyzed PVA (98%) yields arrested, defect-rich tangential textures with very limited annealing, consistent with a more rigid, possibly partially crystalline interfacial layer that pins the director. Increasing its concentration only slightly enhances background director mobility and does not restore equilibration, and shells in 98% PVA are more prone to collapse under repeated nematic–isotropic cycling than shells in  $\sim 88\%$  hydrolyzed PVA, suggesting that such rigid interfacial domains may be mechanically incompatible with the isotropic bulk.

- A hydrolysis-dependent scenario, in which  $\sim 88\%$  hydrolyzed PVA may be more likely to form a soft amorphous interfacial layer, whereas 98 % hydrolyzed PVA may be more prone to forming shear-induced crystalline domains, provides a coherent qualitative explanation for these behaviors and highlights how LC shells can act as optical reporters of interfacial polymer ordering.

These findings underline that, for biosensing applications, the choice and hydrolysis degree of PVA are not merely technical details: they strongly influence whether shells can anneal to well-defined equilibrium textures or instead display robust, arrested patterns that report interfacial crystallization.

## 5.6 Overall conclusions for PVA-stabilized LC shells

In shells stabilized by moderately hydrolyzed PVA ( $\sim 88\%$ ), the director field reliably anneals into well-defined tangential equilibrium textures on a characteristic time scale  $t_{\text{eq}}(h_{\text{eq}})$ , providing a reproducible baseline for subsequent sensing experiments.

In contrast, shells stabilized by nearly fully hydrolyzed PVA ( $\geq 98\%$ ) exhibit arrested, defect-rich tangential patterns and are more prone to collapse under repeated nematic–isotropic cycling, consistent with a rigid interfacial layer that both pins the director and reduces mechanical robustness.

For sensing applications, however, equilibrated shells must remain intact even when polymer-stabilizer coverage is reduced to the minimum level required for mechanical stability, minimizing perturbation of the sensing interface. The next chapter shifts from director-field annealing to shell lifetimes, examining how low PVA concentrations govern rupture pathways.

## Chapter 6

# Lifetimes of nematic shells stabilized by low concentrations of PVA

This chapter examines the lifetimes of LC shells stabilized with PVA. We investigate how efficiently different low concentrations of aqueous PVA solutions stabilize 5CB shells. The lifetime of liquid-crystal shells is a critical parameter, because any practical biosensor must be robust and convenient to use.

In what follows, we adopt a simple working terminology for the low-molar-mass PVA grade used most extensively in this chapter ( $M_w = 13\text{--}23 \text{ kg mol}^{-1}$ ). Within the concentration window explored here, we refer to PVA concentrations in the range 0.01–0.05 wt.% as *low PVA concentrations*, and to concentrations at or below 0.001 wt.% as *ultra-low PVA concentrations*. Concentrations in the intermediate range 0.001–0.01 wt.% are treated as a transition regime between these two limits. This working classification is used purely as a convenient shorthand for the concentrations studied in this chapter and is not intended as a general definition of low or ultra-low PVA concentrations.

## 6.1 Initial analysis of nematic-shell lifetimes

In our first series of microfluidic production experiments on nematic shells, we identified 0.01 wt.% PVA ( $M_w = 13\text{--}23 \text{ kg mol}^{-1}$ , 87–89 % hydrolyzed; all experiments in this chapter use this degree of hydrolysis) as the lowest concentration that could still yield relatively stable shells with a collection efficiency in the 60–80 % range. Shells produced under these conditions could survive for up to 2–3 weeks at RT. This behavior is consistent with the picture developed in Secs. 3.2 and 3.2.2: interfacial-tension measurements on PVA–oil–water systems suggest that PVA concentrations in the range 0.01–0.05 wt.% correspond to relatively low interfacial coverage compared with the  $\sim 1$  wt.% PVA levels often used for robust stabilization in related systems. Even at these low concentrations, our observations are consistent with the adsorbed PVA being sufficient to maintain tangential anchoring and to provide an effective steric barrier against coalescence and premature shell rupture on experimentally relevant time scales. We also performed some preliminary analogous tests for shells stabilized by higher-molar-mass PVA solutions within this concentration range, but these data were not analyzed in comparable depth, both because such formulations were used less frequently in this work and because lifetime experiments, together with their subsequent analysis, are intrinsically time-consuming.

To quantify the effect of low PVA weight fraction on shell lifetime, we first prepared 5CB shells using low-molar-mass PVA at 0.01, 0.025, and 0.05 wt.% (corresponding to 0.006, 0.014, and 0.028  $\mu\text{mol mL}^{-1}$ , respectively), and matching molar concentrations for higher-molar-mass grades. For each experiment, shells with diameters of  $\approx 150 \mu\text{m}$  were collected in six rectangular glass capillaries with an inner cross section of  $0.20 \times 2.00 \text{ mm}^2$  and a length of 30–33 mm, typically containing  $\sim 800\text{--}1100$  shells per capillary. All capillaries were sealed with epoxy and stored horizontally at RT in an incubator between microscopy observations.

Although this method allowed systematic sampling, lifetime measurements still

showed substantial variability between capillaries, which we attribute to possible small differences in epoxy sealing and filling, as well as occasional small trapped air pockets or headspace near the sealed capillary openings that can perturb local pressure and flow and, in some cases, promote slow evaporation [190,191]. Similar bubble- and evaporation-related effects in long-term droplet storage and incubation in capillaries and microfluidic channels have been reported in droplet-based microfluidic studies [192,193]. We therefore interpret the variability between capillaries as reflecting not only stochastic shell rupture events, including occasional chain-popping cascades in which the collapse of one shell may in turn destabilize its neighbors, but also uncontrolled differences in their microenvironments. The error bars in Fig. 6.1 report the standard error of the mean (SEM) over six capillaries per time point, quantifying the uncertainty in the average survival fraction; these SEM values remain relatively large even though all capillaries were collected from the same production batch. Figure 6.1 summarizes the resulting dependence of 5CB-shell lifetime on PVA concentration for the 13–23 kg mol<sup>−1</sup> grade.

### Calculation of the standard error of the mean

For each time point  $t$ , we report the mean shell survival percentage  $\bar{x}$  and the standard error of the mean,  $\text{SEM} = \sigma/\sqrt{N}$  with  $\sigma = \sqrt{\frac{1}{N-1} \sum_{i=1}^N (x_i - \bar{x})^2}$ , where  $N$  is the number of replicate measurements  $x_i$ , with  $x_i$  denoting the fraction (%) of intact 5CB shells in replicate  $i$  at time  $t$ . SEM quantifies the uncertainty in the estimate of the mean and is therefore smaller than the population standard deviation, making it a more appropriate error bar when comparing mean values.

**Example (at  $t = 24$  h).** Six replicate measurements {93.94, 94.46, 87.89, 92.175, 83.113, 90.485} % were obtained after 24 h at a PVA concentration of 0.028  $\mu\text{mol mL}^{-1}$  (13–23 kg mol<sup>−1</sup>). These data yield  $\bar{x} = 90.34\%$ ,  $\sigma = 4.28\%$ ,  $N = 6$ , and  $\text{SEM} = \sigma/\sqrt{N} \approx 1.75\%$ . These SEM values (rather than  $\pm 1\sigma$  standard deviations of the replicates) are used as the error bars in our decay-curve plots. In particular, Fig. 6.1

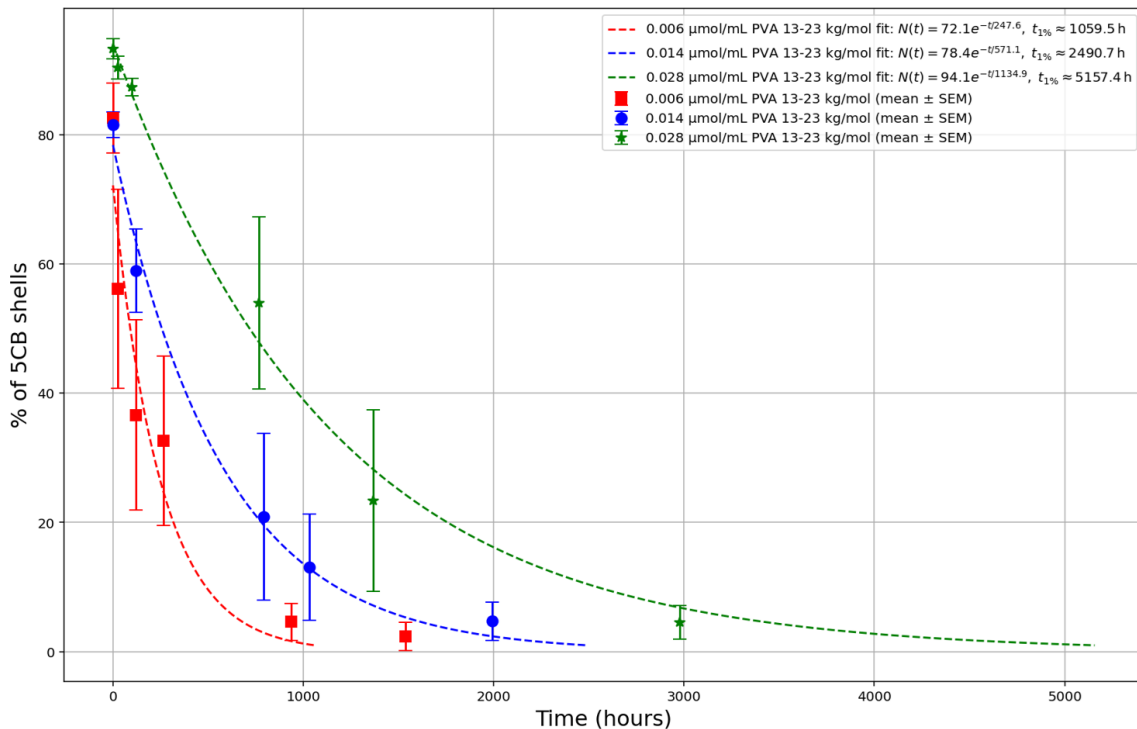


Figure 6.1: Lifetime of 5CB nematic shells stabilized by low-molar-mass PVA at 0.01, 0.025, and 0.05 wt.%. Shell populations decay approximately exponentially in time. Error bars represent the SEM from six capillaries for each measurement.

shows that higher PVA concentrations yield a larger initial shell fraction in the capillaries (5CB shells/(shells + droplets)).

## 6.2 Shell stability at minimum PVA concentrations

Our goal here is to determine how far the PVA concentration can be reduced while still giving acceptable shell lifetimes and initial production/collection yields. To probe the limit of stabilizer coverage, we prepared shells with PVA concentrations in the range  $5 \times 10^{-4}$ – $9 \times 10^{-4}$  wt.%, i.e. below 0.001 wt.%; for example, 0.0005 wt.% PVA corresponds to  $\approx 2.8 \times 10^{-4} \mu\text{mol mL}^{-1}$  for the 13–23 kg mol $^{-1}$  grade. At such ultra-low PVA levels, the interfacial PVA layer is expected to be very sparse, consistent with the adsorption and interfacial-tension studies reviewed in Sec. 3.2.2. We therefore monitored shells in this regime by time-resolved polarizing and bright-field microscopy to characterize their popping modes and compare their stability with

the more strongly stabilized cases. Somewhat surprisingly, even at these ultra-low PVA levels some shells remained intact for tens of minutes, and in some cases for many hours. Although ultra-low PVA levels could transiently stabilize shells, the initial production yield in this regime was on average significantly lower than in experiments using 0.01 wt.% PVA or higher. These observations are consistent with a very sparse polymer layer still providing transient stabilization, even though the overall stability remains highly variable. Careful inspection of time-resolved image series nevertheless revealed rare, interaction-mediated pathways, including fusion events between shells and droplets in addition to the more common direct popping into droplets. In the following, we describe these fusion events and how we incorporate them into a kinetic model for shell lifetimes.

### 6.2.1 Collapse of shells at ultra-low PVA concentrations

As discussed in Sec. 3.2, PVA adsorbs at the LC–aqueous interface and sterically stabilizes nematic droplets and shells, preventing coalescence [23]. When the stabilizer concentration is too low, this protection is incomplete and shells can collapse into droplets after a short time (typically within about 20 min after production). Figure 6.2 shows a representative event: the shell in panels (a–d) rapidly pops into a single 5CB droplet (e). At an ultra-low stabilizer concentration (PVA 88 % hydrolyzed), the defect pair usually appears to merge at the thinnest point of the shell shortly before collapse, as seen in Fig. 6.2c. In our experiments, such popping events were the most frequently observed route by which shells were lost at these ultra-low PVA levels.

Panel (a) of Fig. 6.3 shows the shell-popping kinetics at ultra-low PVA concentrations. The decay of the shell population noticeably deviates from a single exponential: the popping rate is initially low but increases sharply after approximately 7–25 min. We interpret this behavior in terms of defect migration on an already asymmetric shell. Because 5CB is slightly denser than the aqueous phase, the inner core is displaced toward the upper pole, where topological defects accumulate and establish

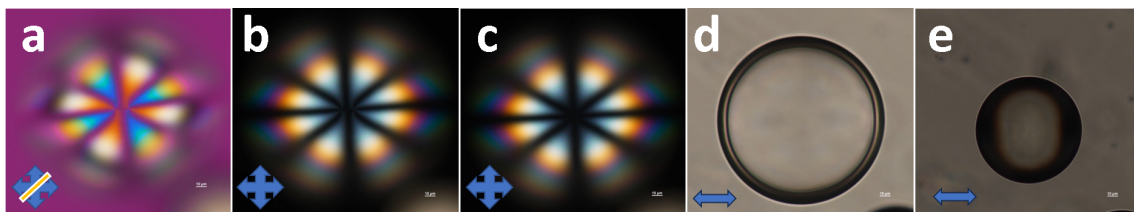


Figure 6.2: Popping of a 5CB shell (a–d), stabilized in  $9 \times 10^{-6}$  wt.% PVA ( $5 \times 10^{-6}$   $\mu\text{mol/mL}$ ), into a 5CB droplet (e), shown in different microscopy modes. Between (a) and (e), the shell collapses into a droplet within  $\sim 70$  s. Thin white scale bar:  $10 \mu\text{m}$ ; same magnification in all panels.

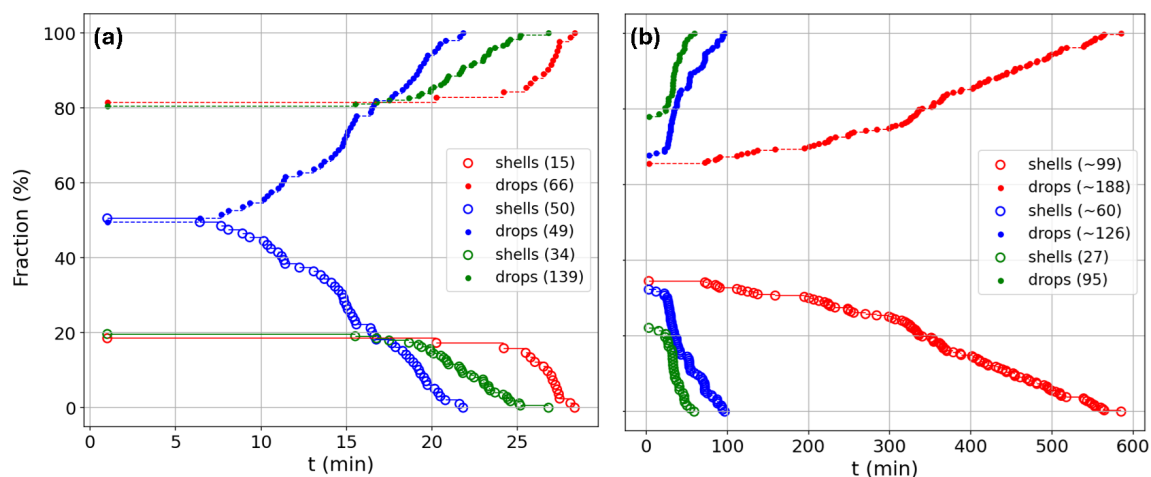


Figure 6.3: Popping kinetics of 5CB shells at two PVA concentrations,  $9 \times 10^{-6}$  and  $1.8 \times 10^{-4}$  wt.% PVA ( $13\text{--}23 \text{ kg mol}^{-1}$ ). Panels (a) and (b) show the fractions of shells (open circles) and droplets (filled circles) remaining in the field of view over time for three repeat experiments (red, green, blue) at each concentration. Note the different time scales on the x-axes.

a thickness gradient. In line with the gravity-driven annealing analysis in Chapter 5, we expect this asymmetry to develop on a time scale short compared with the tens-of-minutes to hours popping times considered here, so we treat the thickness gradient as effectively constant. Defects then migrate along this gradient and approach each other; when their separation becomes of order  $\sim 5 \mu\text{m}$  or less, the shell typically ruptures. Circles in Fig. 6.3a denote shells and dots denote droplets; the legend indicates the initial number of observed shells and droplets.

Compared with the relaxation experiments on 5CB shells in Chapter 5, shells stabilized with 0.5 wt.% PVA exhibit defect separations that typically saturate at  $20\text{--}60 \mu\text{m}$ , with the exact value depending on the mean wall thickness and on the

defect configuration. By contrast, in the ultra-low-PVA regime the shells usually rupture once the defect separation has decreased to about 5  $\mu\text{m}$  or less. These observations suggest that low PVA coverage allows defects to approach roughly an order of magnitude closer before collapse, even for shells with similar geometry. This contrast with the results presented in Chapter 5 provides a key constraint on possible mechanisms that link defect motion to shell rupture.

### 6.2.2 Shell–droplet fusion at ultra-low PVA concentrations

During repeated observations under the same ultra-low-PVA conditions, we occasionally observed a different pathway. Instead of collapsing directly, some shells first merged with neighboring droplets and then survived as thicker shells for several minutes before eventually popping. These shell–droplet fusion events are surprising in view of the established steric-stabilizing role of PVA (Sec. 3.2, Sec. 3.2.1), because fusion requires intimate contact between LC interfaces that are only sparsely covered by polymer.

Figure 6.4 illustrates one such event. In Fig. 6.4a the shell and droplet are in contact, and in (b) the 5CB droplet merges with the shell, increasing its average wall thickness by approximately a factor of two (assuming that the droplet originally formed by collapse of a shell of similar diameter). This fusion also shows that increasing the LC volume, and thus the mean wall thickness, can be accompanied by a stronger thickness asymmetry: after fusion, the four  $+\frac{1}{2}$  surface defects move closer together in the upper hemisphere of the shell (Fig. 6.4c,d) than they were before the merger (a), indicating extreme thinning of the upper cap until the shell pops (e). These occasional shell–droplet fusion events naturally raised the question of whether neighboring shells could also merge after collection, either in sealed capillaries or in storage vials or Petri dishes.

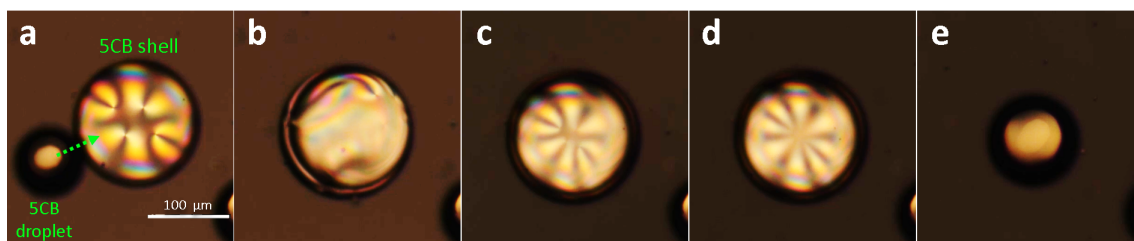


Figure 6.4: POM images of fusion between a 5CB shell and a 5CB droplet (a), followed by thinning (d) and popping (e) of the shell (brightness and contrast digitally enhanced). The shell was stabilized in  $5 \times 10^{-4}$  wt.% PVA ( $13\text{--}23 \text{ kg mol}^{-1}$ ). (a)  $\sim 30$  min after production; (b) immediately after shell–droplet fusion; (c) 20 s after fusion; (d) 140 s after fusion, just before popping; (e) larger droplet after shell popping. White scale bar in (a):  $100 \mu\text{m}$ ; same magnification in all panels.

### 6.2.3 Shell–shell fusion at ultra-low PVA concentrations

Within the same ultra-low-PVA regime, we even more rarely captured a second, rarer fusion pathway in which two 5CB shells merge inside the capillary, as illustrated in Fig. 6.5, with aqueous phases identical to those in the shell–droplet case. To the best of our knowledge, such shell–shell fusion has not been documented previously for PVA-stabilized 5CB shells.

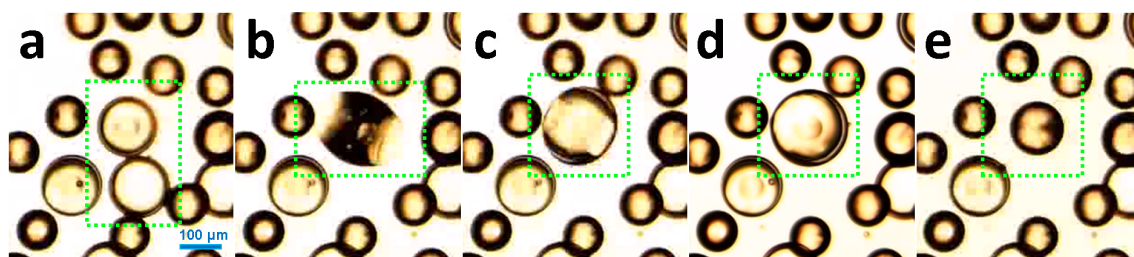


Figure 6.5: Fusion of two 5CB shells and subsequent popping. (a) Two neighboring shells before fusion ( $\sim 5$  min after production). (b) Intermediate double-core shell formed  $\sim 4$  s after initial fusion. (c) Rapid complete fusion into a single thicker shell. (d) About 25 s after complete fusion, just before popping. (e) Larger droplet after shell popping. Blue scale bar in (a):  $100 \mu\text{m}$ ; same magnification in all panels.

In Fig. 6.5a the two shells make contact, then form a double-core shell structure (b), fully fuse into a single shell (c,d), and ultimately pop (e). The resulting shell in (d) has an increased diameter of  $\sim 190 \mu\text{m}$ , compared with  $\sim 146 \mu\text{m}$  for each of the two shells in (a), indicating not only a thicker average LC wall but also an enlarged inner core.

Although such fusion events typically remain rare under the microscope (especially at much higher stabilizer concentrations), in experiments using ultra-low PVA concentrations there may be shells that have already fused within seconds or a minute after collection. An indirect indication of this is the presence of shells that initially appear larger or with a greater average wall thickness than most others at the start of observation. Besides minimizing PVA concentration, an additional condition for any fusion event, whether between shells or between shells and droplets, is that the shells must be in direct contact with neighboring shells or droplets. If the initial proportion of such contacts is low, the probability of fusion significantly decreases.

Taken together, these observations indicate that shell loss at ultra-low PVA levels is not governed by a single route but instead by a small set of interaction-mediated pathways: shells can undergo direct popping or fusion-mediated rupture, typically followed by a shortened lifetime of the merged shells. To incorporate these pathways into a quantitative description, we developed a kinetic model that explicitly tracks the main species present in the capillaries (shells, droplets, fused shells, fused droplets) and relates their time evolution through coupled rate equations. The resulting model comprises five coupled, nonlinear ordinary differential equations describing the key events of shell popping and fusion and provides a minimal framework for interpreting the lifetime data in this regime.

#### 6.2.4 Theoretical kinetic model for shell popping and fusion

**Geometry of the pristine (*s*) shell.** Because our microfluidic technique can produce nearly monodisperse shells (when production is successful), we can simplify the analysis far more than in studies of polydisperse multiple emulsions, such as those common in food-science applications [194–197]. We therefore assume that directly after production we have a single species, a liquid-crystal shell (*s*), with aqueous inner volume  $v_i = \frac{4}{3}\pi r_i^3$  and LC volume  $v_{LC} = \frac{4}{3}\pi(r_o^3 - r_i^3)$ .

From spherical geometry we obtain

$$\mathbf{r}_i = \sqrt[3]{\frac{3\mathbf{v}_i}{4\pi}}, \quad \mathbf{r}_o = \sqrt[3]{\frac{3(\mathbf{v}_i + \mathbf{v}_{LC})}{4\pi}}. \quad (6.1)$$

and the mean wall thickness

$$\mathbf{d}_0 = \mathbf{r}_o - \mathbf{r}_i = \sqrt[3]{\frac{3}{4\pi}} [\sqrt[3]{\mathbf{v}_i + \mathbf{v}_{LC}} - \sqrt[3]{\mathbf{v}_i}]. \quad (6.2)$$

**Small droplet ( $d$ ) produced by collapse.** Collapse removes the aqueous core.

The LC volume  $v_{LC}$  forms a droplet of radius

$$\mathbf{r}_d = \sqrt[3]{\frac{3\mathbf{v}_{LC}}{4\pi}}. \quad (6.3)$$

**Mixed shell  $S$  (hetero-fusion  $d + s$ ).** Here  $v_i^S = v_i$  and  $v_{LC}^S = 2v_{LC}$ . Then

$$\mathbf{r}_i^S = \mathbf{r}_i, \quad \mathbf{r}_o^S = \sqrt[3]{\frac{3(\mathbf{v}_i + 2\mathbf{v}_{LC})}{4\pi}}, \quad \mathbf{d}_0^S = \mathbf{r}_o^S - \mathbf{r}_i^S = \sqrt[3]{\frac{3}{4\pi}} [\sqrt[3]{\mathbf{v}_i + 2\mathbf{v}_{LC}} - \sqrt[3]{\mathbf{v}_i}]. \quad (6.4)$$

**Double shell  $SS$  (homo-fusion  $s + s$ ).** For a double shell the volumes are  $v_i^{SS} = 2v_i$  and  $v_{LC}^{SS} = 2v_{LC}$ , so

$$\mathbf{r}_i^{SS} = \sqrt[3]{2} \mathbf{r}_i, \quad \mathbf{r}_o^{SS} = \sqrt[3]{2} \mathbf{r}_o, \quad \mathbf{d}_0^{SS} = \sqrt[3]{2} \mathbf{d}_0 \approx 1.26 \mathbf{d}_0. \quad (6.5)$$

**Large droplet  $D$ .** Any pathway involving  $2v_{LC}$  of LC (i.e., fusion of two small droplets, two shells, or a droplet with a shell) yields

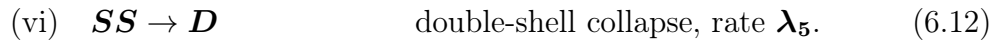
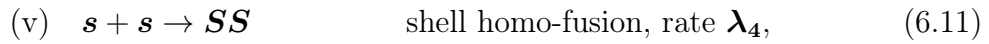
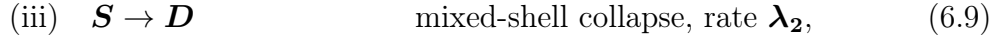
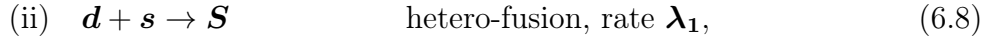
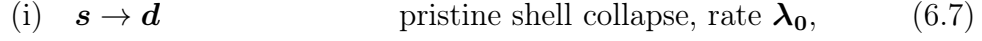
$$\mathbf{r}_D = \sqrt[3]{\frac{3(2\mathbf{v}_{LC})}{4\pi}} = \sqrt[3]{2} \mathbf{r}_d \approx 1.26 \mathbf{r}_d. \quad (6.6)$$

Geometrically, the average wall thicknesses satisfy

$$\mathbf{d}_0 < \mathbf{d}_0^{SS} < \mathbf{d}_0^S \quad \text{for all realistic ratios } \alpha = \frac{\mathbf{v}_i}{\mathbf{v}_{LC}} > 0.$$

### 6.2.5 Kinetic pathways

We consider six elementary processes with rate constants  $\lambda_0$ – $\lambda_5$ :



**Rate equations.** Let  $N_s, N_d, N_S, N_{SS}, N_D$  be the species populations at time  $t$ .

With the above labeling, the kinetics are

$$\dot{N}_s = -\lambda_0 N_s - \lambda_1 N_s N_d - \lambda_4 N_s^2, \quad (6.13)$$

$$\dot{N}_d = \lambda_0 N_s - \lambda_1 N_s N_d - \lambda_3 N_d^2, \quad (6.14)$$

$$\dot{N}_S = \lambda_1 N_s N_d - \lambda_2 N_S, \quad (6.15)$$

$$\dot{N}_{SS} = \lambda_4 N_s^2 - \lambda_5 N_{SS}, \quad (6.16)$$

$$\dot{N}_D = \lambda_2 N_S + \lambda_3 N_d^2 + \lambda_5 N_{SS}. \quad (6.17)$$

### 6.2.6 Expected curves for reasonable rate values

Following the kinetic scheme for shell collapse and fusion developed above, and considering an idealized condition in which, immediately after collection, each shell is in contact with at least one other shell, we select illustrative popping and fusion rate coefficients for a PVA concentration of order 0.0001 wt.%, guided by our initial

experimental observations and physical intuition:

$\lambda_0 = 0.1$	shell [s] $\rightarrow$ droplet [d],
$\lambda_1 = 2 \times 10^{-4}$	shell [s] + droplet [d] $\rightarrow$ shell [S],
$\lambda_2 = 0.15$	shell [S] $\rightarrow$ droplet [D],
$\lambda_3 = 10^{-6}$	droplet [d] + droplet [d] $\rightarrow$ droplet [D],
$\lambda_4 = 10^{-4}$	shell [s] + shell [s] $\rightarrow$ shell [SS],
$\lambda_5 = 0.2$	shell [SS] $\rightarrow$ droplet [D].

Here,  $\lambda_0$ – $\lambda_5$  denote the popping and fusion rates. At the numerical level, this five-species kinetic model, Eqs. (6.13)–(6.17), with the above rate constants is implemented and solved in Appendix C. Simulating the time evolution of a capillary segment initially containing  $\sim 100$  shells (reflecting relatively realistic conditions, except for the idealized collection yield) yields the curves in Fig. 6.6a.

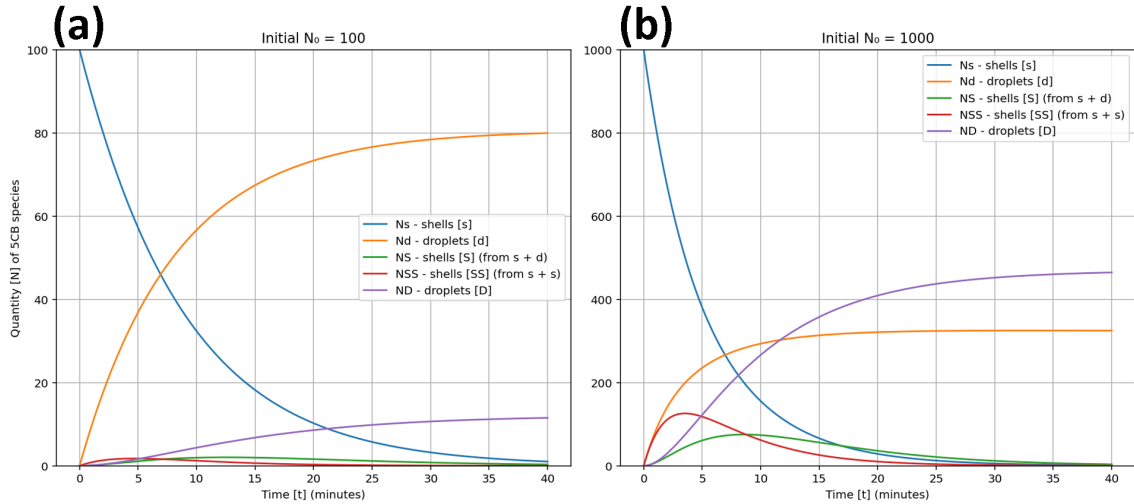


Figure 6.6: Time evolution of 5CB shells into different species for identical rate constants  $\lambda_0 = 0.1$ ,  $\lambda_1 = 2 \times 10^{-4}$ ,  $\lambda_2 = 0.15$ ,  $\lambda_3 = 10^{-6}$ ,  $\lambda_4 = 10^{-4}$ ,  $\lambda_5 = 0.2$ . Panel (a) starts from 100 shells, panel (b) from 1000 shells.

Figure 6.6a shows that fusion between shells and between shells and droplets remains comparatively rare: the fused species reach peak fractions of at most about 2%, although even these rare events increase the predicted number of large 5CB droplets [D] (purple curve). The model predicts that within the first minutes it is

more likely to observe fusion events between shells than between shells and droplets, which is expected because at the start of shell collection there are more shells than droplets (especially in an idealized model). This trend is consistent with our observations in Figs. 6.4 and 6.5.

If we keep all rate values the same but assume an initial shell density ten times higher, i.e.,  $\sim 1000$  shells instead of 100, fusion events become significantly more likely. This is a less realistic scenario, but it could in principle be approached if, immediately after collection and sealing, the capillary is tilted so that shells and droplets accumulate at one end. The resulting model curves are shown in Fig. 6.6b.

### 6.2.7 Analyzing the popping rates of 5CB shells

Following the experimental approach used to parameterize our theoretical model, we did not image and count shells and droplets in the entire set of capillaries. Instead, for each experiment we selected a region of a rectangular capillary that contained a sufficient number of shells and recorded this field of view over time. Figure 6.3 shows the fractions of shells and droplets in the field of view for three repeat experiments at each of the two ultra-low PVA concentrations.

As shown in Fig. 6.3a, the decay of the shell population at  $9 \times 10^{-6}$  wt.% PVA deviates strongly from a single exponential, whereas panel (b) shows the corresponding trajectories at  $1.8 \times 10^{-4}$  wt.% PVA.

**Steric stabilization of the thinnest region.** Adsorbed PVA is expected to modify this balance primarily by sterically stabilizing the thinnest region of the shell, rather than through large changes in the density mismatch or interfacial tension between 5CB and the aqueous phase. Vinyl acetate segments that partition into the LC on both sides of the thin region repel each other and help to maintain a finite minimal thickness. At high PVA concentrations this steric repulsion keeps the thinnest point from collapsing, whereas at ultra-low PVA concentrations there is too little PVA to sustain this effect, so the two LC–water interfaces can approach

each other closely enough that the shell pops when the defects are about to merge. This picture is consistent with classical steric stabilization, where polymer chains at opposing interfaces repel each other as they approach, preserving conformational entropy and preventing collapse [173].

**Anchoring and defect-line configuration.** A more speculative, complementary possibility is that PVA coverage may also affect the anchoring strength and three-dimensional shape of the disclination lines, which are known to depend sensitively on thickness heterogeneity and elastic anisotropy in nematic shells [198]. At high surface coverage, amphiphilic PVA may locally soften the effective tangential anchoring and allow the disclination line connecting two surface defects to bend into a U-shape that remains on the same side of the shell. In such a configuration there is little energetic gain in moving toward the thinnest region, and the defects can remain separated by tens of micrometers without driving extreme thinning. At low PVA coverage, by contrast, tangential anchoring is stronger and the defect lines more readily connect inner and outer interfaces; the defects then continue to migrate toward the thinnest point until they nearly merge. In this view, the critical step is not thickness reduction alone but the final approach and possible merging of defects in an already very thin region, which may trigger the observed popping.

Finally, we examined shell stability when 5CB was stabilized with a higher-molar-mass PVA (85–124 kg mol<sup>-1</sup>, 87–89 % hydrolyzed) at very low bulk concentrations. Figure 6.7 summarizes two experiments at  $5 \times 10^{-6}$  and  $5 \times 10^{-4}$  μmol/mL PVA. At the lower concentration almost all shells collapse within about 20 min, whereas at the higher concentration most shells still rupture within 30–40 min, although a small fraction survives for up to ~ 50–55 min. Thus, increasing the high-molar-mass PVA concentration by a factor of 100 from an already extremely dilute baseline extends shell survival only modestly, even though it roughly doubles the initial fraction of shells during production and collection, as seen in Fig. 6.7. For comparison, shells stabilized earlier in this chapter with 0.01 wt.% low-molar-mass PVA (13–23 kg mol<sup>-1</sup>,

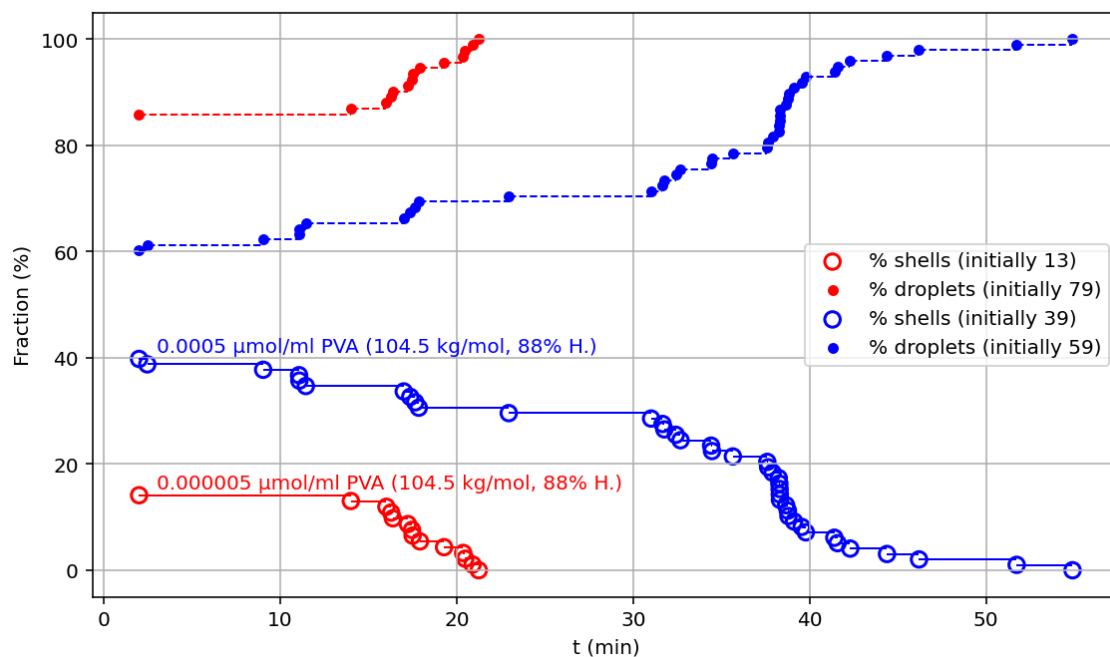


Figure 6.7: Popping kinetics of 5CB shells stabilized with very low concentrations of PVA ( $85\text{--}124\text{ kg mol}^{-1}$ ). Blue symbols:  $5 \times 10^{-4}\text{ }\mu\text{mol/mL PVA}$  ( $\approx 5 \times 10^{-3}\text{ wt.}\%$ ); red symbols:  $5 \times 10^{-6}\text{ }\mu\text{mol/mL PVA}$  ( $\approx 5 \times 10^{-5}\text{ wt.}\%$ ). Open circles show the fraction of shells and filled circles the fraction of droplets remaining in the field of view as a function of time; dashed lines are piecewise-linear fits to guide the eye.

87–89 % hydrolyzed) remain stable for weeks, indicating that both of these high-molar-mass conditions in Fig. 6.7 correspond to very weak stabilization. This behavior is consistent with the picture in Sec. 3.2.2, where interfacial properties are governed primarily by the number and nature of adsorbing segments rather than by molecular weight alone.

The corresponding bright-field micrographs in Fig. 6.8 show the initial state of the same two shell dispersions from Fig. 6.7. In both dispersions the shells and droplets have comparable sizes, but the higher PVA concentration leads to a larger number of intact shells in the field of view. Together, Figs. 6.7 and 6.8 highlight this modest increase in survival and initial yield at the higher concentration, while both conditions remain in a regime of weak overall stabilization compared with the weeks-long lifetimes achieved at 0.01 wt.% low-molar-mass PVA.

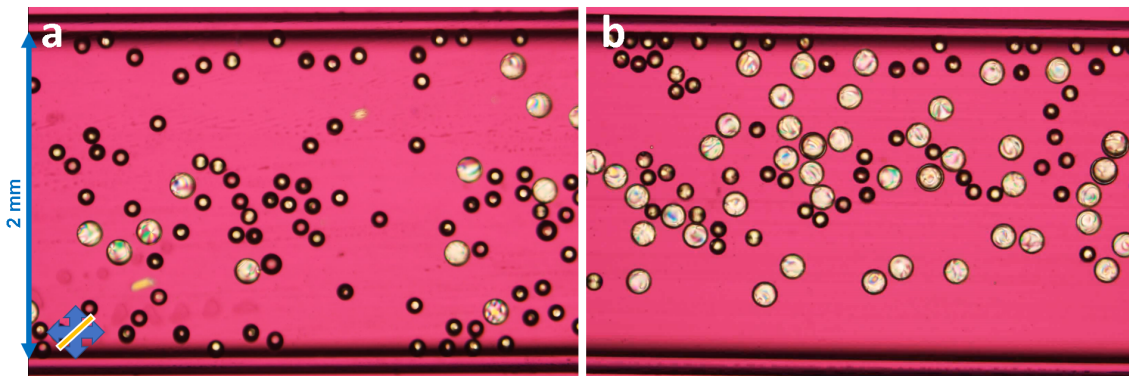


Figure 6.8: Freshly produced 5CB shells stabilized with very low concentrations of higher-molar-mass PVA ( $85\text{--}124\text{ kg mol}^{-1}$ ). (a)  $5 \times 10^{-6}\text{ }\mu\text{mol/mL}$  PVA ( $\approx 5 \times 10^{-5}\text{ wt.}\%$ ); (b)  $5 \times 10^{-4}\text{ }\mu\text{mol/mL}$  PVA ( $\approx 5 \times 10^{-3}\text{ wt.}\%$ ). The blue double arrow in (a) indicates the 2 mm inner height of the capillary.

## 6.3 Summary and outlook

### Conclusions

- *PVA concentration affects shell lifetime.* We showed that even at  $9 \times 10^{-6}\text{ wt.}\%$  low-molar-mass PVA ( $13\text{--}23\text{ kg mol}^{-1}$ ), shells collected in glass capillaries with inner dimensions  $0.20 \times 2.00\text{ mm}^2$  can survive for 20–30 min. At 0.01 wt.% PVA, 5CB shells can be stabilized for weeks, with an initial yield in the 60–80 % range. Higher PVA concentrations further increase the shell lifetime.
- *Shell collapse at ultra-low PVA concentrations is not single-exponential.* Survival curves exhibit non-exponential decay, consistent with effective rate constants that vary with time as defects anneal.
- *The final separation between defects is smaller at extremely low PVA concentrations.* At  $9 \times 10^{-6}\text{ wt.}\%$  PVA, shells typically rupture when the separation between the two defects has decreased to  $\sim 5\text{ }\mu\text{m}$  or less, about an order of magnitude lower than the equilibrium separations (tens of micrometers) observed for the moderately stabilized shells studied in Chapter 5 using 0.5 wt.% PVA. This indicates that extremely low PVA allows much more pronounced thin-

ning in the defect region before collapse. Our observations, together with the comparative results in Chapter 5, also suggest that the mean wall thickness influences the final defect spacing, with thicker shells tending to allow defects to approach more closely.

- *High-molar-mass PVA at very low bulk concentrations provides only weak stabilization*, consistent with shell lifetime in this regime being limited mainly by insufficient interfacial coverage rather than by polymer molar mass alone.
- *A coupled kinetic model captures fusion and collapse events*. By introducing a coupled kinetic scheme with rate constants  $\lambda_0$ – $\lambda_5$  for shell→droplet conversion, shell–droplet and shell–shell fusion, and subsequent collapse, we show that the model can qualitatively reproduce the main features of both the dominant popping kinetics and the rare fusion events and provides a basis for relating model rate constants to experimentally observed shell and droplet lifetimes.

## Outlook

- *Alternative stabilizers*. Test other amphiphilic polymers and block copolymers to compare steric and electrostatic stabilization and to tune shell lifetimes.
- *Geometry and confinement effects*. Systematically vary capillary cross-section, shell wall thickness, and shell size to quantify geometry and confinement effects.
- *Temperature and rheology*. Explore how temperature-dependent viscosities of 5CB and PVA solutions influence shell thinning dynamics and rupture thresholds.
- *Integration into sensors*. Further refine and use the lifetime model to define reliable operating windows for LC-shell-based biosensors and photonic elements, balancing mechanical stability with responsiveness to analytes.

Having shown how to keep nematic shells alive for experimentally useful times, we now turn from lifetime to response. The next chapter focuses on how they register changes at their interfaces through altered director fields, defects, and optical textures.

## Chapter 7

# Electrolyte and endotoxin effects on textures in nematic shells

Over the past decade, nematic 5CB droplets have been investigated as an optical sensing platform for picogram-per-milliliter concentrations of bacterial lipopolysaccharides (LPS) [81, 138, 139]. In these studies, the droplets typically operate via field-induced ordering transitions from bipolar to radial textures, which are readily observed by POM. However, high sensitivity is usually achieved only for very small droplets ( $\leq 0.01$  mm), which requires high-magnification objectives. In contrast, double emulsions in the form of 5CB shells can easily reach diameters of 0.1–0.3 mm while preserving rich defect phenomenology. This chapter presents initial observations and working hypotheses on how electrolyte composition and LPS adsorption affect the director field of 5CB shells. Because of their larger size, nematic 5CB shells may offer a more practical platform for LPS detection, allowing optical readout at lower magnification than droplets. For practical sensing applications, however, response speed is as important as sensitivity. To test these effects under well-defined conditions, we prepared 5CB shells stabilized by PVA and exposed them to electrolyte and LPS environments, as summarized below. For a broader context, several reviews summarize liquid-crystal-based chemical and biological sensing, including nematic

films, droplets, and colloidal systems [158, 176, 177, 199].

## Sample preparation and shell production

In most experiments, 5CB shells were stabilized by PVA (87–89 % hydrolyzed,  $M_w = 13\text{--}23 \text{ kg mol}^{-1}$ ) dissolved at 0.025 wt.% in both the inner and outer aqueous phases; in a subset of experiments, shells were prepared without PVA. Unless stated otherwise, the inner and outer aqueous phases were either distilled water or endotoxin-free Dulbecco’s phosphate-buffered saline (PBS, cat. TMS-012-A; 137 mM NaCl, 2.7 mM KCl, 10 mM  $\text{Na}_2\text{HPO}_4$ , 1.8 mM  $\text{KH}_2\text{PO}_4$ ; pH 7.0–7.1, ionic strength  $I \approx 0.17 \text{ M}$ ). LPS from *E. coli* O127:B8 was added to the aqueous phases at the concentrations indicated for each experiment. Sodium dodecyl sulfate (SDS, 5  $\mu\text{M}$ ) was included in the outer aqueous phase as a surfactant during shell generation and during the production of simple 5CB droplet emulsions. In a subset of LPS experiments, this trace amount of SDS was deliberately retained to improve the dispersion of LPS in the aqueous phase and to mitigate its tendency to form self-aggregates (see Sec. 3.4.5).

The 5CB shells were produced at RT using a coaxial glass-capillary microfluidic device controlled by a Fluigent MFCS-EZ pressure controller, following the approach of Weitz [163]. The full geometry of the setup and the production protocol are described in Appendix A.2; briefly, double emulsions (LC shells) were formed using an inner capillary with an inner-orifice diameter of  $\sim 70 \mu\text{m}$  and a collecting capillary with an inner diameter of  $\sim 180 \mu\text{m}$ .

## 7.1 Electrolyte effects on nematic shells

### 7.1.1 Ionic-strength effects on shell director fields

**Histogram analysis.** To quantify how defect patterns depend on electrolyte composition, we classified shells by their surface-defect topology and compiled the percentage distributions shown in Fig. 7.1. In these experiments, shells were stabilized with 0.025 wt.% PVA and the inner and outer aqueous phases contained either distilled water, PBS ( $I \approx 0.17$  M), or PBS with  $0.1 \text{ mg mL}^{-1}$  LPS.

In distilled water,  $\sim 87\%$  of shells exhibit the familiar tetravalent configuration, with four isolated  $+\frac{1}{2}$  surface disclinations clustered around the thinnest upper pole. Replacing water with PBS reduces the fraction of tetravalent shells to  $\sim 42\%$  and simultaneously increases the occurrence of “ $1 + 2 \times \frac{1}{2}$ ” textures (one apparent  $+1$  and two  $+\frac{1}{2}$  defects) from  $\sim 12\%$  to  $\sim 45\%$ . In addition, PBS alone occasionally yields textures that project optically as  $+\frac{3}{2} + \frac{1}{2}$  or as  $+2$  defects, although in the latter case we cannot exclude tightly spaced clusters of  $+\frac{1}{2}$  defects that are not optically resolved. These trends suggest that ionic strength modifies the effective anchoring and/or shell-thickness profile, consistent with the EDL-based discussion in Secs. 3.3–3.3.3.

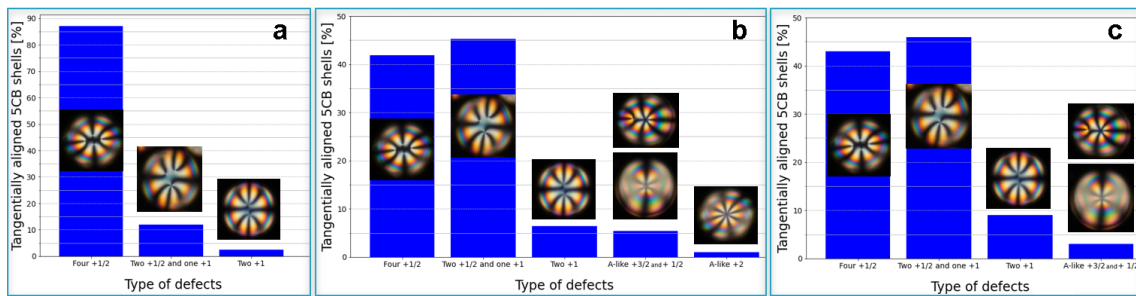


Figure 7.1: Percentage distribution of 5CB shells with different defect configurations. (a) Shells stabilized in aqueous 0.025 wt.% PVA (distilled water). (b) Shells stabilized in 0.025 wt.% PVA in PBS. (c) Shells stabilized in 0.025 wt.% PVA in PBS in the presence of  $0.1 \text{ mg mL}^{-1}$  LPS.

Representative examples of these rare configurations are shown in Fig. 7.2. Each

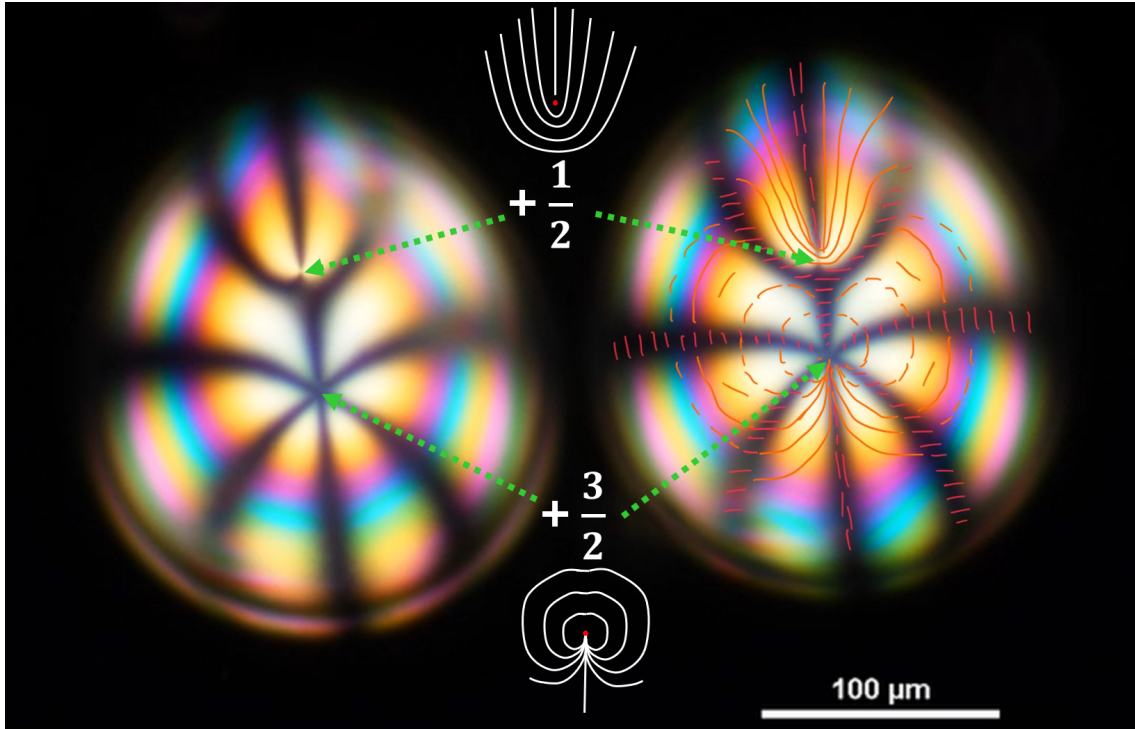


Figure 7.2: POM images of two 5CB shells stabilized by 0.025 wt.% PVA in PBS, each exhibiting an apparent  $+\frac{3}{2}$  and a  $+\frac{1}{2}$  surface defect near the thinnest pole. Dashed green arrows indicate the correspondence between the optical textures and the schematic director fields sketched in red on the right-hand shell. Insets with white lines show idealized director configurations for isolated  $+\frac{1}{2}$  and  $+\frac{3}{2}$  defects (redrawn after Fumeron and Berche [201]).

shell in this image, stabilized by 0.025 wt.% PVA in PBS, exhibits an apparent  $+\frac{3}{2}$  and  $+\frac{1}{2}$  surface defect located near the thinnest pole of the shell. To the best of our knowledge, such  $+\frac{3}{2}$ -like textures have not previously been reported for achiral nematic shells; previous observations of  $+\frac{3}{2}$  defects in spherical shells concern cholesteric (chiral nematic) shells with helical order [200]. An alternative interpretation is that the apparent  $+\frac{3}{2}$  defect corresponds to three closely spaced  $+\frac{1}{2}$  disclinations whose cores are not optically resolved. In either case, these examples represent an extreme case of defect coalescence promoted by the presence of PBS at the thinnest pole and appear to be rare, occurring in only a few percent of the shells examined in our experiments.

Based on simulations by Long *et al.* [32], three-dimensional nematic disclination lines that terminate on a substrate generally exhibit a mixture of local core structures

rather than a single, purely wedge-type singularity. Along a given line, the director field may locally resemble a  $+\frac{1}{2}$  wedge, a  $-\frac{1}{2}$ -like configuration, or a twist-dominated segment, and these characters vary continuously along the contour. In the planar cell geometry analyzed in Ref. [32], the simulated disclination arch connects two  $+\frac{1}{2}$  surface defects on the same substrate, and the green director cylinders in Fig. 7.3 emphasize the coexistence of wedge- and twist-like distortions along a single line.

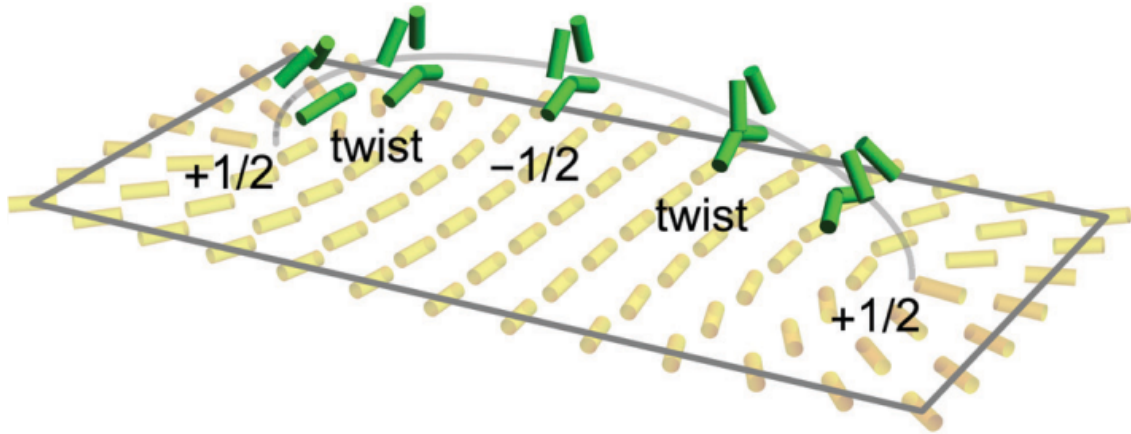


Figure 7.3: Schematic director field around a disclination line in a 3D nematic LC, adapted from Long *et al.* [32] with permission from The Royal Society of Chemistry. In the simulated planar cell the line connects two  $+\frac{1}{2}$  surface disclinations on the same substrate. Green cylinders show the bulk director around the disclination line, and yellow cylinders the director at the bottom substrate, highlighting the coexistence of wedge- and twist-like segments along a single line.

In our shells, however, the global topology of the defect network is constrained by the spherical geometry, the presence of both inner and outer LC–water interfaces, and the thickness gradient. As argued in Chapter 5, it is energetically favorable for each  $+\frac{1}{2}$  surface disclination on the outer interface to be connected to a corresponding  $+\frac{1}{2}$  defect on the inner interface by a disclination line that threads the shell approximately along the local surface normal. Such cross-side pairing minimizes the total length of the defect lines and explains why the defects migrate to and accumulate at the thinnest region of the shell. The three-dimensional shape of these lines cannot be resolved in our polarizing-microscopy experiments, but by analogy with the simulations of Long *et al.* we expect them to exhibit, at least qualitatively, a generic

mixture of wedge-like sections near the interfaces and twist-dominated segments in the shell interior. Thus, Fig. 7.3 should be regarded as an illustration of the local wedge–twist structure of a disclination line, rather than as evidence that two  $+\frac{1}{2}$  defects on the same side of the shell are directly connected.

An effective surface-normal field—either imposed by external electrodes (Sec. 2.9.3) or arising from the electrical double layers at the LC–water interfaces (Sec. 3.3.3)—competes with planar anchoring and tends to rotate the director towards radial alignment for  $\Delta\varepsilon > 0$ , analogous to the Frederiks transition in flat cells (Sec. 2.9). Stronger normal fields in PBS therefore lower the elastic penalty for locally radial director configurations near defect cores and inversion walls and thus provide a natural route to enhanced defect coalescence. This is the central assumption behind the curvature-modulated capacitor picture developed below.

Since the twist elastic constant  $K_2$  of 5CB is the smallest of the three Frank constants, twist deformations along disclination lines are relatively inexpensive whenever they are compatible with confinement and boundary conditions. Around 30 °C, published measurements of the static elastic constants for 5CB show that  $K_1$  and  $K_3$  become comparable ( $K_1 \approx 5.3$  pN,  $K_3 \approx 5.8$  pN), while  $K_2$  remains lower ( $\approx 3.2$  pN) [43], as summarized in Table 7.1.

Table 7.1: Elastic constants of 5CB at 24 °C and 30 °C. Data from Iglesias *et al.* [43].

parameter	5CB at 24 °C	5CB at 30 °C
$K_1$ (pN)	6.5	5.3
$K_2$ (pN)	3.5	3.2
$K_3$ (pN)	9.8	5.8

### 7.1.2 Curvature-modulated interfacial “capacitor” model

We now introduce a working hypothesis that links the ionic-strength dependence in Fig. 7.1 to curvature-modulated electrostatics. In PBS, both aqueous phases of a nematic shell contain mobile ions and can be treated as reasonably conducting,

whereas the 5CB layer is a comparatively poor conductor that acts primarily as an anisotropic dielectric. To leading order, the shell can therefore be viewed as a curved capacitor: two LC–water interfaces that carry electrical double layers (EDLs; cf. Sec. 3.3) separated by a thin nematic film serving as a dielectric spacer. Electric fields arising from a small imbalance between the inner and outer EDLs then couple to the director and modify defect interactions.

▷ **Local capacitance.** We model a small interfacial patch at position  $\mathbf{r}$  as a parallel-plate capacitor of area  $A(\mathbf{r})$ , local shell thickness  $d(\mathbf{r})$ , and effective permittivity  $\varepsilon_{\text{eff}}(\mathbf{r})$ . Its local capacitance is

$$C(\mathbf{r}) = \frac{\varepsilon_0 \varepsilon_{\text{eff}}(\mathbf{r}) A(\mathbf{r})}{d(\mathbf{r})}. \quad (7.1)$$

In the thin-shell limit,  $d(\mathbf{r}) \ll R_{\text{out}}$ , the local field across the nematic layer is approximately uniform, so that the shell behaves locally as a parallel-plate capacitor, in analogy with the standard treatment of spherical and cylindrical capacitors in elementary electrodynamics texts [202].

The effective permittivity is then

$$\varepsilon_{\text{eff}}(\mathbf{r}) = \varepsilon_{\perp} + (\varepsilon_{\parallel} - \varepsilon_{\perp}) (\mathbf{n}(\mathbf{r}) \cdot \hat{\mathbf{d}}(\mathbf{r}))^2, \quad (7.2)$$

where  $\hat{\mathbf{d}}(\mathbf{r})$  is the local surface normal directed from the inner to the outer aqueous phase (cf. Fig. 7.4). For 5CB at RT, typical values are  $\varepsilon_{\parallel} \approx 20$  and  $\varepsilon_{\perp} \approx 7$ , giving a dielectric anisotropy  $\Delta\varepsilon = \varepsilon_{\parallel} - \varepsilon_{\perp} \approx 13$  [42, 43].

▷ **Bulk vs. defect permittivity.** In a defect core, the director is locally disordered and the dielectric tensor can be approximated by its isotropic average

$$\varepsilon_{\text{iso}} = \frac{2\varepsilon_{\perp} + \varepsilon_{\parallel}}{3} \approx 11.3, \quad (7.3)$$

i.e. by averaging the two transverse ( $\varepsilon_{\perp}$ ) and one longitudinal ( $\varepsilon_{\parallel}$ ) principal com-

ponents. In contrast, for a tangentially aligned shell far from defects the director lies predominantly in the interface plane, so that  $\varepsilon_{\text{eff, tan}} \approx \varepsilon_{\perp}$ . Equations (7.1) and (7.3) therefore predict a larger local capacitance inside defects than in the surrounding tangentially aligned regions. This contrast between regions with different permittivities, and the associated build-up of interfacial charge, is in the spirit of Maxwell–Wagner–Sillars interfacial polarization in heterogeneous dielectrics [51, 52].

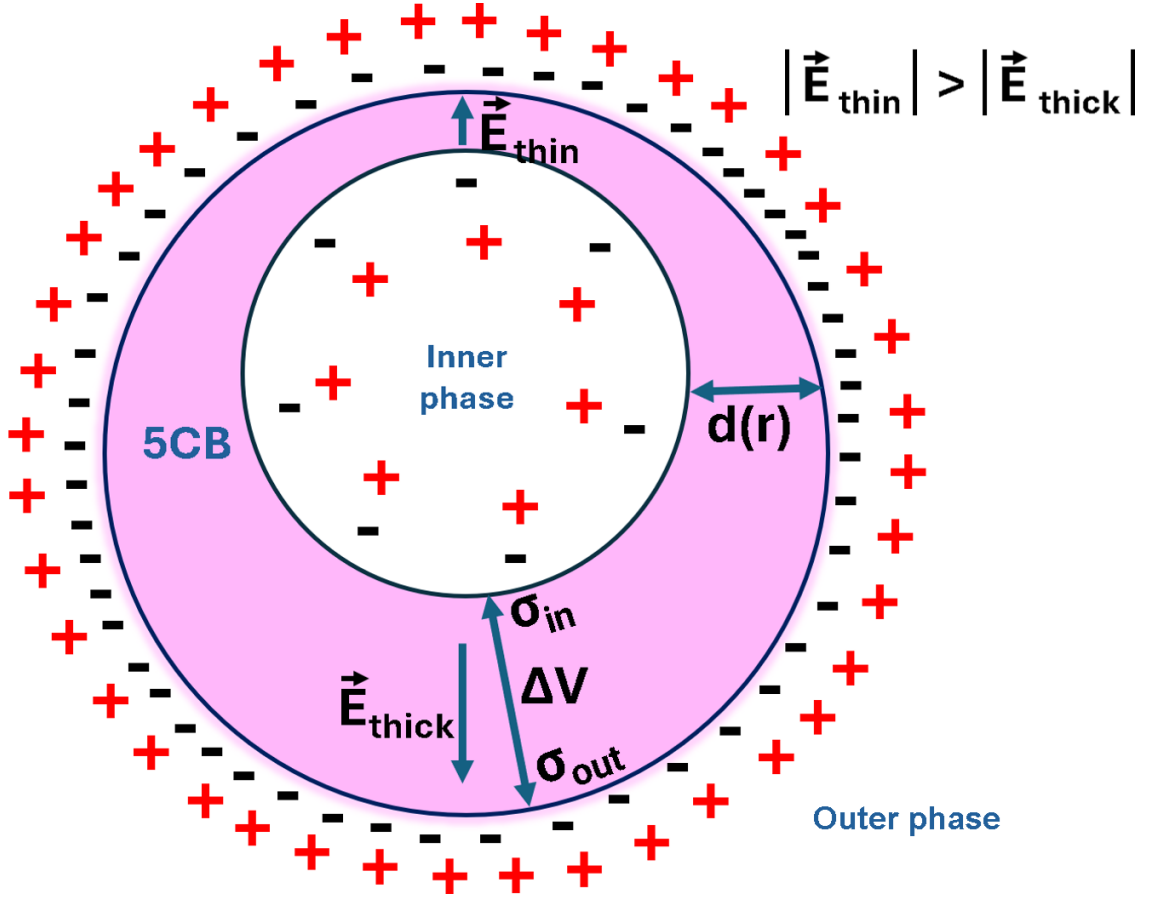


Figure 7.4: Qualitative sketch of charge distribution in a 5CB shell (cross-sectional view). The outer LC–water interface is convex and has a larger area than the concave inner interface, so more ions can adsorb at the outer surface. Theoretical studies of electric double layers on curved surfaces further show that convex and concave interfaces of the same material can have slightly different capacitances and ion distributions [84–87]. We therefore hypothesize a small curvature-induced asymmetry in mean surface charge,  $\Delta\sigma = \sigma_{\text{out}} - \sigma_{\text{in}} \neq 0$  (sign schematic). The resulting internal electric field is expected to be strongest where the shell is thinnest,  $|\mathbf{E}_{\text{thin}}| > |\mathbf{E}_{\text{thick}}|$ , which may favour defect coalescence in the thin cap.

▷ **Curvature-induced charge imbalance between the two interfaces.** The inner and outer LC–water interfaces are chemically identical (same PVA stabilizer and PBS composition), but they differ in both curvature and area: the outer interface is convex with radius  $R_{\text{out}}$  and larger area, whereas the inner interface is concave with radius  $R_{\text{in}} < R_{\text{out}}$  and smaller area. Theoretical studies of EDLs on curved electrodes and in porous materials show that convex and concave surfaces of the same material can host double layers with measurably different capacitances and ion-density profiles, even at the same applied potential [84–87]. Motivated by these results, we hypothesize that the combined effect of opposite curvature signs, different radii, and PVA adsorption leads to a small but finite difference between the mean surface charge densities at the two interfaces,  $\sigma_{\text{out}} \neq \sigma_{\text{in}}$ . To first approximation, we treat these mean surface charge densities as azimuthally uniform and focus on how local variations in thickness and permittivity modulate the local charge imbalance  $\Delta\sigma(\mathbf{r})$  around the mean values. This assumption is not derived from a full Poisson–Boltzmann calculation, but it provides a minimal working model consistent with the schematic in Fig. 7.4.

▷ **Potential drop and field distribution.** Because both aqueous phases are reasonably conducting, the inner and outer LC–water interfaces can be treated as equipotential surfaces on experimental time scales. The potential difference  $\Delta V$  between them is therefore, to a good approximation, independent of position along the shell. For a local capacitor element, the charge imbalance per unit area associated with this potential drop is

$$\Delta\sigma(\mathbf{r}) = \sigma_{\text{out}}(\mathbf{r}) - \sigma_{\text{in}}(\mathbf{r}) = \frac{C(\mathbf{r})}{A(\mathbf{r})} \Delta V = \varepsilon_0 \varepsilon_{\text{eff}}(\mathbf{r}) \frac{\Delta V}{d(\mathbf{r})}. \quad (7.4)$$

Equation (7.4) shows that, for fixed  $\Delta V$ , the charge imbalance per unit area is largest where the shell is thinnest and/or where  $\varepsilon_{\text{eff}}$  is enhanced, for instance inside defect

cores. The corresponding normal electric field is, to the same level of approximation,

$$|\mathbf{E}(\mathbf{r})| \simeq \frac{\Delta V}{d(\mathbf{r})}, \quad (7.5)$$

and is therefore strongest primarily in the thinnest regions. Thus, curvature and thickness gradients concentrate both charge and field near the thin top of the shell.

▷ **Electro-elastic coupling and defect migration.** The coupling of this field to the nematic degrees of freedom enters via the standard electrostatic free-energy density (cf. Sec. 2.9)

$$f_{\text{elec}} = -\frac{1}{2} \varepsilon_0 \Delta \varepsilon (\mathbf{n} \cdot \mathbf{E})^2. \quad (7.6)$$

For our purposes, the total shell free energy can be schematically written as  $F \simeq F_{\text{elastic}} + F_{\text{elec}} + F_s$ , where  $F_{\text{elastic}}$  is the Oseen–Frank bulk contribution (Sec. 2.4),  $F_{\text{elec}}$  is the volume integral of Eq. (7.6), and  $F_s$  the surface anchoring term (Sec. 2.5). The free energy is minimized when defect lines migrate towards regions where the electrostatic energy gain from aligning  $\mathbf{n}$  with  $\mathbf{E}$  outweighs the elastic cost of splay and bend. Because Eq. (7.5) implies that  $|\mathbf{E}|$  is largest near the thinnest part of the shell, the electrostatic term reinforces the thickness-driven defect migration reported previously for shells without added salt, rather than changing the direction of migration [54, 203, 204]. The new ingredient of this model is therefore not where defects accumulate (they still gather near the thinnest region), but how ionic strength and interfacial polarization can lower the energetic barrier for their partial coalescence.

▷ **Field-induced core rearrangements and defect mergers.** Although the tangential anchoring at the LC–water interfaces remains strong, the enhanced field in the shell interior near the thin pole can partially tilt the director away from purely tangential alignment, in close analogy to the bulk reorientation in a planar Frederiks transition where the surface director remains nearly fixed. In the wedge–twist picture of defect lines discussed above, such a normal field disfavors twist-dominated segments that keep  $\mathbf{n}$  far from  $\mathbf{E}$ , while favoring splay- and bend-dominated configurations

more closely aligned with the field. The resulting changes in line tension and core structure can reduce the repulsive interaction between neighboring  $+\frac{1}{2}$  defects, so that in PBS the same thickness gradient that yields four separated  $+\frac{1}{2}$  defects in distilled water now more readily permits partial mergers into effective  $+1$  boojums and  $+\frac{3}{2}$  surface defects, the latter likely corresponding to a  $+1$  boojum adjacent to a  $+\frac{1}{2}$  disclination line. This qualitative trend is consistent with simulations of field-driven nematic shells, which show that stronger aligning fields promote coalescence of  $+\frac{1}{2}$  defects into higher-valence defects and more general reconfigurations of the defect network (see Sec. 2.9.3) [53]. Related simulations for shells with displaced inner droplets demonstrate that external fields can reorganize the defect structure and modify defect valence and topology [204].

▷ **Implications and limitations.** Within this curvature-modulated capacitor picture, we expect that increasing the bulk salt concentration will strengthen the interfacial polarization and the effective double-layer capacitance, so that for a given asymmetry between the two interfaces the electric field magnitude  $|\mathbf{E}|$  in the thinnest region is enhanced according to Eq. (7.5). Through Eq. (7.6) a stronger normal field increases the energetic gain of configurations with locally more radial director and thus tends to lower the barrier for defect mergers, providing a possible explanation for the ionic-strength dependence of defect statistics in Fig. 7.1. We emphasize that this is a deliberately minimal, qualitative model: a full treatment would require solving the coupled Poisson–Boltzmann and nematostatics problem in the actual shell geometry, including curvature-dependent EDL structure, which is beyond the scope of this thesis. Instead, the present framework is intended as a physically motivated working hypothesis that rationalizes our observations and suggests directions for future, more quantitative modeling.

### 7.1.3 Effect of PBS ions on PVA anchoring

As a complementary mechanism, ions in PBS may screen the interfacial electric double layer and modify the hydration and hydrogen-bonding environment of the adsorbed PVA layer at the LC–water interface, thereby reducing the effective anchoring coefficients  $W_\Theta$  and/or  $W_\phi$  that enter the Rapini–Papoular surface energy density  $f_s$  in Eq. (2.6). In the notation of Eq. (2.3), where  $F_{\text{Frank}}$  denotes the Oseen–Frank bulk elastic energy and  $F_s = \int_{\partial V} f_s dA$  the surface anchoring contribution, such a change would correspond to lowering  $F_s$  and thus shifting the balance between bulk elastic ( $F_{\text{Frank}}$ ), electrostatic ( $F_{\text{elec}}$ ), and surface terms. Equivalently, the anchoring extrapolation lengths  $\ell_\Theta = K_{\text{eff}}/W_\Theta$  and  $\ell_\phi = K_{\text{eff}}/W_\phi$  (Eq. (2.7)) are expected to increase in PBS, so the director in the shell interior is less tightly constrained by the tangential easy axis imposed by PVA. **In practice, such a reduction in anchoring strength is expected to favor defect mergers, because the elastic penalty associated with locally more radial director configurations around +1 defects becomes less severe when anchoring is weaker.**

## 7.2 Impact of LPS on LC ordering in shells

Motivated by droplet-based endotoxin sensors using 5CB [81, 138, 139] and by the discovery of lipid islands on liquid-crystal shells by Sharma *et al.* [175], we next examined how amphiphilic LPS influences the director field in 5CB shells. In droplets, picogram-per-milliliter concentrations of LPS have been shown to trigger bipolar-to-radial transitions by accumulating at the LC–water interface and, in some cases, at defect sites [81, 138]. In shells, however, the presence of two curved interfaces, a thickness gradient, and pre-existing topological defects introduces additional ways for LPS adsorption to couple to curvature and topology.

Here we focus on LPS from *E. coli* O127:B8. Its three-part molecular architecture (lipid A, core oligosaccharide, O-antigen), aggregation behavior in aqueous buffers,

and relevance for endotoxin testing were summarized in Secs. 3.4.4 and 3.4.5. In what follows, we only recall those features that are directly relevant for interpreting the shell experiments, namely the tendency of LPS to form bilayer-derived aggregates at very low critical aggregation concentrations, and its ability to impose strong anchoring at LC–water interfaces.

### 7.2.1 Shells without PVA: defect-seeded lipid islands

To probe LPS effects in the absence of polymer stabilizer, we produced 5CB shells without PVA, using only 5  $\mu\text{M}$  SDS in both inner and outer aqueous phases. These shells were mechanically fragile and remained stable for at most 8 h, but before rupture they developed interfacial islands at defects, which we tentatively attribute to LPS aggregation at the LC–water interface. Figure 7.5 shows a time series for a representative shell with inner phase “5  $\mu\text{M}$  SDS + 10  $\mu\text{g}/\text{mL}$  LPS in PBS” and outer phase “5  $\mu\text{M}$  SDS in PBS”. Initially, the shell exhibits a bipolar-like texture with one +1 defect in the field of view (its antipodal partner lies outside the imaging area). At this defect, a spindle-shaped microdomain (“island”) nucleates, which we interpret as an LPS-rich patch at the LC–water interface. The defect–island pair then migrates toward the thicker hemisphere of the shell, consistent with motion guided by the thickness gradient; before collapse, the shell evolves into a hybrid-like texture without visible islands.

This behavior indicates that LPS tends to accumulate at defect cores, in agreement with the defect-localized endotoxin mechanism inferred for LC droplets [81, 138]. By relocating both the high-splay +1 defect and its associated LPS-rich island into regions of greater shell thickness, where curvature-induced elastic distortions and line tension are reduced, the shell lowers its combined elastic and interfacial free energy. The resulting curvature-directed drift is qualitatively similar to the motion of phospholipid (DLPC) islands from thin to thick regions on PVA-stabilized shells reported by Sharma *et al.* [175].

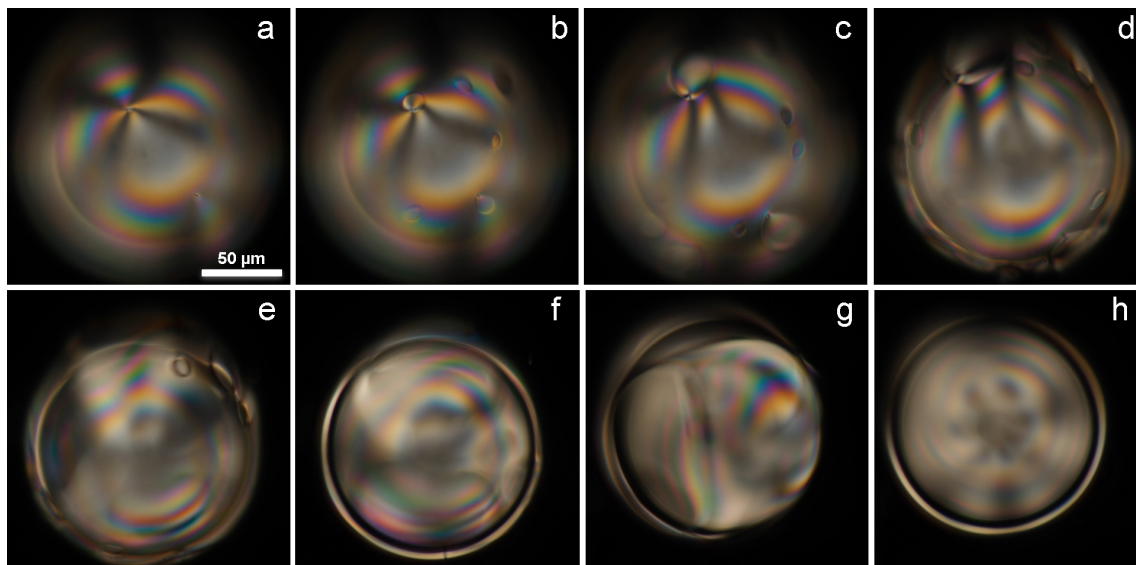


Figure 7.5: **LPS-induced island formation on a 5CB shell without PVA.** Time series of a 5CB shell with inner phase: 5  $\mu\text{M}$  SDS and 10  $\mu\text{g/mL}$  LPS in PBS; outer phase: 5  $\mu\text{M}$  SDS in PBS. A +1 defect nucleates a lipid-rich island that subsequently migrates toward the thicker hemisphere. Time after production: (a) 6 min, (b) 8 min, (c) 11 min, (d) 16 min, (e) 28 min, (f) 35 min, (g) 4 h, (h) 8 h (shortly before shell rupture). White scale bar in (a): 50  $\mu\text{m}$ ; same magnification in all panels.

When both inner and outer phases contained 100  $\mu\text{g/mL}$  LPS in PBS and no PVA, we observed a mixture of tangentially aligned shells and shells with hybrid alignment. Hybrid shells were identified by a single defect at the center of the upper pole, indicating approximately radial alignment on one side and tangential alignment on the other. This apparent asymmetry arises even though the bulk compositions of the two aqueous phases are nominally identical. A simple interpretation is that the two interfaces do not experience identical adsorption conditions:

- **Curvature-dependent adsorption.** The inner (concave) and outer (convex) LC–water interfaces have different radii of curvature and areas. As for other amphiphiles, LPS is expected to partition unevenly between interfaces with different curvature and area, enriching at the interface where its molecular packing is more favorable.
- **Asymmetric adsorption kinetics.** During microfluidic production, the outer interface is in direct contact with the flowing continuous phase, whereas the

inner interface is shielded by the LC layer. This may cause the outer interface to acquire LPS more quickly than the inner one, establishing asymmetric anchoring before the system equilibrates.

- **Hydrodynamic concentration gradients.** Shear and extensional stresses in the microfluidic device may generate transient gradients in LPS concentration near the interfaces. We hypothesize that if one interface effectively crosses an anchoring threshold earlier than the other, the shell may become kinetically trapped in a hybrid state.

As a result, some shells adopt a hybrid alignment even though the inner and outer aqueous phases are nominally identical in bulk composition at the time of production.

### 7.2.2 Slow LPS island nucleation in PVA-stabilized shells

In related work, Sharma *et al.* [175] showed that on PVA-stabilized shells phospholipid (DLPC) islands form once the lipid surface coverage exceeds a critical value and then grow and migrate along shell-thickness gradients. Motivated by this, we examined LPS-driven island formation in PVA-stabilized 5CB shells. In our experiments, shells were produced with inner phase “0.025 wt.% PVA (13–23 kg mol<sup>−1</sup>, 87–89 % hydrolyzed) in PBS” and outer phase “0.0125 wt.% PVA in PBS + 0.25 mg mL<sup>−1</sup> LPS”. Shells were stored in glass capillaries with rectangular cross-sections and monitored over three weeks at RT.

Initially, all shells exhibited uniform tangential alignment with the usual eight-brush (“flower-like”) texture, and no discrete LPS-rich islands were visible. Over the course of several days to weeks, however, lipid-rich islands nucleated and grew on a subset of shells, as illustrated in Fig. 7.6 for a representative 5CB shell imaged 14–21 days after first exposure to LPS, with islands already visible in the earliest frame. The onset times varied widely: some shells developed islands after about 4–5 days, others only after more than 10 days, and many remained island-free throughout the

21-day observation period. Typically only  $\sim 5\text{--}10\%$  of shells in a given capillary

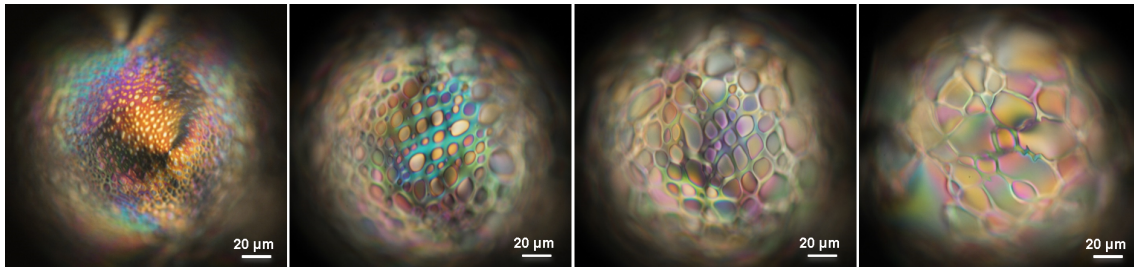


Figure 7.6: **Slow LPS island nucleation on PVA-stabilized 5CB shells.** Inner phase: 0.025 wt.% PVA ( $13\text{--}23\text{ kg mol}^{-1}$ , 87–89 % hydrolyzed) in PBS. Outer phase: 0.0125 wt.% PVA in PBS +  $0.25\text{ mg mL}^{-1}$  LPS. Time after first exposure of shells to LPS in the outer phase: (a) 14 days, (b) 15 days, (c) 17 days, (d) 21 days. Islands appear preferentially near the thinnest poles and grow over time.

developed clearly visible islands. Thus, in contrast to the DLPC system of Ref. [175], island nucleation in our LPS/PVA system is much slower and more heterogeneous from shell to shell.

In the DLPC system of Sharma *et al.*, islands appear once the local lipid surface coverage exceeds a critical fraction, and then grow and coarsen under the combined influence of lipid phase separation and nematic elasticity [175]. Our LPS experiments differ in time scale and heterogeneity: the first islands appear only after several days and only on a minority of shells, yet the qualitative sequence “no visible islands  $\rightarrow$  island nucleation  $\rightarrow$  island growth and migration toward thicker regions” is similar. We therefore interpret our observations as being consistent with a threshold-coverage scenario for LPS on PVA-stabilized shells, in which only shells that stochastically reach a sufficiently high local surface coverage within the experimental time window nucleate visible islands, even though the critical LPS surface coverage is not determined explicitly. Within this picture, competition between LPS and PVA for interfacial sites naturally slows the arrival of LPS at the LC–water interface and broadens the spread of times at which islands first appear.

## Brief discussion and assumptions

At room temperature, 5CB shells exposed to amphiphilic LPS can develop spindle-shaped islands at the LC–water interface whose nucleation, growth, and migration qualitatively resemble the DLPC islands on LC shells reported by Sharma *et al.* [175]. Despite this visual similarity, the molecular characteristics of LPS call for a distinct interpretation. As summarized in Secs. 3.4.4 and 3.4.5, LPS is a multitailed, highly charged glycolipid that self-assembles into bilayer-derived lamellae and vesicles at very low critical aggregation concentrations, with aggregate morphology strongly modulated by ions and surfactants [111, 119]. The assumptions below outline a working picture that is consistent with both our shell observations and this broader literature.

- **Large effective normal anchoring strength.** LPS contains multiple anionic phosphate, carboxylate, and sugar groups on a bulky oligosaccharide headgroup, which can form dense networks of hydrogen bonds and ion bridges with interfacial water and counterions. It is therefore plausible that condensed LPS-rich patches favor nearly normal alignment of the LC at the interface, in analogy to the strong anchoring inferred for phospholipid islands on LC shells [175]. A large anchoring coefficient  $W$  reduces the characteristic elastic length  $d_{\min} \simeq K/W$ , which would allow islands to remain stable even when the local shell thickness in the thinnest hemisphere is comparable to this length, while still experiencing a drive to migrate into slightly thicker regions where the elastic cost of hybrid (normal/tangential) alignment is lower.
- **Slow nucleation consistent with a threshold in local LPS coverage.** Light-scattering and fluorescence-correlation studies show that LPS forms premicellar oligomers below an apparent critical micelle concentration and larger micellar aggregates above it [111, 205]. Together with the presence of an adsorbed PVA layer, this suggests that LPS reaches the LC–water interface

slowly and in a polydisperse manner. By analogy with DLPC monolayers on LC shells, where islands appear once the local lipid coverage exceeds a critical value and then grow quickly [175], and with other liquid-crystal biosensors that respond once a critical surface coverage of amphiphile is reached [183], we assume that LPS islands nucleate only when the local surface coverage first surpasses a threshold. Because shell geometry, local PVA coverage, and LPS transport paths vary from shell to shell, it is plausible that only a minority of shells attain this threshold within the experimental time window, consistent with our preliminary observations of typically several-day delays and a low ( $\sim 5\%$ ) fraction of initially island-bearing shells.

- **Possible cooperative growth after nucleation.** Once a supercritical LPS-rich patch has formed, normal anchoring within the island imposes a local elastic distortion of the director field. As argued for DLPC shells [175], the system can reduce its overall free energy by confining this distortion to a smaller area with higher LPS coverage. This mechanism would tend to accelerate island growth after nucleation. In our experiments, islands that do appear indeed grow perceptibly between imaging sessions, but we did not quantify area growth rates or elastic fields, so any cooperative “elastic feedback” should be regarded as a plausible but unproven interpretation.
- **Polydisperse coverage and coarsening.** Because LPS is supplied as aggregates with a broad size distribution, the instantaneous surface coverage  $\varepsilon_p$  is expected to vary strongly in space and between shells [111, 205]. This scenario would naturally produce a wide range of initial island sizes. Once islands exist, line tension and nematic elasticity may favor coarsening via Ostwald ripening and the merging of nearby islands, similar to the tactoid-like coarsening observed for DLPC islands [175].
- **Competition with PVA at the interface.** Even at 0.01–0.025 wt.% PVA,

a polymeric layer is expected to adsorb at the 5CB–water interface and to maintain tangential anchoring, as discussed in Sec. 3.3.3. LPS is therefore likely to displace or intercalate into the PVA layer to gain access to the interface. This competition can significantly slow the build-up of LPS surface coverage and effectively raise the threshold for island nucleation, helping to explain why island formation in PVA-stabilized shells is much slower than in PVA-free shells and than in the DLPC system of Sharma *et al.* [175].

### 7.3 Summary and outlook

This chapter examined how aqueous electrolytes and bacterial lipopolysaccharides (LPS) influence the director fields and defect configurations of nematic 5CB shells stabilized by PVA.

In the first part, we focused on the role of PBS ions. Histogram analysis showed that replacing distilled water with PBS substantially changes the defect statistics: the fraction of tetravalent shells with four  $+\frac{1}{2}$  surface disclinations around the thinnest pole is reduced, while textures with more  $+1$  defects become more common, including the occasional appearance of director field configurations with  $+\frac{1}{2}$  and  $+\frac{3}{2}$ . These observations motivated a curvature-modulated interfacial “capacitor” model in which the two LC–water interfaces carry slightly different mean surface charge densities and, together with the anisotropic dielectric response of 5CB, generate electric fields that are strongest in the thinnest regions of the shell. In this picture, the electric field reinforces the thickness-driven migration of defects toward the thin pole and lowers the energetic barrier for their partial coalescence into higher-valence defects. As a complementary effect, PBS ions may screen charged or polar groups within the adsorbed PVA layer, thereby reducing the effective tangential anchoring and further facilitating defect mergers. Although deliberately minimal and qualitative, this capacitor-based framework provides a plausible route by which ionic strength

and curvature together tune defect topology in nematic shells and suggests clear targets for future numerical work that couples Poisson–Boltzmann electrostatics to nematostatics in the full shell geometry.

In the second part, we turned to endotoxin (LPS) and its impact on nematic ordering. Control experiments on 5CB droplets reproduced the well-known bipolar-to-radial transition at LPS levels down to at least 100 pg/mL, consistent with previous droplet-based LC biosensors [81, 138, 139]. When LPS was introduced to 5CB shells without PVA, +1 defects frequently seeded lipid-rich islands that remained bound to the defects and migrated from the thinnest toward the thickest hemisphere. This behavior is consistent with LPS preferentially accumulating at defect cores and with a reduction of the total elastic and interfacial free energy when strongly anchoring LPS-rich domains are relocated into regions where curvature-induced distortions are less costly. At higher LPS concentrations in PVA-stabilized shells, islands did not appear immediately. Instead, LPS first bound to a small subset of shells in a capillary, and lipid islands appeared only there, after delays of several days. A simple, preliminary interpretation is that once certain shells begin to accumulate LPS, they may locally deplete the surrounding solution, creating a concentration gradient that drives additional LPS toward those same “seeded” shells and accelerates further adsorption. Because the adsorbed PVA layer competes with LPS for interfacial sites, this build-up of LPS surface coverage is expected to be slow and heterogeneous in time, so that within a few days only a minority of shells appear to reach the coverage required for visible island formation. This working picture is qualitatively consistent with the aggregation pathways and critical aggregation concentrations reviewed in Sec. 3.4.5.

Taken together, these results highlight nematic 5CB shells as a versatile platform in which electrolyte composition, curvature, shell thickness, and amphiphile chemistry jointly control defect organization and optical response. The interfacial capacitor model suggests that ionic strength can be used to tune defect coalescence

by modulating interfacial charge distributions and internal fields, while the LPS experiments show that amphiphile adsorption can generate defect-bound islands whose nucleation and migration appear to be sensitive to both interfacial competition (with PVA) and shell geometry. Future work combining direct measurements of surface charge densities and electric fields, quantitative assays of LPS surface coverage (for example, using fluorescently labeled LPS analogs), and systematic variation of PBS, SDS, and PVA concentrations will be important to test and refine the proposed mechanisms. Such studies should help bridge the gap between the qualitative picture developed here and predictive models, and could guide the design of shell-based liquid-crystal systems for applications ranging from reconfigurable optics to endotoxin and amphiphile sensing at curved LC interfaces.



## Chapter 8

# Overall conclusions and outlook

This thesis has examined how nonionic polymer stabilizers and ionic solutes jointly influence the optical response, defect dynamics, stability, and biochemical sensitivity of nematic liquid-crystal shells. Using reflection-mode POM, time-resolved defect tracking, lifetime measurements, and controlled electrolyte/LPS perturbations, we probed how shell curvature, gravity-induced thickness gradients, PVA chemistry, and ionic environments act together to organize director fields and defects.

We showed that shell birefringence can support polarization-controlled total internal reflection in achiral nematic shells. Under suitable incident polarization, tangentially anchored shells exhibit bright antipodal spots in reflection, whereas radially anchored shells give rotating bright arcs. These signatures are consistent with birefringence-modulated total internal reflection along guided paths inside the shell and are strongly polarization dependent. Because they can be resolved at modest numerical aperture and magnification, they are compatible with low-cost, reflection-only imaging platforms and indicate that nematic shells can function not only as samples for transmission POM but also as compact optical elements whose director configurations can be inferred from reflection images alone.

We then quantified how gravity-induced thickness gradients and PVA chemistry affect director-field annealing in tangentially aligned 5CB shells. For shells stabilized

with moderately hydrolyzed PVA (87–89 %), buoyancy off-centers the inner droplet and creates a wall-thickness gradient that drives  $+1$  and  $+\frac{1}{2}$  defects toward the thinner hemisphere. As the director field relaxes toward a lower-energy configuration, the pairwise separations between defects decrease approximately exponentially in time and approach finite plateau values, which define characteristic annealing times that depend on the mean wall thickness. In contrast, shells stabilized with highly hydrolyzed PVA ( $\geq 98\%$ ) also exhibit tangential anchoring but essentially no detectable annealing: numerous  $\pm\frac{1}{2}$  defects remain nearly immobile over experimental time scales. This contrast is consistent with a picture in which moderately hydrolyzed PVA forms a more mobile interfacial layer, whereas highly hydrolyzed PVA yields a more cohesive, possibly partially crystalline interfacial film that pins the director, making nematic shells sensitive optical reporters of interfacial polymer organization.

Next, we investigated the lifetimes of shells stabilized by very low concentrations of low- and high-molar-mass PVA and developed a simple kinetic description for shell collapse and fusion. Shell populations do not decay as a single exponential: at low stabilizer concentrations, popping rates accelerate as inner cores migrate upward, shells thin at their upper poles, and defects merge. Rare fusion events between shells or between shells and droplets occur when stabilizer coverage is minimal. A coupled kinetic scheme that includes shell collapse, shell–droplet fusion, shell–shell fusion, and subsequent rupture of mixed shells captures the dominant decay and qualitatively accounts for the observed fusion pathways. Within this framework, the rate constant for the dominant shell–to–droplet popping process can be fitted to the experimental decay curves, and representative, order-of-magnitude values for the much rarer fusion events can be used to explore how interfacial polymer coverage may influence encounter frequencies and shell lifetimes.

Finally, we examined how added electrolytes and bacterial endotoxin (LPS) reshape director-field textures and interfacial organization in PVA-stabilized 5CB shells. Replacing distilled water with PBS ( $I \approx 0.17$  M) shifts defect statistics from

predominantly tetravalent textures with four  $+\frac{1}{2}$  defects toward configurations with more  $+1$  defect pairs and occasional  $+\frac{3}{2}$ -like patterns. To rationalize these trends, we proposed a curvature-selective interfacial-capacitor hypothesis, in which a small asymmetry between the inner and outer electrical double layers produces a thickness-modulated internal field that can promote defect coalescence in the thinnest regions of asymmetric shells. In the presence of LPS, preliminary observations indicate that lipid-rich microdomains can nucleate at or near defect cores and then migrate along thickness gradients, consistent with a reduction in combined elastic and interfacial free energy. In PVA-stabilized shells, this process is slow and heterogeneous, with only a subset of shells developing visible islands over several days, underscoring the role of interfacial competition between PVA and LPS.

Overall, these results indicate that nematic LC shells are tunable soft-matter systems in which nonionic stabilizers set anchoring and mechanical robustness, gravity defines a preferred direction for thickness gradients and defect motion, and ionic solutes (PBS, LPS) provide additional handles on defect topology and interfacial morphology. The combined optical, kinetic, and electrostatic perspectives developed here point toward using LC shells as reconfigurable optical elements whose textures can be dynamically adjusted and as platforms for LC-based biosensing in which biochemical interactions are transduced into changes in defect configurations and interfacial domains. Future work that more tightly couples electrostatics and nematostatics, integrates photopolymerizable or elastomeric nematics, and tailors specific biomolecular interactions at one or both LC–water interfaces could more directly connect the physics explored in this thesis to applications in photonics, biosensing, and responsive materials.



# Appendices



## Appendix A

# Microfluidic device fabrication and shell production

### A.1 Capillary preparation and device assembly

The following sections outline each step involved in fabricating a microfluidic device, presented in the same order as the process itself.

#### A.1.1 Cutting capillaries

The fabrication of a microfluidic device begins with the preparation of glass capillaries. A long (10 cm) cylindrical capillary with an outer diameter of approximately 1 mm ( $\pm 0.01$  mm) is selected. This capillary is then placed into a micropipette puller (e.g., P-100, Sutter Instrument), which uses heat to soften the glass and simultaneously applies tension to pull the tube. This process produces two tapered capillaries with pointed ends.

To obtain the desired orifice size, the tapered ends of the capillaries are refined using a microforge (e.g., Narishige MF-900). In this step, the capillary is secured in a holder and aligned near a heated glass element (Fig. A.1a). By adjusting the position and applying heat, the capillary is selectively softened and then separated

at a precise location, yielding a clean break (Fig. A.1b).

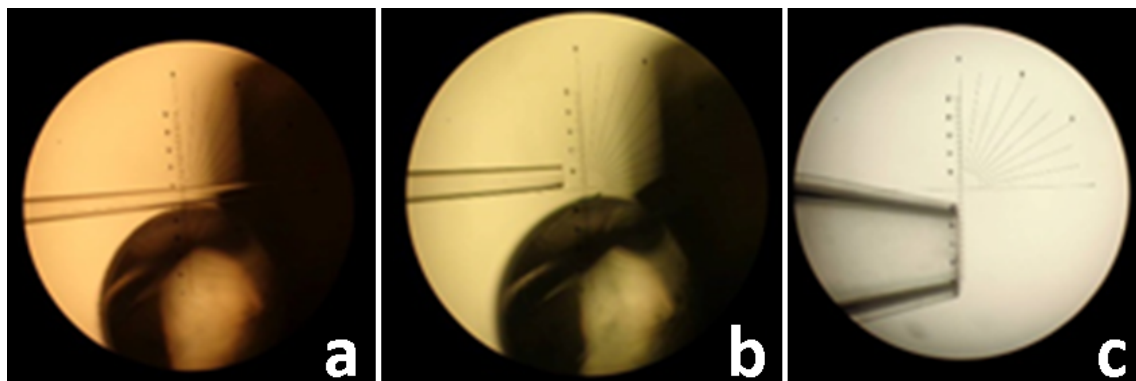


Figure A.1: Preparing and checking the ends of capillaries for the microfluidic device. (a) - the end of the inlet capillary installed in a microforge, before cut, and (b) - after applying the local heat and breaking it. (c) - the end with an opening of outlet (collection) capillary, cut, and then polished using a sandpaper.

For a complete microfluidic setup (Fig. A.2a), two capillaries with different orifice diameters are required. One functions as the inlet, with an orifice diameter between  $60\text{--}80\text{ }\mu\text{m}$ , and the other serves as the outlet (Fig. A.2b), with an orifice diameter ranging from  $150\text{--}300\text{ }\mu\text{m}$ , depending on the needed maximum possible diameter of shells. Since the microforge is limited to creating openings smaller than approximately  $100\text{ }\mu\text{m}$ , larger orifices are produced by manually expanding the cut using fine sandpaper (Fig. A.1c).

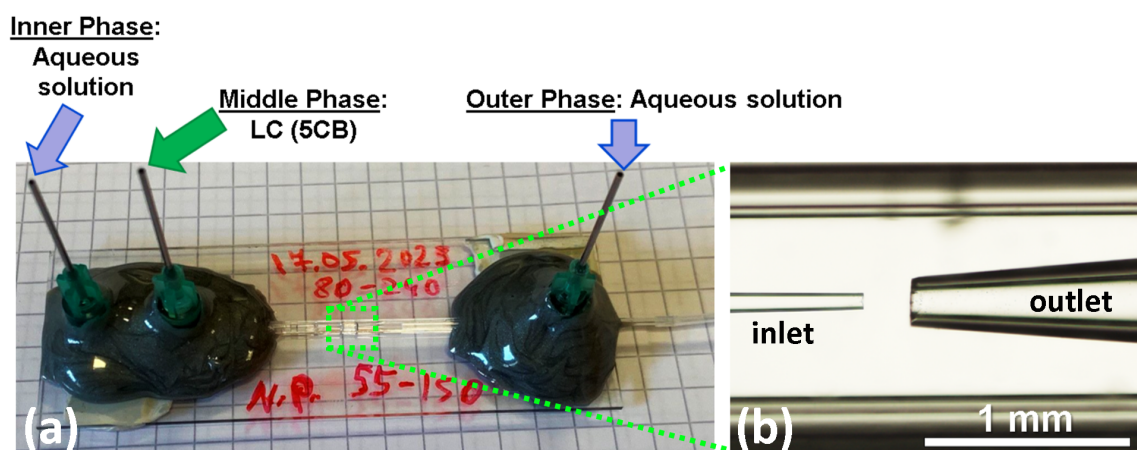


Figure A.2: Homemade glass capillary microfluidic device: (a) device overview with cannulas for the inner, middle, and outer phases; (b) junction region with inlet and outlet (collection) capillaries.

The next stage involves the chemical treatment of the capillaries to tailor their surface properties. This step is described in the following section.

### A.1.2 Surface treatment of capillaries

To ensure proper flow behavior in the microfluidic device, the capillary surfaces must be modified to have selective wettability: the outer walls of inlet capillaries should be hydrophobic, while the inner walls of outlet capillaries are preferably hydrophilic.

Before applying any surface-specific chemical treatments, the capillaries undergo plasma treatment. Using a handheld plasma generator, we scan the glass surfaces with plasma. This step provides two key advantages: it effectively removes residual organic contaminants without damaging the glass structure, and it enhances the density of hydroxyl (OH) groups on the surface, promoting better chemical bonding in subsequent treatments.

To make the outer surface of the inlet capillary water-repellent, a hydrophobic coating is applied via silanization. This involves immersing the capillary in a dilute solution of an alkoxysilane compound, which forms a covalently bonded monolayer on the glass. Plasma treatment promotes the formation of Si–O–Si linkages between the silica surface and the alkoxysilane headgroups, resulting in a surface coated with nonpolar fluorinated alkyl tails. This transformation reduces the surface energy and provides hydrophobicity. For this step, we prepare a 3 vol.% solution of nonafluorohexyltriethoxysilane (SIN6597.65) in deionized water and submerge the capillaries for 10–15 minutes. Afterward, they are rinsed thoroughly with DI water and kept at 120 °C for one hour to complete the silanization.

When needed, the inner surface of the outlet capillary is treated hydrophilic to encourage water to uniformly wet the glass, thereby minimizing adhesion of the flowing LC shells or droplets. For this purpose, we prepare a hydrophilic treatment solution consisting of 2 vol.% methoxy(triethylenoxy)propyltrimethoxysilane (SIM6493.4), dissolved in a mixture of 10 vol.% isopropanol and 88 vol.% DI water. The solution

is introduced into the capillaries via syringe and allowed to sit for 30 minutes. After treatment, the capillaries are flushed twice with DI water to remove residual reagents. The resulting silane layer presents triethylene glycol units toward the aqueous phase, giving the inner wall a hydrophilic, PEG-like character.

## A.2 Shell production

LC shells, each containing and surrounded by aqueous phases of PVA or surfactant, were produced using a coaxial glass capillary microfluidic setup, following the method of Weitz [163]. The inner aqueous phase, immiscible with the LC middle phase, was injected through a tapered cylindrical capillary (typically 0.07 mm inner orifice diameter), which had been inserted into a square cross-section capillary (Fig. A.3).

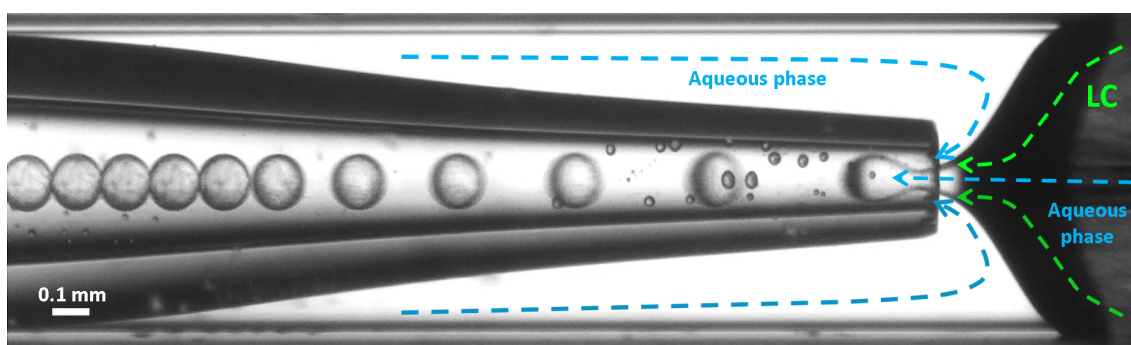


Figure A.3: Bright-field microscopy image of LC shell production. Blue dashed arrows represent the direction of the inner and outer aqueous phases, whereas green arrows represent the middle LC phase.

The LC phase flowed in the same direction around the inlet capillary inside the square channel. Meanwhile, the continuous phase, identical in composition to the inner aqueous solution, was driven in the opposite direction through the same square cross-section capillary. At suitably low flow rates, the LC phase broke off near the tip of the inner capillary in a dripping regime, forming double emulsions (LC shells) that were transported by the continuous phase. This three-phase system was hydrodynamically flow-focused into an outlet (collection capillary) with an inner orifice diameter of  $\sim 0.18$  mm. All liquids were held in closed vials and pressurized

with high precision using a Fluigent MFCS-EZ pneumatic flow controller, enabling stable flow through microfluidic tubing toward the coaxial capillary setup. Shells were typically collected and imaged in rectangular glass capillaries with internal dimensions  $0.20 \times 2.00 \text{ mm}^2$ .

**Dripping regime and Rayleigh–Plateau breakup.** At suitably low flow rates and capillary numbers, the LC middle phase emerging from the inner capillary forms a cylindrical thread that breaks up into droplets via the classical Rayleigh–Plateau capillary instability [206]. In the simplest case of an unconfined jet, small azimuthally symmetric perturbations of the thread radius grow when their wavelength exceeds the jet circumference, i.e. when  $\lambda > 2\pi R$ , and surface tension then drives the fluid to reorganize into nearly spherical droplets to minimize interfacial area. In the confined coaxial microfluidic geometry used here, the same capillary-driven breakup of the middle phase, combined with shear from the continuous phase, produces monodisperse water–LC–water double emulsions in the dripping regime, as demonstrated in the microcapillary device of Utada *et al.* [163] and in related microfluidic-emulsion studies.



## Appendix B

# Counting shells and droplets

To quantify LC shells and droplets, we implemented an automated Python image-analysis algorithm (outlined in Listing B.1). The workflow comprises: (i) preprocessing (BGR→grayscale conversion and median blurring to suppress noise), (ii) gradient-based Canny edge detection and (iii) circular-object detection via the Hough Circle Transform across radius ranges corresponding to shells and droplets; an example is shown in Fig. B.1. Although effective, counting along  $\sim 3$  cm capillaries remains time-consuming because it requires non-overlapping video frames or photographs without repeated segments. In practice, the detection thresholds—radii of objects as well as gradient/Canny and Hough parameters—must often be tuned to maximize detection accuracy.

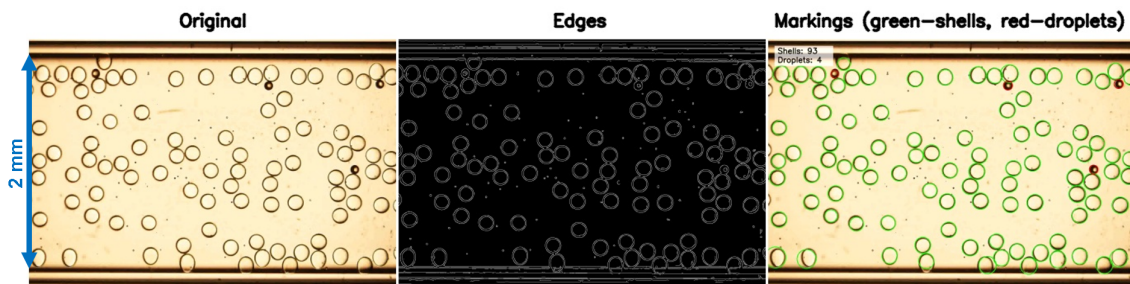


Figure B.1: Representative frame. Left: bright-field original. Middle: a preprocessing stage (grayscale + median blur). Right: final detections using the Hough Circle Transform, with shells (93, green) and droplets (4, red) overlaid after applying gradient-, diameter-, and additional thresholding criteria.

The following base of our script detects and annotates circular LC objects using Canny edge detection followed by Hough-circle transform. It relies on OpenCV (`cv2`) for image I/O and vision operations, NumPy for array handling, and `os` for file management. In addition, the script generates a stepwise report in a three-panel collage format. Radius values in pixels, Canny/Hough thresholds, and optional morphology toggles can be adjusted to suit different micrographs.

Listing B.1: LC circle detection &amp; counting in Python

```

1  import cv2, numpy as np, os  # OpenCV for computer vision operations
    ↪ (color convert, blur, edges, HoughCircles, drawing); NumPy for
    ↪ arrays; os for file Input/Output (I/O)
2  def process_image(
3      image_path: str,
4      out_dir: str = "results",
5      # Canny + Hough tunables
6      canny_low: int = 50,
7      canny_high: int = 100,
8      dp: float = 1.0,
9      min_dist: int = 32,
10     hough_param1: int = 50,
11     hough_param2: int = 19,
12     min_radius: int = 10,
13     max_radius: int = 36,
14     # radius bands (px): droplets = smaller, shells = larger
15     droplet_band: tuple[int, int] = (11, 23),
16     shell_band: tuple[int, int] = (24, 35),):
17     """
18     Detect circular LC objects (shells vs. droplets) using Canny +
    ↪ HoughCircles,
19     draw per-object IDs, and overlay a compact count panel.

```

```
20     Returns: (shell_count, droplet_count)
21     """
22     os.makedirs(out_dir, exist_ok=True)
23
24     # --- load & preprocess ---
25     img = cv2.imread(image_path)                # BGR in OpenCV
26     if img is None:
27         raise IOError(f"Could not read image: {image_path}")
28     gray = cv2.cvtColor(img, cv2.COLOR_BGR2GRAY)
29     blur = cv2.medianBlur(gray, 5)
30     edges = cv2.Canny(blur, canny_low, canny_high)
31     cv2.imwrite(os.path.join(out_dir, "edges.jpg"), edges)
32
33     # --- detect circles ---
34     circles = cv2.HoughCircles(
35         edges, cv2.HOUGH_GRADIENT,
36         dp=dp, minDist=min_dist,
37         param1=hough_param1, param2=hough_param2,
38         minRadius=min_radius, maxRadius=max_radius)
39
40     # --- classify + annotate ---
41     droplet_min, droplet_max = droplet_band
42     shell_min, shell_max = shell_band
43     annotated = img.copy()
44     shell_count = droplet_count = 0
45     if circles is not None:
46         circles = np.uint16(np.around(circles[0]))
47         for (x, y, r) in circles:
48             if droplet_min <= r <= droplet_max:
49                 droplet_count += 1
```

```

50         color, label = (0, 0, 255), f"D{droplet_count}" # red
51     elif shell_min <= r <= shell_max:
52         shell_count += 1
53         color, label = (0, 255, 0), f"S{shell_count}" # green
54     else:
55         continue
56     cv2.circle(annotated, (int(x), int(y)), int(r), color, 2)
57     # outlined label for readability
58     cv2.putText(annotated, label, (int(x) - 10, int(y) - 10),
59                 cv2.FONT_HERSHEY_SIMPLEX, 0.8, (255, 255, 255),
60                 ↪ 3, cv2.LINE_AA)
61     cv2.putText(annotated, label, (int(x) - 10, int(y) - 10),
62                 cv2.FONT_HERSHEY_SIMPLEX, 0.8, (0, 0, 0), 2,
63                 ↪ cv2.LINE_AA)
64
65     else:
66         print("No circles detected. Consider tuning
67         ↪ thresholds/parameters.")
68
69     # --- small on-image count panel ---
70     panel_x, panel_y, panel_w, panel_h = 20, 20, 230, 70
71     H, W = annotated.shape[:2]
72     panel_w = min(panel_w, max(0, W - panel_x))
73     panel_h = min(panel_h, max(0, H - panel_y))
74     cv2.rectangle(annotated, (panel_x, panel_y),
75                   (panel_x + panel_w, panel_y + panel_h),
76                   (255, 255, 255), -1)
77     cv2.putText(annotated, f"Shells: {shell_count}", (panel_x + 10,
78                 ↪ panel_y + 28),
79                 cv2.FONT_HERSHEY_SIMPLEX, 0.8, (0, 0, 0), 2,
80                 ↪ cv2.LINE_AA)

```

```
75     cv2.putText(annotated, f"Droplets: {droplet_count}", (panel_x + 10,
↪ panel_y + 58),
76                 cv2.FONT_HERSHEY_SIMPLEX, 0.8, (0, 0, 0), 2,
↪ cv2.LINE_AA)
77
78     # --- save & report ---
79     out_path = os.path.join(out_dir, "annotated.jpg")
80     cv2.imwrite(out_path, annotated)
81     print(f"Shells (r in [{shell_min},{shell_max}] px):
↪ {shell_count}")
82     print(f"Droplets (r in [{droplet_min},{droplet_max}] px):
↪ {droplet_count}")
83     print(f"Saved: {out_path}")
84     return shell_count, droplet_count
85
86 def main():
87     # Tweak thresholds/bands for your micrographs
88     image_path = "Shells.png"
89     shells, droplets = process_image(image_path)
90     print("Done.")
91 if __name__ == "__main__":
92     main()
```



## Appendix C

# Numerical solution of a coupled kinetic model for popping and fusion of 5CB shells

As derived in Sec. 6.2.4, we describe shell popping and fusion using a set of five coupled rate equations. The Python script below implements this model, solving the system numerically with SciPy's `solve_ivp` (adaptive Runge–Kutta, RK45) and plotting the time evolution of each species via Matplotlib. By adjusting the rate constants and initial conditions, we can systematically explore and compare different kinetic scenarios.

Listing C.1: Kinetic-model ODE solver in Python

```
1 import numpy as np, matplotlib.pyplot as plt
2 from scipy.integrate import solve_ivp
3
4 def rate_equations(t, y,  $\lambda_0$ ,  $\lambda_1$ ,  $\lambda_2$ ,  $\lambda_3$ ,  $\lambda_4$ ,  $\lambda_5$ ):
5     """
6     Compute derivatives for  $y = [N_s, N_d, N_S, N_{SS}, N_D]$ :
7      $N_s$  = initial shells [s]
```

```

8     Nd = droplets [d]
9     NS = shells [S] (s + d)
10    NSS = shells [SS] (s + s)
11    ND = big droplets [D]
12    """
13    Ns, Nd, NS, NSS, ND = y
14    dNs_dt = -λ0*Ns - λ1*Ns*Nd - λ4*Ns**2
15    dNd_dt = λ0*Ns - λ1*Ns*Nd - λ3*Nd**2
16    dNS_dt = λ1*Ns*Nd - λ2*NS
17    dNSS_dt = λ4*Ns**2 - λ5*NSS
18    dND_dt = λ2*NS + λ3*Nd**2 + λ5*NSS
19    return [dNs_dt, dNd_dt, dNS_dt, dNSS_dt, dND_dt]
20
21 def solve_system(N0, λ0, λ1, λ2, λ3, λ4, λ5, t_end=40,
22                 num_points=1000):
23     """Integrate the ODEs from t=0 to t_end starting with N0
24        shells."""
25     y0 = [N0, 0, 0, 0, 0]
26     t_eval = np.linspace(0, t_end, num_points)
27     sol = solve_ivp(
28         lambda t, y: rate_equations(t, y, λ0, λ1, λ2, λ3, λ4,
29                                     λ5),
30         [0, t_end], y0, t_eval=t_eval, method='RK45')
31     return sol
32
33 def main():
34     # Rate constants
35     λ0, λ1, λ2, λ3, λ4, λ5 = 0.1, 0.0002, 0.15, 1e-6, 1e-4,
36                               0.2
37     N0 = 1000.0 # number of initial shells #

```

```
34     sol = solve_system(N0,  $\lambda_0$ ,  $\lambda_1$ ,  $\lambda_2$ ,  $\lambda_3$ ,  $\lambda_4$ ,  $\lambda_5$ )
35     labels = ['Ns - shells [s]',
36              'Nd - droplets [d]',
37              'NS - shells [S] (s+d)',
38              'NSS - shells [SS] (s+s)',
39              'ND - droplets [D]']
40
41     plt.figure(figsize=(10, 6))
42     for i, lbl in enumerate(labels):
43         plt.plot(sol.t, sol.y[i], label=lbl)
44     plt.xlabel('Time [min]')
45     plt.ylabel('Quantity of species')
46     plt.legend()
47     plt.grid(True)
48     plt.tight_layout()
49     plt.show()
50
51 if __name__ == '__main__':
52     main()
```



## References

- [1] T. Sluckin, D. Demus, and H. Stegemeyer. *Crystals That Flow*. Taylor & Francis, London & New York, 2004.
- [2] F. Reinitzer. *Monatsh. Chem.*, 9:421–441, 1888.
- [3] O. Lehmann. *Z. Phys. Chem.*, 4:462–472, 1889.
- [4] P.-G. de Gennes and J. Prost. *The Physics of Liquid Crystals*. Oxford University Press, Oxford, 2 edition, 1993.
- [5] L. S. Hirst. *Fundamentals of Soft Matter Science*. CRC Press, Boca Raton, 2019.
- [6] J. W. Goodby. Microscopy applications | liquid crystals. In P. Worsfold, A. Townshend, and C. Poole, editors, *Encyclopedia of Analytical Science*, pages 74–84. Elsevier, Oxford, 2 edition, 2005.
- [7] J. Peatross and M. Ware. *Physics of Light and Optics*. Brigham Young University, Provo, Utah, 2025. 2015 edition; January 31, 2025 revision.
- [8] E. Hecht. *Optics*. Pearson Education Limited, Harlow, UK, 5th edition, 2017. Global Edition; adaptation of the North American edition (ISBN 978-0-13-397722-6).
- [9] M. Born. *Sitzungsber. Kgl. Preuss. Akad. Wiss. Berlin*, 30:614–650, 1916.

- 
- [10] R.-P. Pan, T.-R. Tsai, C.-Y. Chen, and C.-L. Pan. *J. Biol. Phys.*, 29:335–338, 2003.
- [11] D. A. Dunmur and K. Toriyama. *Liq. Cryst.*, 1(2):169–180, 1986.
- [12] M. R. Wilson and D. A. Dunmur. *Liq. Cryst.*, 5(3):987–999, 1989.
- [13] J. P. F. Lagerwall. *Liq. Cryst.*, 0(0):1–15, 2023.
- [14] I. Dierking. *Textures of Liquid Crystals*. WILEY-VCH Verlag GmbH Co. KGaA, 1 edition, 2003.
- [15] F. C. Frank. *Discuss. Faraday Soc.*, 25:19–28, 1958.
- [16] E. T. Samulski, D. Reyes-Arango, A. G. Vanakaras, and D. J. Photinos. *Nanomaterials*, 12(1):93, 2022.
- [17] C. W. Oseen. *Trans. Faraday Soc.*, 29(140):883–899, 1933.
- [18] M. Kl’eman and O. D. Lavrentovich. *Soft Matter Physics: An Introduction*. Springer, New York, 2003.
- [19] B. Jerome. *Rep. Prog. Phys.*, 54(3):391–451, 1991.
- [20] J.-B. Fournier and P. Galatola. Modeling planar degenerate wetting and anchoring in nematic liquid crystals. arXiv:cond-mat/0602543, 2006. Journal ref.: *Europhys. Lett.* 72 (2005) 403–409.
- [21] A. Rapini and M. Papoular. *J. Phys. Colloques*, 30(C4):54–56, 1969.
- [22] J. M. Brake and N. L. Abbott. *Langmuir*, 18(16):6101–6109, 2002.
- [23] J. Noh, K. Reguengo De Sousa, and J. P. F. Lagerwall. *Soft Matter*, 12(2):367–372, 2016.
- [24] J. F. Nye. *Physical Properties of Crystals: Their Representation by Tensors and Matrices*. Clarendon Press, 1957.

- [25] A. Echalier, R. L. Glazer, V. F"ul"op, and M. A. Geday. *Acta Crystallogr. D*, 60(4):696–702, 2004.
- [26] Edmund Optics. Understanding waveplates and retarders. Edmund Optics Knowledge Center (application note). Accessed 2025-09-04.
- [27] J. G. Delly. The michel-l'evy interference color chart — microscopy's magical color key. White paper, Hooke College of Applied Sciences, The McCrone Group, Westmont, IL, 2012.
- [28] K. Harth and R. Stannarius. *Front. Phys.*, 8:112, 2020.
- [29] P. E. Cladis and M. Kl'eman. *J. Phys.*, 33:591–598, 1972.
- [30] R. B. Meyer. Structural problems in liquid crystal physics. In R. Balian and G. Weill, editors, *Molecular Fluids*, Les Houches Summer School, Session XXV, 1973. Gordon and Breach, New York, 1976. Introduces the escape into the third dimension mechanism.
- [31] I. W. Stewart. *The Static and Dynamic Continuum Theory of Liquid Crystals*. Taylor Francis, London, 2004.
- [32] C. Long, X. Tang, R. L. B. Selinger, and J. V. Selinger. *Soft Matter*, 17(8):2265–2278, 2021.
- [33] V. Fr'eedericksz and A. Repiewa. *Z. Phys.*, 42(7):532–546, 1927.
- [34] V. Fr'eedericksz and V. Zolina. *Trans. Faraday Soc.*, 29:919–930, 1933.
- [35] G. E. Volovik and O. D. Lavrentovich. *Sov. Phys. JETP*, 58(6):1159–1166, 1983. Translated from *Zh. Eksp. Teor. Fiz.* 85, 1997–2008 (1983).
- [36] M. Humar and I. Muševič. *Opt. Express*, 19(21):19836–19844, 2011.
- [37] J. K. Whitmer, X. Wang, N. L. Abbott, and J. J. de Pablo. *Phys. Rev. Lett.*, 111(22):227801, 2013.

- 
- [38] X. Wang, D. S. Miller, J. J. de Pablo, and N. L. Abbott. *Soft Matter*, 10(44):8821–8828, 2014.
- [39] S. Mkaddem and Jr. Gartland, E. C. *Phys. Rev. E*, 62(5):6694–6705, 2000.
- [40] A. Majumdar. *Eur. J. Appl. Math.*, 23(1):61–97, 2012.
- [41] S. Kralj and S. Žumer. *Phys. Rev. A*, 45(4):2461–2470, 1992.
- [42] A. Bogi and S. Faetti. *Liq. Cryst.*, 28(5):729–739, 2001.
- [43] W. Iglesias, N. L. Abbott, E. K. Mann, and A. J’akli. *ACS Appl. Mater. Interfaces*, 4(12):6884–6890, 2012.
- [44] R. Geršak and S. Čopar. *Crystals*, 10(5):393, 2020.
- [45] J. W. Doane, N. A. Vaz, B.-G. Wu, and S. Žumer. *Appl. Phys. Lett.*, 48(4):269–271, 1986.
- [46] A. Fern’andez-Nieves, D. R. Link, D. Rudhardt, and D. A. Weitz. *Phys. Rev. Lett.*, 92(10):105503, 2004.
- [47] H. Stark. *Phys. Rev. E*, 66(3):032701, 2002.
- [48] F. Alouges, A. Chambolle, and D. Stantejsky. *Arch. Ration. Mech. Anal.*, 241(3):1403–1457, 2021.
- [49] International Union of Pure and Applied Chemistry (IUPAC). magnetic flux density, 2025. IUPAC Compendium of Chemical Terminology (the "Gold Book"), 5th ed., Online version 5.0.0. Accessed 2025-10-01.
- [50] S. Ettinger, C. G. Slaughter, S. Hurtado Parra, J. M. Kikkawa, P. J. Collings, and A. G. Yodh. *Phys. Rev. E*, 108(2):024704, 2023.
- [51] B. Lestriez, A. Maazouz, J.-F. Gerard, H. Sautereau, G. Boiteux, G. Seytre, and D. E. Kranbuehl. *Polymer*, 39(26):6733–6742, 1998.

- [52] M. Samet, A. Kallel, and A. Serghei. *J. Compos. Mater.*, 56(20):3197–3217, 2022.
- [53] G. Skačej and C. Zannoni. *Phys. Rev. Lett.*, 100(19):197802, 2008.
- [54] T. L’opez-Le’on and A. Fern’andez-Nieves. *Colloid Polym. Sci.*, 289(4):345–359, 2011.
- [55] C. B. de Ara’ujo, E. J. L. de Oliveira, M. L. Lyra, L. V. Mirantsev, and I. N. de Oliveira. *Soft Matter*, 18:4189–4196, 2022.
- [56] P. Kurioz, M. Kralj, B. S. Murray, C. Rosenblatt, and S. Kralj. *Beilstein J. Nanotechnol.*, 9:109–118, 2018.
- [57] Y. Ishii, Y. Zhou, K. He, Y. Takanishi, J. Yamamoto, J. J. de Pablo, and T. Lopez-Leon. *Soft Matter*, 16:8169–8178, 2020.
- [58] L. W. Honaker, A. Sharma, A. Schanen, and J. P. F. Lagerwall. *Crystals*, 11(6):687, 2021.
- [59] A. Fern’andez-Nieves, V. Vitelli, A. S. Utada, D. R. Link, M. M’arquez, D. R. Nelson, and D. A. Weitz. *Phys. Rev. Lett.*, 99(15):157801, 2007.
- [60] A. Sharma, R. Kizhakidathazhath, and J. P. F. Lagerwall. *Soft Matter*, 19:2637–2645, 2023.
- [61] E. L. Correia, N. Brown, A. Ervin, D. V. Papavassiliou, and S. Razavi. *Langmuir*, 38(23):7179–7189, 2022.
- [62] J. M. Brake, A. D. Mezera, and N. L. Abbott. *Langmuir*, 19(16):6436–6442, 2003.
- [63] M. S. Manga, L. Higgins, A. A. Kumar, B. T. Lobel, D. W. York, and O. J. Cayre. *Polym. Chem.*, 14(45):5049–5059, 2023.
- [64] C. Monteux. *C. R. Phys.*, 15(8–9):775–785, 2014.

- 
- [65] J. M. G. Lankveld and J. Lyklema. *J. Colloid Interface Sci.*, 41(3):454–465, 1972.
- [66] M. Rubinstein and R. H. Colby. *Polymer Physics*. Oxford University Press, Oxford, 2003.
- [67] P. J. Flory. *Principles of Polym. Chem.* Cornell University Press, Ithaca, NY, 1953.
- [68] A. F. H. Ward and L. Tordai. *J. Chem. Phys.*, 14(7):453–461, 1946.
- [69] J. M. G. Lankveld. *Adsorption of polyvinyl alcohol on paraffin–water interfaces and the properties of paraffin-in-water emulsions stabilized by polyvinyl alcohol*. PhD thesis, Agricultural University Wageningen, Wageningen, The Netherlands, 1970. Ph.D. thesis.
- [70] A. Sharma, V. S. R. Jampani, and J. P. F. Lagerwall. *Langmuir*, 35(34):11132–11140, 2019.
- [71] J. Noh. *Tuning Self-Assembly in Liquid Crystal Shells: From Interfacial- to Polymer-Stabilization*. PhD thesis, University of Luxembourg, 2018.
- [72] T. Lopez-Leon and A. Fern’andez-Nieves. *Phys. Rev. E*, 79(2):021707, 2009.
- [73] International Union of Pure and Applied Chemistry. *Compendium of Chemical Terminology (the “Gold Book”)*. Blackwell Scientific Publications, Oxford, 2 edition, 1997. Online version (2019–), created by S. J. Chalk.
- [74] P. C. Hiemenz and R. Rajagopalan. *Principles of Colloid and Surface Chemistry*. Marcel Dekker, New York, 3rd, revised and expanded edition, 1997. eBook reprint available from Taylor Francis (CRC Press), 2016.
- [75] J. N. Israelachvili. *Intermolecular and Surface Forces*. Academic Press, 3 edition, 2011.

- [76] R. J. Carlton, J. K. Gupta, C. L. Swift, and N. L. Abbott. *Langmuir*, 28(1):31–36, 2012.
- [77] H. Ramezani-Dakhel, M. Sadati, R. Zhang, M. Rahimi, K. Kurtenbach, B. Roux, and J. J. de Pablo. *ACS Cent. Sci.*, 3(12):1345–1349, 2017. PMID: 29296676.
- [78] W. Kunz, J. Henle, and B. W. Ninham. *Curr. Opin. Colloid Interface Sci.*, 9(1-2):19–37, 2004.
- [79] R. J. Carlton, C. D. Ma, J. K. Gupta, and N. L. Abbott. *Langmuir*, 28(35):12796–12805, 2012.
- [80] J. E. Hallett, D. W. Hayward, T. Arnold, P. Bartlett, and R. M. Richardson. *Soft Matter*, 13(33):5535–5542, 2017.
- [81] D. S. Miller and N. L. Abbott. *Soft Matter*, 9(2):374–382, 2013.
- [82] A. V. Dubtsov, S. V. Pasechnik, D. V. Shmeliova, A. Sh. Saidgaziev, E. Gongadze, A. Iglič, and S. Kralj. *Soft Matter*, 14(47):9619–9630, 2018.
- [83] K. He, Y. Zhou, H. Ramezani-Dakhel, J. J. de Pablo, A. Fernandez-Nieves, and T. Lopez-Leon. *Soft Matter*, 18(7):1395–1403, 2022.
- [84] J. Yang, A. Gallegos, C. Lian, S. Deng, H. Liu, and J. Wu. *Chin. J. Chem. Eng.*, 31:145–152, 2021.
- [85] C. Lian, D.-E. Jiang, H. Liu, and J. Wu. *J. Phys. Chem. C*, 120(16):8704–8710, 2016.
- [86] G. Feng, D.-E. Jiang, and P. T. Cummings. *J. Chem. Theory Comput.*, 8(3):1058–1063, 2012.
- [87] A. Reindl, M. Bier, and S. Dietrich. *J. Chem. Phys.*, 146(15):154704, 2017.
- [88] M. J. Rosen. *Frontmatter*, pages i–xiii. John Wiley Sons, Ltd, 2004.

- 
- [89] Q. Li, C. Wen, J. Yang, X. Zhou, Y. Zhu, J. Zheng, G. Cheng, J. Bai, T. Xu, J. Ji, S. Jiang, L. Zhang, and P. Zhang. *Chem. Rev.*, 122(23):17073–17154, 2022.
- [90] C. Tanford. *The Hydrophobic Effect: Formation of Micelles and Biological Membranes*. Wiley-Interscience, New York, 2 edition, 1980.
- [91] J. N. Israelachvili, D. J. Mitchell, and B. W. Ninham. *J. Chem. Soc., Faraday Trans. 2*, 72:1525–1568, 1976.
- [92] A. W. Adamson and A. P. Gast. *Physical Chemistry of Surfaces*. Wiley-Interscience, New York, 6 edition, 1997.
- [93] IUPAC. critical micelle concentration (cmc). IUPAC Compendium of Chemical Terminology (Gold Book), 2014. Accessed 2025-10-02.
- [94] IUPAC. Krafft point. IUPAC Compendium of Chemical Terminology (the "Gold Book"), 2014. Definition per IUPAC Gold Book; online version 5.0.0 (2025).
- [95] W. C. Griffin. *J. Soc. Cosmet. Chem.*, 5:249–256, 1954.
- [96] L. N. Tan, V. J. Orler, and N. L. Abbott. *Langmuir*, 28(15):6364–6376, 2012.
- [97] N. Popov, A. Smirnova, N. Usol'tseva, and P. Popov. *Liq. Cryst. Their Appl.*, 17:34–42, 2017.
- [98] D. Lombardo, M. A. Kiselev, S. Magaz'u, and P. Calandra. *Adv. Condens. Matter Phys.*, 2015(1):151683, 2015.
- [99] D. D. Lasic. *Liposomes: From Physics to Applications*. Elsevier, Amsterdam, 1993.
- [100] T. M. Allen and P. R. Cullis. *Adv. Drug Deliv. Rev.*, 65(1):36–48, 2013.

- [101] M. D’Angelo, A. Fucello, G. Onori, and A. Santucci. Ir study of the water structure in aot-h<sub>2</sub>o-ccl<sub>4</sub> microemulsions. In P. Lagner and O. Glatter, editors, *Trends in Colloid and Interface Science VII*, volume 93 of *Progress in Colloid Polymer Science*, pages 350–352. Steinkopff, 1993.
- [102] M. Kotlarchyk, S.-H. Chen, J. S. Huang, and M. W. Kim. *Phys. Rev. A*, 29(4):2054–2069, 1984.
- [103] C. R. H. Raetz and C. Whitfield. *Annu. Rev. Biochem.*, 71:635–700, 2002.
- [104] J. R. Sheehan, C. Sadlier, and B. O’Brien. *BJA Educ.*, 22(6):224–230, 2022.
- [105] B. S. Park and J.-O. Lee. *Exp. Mol. Med.*, 45(12):e66, 2013.
- [106] C. Schwechheimer and M. J. Kuehn. *Nat. Rev. Microbiol.*, 13(10):605–619, 2015.
- [107] A. Kulp and M. J. Kuehn. *Annu. Rev. Microbiol.*, 64:163–184, 2010.
- [108] M. Mueller, B. Lindner, R. Dedrick, A. B. Schromm, and U. Seydel. *J. Endotoxin Res.*, 11:299–303, 2005.
- [109] Centers for Disease Control and Prevention. Technical information | *E. coli* infection, May 2024. Page last reviewed May 14, 2024.
- [110] A. S. Cross. *Microbiol. Mol. Biol. Rev.*, 87(3):e0004522, 2023.
- [111] N. C. Santos, A. C. Silva, M. A. R. B. Castanho, J. Martins-Silva, and C. Saldanha. *ChemBioChem*, 4(1):96–100, 2003.
- [112] E. T. Rietschel, T. Kirikae, F. U. Schade, U. Mamat, G. Schmidt, H. Loppnow, A. J. Ulmer, U. Zähringer, U. Seydel, F. Di Padova, M. Schreier, and H. Brade. *FASEB J.*, 8(2):217–225, 1994.
- [113] C. A. Schnaitman and J. D. Klena. *Microbiol. Rev.*, 57(3):655–682, 1993.

- 
- [114] C. M. Reynolds and C. R. H. Raetz. *Biochemistry*, 48(40):9627–9640, 2009.
- [115] H. Nikaido. *Microbiol. Mol. Biol. Rev.*, 67(4):593–656, 2003.
- [116] F. Di Lorenzo, C. De Castro, A. Silipo, and A. Molinaro. *FEMS Microbiol. Rev.*, 43(3):257–272, 2019.
- [117] G. Samuel and P. Reeves. *Carbohydr. Res.*, 338(23):2503–2519, 2003.
- [118] S. Snyder, D. Kim, and T. J. McIntosh. *Biochemistry*, 38(33):10758–10767, 1999.
- [119] P. Garidel, M. Rappolt, A. B. Schromm, J. Howe, K. Lohner, J. Andr<sup>a</sup>, M. H. J. Koch, and K. Brandenburg. *Biochim. Biophys. Acta – Biomembr.*, 1715(2):122–131, 2005.
- [120] P. G. Adams, L. Lamoureux, K. L. Swingle, H. Mukundan, and G. A. Monta no. *Biophys. J.*, 106(11):2395–2407, 2014.
- [121] E. Ribi et al. *J. Bacteriol.*, 92:1493–1509, 1966.
- [122] C. Galanos, O. L<sup>u</sup>deritz, E. T. Rietschel, O. Westphal, H. Brade, L. Brade, M. Freudenberg, U. Schade, M. Imoto, H. Yoshimura, S. Kusumoto, and T. Shiba. *Eur. J. Biochem.*, 148(1):1–5, 1985.
- [123] R. S. Munford, J. M. Andersen, and J. M. Dietschy. *J. Clin. Investig.*, 68(6):1503–1513, 1981.
- [124] C. H. Lang, C. Silvis, N. Deshpande, G. Nystrom, and R. A. Frost. *Shock*, 19(6):538–546, 2003.
- [125] A. M. Staub. In R. L. Whistler and M. L. Wolfrom, editors, *Methods in Carbohydrate Chemistry*, volume 5, pages 92–93. Academic Press, New York, 1965.

- [126] O. Westphal and K. Jann. In R. L. Whistler and M. L. Wolfrom, editors, *Methods in Carbohydrate Chemistry*, volume 5, pages 83–91. Academic Press, New York, 1965.
- [127] L. A. Clifton, M. W. A. Skoda, A. P. Le Brun, F. Ciesielski, I. Kuzmenko, S. A. Holt, and J. H. Lakey. *Langmuir*, 31(1):404–412, 2015.
- [128] M. A. Noronha, N. A. D’Angelo, G. P’erez-S’anchez, P. Severino, M. A. Foglio, T. L. Greaves, J. F. B. Pereira, and A. M. Lopes. *J. Mol. Liq.*, 372:121154, 2023.
- [129] J. Aguiar, P. Carpena, J. A. Molina-Bol’ivar, and C. C. Ruiz. *J. Colloid Interface Sci.*, 258:116–122, 2003.
- [130] United States Pharmacopeial Convention. General chapter <85> bacterial endotoxins test. USP–NF (current edition), 2024. Harmonized with Ph. Eur. 2.6.14 and JP 4.01 via ICH Q4B Annex 14. Accessed 2025-10-11.
- [131] U.S. Food and Drug Administration. The bacterial endotoxins specification—points to consider. <https://www.fda.gov/media/183132/download>, 2024. Includes K/M limits: 5 EU/kg (non-intrathecal), 0.2 EU/kg (intrathecal). Accessed 2025-10-11.
- [132] Lonza. How do i convert eu to ng of endotoxin?, 2024. EC-2: 5 EU/ng; current RSE EC-7: ~10 EU/ng. Accessed 2025-10-11.
- [133] European Pharmacopoeia Commission. 2.6.14. bacterial endotoxins. European Pharmacopoeia, General Chapter 2.6.14, 2014. Accessed 2025-10-11.
- [134] European Directorate for the Quality of Medicines HealthCare (EDQM). Recombinant factor c: new ph. eur. chapter available as of 1 july 2020, 2020. Ph. Eur. 2.6.32; effective 1 January 2021. Accessed 2025-10-11.

- [135] M. Piehler, R. Roeder, S. Blessing, and J. Reich. *Microorganisms*, 8(3):418, 2020.
- [136] P. Sondhi, M. H. U. Maruf, and K. J. Stine. *Biosensors*, 10(1):2, 2019.
- [137] L. Mazgaeen and P. Gurung. *Int. J. Mol. Sci.*, 21(2):379, 2020.
- [138] I. H. Lin, D. S. Miller, P. J. Bertics, C. J. Murphy, J. J. de Pablo, and N. L. Abbott. *Science*, 332(6035):1297–1300, 2011.
- [139] S. Jiang, J. Noh, C. Park, A. D. Smith, N. L. Abbott, and V. M. Zavala. *Analyst*, 146(4):1224–1233, 2021.
- [140] K. Saha, S. S. Agasti, C. Kim, X. Li, and V. M. Rotello. *Chem. Rev.*, 112:2739–2779, 2012.
- [141] T. Kuila, S. Bose, P. Khanra, A. K. Mishra, N. H. Kim, and J. H. Lee. *Biosens. Bioelectron.*, 26:4637–4648, 2011.
- [142] K. C. Sekhar and S. S. C. Chakra Rao. *Indian J. Anaesth.*, 58(3):350–352, 2014.
- [143] M. Cremer. *"Uber die Ursache der elektromotorischen Eigenschaften der Gewebe, zugleich ein Beitrag zur Lehre von den polyphasischen Elektrolytketten.* Oldenbourg, 1906.
- [144] W. S. Hughes. *J. Am. Chem. Soc.*, 44(12):2860–2867, 1922.
- [145] E. G. Griffin and J. M. Nelson. *J. Am. Chem. Soc.*, 38(3):722–730, 1916.
- [146] J. M. Nelson and E. G. Griffin. *J. Am. Chem. Soc.*, 38(5):1109–1115, 1916.
- [147] D. R. Th’evenot, K. Toth, R. A. Durst, and G. S. Wilson. *Biosens. Bioelectron.*, 16(1–2):121–131, 2001.
- [148] L. C. Clark and C. Lyons. *Ann. N. Y. Acad. Sci.*, 102:29–45, 1962.

- [149] G. G. Guilbault and Jr. Montalvo, J. G. *J. Am. Chem. Soc.*, 91(8):2164–2165, 1969.
- [150] Yellow Springs News. Yellow springs instruments: Model 23a’s revolutionary legacy, 2021. Accessed 2024-10-29.
- [151] M. C. Vestergaard and E. Tamiya. Nanobiosensors and nanobioanalyses: A review. In M. C. Vestergaard, K. Kerman, I.-M. Hsing, and E. Tamiya, editors, *Nanobiosensors and Nanobioanalyses*, pages 3–20. Springer, Tokyo, 2015.
- [152] Biosensors market size, share trends analysis report by technology (electro-chemical, thermal, piezoelectric), by application, by end-user, and segment forecasts, 2024–2030. Report, Horizon Databook, Healthcare Industry, 2024. Report ID: 978-1-68038-321-8, 110 pages, PDF.
- [153] V. Velusamy, K. Arshak, O. Korostynska, K. Oliwa, and C. Adley. *Biotechnol. Adv.*, 28:232–254, 2010.
- [154] A. Sinha, Dhanjai, A. K. Stavrakis, and G. M. Stojanovi’c. *Talanta*, 244:123425, 2022.
- [155] S. Li, H. Li, Y. Lu, M. Zhou, S. Jiang, X. Du, and C. Guo. *Biosensors*, 13(10):909, 2023.
- [156] S. Khosravi, S. Soltanian, A. Servati, A. Khademhosseini, Y. Zhu, and P. Servati. *Biosensors*, 13(7):684, 2023.
- [157] Z. Lei and B. Guo. *Adv. Sci.*, 9(4):e2102924, 2022.
- [158] R. J. Carlton, J. T. Hunter, D. S. Miller, R. Abbasi, P. C. Mushenheim, L. N. Tan, and N. L. Abbott. *Liq. Cryst. Rev.*, 1(1):29–51, 2013.
- [159] P. Popov, E. K. Mann, and A. J’akli. *J. Mater. Chem. B*, 5(26):5061–5078, 2017.

- 
- [160] G. Barbero and L. R. Evangelista. Adsorption phenomena and anchoring energy in nematic liquid crystals, 2014.
- [161] P. Popov, E. K. Mann, and A. Jákli. *Phys. Rev. Appl.*, 1:034003, 2014.
- [162] Z. Wang, T. Xu, A. Noel, Y.-C. Chen, and T. Liu. *Soft Matter*, 17(18):4675–4702, 2021.
- [163] A. S. Utada, E. Lorenceau, D. R. Link, P. D. Kaplan, H. A. Stone, and D. A. Weitz. *Science*, 308(5721):537–541, 2005.
- [164] Q. Brosseau, J. Vignon, and J.-C. Baret. *Soft Matter*, 10(17):3066–3076, 2014.
- [165] S.-Y. Tang, I. D. Joshipura, Y. Lin, K. Kalantar-Zadeh, A. Mitchell, K. Khoshmanesh, and M. D. Dickey. *Adv. Mater.*, 28(4):604–609, 2015.
- [166] J. Noh, B. Henx, and J. P. F. Lagerwall. *Adv. Mater.*, 28(46):10170–10174, 2016.
- [167] A. Sengupta, S. Herminghaus, and C. Bahr. *Liq. Cryst. Rev.*, 2(2):73–110, 2014.
- [168] S. Sivakumar, K. L. Wark, J. K. Gupta, N. L. Abbott, and F. Caruso. *Adv. Funct. Mater.*, 19(14):2260–2265, 2009.
- [169] Y. Wei and C.-H. Jang. *Sens. Actuators B: Chem.*, 254:72–80, 2018.
- [170] P. Bao, D. A. Paterson, P. L. Harrison, K. Miller, S. Peyman, J. C. Jones, J. Sandoe, S. D. Evans, R. J. Bushby, and H. F. Gleeson. *Lab Chip*, 19(6):1082–1089, 2019.
- [171] D. A. Paterson, P. Bao, R. H. Abou-Saleh, S. A. Peyman, J. C. Jones, J. A. T. Sandoe, S. D. Evans, H. F. Gleeson, and R. J. Bushby. *Langmuir*, 36(23):6436–6446, 2020.

- [172] M. C. D. Carter, D. S. Miller, J. Jennings, X. Wang, M. K. Mahanthappa, N. L. Abbott, and D. M. Lynn. *Langmuir*, 31(47):12850–12855, 2015.
- [173] A. Sharma and J. P. F. Lagerwall. *Liq. Cryst.*, 45(13–15):2319–2328, 2018.
- [174] Y. Xie, Y. Li, H. Lin, X. Wang, W. Liao, Z. Liu, and L. Lin. *Anal. Chem.*, 96(28):11472–11478, 2024.
- [175] A. Sharma, D. Gupta, G. Scalia, and J. P. F. Lagerwall. *Phys. Rev. Res.*, 4(1):013130, 2022.
- [176] N. Popov, L. W. Honaker, M. Popova, N. Usol’tseva, E. K. Mann, A. Jákli, and P. Popov. *Materials*, 11(1):20, 2018.
- [177] R. Qu and G. Li. *Biosensors*, 12:205, 2022.
- [178] N. Popov and J. P. F. Lagerwall. *Front. Soft Matter*, 2, 2022.
- [179] Y. Geng, J. Noh, I. Drevensek-Olenik, R. Rupp, and J. P. F. Lagerwall. *Liq. Cryst.*, 44(11-12):1924–1938, 2017.
- [180] Y. Geng, J. H. Jang, K. G. Noh, J. H. Noh, J. P. F. Lagerwall, and S. Y. Park. *Eur. Phys. J. Spec. Top.*, 6(1):1700923, 2018.
- [181] R. Nandi and S. K. Pal. *Analyst*, 143(5):1046–1052, 2018.
- [182] K. Yuan, R. Huang, K. Gong, Z. Xiao, J. Chen, S. Cai, J. Shen, Z. Xiong, and Z. Lin. *Anal. Bioanal. Chem.*, 415(18):4401–4410, 2023.
- [183] R. Xie, N. Li, Z. Li, J. Chen, K. Li, Q. He, L. Liu, and S. Zhang. *Biosensors*, 12(9):758, 2022.
- [184] H.-L. Liang, S. Schymura, P. Rudquist, and J. P. F. Lagerwall. *Phys. Rev. Lett.*, 106(24):247801, 2011.

- 
- [185] J. Noh, Y. Wang, H.-L. Liang, V. S. R. Jampani, A. Majumdar, and J. P. F. Lagerwall. *Phys. Rev. Res.*, 2(3):033160, 2020.
- [186] G. J. Fleer and J. van Male. *Macromolecules*, 32(3):825–844, 1999.
- [187] R. J. Fong, A. Robertson, P. E. Mallon, and R. L. Thompson. *Polymers*, 10(9):1036, 2018.
- [188] C. Liu, X. Yu, Y. Li, X. Zhao, Q. Chen, and Y. Han. *Polymer*, 229:123960, 2021.
- [189] F. Mura and A. Zaccone. *Phys. Rev. E*, 93(4):042803, 2016.
- [190] I. Pereiro, A. Fomitcheva Khartchenko, L. Petrini, and G. V. Kaigala. *Lab Chip*, 19(14):2296–2314, 2019.
- [191] J. H. Sung and M. L. Shuler. *Biomed. Microdevices*, 11(4):731–738, 2009.
- [192] H. Song, D. L. Chen, and R. F. Ismagilov. *Angew. Chem. Int. Ed.*, 45(44):7336–7356, 2006.
- [193] D. L. Chen and R. F. Ismagilov. *Curr. Opin. Chem. Biol.*, 10(3):226–231, 2006.
- [194] N. Garti and A. Benichou. Recent developments in double emulsions for food applications. In *Gums and Stabilizers for the Food Industry*, volume 7. Marcel Dekker, Inc., New York, 2004.
- [195] M. Matos, G. Guti’errez, O. Iglesias, J. Coca, and C. Pazos. *J. Food Eng.*, 166:212–220, 2015.
- [196] T. Luo and Z. Wei. *Food Front.*, 4(4):1622–1642, 2023.
- [197] G. Muschiolik and E. Dickinson. *Compr. Rev. Food Sci. Food Saf.*, 16(3):532–555, 2017.

- [198] D. Seč, T. Lopez-Leon, M. Nobili, C. Blanc, A. Fernandez-Nieves, M. Ravnik, and S. Žumer. *Phys. Rev. E*, 86(2):020705, 2012.
- [199] A. M. Lowe and N. L. Abbott. *Chem. Mater.*, 24(5):746–758, 2012.
- [200] A. Darmon, M. Benzaquen, S. Čopar, O. Dauchot, and T. Lopez-Leon. *Soft Matter*, 12(46):9280–9288, 2016.
- [201] S. Fumeron and B. Berche. *Eur. Phys. J. Spec. Top.*, 232(11):1813–1833, 2023.
- [202] D. J. Griffiths and D. F. Schroeter. *Introduction to Electrodynamics*. Cambridge University Press, Cambridge, 5 edition, 2023.
- [203] M. A. Bates, G. Skačej, and C. Zannoni. *Soft Matter*, 6(3):655–663, 2010.
- [204] M. A. Bates. *Liq. Cryst.*, 45(13-15):2390–2399, 2018.
- [205] L. Yu, M. Tan, B. Ho, J. L. Ding, and T. Wohland. *Anal. Chim. Acta*, 556(1):216–225, 2006.
- [206] L. Rayleigh. *Proc. Lond. Math. Soc.*, 10(1):4–13, 1878.